AD-A235 718

Geotechnical Properties of Periplatform Carbonate Sediments

DTIC
ELECTE
MAY 15 1991
S
B
D

D. L. Lavoie
Seafloor Geosciences Division
Ocean Science Directorate
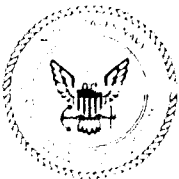
91 5 15 019

Foreword

Seafloor geoacoustic models are basic information required to understand acoustic propagation in bottom-interacting situations, such as slope and shelf environments. This report, supported by the Naval Oceanographic and Atmospheric Research Laboratory's* basic research program, details the relationship between effective stress and subbottom depth and geotechnical and geoacoustic properties, including porosity, permeability, compressional and shear wave velocity, shear modulus, and density for midwater depth carbonate sediments. The results can be used to support Mine Warfare, Mine Countermeasures, Amphibious Warfare, Special Warfare and Antisubmarine Warfare efforts.

W. B. Moseley
Technical Director
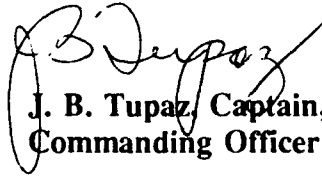
J. B. Tupaz, Captain, USN
Commanding Officer

Executive Summary

Periplatform sediments from the slopes north of Little Bahama Bank and Exuma Sound were studied extensively for use as a model for sediments in other similar environments within the upper 50 to 150 m below the sea floor where mechanical consolidation is the dominant diagenetic process. The depth at which consolidation is the dominant diagenetic process varies, depending on sediment fabric and grain size. Matrix-supported sediments have a higher proportion of metastable minerals and undergo diagenesis earlier and at shallower depths than grain-supported sediments.

Periplatform sediments consolidate differently than marine clays. Overall, they consolidate less and do not reach as low a void ratio as do marine clays under mechanical consolidation. A volume change model developed from deep-water carbonates appears to be equally applicable to shallow-water and midwater carbonates when consolidation is the dominant process. The major differences in periplatform sediment properties affected by consolidation seem to be roughly controlled by fabric grain size and particle type. Grain-supported sediments have higher permeabilities than matrix-supported sediments because the pore throats are protected by grains. The relationship between permeability and porosity is also controlled by the fabric; total porosity is not a good predictor of permeability. In addition, porometry changes during consolidation revealed changes in pore size and numbers that were a function of matrix composition and grain support.

Physical and acoustic properties vary as a function of effective stress and have been derived for both grain- and matrix-supported periplatform sediments. Compressional wave velocities of periplatform sediments are similar to those predicted using regression equations derived for deep-water carbonates. However, shear modulus and shear wave velocity, measured using duomorphs in the laboratory during consolidation, are significantly lower than predicted using deep-water regression equations. Duomorph technology was used successfully to measure shear modulus and shear wave velocity in the laboratory, although further theoretical work may have to be done to improve their performance at high effective stress levels.

i

Acknowledgments

Contents

iii

Geotechnical and Geoacoustic Properties of Periplatform Sediments

Synopsis

Geoacoustic models of the seafloor are basic information required to understand acoustic propagation in bottom-interacting situations. A geoacoustic model, as defined by E. L. Hamilton (1980), is a model of the real sea floor with emphasis on measured, extrapolated, and predicted values of those properties important in underwater acoustics and aspects of geophysics involving sound transmission. Implicit in this definition is the understanding that measured data are frequently not available for modeling and must be estimated and predicted. Valid predictions can be made only when the seafloor properties within the range of interest (i.e., the water-sediment interface to a depth of several hundred meters, depending upon frequency) are well understood. The sediment properties required for modeling acoustic propagation include compressional and shear wave velocity, attenuation, and density as a function of depth or effective stress. These parameters are well understood for terrigenous marine sediments and deep-water carbonate sediments, i.e., foraminiferal oozes. Little data of the appropriate type and resolution is available for carbonate sediments found in shallow-water and midwater depth environments in less than 2000 m of water.

The research reported in the appendix is an outgrowth of earlier efforts to provide geoacoustic models to the U.S. Navy for carbonate environments occurring in less than 2000-m water depth (Lavoie and Matthews, 1983; Lambert and others, 1984; Lavoie, 1984). Because of the lack of data, geoacoustic parameters for sediments in these areas had to be estimated from measurements on deep-water carbonate sediments of very different composition.

The Naval Oceanographic and Atmospheric Research Laboratory participated in Ocean Drilling Leg 101. During this exercise shallow-water and midwater depth carbonate sediments from a few deep drill holes were studied extensively by participating scientists. Many differences in geotechnical and geoacoustic properties between these carbonates and deeper water carbonate sediments were

noted. In March 1987, it became possible to return to the Bahamas to collect a number of shallow piston cores, with the material recovered dedicated to geotechnical analyses. These cores form the basis of this research, and earlier Leg 101 data were included where relevant.

The research reported in the appendix has three objectives. The first objective is to study the consolidation behavior of samples from these cores. The purpose is to characterize the physical and mechanical properties of typical carbonates sediments found on slopes to depths of 2000 m. It is assumed that sediments found in the Bahamas are typical carbonate sediments and can be used as a model for carbonate sediments in other regions. Therefore, geoacoustic properties of these carbonate sediments are defined so that data can be extrapolated to regions comprised of similar sediments.

The second objective is to adapt a technique, originally designed to measure the complex modulus of solid propellant, to measure the shear modulus of sediment under loading conditions in the laboratory. To this end, multiple sensors called "duomorphs" were built and tested in consolidometers under various conditions and with different sediments. The ultimate goal is to develop a quick and reliable method for measuring shear velocity not only in the lab but in situ.

Finally, realizing that the fabric of a sediment profoundly affects the properties and the behavior of a sediment, the third objective is to look at the structure of the sediment in terms of its constituent particles, especially the arrangement of these particles and pore spaces as a function of effective stress. The results are integrated into a model for periplatform sediments that can be used to estimate and predict geotechnical and geoacoustic parameters for similar sediments in other regions.

Results and Recommendations

A summary of the relevant results follows: Periplatform oozes consolidate differently than marine clays. They consolidate less overall and do not reach as low

a void ratio as do marine clays under mechanical consolidation.

Compressional wave velocities of periplatform oozes measured here are similar to those predicted by Hamilton (1980) for deep-water carbonate sediments. However, the shear modulus and shear wave velocity values are significantly lower than predicted by Hamilton, but are essentially the same as those measured by Schultheiss (1985) on nanofossil oozes.

The independent measurements of shear wave velocity using duomorphs duplicated the original bender element transducer measurements therefore, the early measured values were likely valid, and duomorphs appear to be a feasible alternative to shear wave bender-element transducers. Further theoretical work may have to be done to improve their performance at higher effective stress levels. In their present state, the duomorphs should be adaptable to an in situ configuration.

The relationship between permeability and porosity depends on the sediment fabric. Permeability, porosity, and porometry determinations using image analysis reveal changes in fabric that are difficult to determine visually in SEM micrographs. In general, permeability decreases with consolidation. Samples composed of aragonite needles have the highest permeability; samples with coccolith matrices have the lowest. Grain-supported sediments tend to have higher permeabilities because the pore throats are protected by the grains and are less affected by consolidation than they are in matrix-supported sediments. Carbonate samples with grain-supported fabrics display slight changes in

permeability until loads sufficient to cause grain crushing are reached. At that point, permeability suddenly decreases. When samples of all fabric types are considered together, total porosity is not a good predictor of permeability. Intraparticle porosity and interparticle porosity may not be interconnected and may not contribute to permeability. Porosity in sediment with aragonite needle matrices is very different from porosity in sediments with matrices consisting of platey grains.

Changes in porometry due to consolidation are a function of fabric changes. Predominantly matrix-supported samples exhibited an increase in number of pores per unit area and a decrease in average pore size as a result of consolidation. Samples composed predominantly of aragonite needle matrices displayed opposite results.

To predict these properties as a function of effective stress, the following model has been compiled. It is recommended when dealing with periplatform slope carbonates that the properties be estimated using the regression equations outlined.

References

Hamilton, E. L (1980). Geoacoustic modeling of the sea floor. *Journal Acoustical Society America* 68(5):1313-1340.

Schultheiss, P. J. (1985). Physical and Geotechnical Properties of Sediments from the Northwest Pacific: Deep Sea Drilling Project Leg 86. In: Heath, G. R., Bruckle, L. H., and others (eds), *Initial Reports, Deep Sea Drilling Project*, 86, US Government Printing Office, Washington, pp. 701-722.

Physical and Geoacoustic Properties of Periplatform Sediments

	Total	Grain-supported	Matrix-supported
Porosity			
(average)	56.5%	———	———
as (f) of σ'	$n = 0.58 - 1.028 \times 10^{-4}(\sigma') + 3.216 \times 10^{-8}(\sigma'^2) - 3.841 \times 10^{-12}(\sigma'^3)$		
Permeability (cm/s)			
(average)	———	10^{-4}	$10^{-5},\ 10^{-6}$
as (f) of σ'	———	$k = 4.229 \times 10^{-4}\,(\sigma'^{-.821})$;	$k = 2.69 \times 10^{-4}\,(\sigma'^{-.664})$, $\quad k = 2.05 \times 10^{-5}\,(\sigma'^{-.4316})$
as (f) of n	$k = 1.424 \times 10^{-4}\,(n^{6.739})$	$k = 1.486 \times 10^{-4}\,(n^{6.2345})$	$k = 1.665 \times 10^{-4}\,(n^{7.132})$
Wet Bulk Density (Mg/m³)			
(average)	1.74	1.78	1.72
as (f) of σ'	$\rho = 1.74 + 3.499 \times 10^{-6}(\sigma')$		
Vp (m/s)			
(average)	1596	1635	1544
as (f) of σ'	$1596 + .011\,\sigma' + 1.71 \times 10^{-6}(\sigma'^2)$	$1635 + .045\,(\sigma') - 6.547 \times 10^{-6}(\sigma'^2)$;	$1544 + .002\,\sigma' + 4.231 \times 10^{-6}(\sigma'^2)$;
Vs (m/s)			
(average)	23.39		
as (f) of σ'	$Vs = 23.39\,(\sigma'^{.0994})$		
as (f) of Vp	$Vs = -2.087 \times 10^5 + 258.98\,(Vp) - 8.031 \times 10^{-2}\,(Vp^2)$	{between 0-2000 kPa or Vp = 1580-1614}	
	$Vs = -1157 + 1.3957\,(Vp) - 4.0164 \times 10^{-4}(Vp^2$,	{between 2001-5000 kPa or Vp = 1615-1695}	
G (N/m²)			
(average)	9.46×10^5 N/m²		
as (f) of σ'	$G = 9.46 \times 10^5\,(\sigma'^{.2124})$		

Legend:
Geotechnical properties (porosity, permeability, wet unit weight) (38 samples)
Geoacoustic properties (Shear modulus (G), compressional velocity (Vp), shear wave velocity (Vs)) (7 samples)

Appendix

Geotechnical Properties of
Periplatform Carbonate Sediments

Dawn A. Lavoie

GEOTECHNICAL PROPERTIES OF PERIPLATFORM

CARBONATE SEDIMENTS

A Dissertation

by

DAWN L. LAVOIE

Approved as to style and content by:

William Bryant
(Chair of Committee)

Wayne Dunlap
(Member)
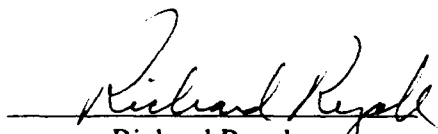
Richard Rezak
(Member)

Richard Bennett
(Member)
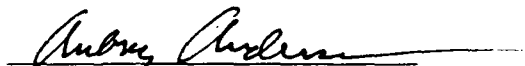
Aubrey Anderson
(Member)

Gilbert T. Rowe
(Head of Department)

December 1989

GEOTECHNICAL PROPERTIES OF PERIPLATFORM

CARBONATE SEDIMENTS

A Dissertation

by

DAWN L. LAVOIE

Submitted to the Office of Graduate Studies of
Texas A&M University
in partial fulfillment of the requirements for the degree of

DOCTOR OF PHILOSOPHY

December 1989

Major Subject: Oceanography

ABSTRACT

Geotechnical Prope ties of Periplatform

Carbonate Sediments. (December 1989)

Dawn L. Lavoie, B.A. University of New Hampshire

M.A. University of Rhode Island

M.S. University of New Orleans

Chair of Adv sory Committee: Dr. William Bryant

Periplatform sediments from the slopes north of little Bahama Bank and Exuma Sound were studied extensively for use as a model for sediments in other similar environments within the upper 50 to 150 meters below the seafloor where mechanical consolidation is the dominant diagenetic process. The depth at which consolidation is the dominant diagenetic process varies, depending on sediment fabric and grain size. Matrix-supported sediments have a higher proportion of metastable minerals and undergo diagenesis earlier and at shallower depths than grain-supported sediments.

Periplatform sediments consolidate differently than marine clays. Overall, they consolidate less and do not reach as low a void ratio as do marine clays under mechanical consolidation. A volume change model developed from deep-water carbonates appears to be equally applicable to shallow- and mid-water carbonates when consolidation is the ? ...inant process. The major differences in periplatform sediment properties affected by consolidation seem to be roughly controlled by fabric grain size and particle type. Grain-supported sediments have higher permeabilities than matrix-supported sediments because the pore throats are protected by grains. The relationship between permeability and porosity is also controlled by the fabric; total porosity is not a good predictor

of permeability. In addition, porometry changes during consolidation revealed changes in pore size and numbers that were a function of matrix composition and grain support.

Physical and acoustic properties vary as a function of effective stress and have been derived for both grain-and matrix-supported periplatform sediments. Compressional wave velocities of periplatform sediments are similar to those predicted using regression equations derived for deep-water carbonates. However, shear modulus and shear wave velocity, measured using duomorphs in the laboratory during consolidation, are significantly lower than predicted using deep-water regression equations. Duomorph technology was used successfully to measure shear modulus and shear wave velocity in the laboratory, although further theoretical work may have to be done to improve their performance at high effective stress levels.

DEDICATION

To my husband

ACKNOWLEDGMENTS

TABLE OF CONTENTS

LIST OF FIGURES

Figure   Page

LIST OF TABLES

CHAPTER I

INTRODUCTION, BACKGROUND, AND SAMPLE DESCRIPTION

INTRODUCTION

Seafloor geoacoustic models are basic information required to understand acoustic propagation in bottom-interacting situations. A geoacoustic model is a model of the real seafloor with emphasis on measured, extrapolated and predicted values of those properties important in underwater acoustics and aspects of geophysics that involve sound transmission (Hamilton 1980). Implicit in this definition is the understanding that measured data are frequently not available for modeling and must be estimated and predicted. Valid predictions can only be made when the seafloor properties within the range of interest (i.e., the water-sediment interface to a depth of several hundred meters, depending upon frequency) are well understood. The sediment properties required for modeling acoustic propagation include compressional and shear wave velocity, attenuation, and density as a function of depth or effective stress. These parameters are well understood for terrigenous marine sediments and deep-water carbonate sediments, i.e., foraminiferal oozes. Little data of the appropriate type and resolution are available for carbonate sediments found in shallow- and mid-water depth environments in less than 2000 m of water.

In addition to naval acoustic requirements for accurate bottom descriptions, the academic community, industry and other government agencies have significant interest in geotechnical research on seafloor stability, which requires quantitative seafloor environmental data (Bennett and others 1982). The relationship between sediment processes (such as erosion, slumping, transport, and consolidation) plays a major role in seafloor stability.

The research reported here is an outgrowth of earlier efforts to provide geoacoustic models to the US Navy for carbonate environments that occur in less than 2000 m water depth (Lavoie and

---

The style and format of this dissertation follow that of Geo-Marine Letters.

Matthews 1983; Lambert and others 1984; Lavoie 1984). Because of the lack of data, geoacoustic parameters for sediments in these areas had to be estimated from measurements on deep-water carbonate sediments of very different composition. During my participation on Ocean Drilling Leg 101, in which shallow- and mid-water depth carbonate sediments from 11 deep drill holes were studied extensively by participating scientists, I noted many differences in geotechnical and geoacoustic properties between these carbonates and deeper-water carbonate sediments. Because sample material was limited, a complete geoacoustic description of these samples was not possible. In March of 1987, I returned to the Bahamas to collect a number of shallow piston cores. The material recovered was used solely for geotechnical analyses. These cores form the basis of this dissertation; the earlier Leg 101 data are included where relevant.

Rationale and Objectives

Relatively little is known about the mechanical consolidation properties of shallow-water slope carbonate sediments. These consolidation properties are important because physical and acoustic properties are dependent on the consolidation state of the sediment. Some of the research issues include the following:

  a. Can the relationships between effective stress and geotechnical and geoacoustic parameters be derived for shallow-water carbonate sediments?

  b. Can predictive models be developed based on these relationships, and will the models be valid for *in situ* sediments?

  c. How does sediment fabric affect consolidation and related properties?

This research is designed to answer the above questions. The first objective is to study the laboratory consolidation behavior of samples from these 1987 piston cores. The purpose is to characterize the physical and mechanical properties of carbonate sediments found on slopes to depths of 2000 m. It is assumed that sediments found in the Bahamas can be used as a model for carbonate sediments in other regions (Austin, Schlager, Palmer and others 1986). Therefore,

geoacoustic properties of these carbonate sediments are determined so that data can be extrapolated to regions comprised of similar sediments. This work, in addition to a discussion of traditional consolidation theory, is reported in Chapter II.

The second objective is to adapt a technique, originally designed to measure the complex modulus of solid propellant (Briar and others 1976), for use in the laboratory to measure the shear modulus of sediment under loading conditions. To this end, multiple sensors called "duomorphs" were built and tested in consolidometers under various conditions and with different sediments. The ultimate goal is to develop a quick and reliable method for measuring shear velocity not only in the lab but *in situ*. A complete discussion of duomorph sensing and duomorph design can be found in the Appendix A. The results of duomorph measurements of shear modulus and shear wave velocity on periplatform sediments are incorporated into Chapter II.

Because the fabric of a sediment profoundly affects the properties and behavior of a sediment (Bennett and others 1981, Bryant and Bennett 1988), the third objective is to define the structure of the sediment in terms of its constituent particles, especially the arrangement of these particles and pore spaces as a function of effective stress. Much of this work, which involved scanning electron microscopy and image analysis techniques, was done in the summers of 1988 and 1989 in cooperation with Dr. Richard Rezak of Texas A&M University. A discussion of sediment fabric measurement and a more quantitative image analysis description of a few typical samples is included. Scanning electron micrographs depicting each sample can be found in Appendix B.

One of the main thrusts is to develop a reliable geoacoustic model for periplatform sediments. Such a model can be used to estimate and predict geotechnical and geoacoustic parameters for sediments in other similar environments. The geoacoustic model and discussion is found in Chapter III.

SHALLOW AND MID-WATER DEPTH CARBONATE SEDIMENTS

The constituent particles of calcium carbonate sediments are formed as the result of chemical and biochemical processes; they are comprised of the remains of benthonic organisms, detritus abraded from larger carbonate particles, accumulations of planktonic biota, and possibly from direct

precipitation from seawater (Wilson 1975). On carbonate shelves and slopes, in shallow- and mid-water depths, where bank-derived aragonite and magnesian calcite are mixed with *in situ* low-magnesian calcite and aragonite, the sediment is termed periplatform sediment (Schlager and James 1978). The assumption is that the bulk aragonite portion is primarily bank derived. In fact, well-preserved aragonitic pteropods gradually change to severely dissolved pteropod remains in these samples; therefore, a significant portion of aragonite may be derived from oceanic planktonic biota rather than bank derived. These sediments, which we will continue to call periplatform sediment, differ from deep-water oozes in the heterogeneity of various constituent particles and in the large component of reef-derived debris. Shelf and reef sediments are formed by the accumulation of skeletons of three or four groups of large organisms: corals, calcareous algae, molluscs, and bryozoans. Microfossils do not generally occur in large enough numbers on the shelf to form sediments; they are simply too small to overcome the dilution factor of megafossils that have large volumes per specimen (Kennett 1982). Microfossils found in periplatform oozes are predominantly a planktonic contribution. Typical constituents of periplatform oozes include mollusc fragments, algal remnants, pteropods, coccoliths, foraminifers, sponge spicules, rhabdoliths, aragonite needles, pellets, and shell debris. In contrast, deep-water carbonate sediments tend to have fewer types of particles, since the shelf-derived components are missing. The predominant deep-water calcareous constituents are planktonic foraminifers and nanofossils.

DISTRIBUTION OF CARBONATE SEDIMENTS

Because most surface waters are saturated with dissolved calcium carbonate, there is no tendency for tests to dissolve in upper waters immediately after an organism dies. However, due to the pressure and temperature effects on the carbonate equilibrium reaction with increasing depth, the subsurface waters become increasingly undersaturated in calcium carbonate. Increased calcium carbonate solution at depth is the primary factor that controls carbonate distribution and is largely independent of the amount of biologic productivity that occurs in surface waters (Kennett 1982). Calcium carbonate sediments begin undergoing change from the moment of deposition. It has long been accepted that the concentration of calcium carbonate in marine sediments decreases with

OCEAN SEDIMENT DISTRIBUTION
(AFTER ROCKER, 1985)

SHALLOW-WATER CARBONATES   CALCAREOUS OOZE
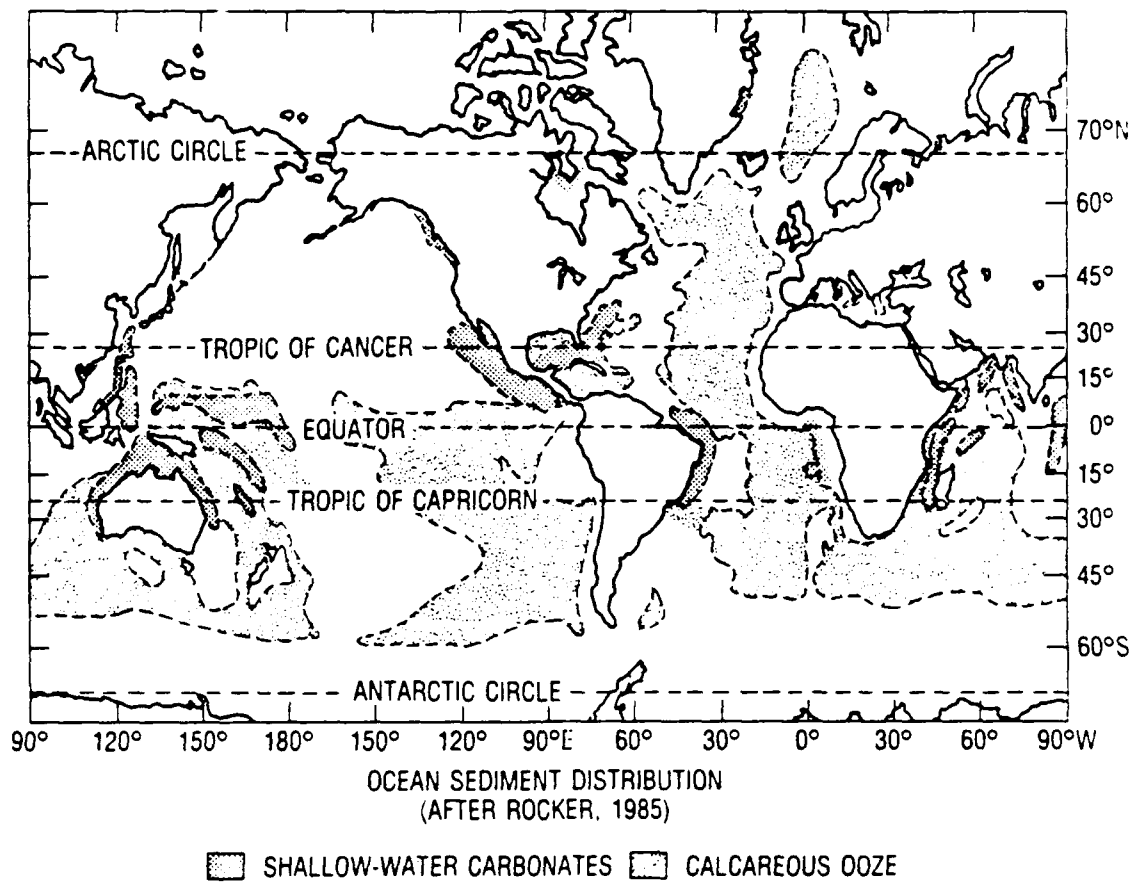
Figure 1. Distribution of calcium carbonate sediments in the world's oceans. Shallow-water carbonates are found in water depths to 2000 m and are called periplatform oozes when they consist of a mixture of bank-derived and planktonic organisms.

depth of water (Bathurst 1970), and that the decrease with overlying water depth of calcium carbonate concentration in carbonate sediments is the result of dissolution of tests (Berger and others 1976). Most calcium carbonate sediments are composed of tests of organisms because inorganic precipitation of calcium carbonate is strongly inhibited by the presence of magnesium ions and by dissolved inorganic matter (Edmond 1974). The depth at which dissolution of tests can first be observed microscopically has been termed the "lysocline" by Berger (1968) and varies with species. Somewhere below the lysocline lies a depth at which the rate of input of solid carbonate due to settling is equalled by the rate of carbonate dissolution. This "carbonate compensation depth" marks the lower boundary of a transition zone between high and low carbonate concentration in the water column. The transition zone is also called the "calcite corrosion zone" (Berger and others 1976).

Calcium carbonate sediments occur in large portions of the world's oceans (Fig. 1). Two-thirds of the carbonate sediments depicted are deep water (below 2000 m) carbonate sediments, predominantly foraminiferal oozes. Shallow-water carbonates that occur on modern reefs and on continental shelves account for about 9% of carbonate deposition, while those on the continental slopes account for 24% (Kennett 1982). In spite of the small numbers of shallow- and mid-water carbonate sediments above 2000 m, they are important beyond their numbers because they are located in areas of critical naval importance. It is evident from the map that various choke points and strategic areas are shallower than the carbonate compensation depth, and therefore are floored with carbonate sediments. Such areas as the Caribbean, the straits of Florida, all of the Bahamas, the Yucatan Channel, and the straits between Cuba and Florida have very little terrigenous input, and the upper surficial sediments are close to 100% calcium carbonate. The shelves and slopes of such critical areas as the Red Sea, the Gulf of Aden, and the Gulf of Oman are also dominated by calcium carbonate. Kings Bay, GA, and southern California have significant carbonate components to their bottom sediments. Finally, less important strategic areas, such as the islands of the South Pacific and the northern shelves and slopes of Australia, are completely carbonate sediments.

BACKGROUND

Once deposition of carbonate sediments has occurred, a number of processes ensue. Catastrophic processes that result in downslope movement and rapid burial preserve much of the calcium carbonate from alteration. Chemical and biological processes take place at the sediment surface after deposition, and they alter the characteristics of the sediment. However, the focus of this study is primarily on the physical processes that occur after burial.

The principle of effective stress asserts that effective stress, also called sediment or intergranular pressure, controls volume change and sediment strength behavior (Mitchell 1976). As sediment consolidates with the increasing load caused by continuous sedimentation, a realignment of grains and a more compact structure results as the fluid is driven out of the sediment (Richards and Hamilton 1967; Bryant and Bennett 1988). Effective stress is defined as the total geostatic stress minus the total pore fluid pressure and is expressed as:

$$\sigma' = \sigma - \mu,$$

where σ' is the effective stress, σ is the total geostatic stress, and μ is the pore fluid pressure. In normally consolidated sediments, the effective stress is greater with increasing depth below the sediment-water interface. Many acoustic and engineering properties depend on the strength, the compressibility and the amount of pore pressure in the sediment. Therefore, as sediment consolidates, acoustic and engineering properties will undergo change. *The effective overburden stress, developed with increasing depth and increasing consolidation below the seafloor, drives the time-dependent changes in geotechnical and geoacoustic properties.* This study is designed upon this principle.

Volume change behavior, or conventional consolidation theory, as presented by Terzaghi (1925), assumes the following conditions:

1. The sediment is saturated.

2. Sediment obeys Darcy's law.

3. Fluid flow is one-dimensional.

4. Small strains exist, i.e., particles do not move out of position.

5. The principle of effective stress governs sediment behavior.

6. Conservation of mass exists.

7. Sediment properties such as porosity, permeability and velocity do not change with depth or time.

All of the above conditions apply to these sediments in the laboratory. However, in carbonate environments and in environments where terrigenous sediments are diluted with calcium carbonate sediments, sediment properties indeed change with time. Carbonate sediments are very susceptible to post-deposition diagenesis, including dissolution, cementation, consolidation, bioerosion, and chemical alteration due to biological activity. Matthews (1980) noted that sudden and marked changes of compressional velocity in sediment sections are associated only with biogenic sediments, excluding lithologic changes. These changes are the result of carbonate sediments forming limestones as a consequence of post-depositional cementation. Although results from laboratory consolidation tests do not replicate *in situ* processes exactly, they provide much useful data that can be extrapolated to the unaltered, i.e., upper, portions of the sedimentary column.

Calcium carbonate sediments do not consolidate to as low a void ratio as terrigenous sediments (Rezak 1974). In fact, there has been an ongoing controversy over the past 20 years as to whether calcium carbonate sediments do consolidate and, if so, to what extent. Bathurst (1970) notes that unconsolidated carbonate sediments have porosities of 50-70%, while the lithified end products have porosities as low as 2-3%, and that the lithified muds show no overt signs of consolidation; foraminifer tests survive uncrushed. He concludes that consolidation occurs only until grains (those particles large enough for matrix material to fit within pores formed by the particles in contact) come into contact and that cement is precipitated within pores in sufficient quantities to stiffen the sediment framework enough to resist further consolidation. Ricken (1987) developed from field measurements the carbonate compaction law, a tool for estimating percent consolidation

(or compaction) and porosity based on the amount of calcium carbonate in a sediment. The documented results indicate that the amount of consolidation decreases with increasing carbonate content. Demars and others (1976) have gone so far as to suggest that carbonate content should be used as an index property, a parameter that describes or distinguishes the behavior of one sediment from another. They report that (1) high-carbonate samples are less compressible than low-carbonate samples and (2) sediments exhibit granular behavior when carbonate contents are greater than 40% and exhibit cohesive behavior when carbonate contents are less than 40%.

To explain the volume change behavior in carbonate sediments that contain more than 80% calcium carbonate, Schlanger and Douglas (1974) developed a model that explains the ideal transition of oozes to chalk and subsequently to limestone (Fig. 2). Their model, based on Pacific deep-water oozes, proposes that the change occurs in two stages. The first stage, within the shallow burial realm (200 m), results in a porosity reduction from approximately 80% to 60%, and the predominant mechanism is consolidation. The second stage, within the deep burial realm (to 1000 m), results in a porosity reduction from approximately 65% to approximately 40%. The dominant process in this stage is cementation, and consolidation is subordinate. The implication is that within the shallow burial regime, where consolidation is the dominant mechanism, velocity/depth functions should be predictable and fairly smooth. Only below 200 m should velocity/depth and density/depth functions vary erratically and in step-like fashion as cementation radically alters the sediment framework. The model, illustrated in Figure 2, accounts for the following conditions and allows calculation of volume change (Schlanger and Douglas 1974):

1. Porosity reduces from a maximum of 80% to a minimum of 40% during consolidation; approximately half this reduction occurs in the upper 200 m.

2. Planktonic foraminifers and many coccoliths disappear.

3. Interstitial cement and calcite fillings in remaining benthonic foraminifers develop.

4. Cement develops to such a degree that the elastic properties and, therefore, compressional and shear wave velocities, diverge significantly from values predicted for sediments, which are merely mechanically consolidated.

OOZE-CHALK-LIMESTONE MODEL

Ooze Stage   ↑   Chalk Stage   ↑ Limestone Stage
            water   water

Shallow burial   Deep burial
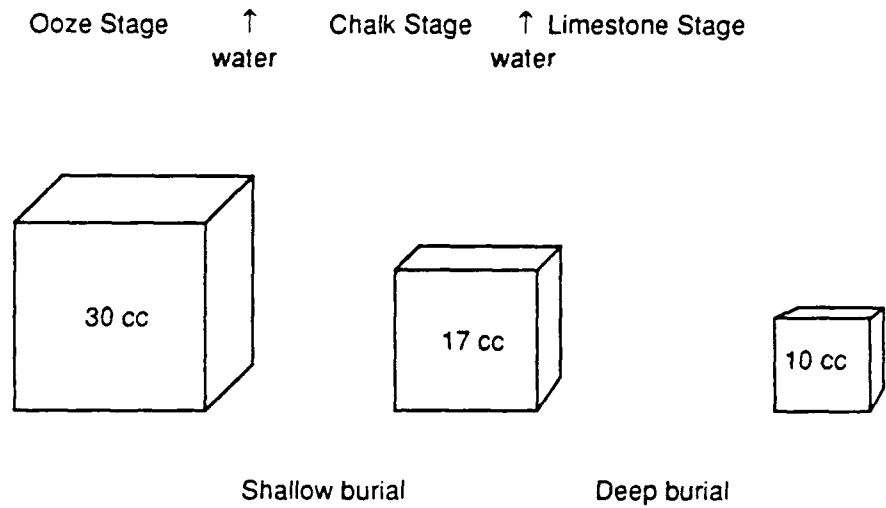
$$H_{ooze} = \frac{(1 - \phi chalk)}{(1 - \phi ooze)} H_{chalk} \qquad H_{chalk} = \frac{(1 - \phi limestone)}{(1 - \phi chalk)} H_{limestone}$$

where

H_{ooze} = the original thickness of the ooze interval,

H_{chalk} = the thickness of the chalk interval,

$H_{limestone}$ = the thickness of a limestone derived from the ooze,

ϕ_{ooze} = original porosity of ooze (i.e. 80%),

ϕ_{chalk} = porosity of the chalk interval, and

$\phi_{limestone}$ = porosity of limestone (i.e. 40%).

Figure 2. Volume change model for deep-water pelagic oozes (modified from Schlanger and Douglas, 1974).

Numerous Pacific Deep Sea Drilling Project (DSDP) sites, including sites 62, 63, and 65, demonstrate the existence of unlithified carbonate oozes to great depths (900 –1000 m) below the seafloor. Johnson and others (1978) looked at these same Pacific carbonate sediments and predicted relatively smooth velocity/density/depth functions based on sonobuoy data throughout the entire sediment column. Lower DSDP shipboard-measured values of velocity and density are explained on the basis of drilling disturbance (Johnson and others 1978). Regression equations were developed for density, compressional wave and shear wave velocity/depth functions for these same Pacific foraminiferal oozes (Hamilton and others 1982; Hamilton 1980). Results from Ocean Drilling Program (ODP) sites in the Bahamas demonstrate that velocity/depth functions vary considerably. The presence of chalk (cemented coccolith oozes) was found in ODP sites in the Bahamas at much shallower depths below the seafloor: at 150 m at sites 630, 631, and 632 on northern Little Bahama Bank, and between 50 and 150 m at sites 633 and 634 in Exuma Sound (Austin, Schlager, Palmer, and others 1986). Clearly there is much disparity in the lithification behavior and, therefore in the velocity/depth and density/depth relationships of carbonate sediments.

Predicting the velocity/depth and density/depth functions of shallow- and mid-water depth carbonate sediments has been a problem for the Naval Ocean Research and Development Activity (NORDA) for the past several years. The Seafloor Geosciences Division collected dredge samples from the West Florida Escarpment in mid-1982 (Fig. 3). These samples are predominantly shelf and slope carbonates of various ages ranging from Holocene to Cretaceous. Measured density is plotted against velocity in Figure 3. For comparison, values calculated from the regression equation developed by Hamilton (1980) for carbonate sediments are plotted also as a line. For further comparison, measured data from samples at ODP site 627 are plotted also. At low wet bulk densities (<2.0 Mg/m^3) the ODP data compare reasonably well with Hamilton's predicted values. It is only at higher wet bulk densities (>2.0 Mg/m^3) that the measured data become significantly different. The increase in velocity at ~2.1 Mg/m^3 reflects significant cementation in ODP site 627 samples.
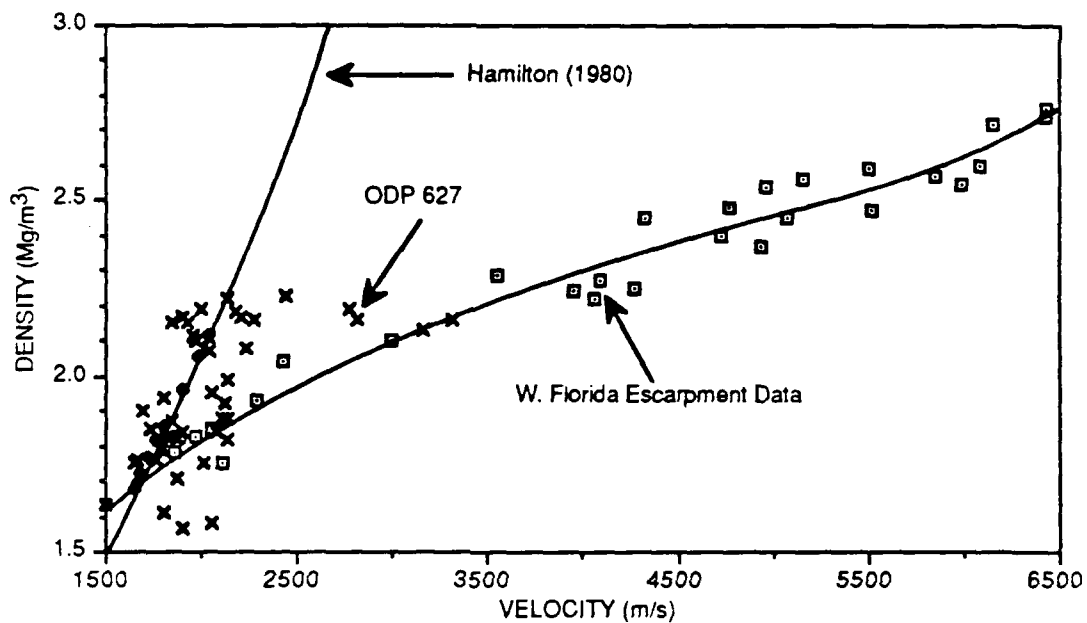
Figure 3. A comparison of wet bulk density and velocity measurements made on West Florida Escarpment dredge samples ranging in age from Holocene to Cretaceous and on periplatform ooze samples recovered from ODP site 627. Predicted values from Hamilton (1980) are plotted for comparison.

Data plotted in Figure 4 further define the problem. Compressional wave velocity (Fig. 4a) and wet bulk density (Fig. 4b) measured on board the RV JOIDES RESOLUTION on samples recovered from ODP sites 627 and 628 are plotted as a function of depth. For comparison, points calculated from Hamilton's regression equations (1980) predicting expected velocity and wet bulk density of carbonate sediments as a function of depth are also plotted. ODP-measured compressional wave velocity values are almost constant with depth, diverging increasingly from Hamilton's predicted values as depth increases. The considerable scatter in ODP wet bulk density values around 400 m into the seafloor results because cemented and uncemented layers were sampled and measured. Despite the scatter, the increase with depth is less than predicted by Hamilton, and the variation in wet bulk density is a function of cemented and uncemented couplets downhole.

Shear wave velocities measured using bender element transducers on samples from ODP site 630, northern Little Bahama Bank, are shown in Figure 5. It was expected that shear wave velocity would show a greater increase as a function of depth than was actually measured. The magnitude of increase in shear wave velocity has been predicted by Hamilton (1980) and Richart (1970) to be much higher. To explain the discrepancy, they hypothesized that shear wave velocity measured in the laboratory under ambient pressures may not be representative of *in situ* values and that the divergence between laboratory-measured and *in situ* values would increase with increasing *in situ* depth. Therefore, shear wave velocity, if measured in the laboratory, should be measured under estimated *in situ* overburden pressures.

ENVIRONMENT

The Bahama Islands were chosen as a source of carbonate sediments for this research because they serve as a modern example for interpreting carbonate platforms and slope environments in the geological record, and because they are easily reached from the continental United States. Eleven sites were drilled in the Bahamas during Leg 101 of the Ocean Drilling Program (Fig. 6) and much of the knowledge gained from ODP Leg 101 can be used to interpret results of this study. The northern Little Bahama Bank and Exuma Sound slopes sampled in this research represent extremes in carbonate slope development. Northern Little Bahama Bank, a gentle 2° to 3° slope, represents
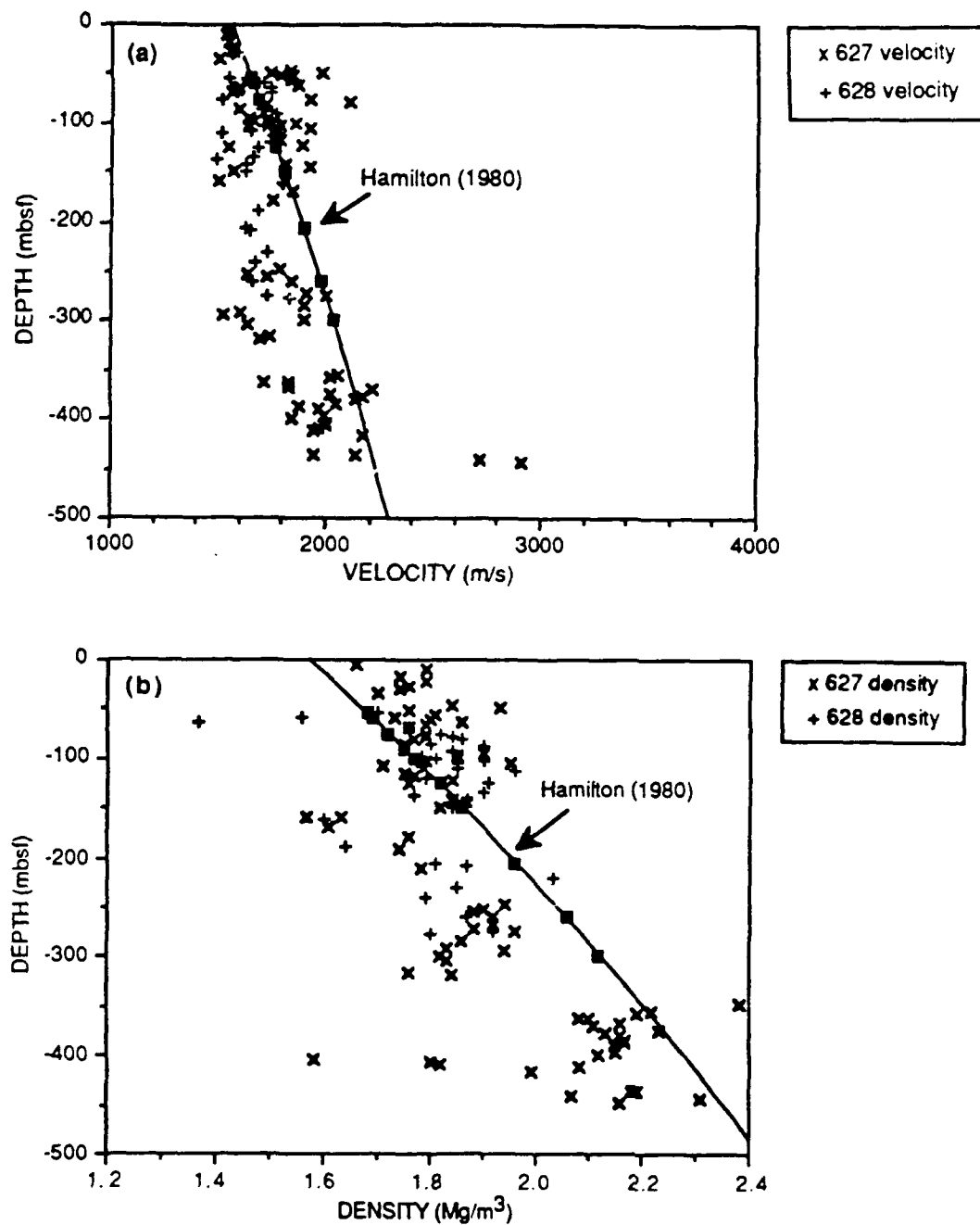
Figure 4. (a) Compressional wave velocity measured from ODP sites 627 and 628 are plotted as a function of depth. (b) Density from the same ODP sites are plotted as a function of depth. In both cases, predicted values by Hamilton (1980) are plotted for comparison.
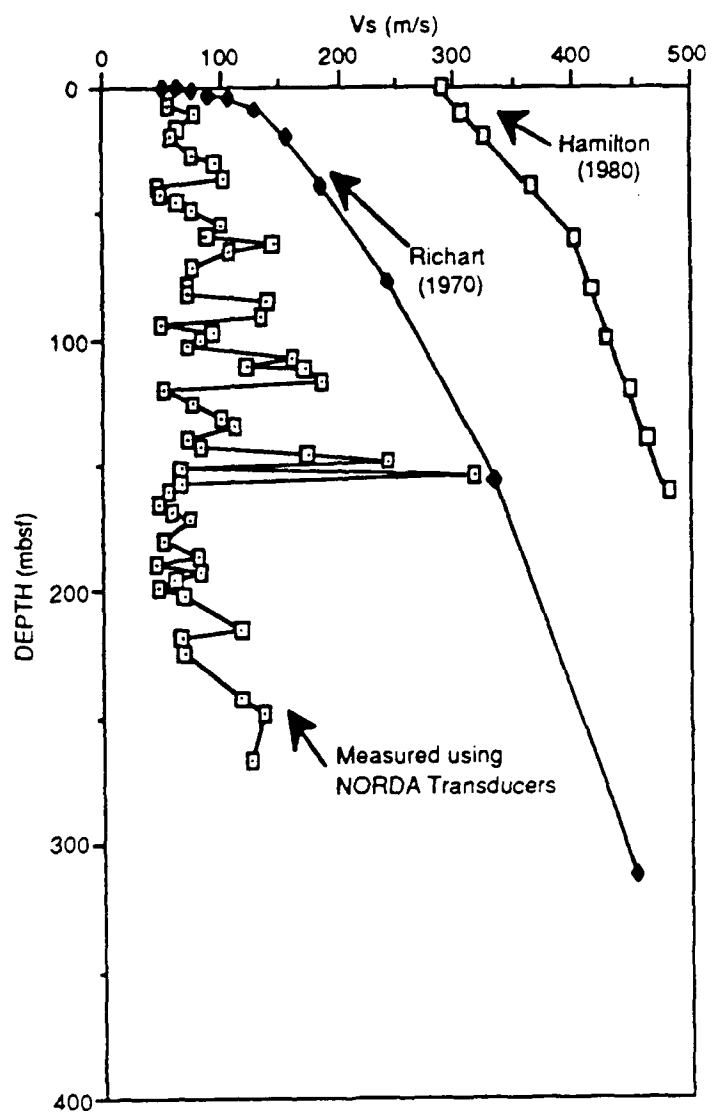
Figure 5. Shear wave velocity measured on periplatform samples from ODP site 630 are compared with predicted values by Hamilton (1980) and Richart (1970).
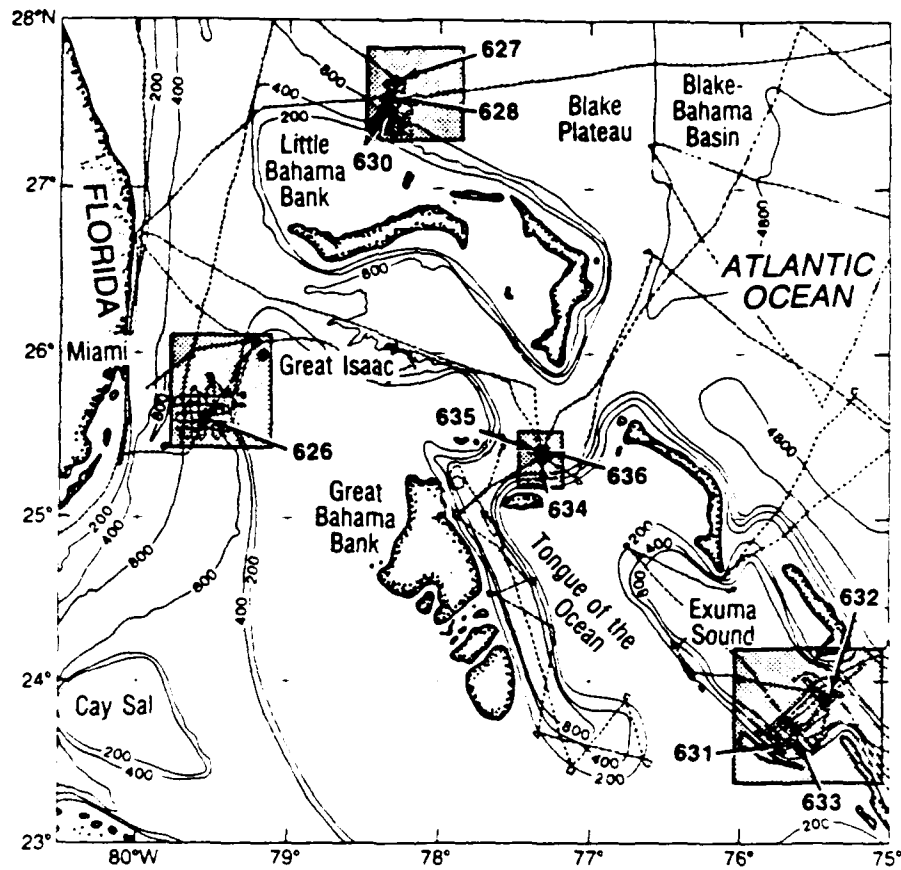
Figure 6. Location map of the Bahamas from Austin, Schlager, Palmer and others (1988).
Samples used in this study were recovered from Little Bahama Bank and Exuma Sound.

an accretionary, depositional slope, an early stage in the evolution of carbonate slopes. Exuma Sound, much steeper at 12° to 14°, represents the final erosional by-pass stage of slope building (Schlager and Ginsburg 1981). Sediment deposition on Exuma Sound is by turbidity currents, which are expected to by-pass the slope and deposit most of the sediments at the toe of the slope.

Analyses of seismic profiles and descriptions of sediments from Leg 101 cores were combine' by Harwood and Towers (1988) to investigate the evolution of Little Bahama Bank, which has been prograding northward since the early Miocene. It was found that midslope and lower slope depositional systems are uncharacteristic of interpreted ancient sedimentary environments. The modern lower slope contains no meandering channels. Gullies incised in the midslope funnel sediments to the base of the slope apron, which results in significant by-passing of sediment on an accretionary margin. Bottom contour currents on the lower slope continue to disperse and redeposit sediments. Holocene gravitational creep has produced large-scale rotational movement of unlithified sediments. Creep lobes extend far into the lower slope, where sediments are disturbed by propagation of and movement along multiple minor detachment surfaces (Harwood and Towers 1988).

Geochemical results from Leg 101 in both Exuma Sound and Little Bahama Bank indicate that diagenetic alteration is particularly rapid in the upper 10 m of the section. However, both sedimentation rates and contents of high magnesian calcite are higher in sediments from Exuma Sound than Little Bahama Bank. Also metastable minerals persist at greater depths in Exuma Sound (Austin, Schlager, Palmer and others 1986). These observations suggest that burial lithification is faster in Exuma Sound and leads to the unusual occurrence of well-cemented Miocene chalk that contains 20% aragonite at less than 300 meters below the seafloor (mbsf) (Austin, Schlager, Palmer and others 1986).

Along the carbonate slopes of the Bahamas, periplatform ooze is generally the matrix sediment. This ooze is fine-grained, clayey-silt mix of platform-derived sediment and tests of planktonic organism (Schlager and James 1978). Compositional and grain-size differences between matrix sediment and turbidites produce an initially heterogeneous sedimentary column. In carbonate

slopes of the Bahama Islands, this heterogeneity is enhanced by differing rates of lithification between periplatform ooze and the interbedded turbidites. The large proportion of the metastable carbonates, aragonite and high-magnesian calcite, in the periplatform ooze enhances the potential for dissolution and diagenetic alteration (Droxler and others 1983; Mullins and others 1985), which leads to an earlier induration of the periplatform ooze compared to the normally coarser, redeposited beds. The interbedded carbonate turbidites have a larger grain size and contain fewer metastable carbonate minerals. As a result, they resist lithification longer than do the adjacent partly or completely indurated chalks. In Leg 101 sediments, rapid burial diagenesis is indicated by shallow, partly lithified ooze and chalk (Eberli 1988; Austin, Schlager, Palmer and others 1986). The early diagenetic alteration of the periplatform ooze leads to a shallower, partial lithification of the ooze in the upper parts of the sections and occasionally produces chalk-ooze couplets, which are spaced regularly at 5- to 25-cm intervals (for example, site 631, Austin, Schlager, Palmer and others 1986) Diagenetic gradients and, consequently, the depths of complete induration, vary at different sites (Swart and Guzidowski 1988). In Exuma Sound, total lithification occurs at considerably shallower depths than along a Little Bahama Bank transect. In the latter, carbonate sand remains unlithified, even where the interlayer ooze has been altered to chalk.

SAMPLE DESCRIPTIONS

The location of cores sampled for this research are shown in Table 1. Both piston cores and gravity cores were recovered by NORDA scientists at each location but, except for a few samples from Little Bahama Bank, most of this research was performed on samples from piston cores because they were longer and appeared to be less disturbed. A shelly layer near the sediment surface on Little Bahama Bank made core penetration difficult. Sampling was done on the basis of x-ray results. All samples were taken from visually homogeneous sections of core. A list of samples tested appears in Table 1. Sample designations are as follows:

ES = Exuma Sound

LBB = Little Bahama Bank

Table 1. Core Location and Sample Depths

LITTLE BAHAMA BANK

Core ID	Depth (m)	Latitude	Longitude	Sample ID	Depth in Core (cm)
LBB 5-H	825	27°24'98	78°21'60	LBB 5H-3	130
LBB 10-P	1035	27°35'67	78°13'41	LBB 10P-1	50
LBB 14-P	925	27°28'00	78°14'96	LBB14P-1	28
LBB 15-H	830	27°25'42	78°15'64	LBB 15H-1	48
LBB 16-P	790	27°25'45	78°14'91	LBB16P-1	90
				LBB16P-2	160

EXUMA SOUND

Core ID	Depth (m)	Latitude	Longitude	Sample ID	Depth in Core (cm)
ES 4-P	1920	23°50'16	75°34'16	ES 4P-1	45
				ES 4P-2	130
				ES 4P-3	225
				ES 4P-4	355
ES 5-P	1957	23°49'76	75°31'15	ES 5P-1	90
				ES 5P-1(2)	95
				ES 5P-2	160
				ES 5P-3	260
				ES 5P-4	360
				ES 5P-5	484
ES 6-P	1980	23°50'21	75°26'40	ES 6P-1	98
				ES 6P-2	190
				ES 6P-3	293
				ES 6P-4	403
ES 7-P	1815	23°48'31	75°22'74	ES 7P-1	87
				ES 7P-2	187
				ES 7P-4	331
				ES 7P-5	437
				ES 7P-6	566
ES 10-P	1837	23°45'02	75°45'83	ES 10P-2	155
				ES 10P-3	250
				ES 10P-4	420

P = piston core

H = hydroplastic or gravity core

-# = section of core from which the sample was removed

Since consolidation testing requires a whole round sample, duplicates were taken from imme-
diately adjacent portions of the core. Approximately 5 to 7 cm of core were needed for each
consolidation sample. Water content and index property measurements came from a central section
of core material. Cuttings were used for grain size and x-ray diffraction. Sample size was minimized
so that duplicates could be taken in close proximity. However, I noted several times that a lithologic
change had occurred in the section between samples. For example, ES 5P-1(2)was intended to be
a duplicate of ES 5P-1 but the change in sediment character was so great that it was designated as
a separate sample. In the case of ES 6P-1, a change in grain size between the top and bottom of the
sample was not noted until after consolidation testing. Where relevant, the designation ES 6P-1 top
or ES 6P-1 bottom is used. It is treated as a single sample in most instances.

Samples were examined with the Scanning Electron Microscope (SEM) to identify fabric
relationships and constituent particles. A brief description of each sample appears in Table 2. The
samples are described as matrix-supported: that is, the grains are floating within the matrix
(Fig. 7a); grain supported (the grains are in contact with each other, Fig. 7b); or in several cases
where the classification was difficult using the SEM, matrix-supported with numerous grains. The
distinction between matrix- and grain-supported sediments is important because matrix-supported
and grain-supported samples will consolidate differently. The matrix material, generally a periplat-
form ooze, was of two main types, either predominantly a coccolith ooze (Fig. 8a) or composed of
a large proportion of aragonite needles (Fig. 8b). When grains and particles, because of breakage
or other reasons, could not be positively identified as to origin, they were called unidentifiable
grains or particles. Grains and particles would often be identified as shell fragments because they
had an aragonite needle structure or because they were planes of calcite. Appendix A contains
representative SEM micrographs of most of the samples.

Table 2. Fabric Descriptions

Sample ID	Matrix/Grain Relationship	Matrix	Grains
ES 4P-1	matrix-supported	coccolith shields (2-4 μm), broken needles/spicules (10 μm length) few rhabdoliths (2-3 μm)	floating grains, foraminifers (~100 μm)
ES 4P-2	matrix-supported	coccolith shields (2-4 μm), broken shell fragments	foraminifers (25-100 μm) and fragments (25-100 μm)
ES 4P-3	matrix-supported	broken fragments (2-5 μm), spicules (2-5 μm), coccolith shields (3-4 μm)	foraminifers (~100 μm), shell fragments 5 (0-150 μm)
ES 5P-1(2)	matrix-supported (many grains)	needles (3 μm), rhabdoliths (5-6 μm), coccolith shields (3-4 μm)	pteropods fragments (100-300 μm) foraminifers (100-200 μm)
ES 5P-3	matrix-supported	very worn needles and fragments (2-3 μm), coccolith shields (3-4 μm)	few
ES 5P-4	matrix-supported	coccolith shields (3-4 μm) with overgrowths, and unidentifiable fragments (3-4 μm)	round (foraminifers) (25 μm)
ES 5P-5	matrix-supported	very worn fragments (3-4 μm) coccoliths with numerous overgrowths (3-4 μm)	occasional foraminifers (25 μm)

Table 2. (cont.)

Sample ID	Matrix/Grain Relationship	Matrix	Grains
ES 6P-1 (top)	grain-supported	few coccolith shields (3-4 μm)	pteropods (200 μm), foraminifers (100 μm), fragments (100-200 μm)
(bottom)	matrix-supported	coccolith shields (3-4 μm) and shell fragments (2-5 μm)	predominantly pteropods (50-200 μm)
ES 6P-2	matrix-supported	very altered coccolith shields (2-3 μm)	pteropods (50-100 μm), unidentifiable grains (25-100 μm)
ES 6P-3	matrix-supported	needle matrix with flat plates of calcite and coccoliths (2-3 μm)	numerous floating grains, predominantly calcareous dinoflagellates (15-25 μm), and corroded pteropod fragments of variable sizes
ES 6P-4	matrix-supported	chalk: Gephyrocapsa, Cyclococcolithus, areas of aragonite needles (2-3 μm) and fine, angular calcite debris.	none
ES7P-1	matrix-supported	calcareous dinoflagellates(10μm), coccolith shields (2-3 μm), aragonite needles (2-3 μm)	pteropods, (100 μm) and skeletal fragments of variable size
ES 7P-2	matrix-supported	coccolith shields with calcite overgrowths (1-3 μm), needles with calcite ppt overgrowths	pteropods (100-200 μm), foraminifers

Table 2. (cont.)

Sample ID	Matrix/Grain Relationship	Matrix	Grains
ES 7P-5	grain-supported	coccoliths(few, 2-3 μm) needles and fragments	pteropods (100-300 μm) unidentifiable, worn grains (50-200 μm)
ES 7P-6	grain-supported	few coccoliths, shell fragments (10 μm) composed of tighly bound aragonite needles (1 μm)	pteropods (100-300 μm) and unidentifiable particles
ES 10P-2	matrix-supported	coccolith shields (2-3 μm), calcite fragments, spicules	foraminifers (25 μm),
ES 10P-3	matrix-supported	coccolith shields (2-3 μm), rabdoliths (5μm), large (100 μm) clusters of aragonite needles (2-3 μm), shell fragments (2-5 μm	aggregates (2 μm), (mostly foraminifers), nondescript skeletal fragments, ostracodes
LBB 10P-1	grain-supported	coccolith shields (2-4 μm), calcareous dinoflagellates (4-5 μm), aragonite needles (1-3 μm)	pteropods (100-300 μm), foraminifers (25 μm and larger), shell fragments (50-100 μm)
LBB 14P-1	grain-supported	coccolith shields (2-3 μm), aragonite needles, spicules	pteropods (500-1000 μm) foraminifers (100-200 μm)
LBB 15H-1	matrix-supported	aragonite needles (2-3 μm) with a few straycoccolith shields (2-3 μm)	floating, include foraminifers, calcareous dinoflagellates and shell fragments (>50 μm)

Table 2. (cont.)

Sample ID	Matrix/ Grain Relationship	Matrix	Grains
LBB 16P-1	grain-supported	large number of aragonite needles (2-4 μm), few coccolith shields (2-4 μm)	foraminifers (25-50 μm), pteropods (50-100 μm), shell fragments (50-300 μm)
LBB 16P-2	grain-supported	coccolith and fragments (2-3 μm)	pteropods, grains (100-300 μm)
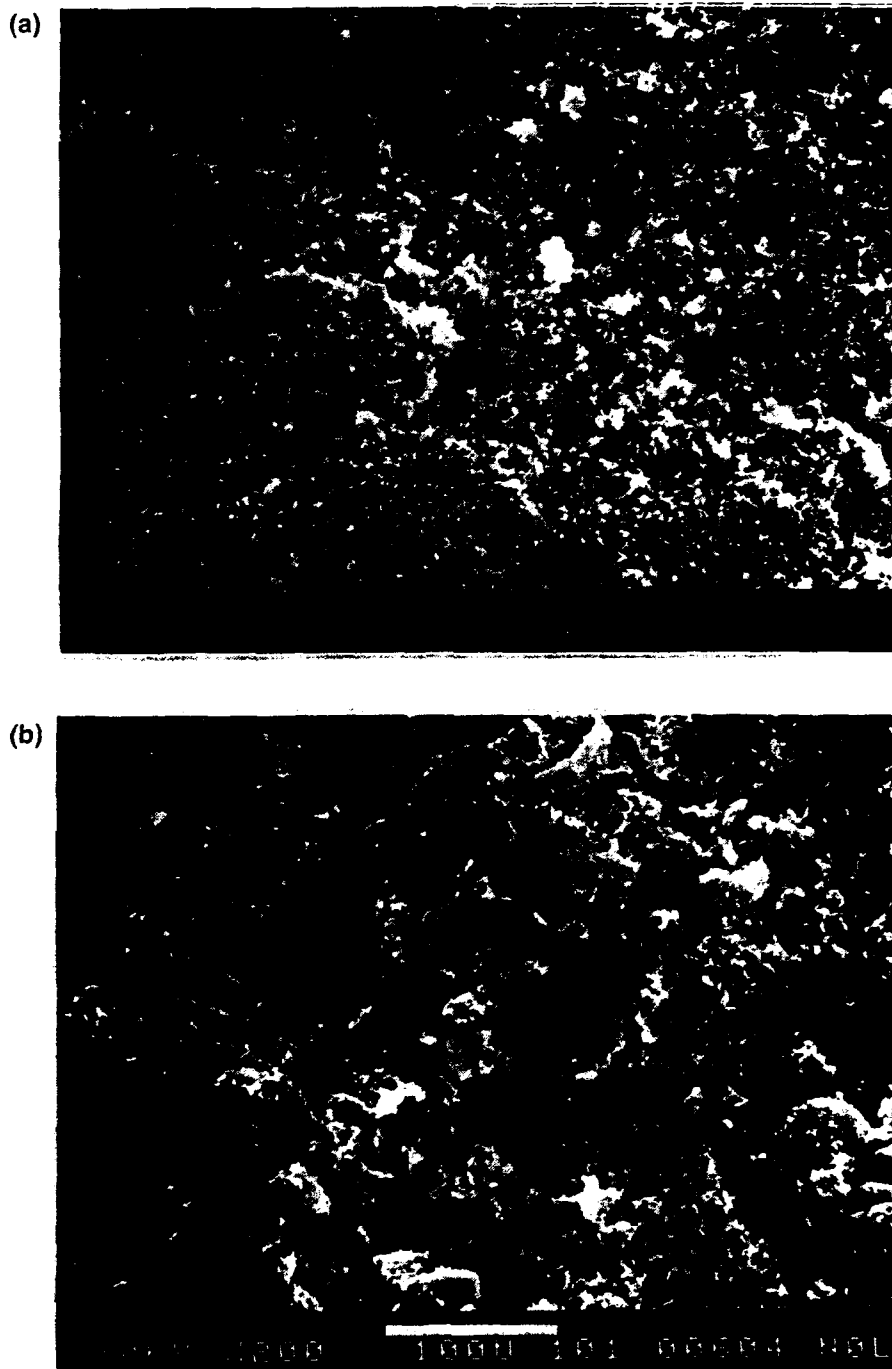
Figure 7. (a) ES 5P-3, a matrix-supported periplatform sediment, has very few grains floating in a matrix composed of worn aragonite needles and coccolith shields. Magnification is 200X. (b) ES 6P-1, a grain-supported periplatform sediment, is composed of grains in contact with each other. Very little matrix sediment is visible. Magnification is 200X.
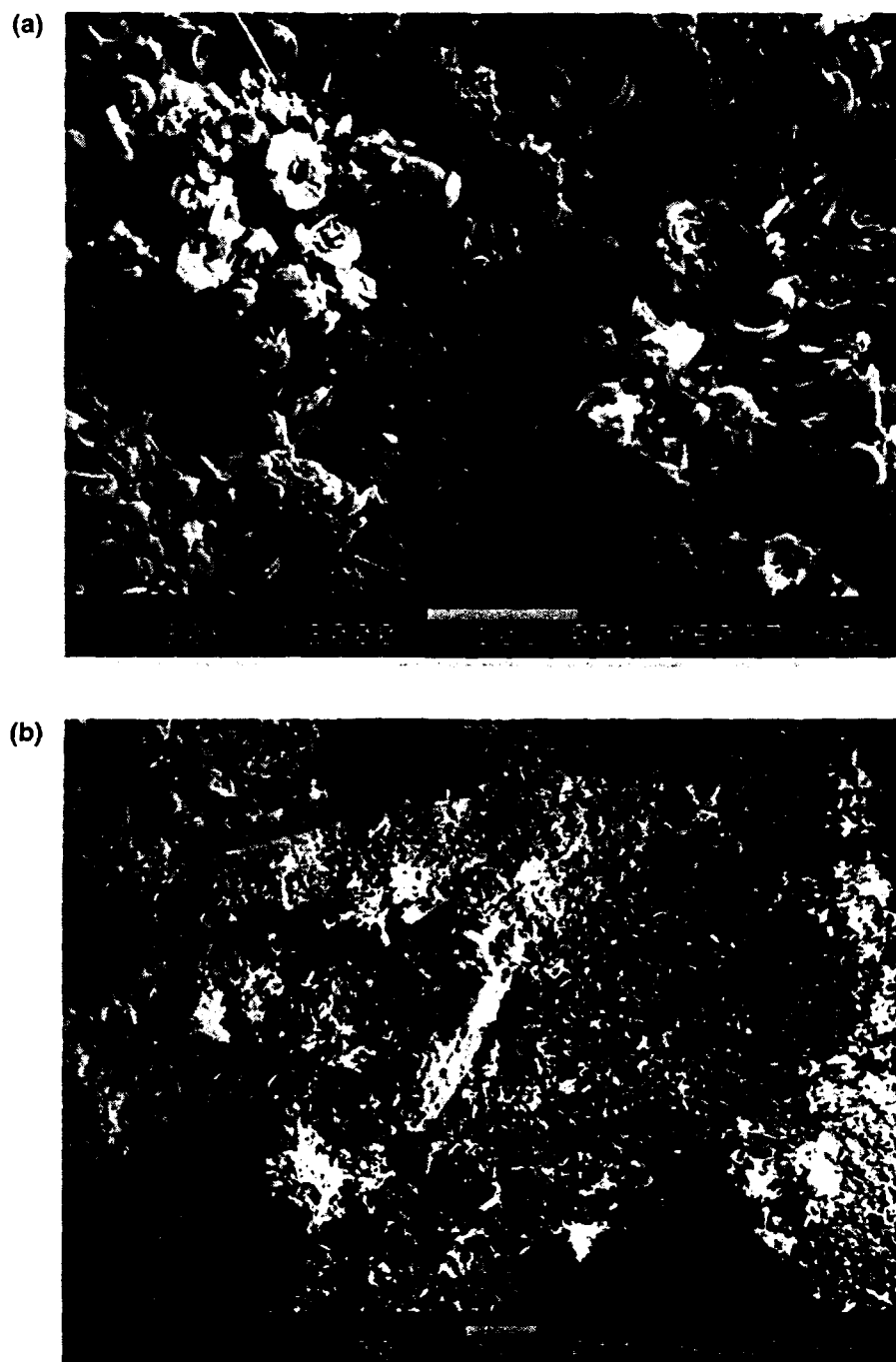
Figure 8. (a) Typical coccolith ooze forms the matrix material of ES 6P-4. Magnification is 2000X. (b) In LBB 15H-1, the matrix material is primarily aragonite needles. The large grain is a pteropod fragment composed of aragonite needles. Magnification is 900X.

Samples were further characterized by results from the following analyses:

1. *Vane Shear* Measurements of shear strength were made with a miniature vane shear device. This technique is particularly well suited for testing cohesive sediments in an undrained condition. When sediments are sheared without loss of pore water (undrained condition), they respond as if they are cohesive material. In this case the angle of internal friction (ϕ) is equal to 0; and thus, σ' = C (friction). Tests were made onboard the USNS LYNCH by inserting the blade perpendicular to the bedding in the ends of cores before sealing. The undrained shear strength (labeled Cohesion in Table 3), of most of these samples is very low, less than 10 kPa in almost all cases. Several of the samples, such as LBB 10P-1 and 16P-1, were very sandy in the exposed core section and drained quickly, so the vane shear results are not considered valid for grain-supported samples in terms of absolute cohesion but are included for comparison .

2. *Grain size* Grain size was determined for all samples by separating four sand-sized fractions by wet sieving and the silt and clay size fractions by pipette analysis. See Folk (1974) for a complete discussion of this technique.

3. *Mineralogy* Total carbonate content was measured using the carbonate bomb technique (Muller and Gastner 1971). In this technique, approximately 0.8 g of carbonate sediment was dissolved in 10 ml of 6N HCl; the resulting CO_2 pressure is proportional to the amount of CO_3 of the dried sediment weight of the sample. A calibration curve for the system was determined using pure reagent grade $CaCO_3$ (Fig. 9a). The regression equation derived from this curve was used to calculate the percent of calcium carbonate present in the sample. The margin of error can be as low as 1% for sediments high in CO_3 but the overall accuracy is usually 2% to 5%.

X-ray diffraction was used to determine percentage of calcite and aragonite. Samples were dried and then powdered. All were x-rayed on a General Electric XRD 5 diffractometer, as powder mounts at 1°/2θ, 30 mÅ and 45 kV. Percent aragonite and percent calcite were determined by calculating the areas under the 26.24 Å and 29.5 Å peaks, respectively, and then comparing that value to a standard curve by R. Lighty from similar samples from the Bahamas (Fig. 9b, personal communication, 1988).

Table 3. Undrained Shear Strength

Sample ID	Cohesion (undisturbed) (kPa)	Cohesion (remolded) (kPa)	Sensitiviity (N/R)
ES 4P-1	1.6	2.0	0.8
ES 4P-2(2)	5.5	3.5	1.6
ES 4P-3	0.3	0	0.3
ES 4P-4	1.4	0.2	6.3
ES 5P-1	0.8	0.6	1.5
ES 5P-2	4.2	1.8	2.3
ES 5P-3	7.5	4.4	1.7
ES 5P-4	1.4	12.3	10.8
ES 5P-5	1.2	0.9	1.3
ES 6P-1	1.2	0.6	2.1
ES 6P-2	3.1	2.6	1.2
ES 6P-3	7.0	1.6	4.3
ES 6P-4	0.4	0	0.4
ES 7P-1	2.8	0.8	3.6
ES 7P-2	5.4	3.5	1.5
ES 7P-4	7.1	2.3	3.0
ES 7P-5	3.3	2.4	1.4
ES 7P-6	1.4	1.5	0.9
ES 10P-2	5.1	2.7	1.9
ES 10P-3	1.7	0.2	7.8
ES 10P-4	2.9	1.7	1.7
LBB 5H-3	DISTURBED		
LBB 10P-1	2.6	0.6	4.2
LBB 10P-3	10.1	0.9	11.3
LBB 14P-1	1.2	0.8	1.4

Legend: ES = Exuma Sound
LBB = Little Bahama Bank
N/R = undisturbed/remolded
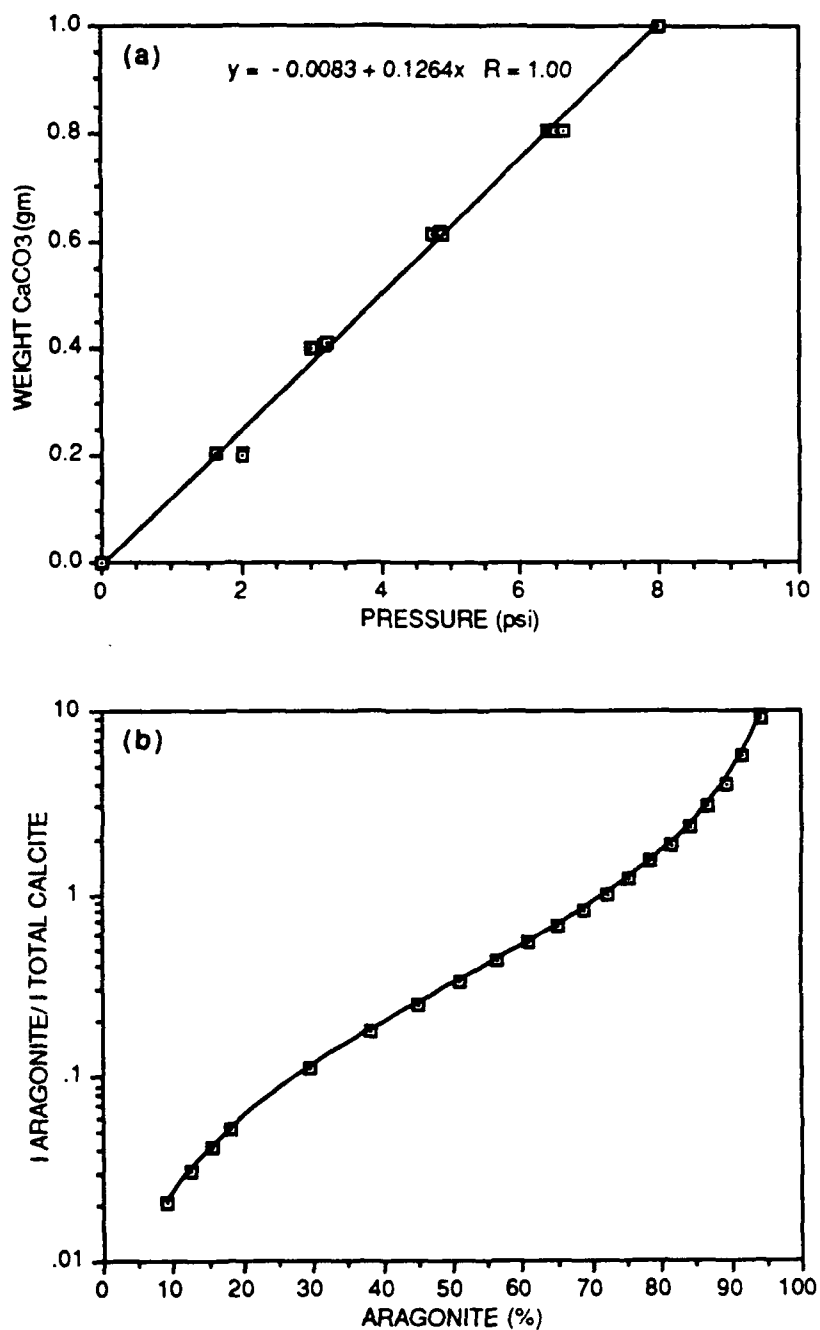
Figure 9. (a) Calibration derived for the carbonate "bomb" using reagent grade calcium carbonate. (b) Calibration curve derived by R. Lighty for calculating percent aragonite and percent calcite from integrated peak areas using x-ray diffraction techniques.

Grain size, total calcium carbonate, and percentage of aragonite and calcite are presented in Table 4. Many of the samples defined as grain supported using the SEM did not have as large a percentage of sand as expected. For example, ES 6P-3 has 39% clay and 47% silt, which is indicative of a matrix-supported sample. The top layer was not analyzed separately. The cuttings were probably not representative of the sample as a whole. ES 7P-5 and ES 7P-6, also defined as grain supported using the SEM, were predominantly sand and silt. Both had ~21% clay. ES 10P-2 and ES 10P-3, which had a smaller clay fraction (21% and 13%), appeared to be matrix supported under the SEM. Although thin section analysis could answer the question of whether the sample merely has many grains or is actually grain supported, it is felt that a gross differentiation is adequate for this research. The fabric and porometry of the samples is further described in Chapter II.

Table 4. Grain Size and Mineralogy

Sample ID	Sand (%)	Silt (%)	Clay (%)	Total Carbonate Content (%)	Aragonate (%)	Calcite (%)
ES 4P-	8	45	47	88	38	62
ES 4P-2	10	47	43	92	26	74
ES 4P-3	4	60	36	92	39	61
ES 4P-4	7	63	30	95	27	73
ES 4P-5	15	70	15	95	47	53
ES 5P-1	11	82	7	94	10	90
ES 5P-1(2)	10	57	33	87	—	—
ES 5P-2	10	51	38	96	30	70
ES 5P-3	6	54	40	94	30	70
ES 5P-4	9	78	13	90	12	88
ES 5P-5	6	57	38	93	10	90
ES 6P-1	14	47	39	88	32	68
ES 6P-2	18	55	27	93	49	51
ES 6P-3	24	45	31	89	40	60
ES 6P-4	6	77	16	95	31	69
ES 7P-1	13	46	42	98	22	78
ES 7P-2	15	60	24	95	40	60
ES 7P-4	16	54	31	91	—	—
ES 7P-5	18	61	21	90	56	44
ES 7P-6	36	42	22	85	65	35
ES 10P-2	20	58	22	89	25	75
ES 10P-3	50	37	13	90	26	74
ES 10P-4	48	31	20	92	27	73
LBB 10P-1	80	10	10	92	22	78
LBB 10P-2	65	31	5	89	19	81
LBB 14P	37	41	23	89	54	46
LBB 15H	13	58	28	88	75	25
LBB 16P-1	27	49	25	92	47	53
LBB 16P-2	24	71	4	93	29	71

Legend: ES = Exuma Sound
LBB = Little Bahama Bank

CHAPTER II

CONSOLIDATION OF PERIPLATFORM SEDIMENTS

INTRODUCTION

In the transition from ooze to chalk, consolidation is an important diagenetic process within the shallow burial realm (Schlanger and Douglas 1974). Consolidation is the process whereby water is removed from the sediment by the application of vertical pressure, which results in a realignment of grains and a more compact structure (Richards and Hamilton 1967; Lambe and Whitman 1969). Some processes of consolidation in the marine environment, such as interparticle bonding and cementation, which are partially a function of time (Skempton 1970), cannot be duplicated in the laboratory. Sediment consolidation in the laboratory does not exactly duplicate the natural process of consolidation in the marine environment. However, laboratory measurements do provide information concerning some of the consolidation processes and of the permeability and porosity depth relationships of marine carbonates that would be unavailable otherwise (Bryant and others 1981). In addition to the consolidation behavior, this study will examine the relationship between consolidation and shear wave velocity and shear modulus, as well as the sediment fabric.

The United States Navy is interested in the measurement of shear wave velocity and shear modulus of marine sediments for acoustic and engineering purposes. Both shear wave velocity and shear modulus are a function of effective stress. To produce results close to *in situ* values, measurements of shear wave velocity and shear modulus should be made during consolidation testing, which reproduces the estimated effective stress state of the *in situ* sediment. Currently, the bender element shear wave transducers used by the Navy are designed to operate only under ambient pressures, and the configuration of these devices makes them unsuitable for incorporation into the consolidometer. A search for a suitable technology led to the duomorph sensor, which was developed in the early 1970s to measure the dynamic modulus of solid propellant *in situ* (Briar and others 1976). The duomorph technology has been adapted in this study to measure the dynamic shear modulus of sediment during loading. From the shear modulus and wet bulk density, the shear

wave velocity of the sediment can be determined as a function of effective stress. The goal was two-fold: (1) to develop (or modify) and test an alternate technique that could be used to measure shear modulus and shear wave velocity and (2) to measure these values as a function of effective stress. The long-range goal (beyond the scope of this work) is to develop an *in situ* probe without the complications of the precise geometry required by the bender element shear wave transducers.

Sediment fabric, i.e., the particulate constituents and their orientation, is one of the factors that control the geotechnical properties of carbonate sediments. Many researchers document that fabric is altered by application of pressure (Terzaghi 1940; Fruth and others 1966; Shinn and others 1977; Shinn and Robbin 1983; Lavoie 1988; Bennett and others 1977; Bennett and others 1989). Based on the measured porosity and permeability changes that resulted from consolidating the sediment, it was expected that changes in both the number and size of pores would be evident as a result of image analysis after consolidation. It was expected that the number of pores observed within the standard SEM frame would increase and the actual area of the pores would decrease after consolidation. The preliminary results of an investigation into the effects of increasing effective stress by mechanical consolidation on carbonate sediment fabric, including reduction of permeability is also presented in this section.

Consolidation tests were carried out on 27 samples obtained from five cores from northern Little Bahama Bank and five cores from Exuma Sound (Figs. 10a, b). A visual description of each sample based on Scanning Electron Microscopy can be found in Table 2. The purpose was (1) to characterize the physical and mechanical properties of periplatform oozes found on slopes and (2) to establish differences between sediments found on both accretionary and on by-pass slopes. The assumption is that the Bahama sediments can be used as a model for extrapolating results to other carbonate environments. In addition, measurements of compressional wave velocity and shear modulus were performed on seven of these samples during consolidation testing. The fabric of most of the samples consolidated was examined using the SEM (Appendix B). Image analysis was performed on six of the samples to test the feasibility of using this technique to quantify the changes in fabric, specifically, pores.
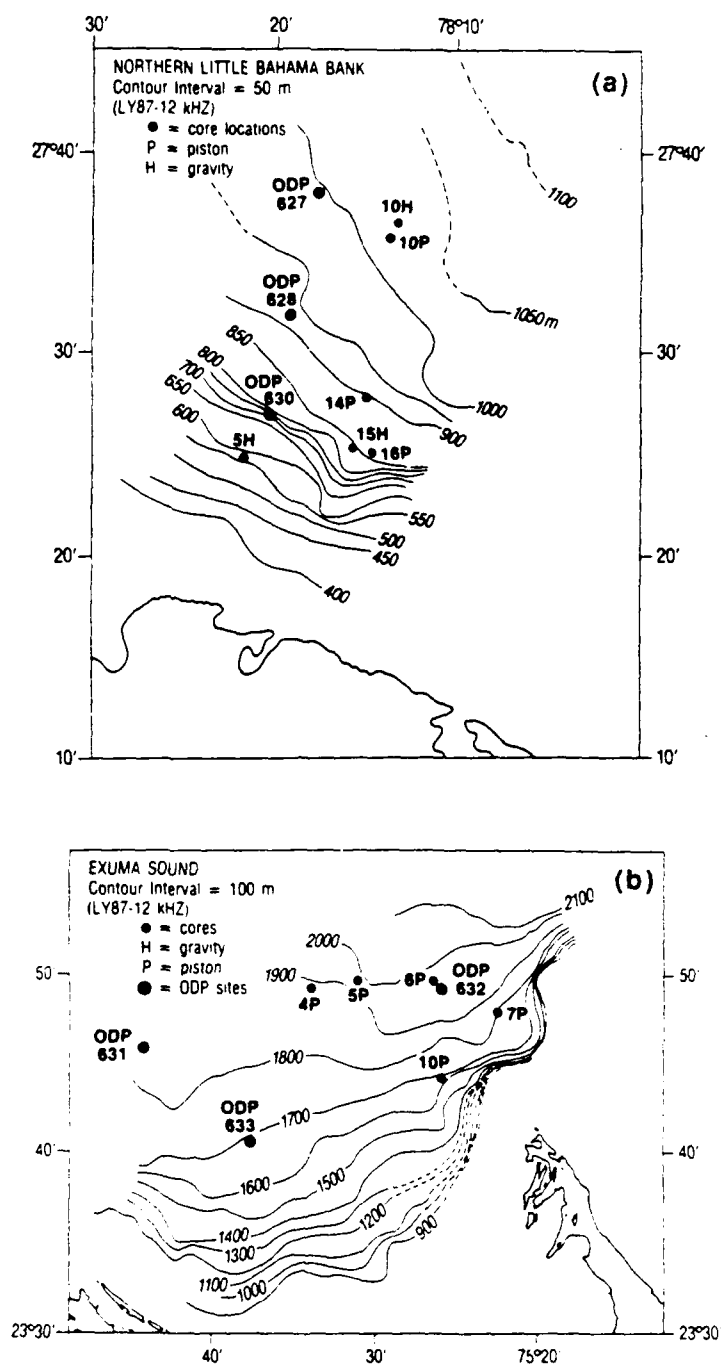
Figure 10. Core location maps. (a) Little Bahama Bank and (b) Exuma Sound. ODP sites are also noted.

CONSOLIDATION CHARACTERISTICS

Changes in the coefficients of consolidation, bulk modulus (and its inverse, compressibility), and permeability can be related directly to the magnitude of the overburden pressure by means of consolidation testing. When a sample is first placed under load, pore water carries the load. As the pore water drains from the sample, the load is transferred to the sediment structure; this transfer results in a realignment of grains and a more compact structure (Richards and Hamilton 1967; Lambe and Whitman 1969; Bryant and Bennett 1988). The reduction in porosity that occurs can be expressed either as porosity (n), which is the ratio of the volume of the voids to the volume of the total sample,

$$n = Vv/Vt,\qquad(1)$$

or as a reduction in void ratio (e), which is the ratio of the volume of voids to the volume of the dry sediment or solid grains alone:

$$e = Vv/Vs.\qquad(2)$$

Since the diameter of the sample is fixed during testing, the void ratio (e) can be calculated from the change in sample height during consolidation testing. The change in sample height is generally plotted against the log of time since loading (Fig. 11a). By extending the two straight-line portions of this plot, it can be determined when primary consolidation is completed. The intersection is taken to be the point where 100% primary consolidation is completed and secondary consolidation begins. Primary consolidation is the initial stage during which free water is expelled and pore pressures can be measured (Bryant and Bennett 1988). A secondary stage of consolidation occurs after the free pore water has been expelled and the sediment grains carry the load. At high loads (~2000 kPa) in carbonate sediments, grain crushing may occur during secondary consolidation.

From the plots of Δh versus log of time, the coefficient of consolidation (Cv_{50}) can be determined:

$$Cv_{50} = Tv_{50}\ (H^2)\ /t_{50},\qquad(3)$$
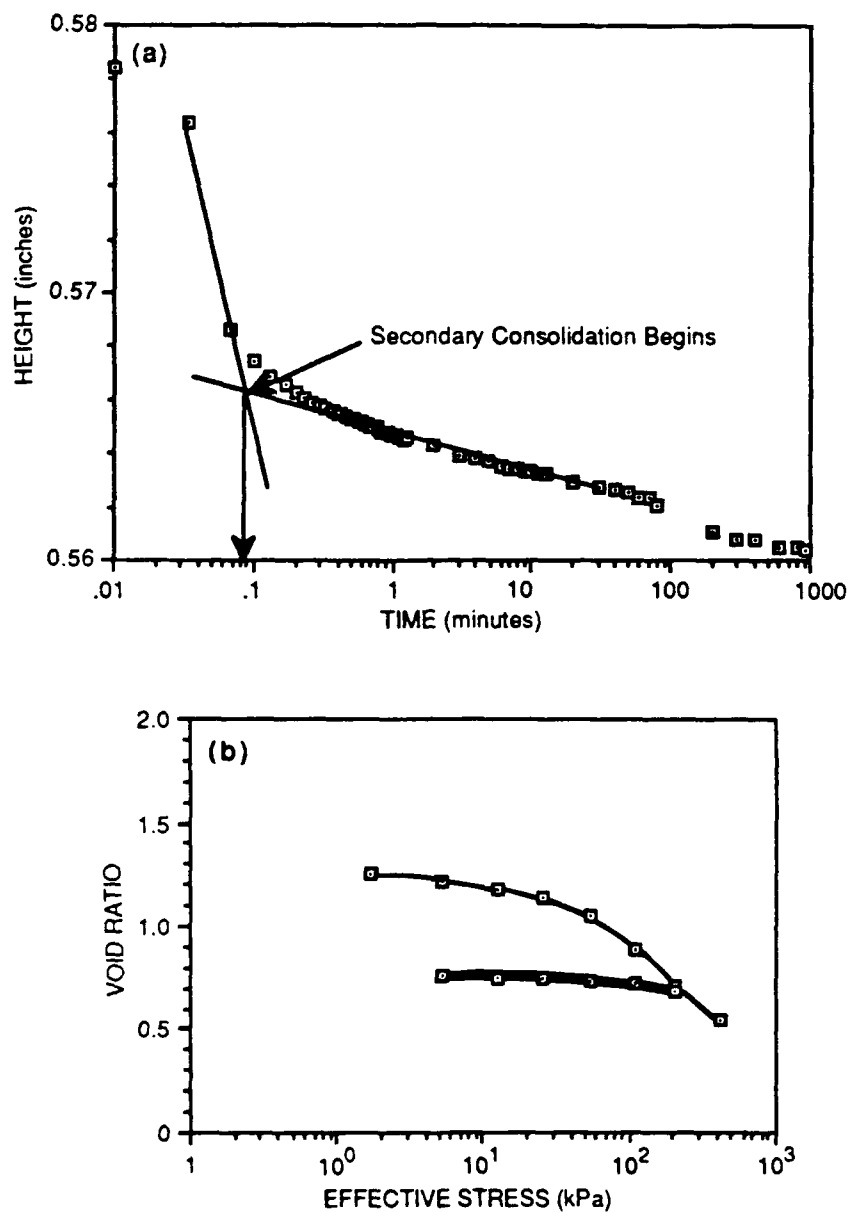
Figure 11. (a) Typical plot of the change in height versus the log of time. Primary consolidation ends and secondary consolidation begins at 0.085 minutes for ES 5P-3 after the 2-kg. load is added. Total load is 3.99 kg, including the cap. (b) The "e-log-σ' " curve. Void ratio for each load increment is plotted versus the effective stress.

where $Tv_{50} = 0.197$, H is half the sample height, since the sample is allowed to drain from both top and bottom and t_{50} is the time which corresponds to d_{50}, the point halfway between d_0 and d_{1000} (Lambe 1951).

Void ratio, e, is calculated:

$$e = \left[\frac{H_0 \gamma s A}{W_s} \right] - 1 \qquad (4)$$

where H_0 is the sample height, γs is the grain density, A is the area of the sample, and W_s is the weight of the sediment. The void ratio is typically plotted as a function of effective stress and is expressed as the "e-log-σ'" curve (Fig. 11b). From the void ratio and effective stress a number of characteristics can be determined. The coefficient of compressibility (Av) is the instantaneous slope:

$$Av = \Delta e / \Delta p, \qquad (5)$$

where Δe is the difference in void ratio between any two consecutive loads and Δp is the difference between those two loads.

The coefficient of one-dimensional compressibility (Mv) can be determined for each load from the slope and void ratio:

$$Mv = Av(1/(1 + e_0)). \qquad (6)$$

Permeability varies with effective stress. During the consolidation process, the pore spaces and pore throats generally become constricted, resulting in a decrease in permeability. When the sediment is grain supported, the pore spaces within the matrix are protected from constriction, at least until grain crushing occurs. When the sediment is matrix supported, considerable volume change may occur as the matrix consolidates and pore spaces become reduced, lowering permeability. Permeability (k), the rate of flow past a specified area, is calculated from

$$k = Cv_{50} * \rho w * Mv_{50}, \qquad (7)$$

where Cv_{50} is the coefficient of consolidation, ρw is the bulk density of water and Mv_{50} is the coefficient of compressibility. Permeability is routinely measured by various techniques in the lab (Lambe 1951; Enos and Sawatsky 1980) and *in situ* (Bennett and others 1989). In this study permeability was measured in the laboratory using a variable head permeameter (see Lambe 1951) for each load increment, beginning with a total vertical pressure of 2 kg/cm² (19.6 kPa). These results, were corrected to 20°C and were then compared to calculated values of permeability. In a saturated soil, water flow is laminar and Darcy's Law can be applied:

$$K = \frac{aL}{A(t_1 - t_0)} \log\left(\frac{h_0}{h_1}\right), \qquad (8)$$

where a is the cross-sectional area of the standpipe, L is the length of sediment, A is the cross-sectional area of the sample, t_0 is the time when water in the standpipe is at h_0, t_1 is the time when water in the standpipe is at h_1, and h_0 and h_1 are the heads between which the permeability is determined.

The consolidation state of a sediment can be determined by comparing the computed effective stress *in situ* ($\sigma o'$) with the maximum past effective stress ($\sigma c'$). If this ratio is 1 (here, the ratio is called the overconsolidation ratio, or OCR), then the sediment is normally consolidated; that is, the current effective stress is equal to any stress applied in the past. If the OCR is greater than 1, then the past stress has been greater than the present applied stress, and the sediment is said to be overconsolidated. If the OCR is less than 1, then the sediment is considered to be underconsolidated. Because the effective overburden stress is nearly zero at the surface, the OCR approaches infinity, giving a distorted consolidation state relationship near the water/sediment interface (Bryant and Bennett 1988). The maximum past pressure, σc, is generally found by applying the Casagrande method (Dunn and others 1980) as follows (Fig. 12):

- The point of maximum curvature is found and a line (a) is drawn tangential to the virgin curve at that point.
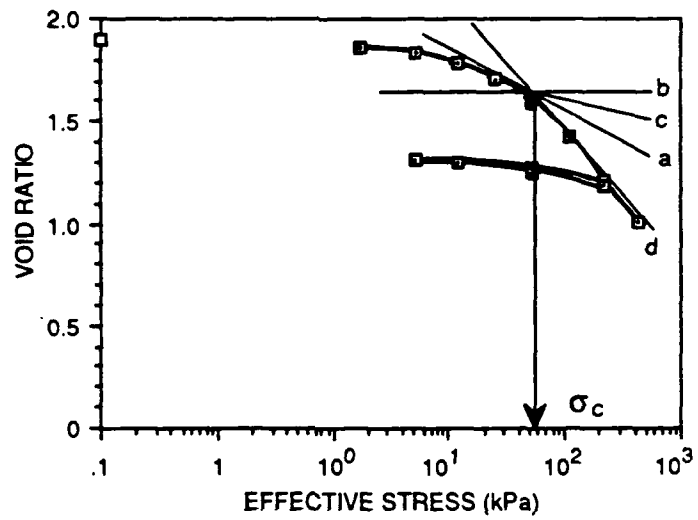
Figure 12. The maximum past pressure, σ_c, is generally found by applying the Casagrande method.

• A line (b) is drawn horizontally through that point.

• The angle formed by these two lines is bisected by the line (c).

• A line (d) is extended upward along the slope of the lower portion of the virgin curve. The point where this line intersects the bisector, c, indicates the maximum past overburden pressure, which can be found by dropping a line to the x axis of effective stress.

The estimated *in situ* effective stress, σ_0', is found:

$$\sigma_0 = \gamma_t * z \tag{9}$$

and

$$\sigma_0' = (\gamma_t - \gamma_{sw}) \, z, \tag{10}$$

where σ' is the total geostatic stress, γ_t the unit weight of sediment, γ_{sw} is the unit weight of water, and z is the depth in meters.

The effective overburden stress (σ') in the marine environment is the unit weight of the overlying sediment times the depth minus the pore pressure; that is, the buoyant weight of the sediment grains in seawater. Estimated depth was converted from effective stress using the following equation (Taylor 1948):

$$z = (\sigma'/\gamma_t - \gamma_{sw}) \tag{11}$$

where σ' is the effective stress, γ_t is the unit weight of sediment, γ_{sw} is the unit weight of seawater, and z is the depth.

DUOMORPH SENSING

Design

The duomorph is a bending plate device designed to operate during vibration. The device consists of a stainless steel plate sandwiched between a pair of piezoceramic crystals. A metallic strain gauge is glued to the center of each crystal (Fig. 13). The piezoceramic crystals are low-power,
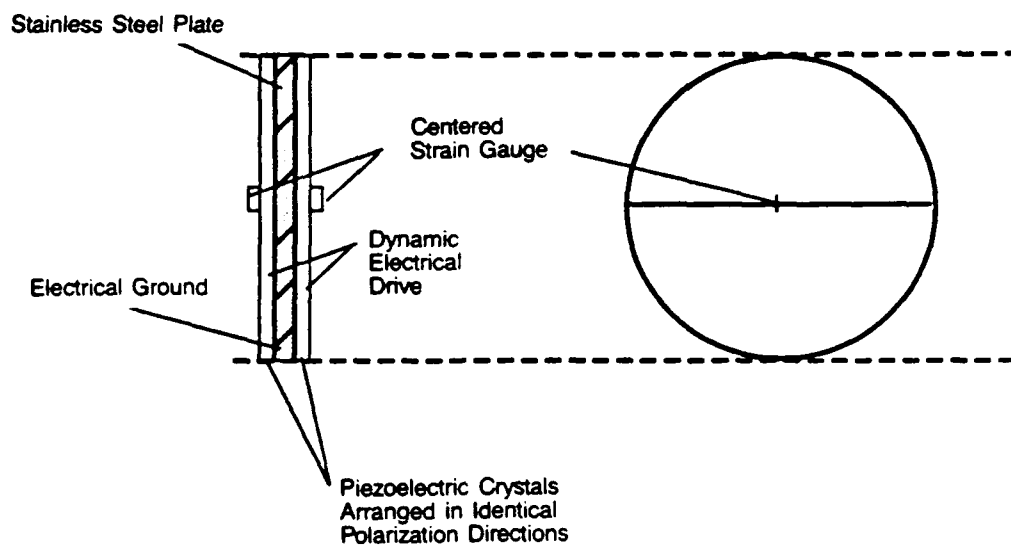
Figure 13. Schematic diagram of the duomorph sensor. Two piezoceramic crystals are adhered to a stainless steel plate. The duomorph sandwich is excited with an alternating current. The resulting deflections are measured with strain gauge technology.

vice versa. When stimulated by an alternating current, the duomorph vibrates in a parabolic fashion (Fig. 14). To measure the modulus of a sediment, the duomorph is embedded in the sediment in a consolidometer. The difference between the unconstrained bending of the duomorph in air and the bending allowed by the sediment while embedded is a function of the sediment dynamic modulus. Much of the theoretical basis for the duomorph is taken from a discussion of classical plate theory (Timoshenko and Woinowsky-Krieger 1959). Inherent assumptions are that (1) classical plate theory represents the behavior of the duomorph, (2) the sediment is elastic and infinite, (3) inertial effects are negligible below 500 Hz, and (4) sediment stresses and deformations are significant only within a cube of material that has edges equal in length to twice the diameter of the duomorph (Briar and others 1976). For a complete discussion of the theory and testing of the duomorphs used, see Appendix A.

Duomorphs were built with varying thicknesses of stainless steel between two piezoceramic crystals. The ones used predominantly for these carbonate sediments were constructed with a plate 0.008 inch thick. The piezoceramic crystals were obtained in two separate lots from Piezo Electric Products, Inc., Metuchen, NJ, 08840. The piezoceramic crystals used were a G-1278 type, fired silver, with a thickness of 0.279 cm and a diameter of 2.54 cm. The crystals used for the first five duomorphs constructed were obtained around 1981. A new lot was purchased in 1988 and allowed to age from 6 months to 1 year before use. On each piezoceramic crystal a 350Ω resistance metallic strain gauge obtained from MicroMeasurements Group, P.O. Box 27777, Raleigh, NC, 27611, was fixed with a 0.152-cm gauge length, a 0.254-cm grid width, an overall length of 0.381 cm, and an overall width of 0.254 cm. The gauges are an "EA" type that measure up to 5% strain.

After the strain gauges were carefully fixed to the crystals with adhesive, the stainless steel plate was carefully sandwiched between the two crystals. Thin wires of equal length were carefully soldered to the crystals, to the steel plate (ground), and to the tabs on the strain gauge. This configuration, where the polarity of the two crystals is in the same direction, is the design of the duomorph used in this study. The duomorph was coated with a combination of Dow Corning resins 184 and 186 to protect the wires and gauges from moisture while embedded in sediment.
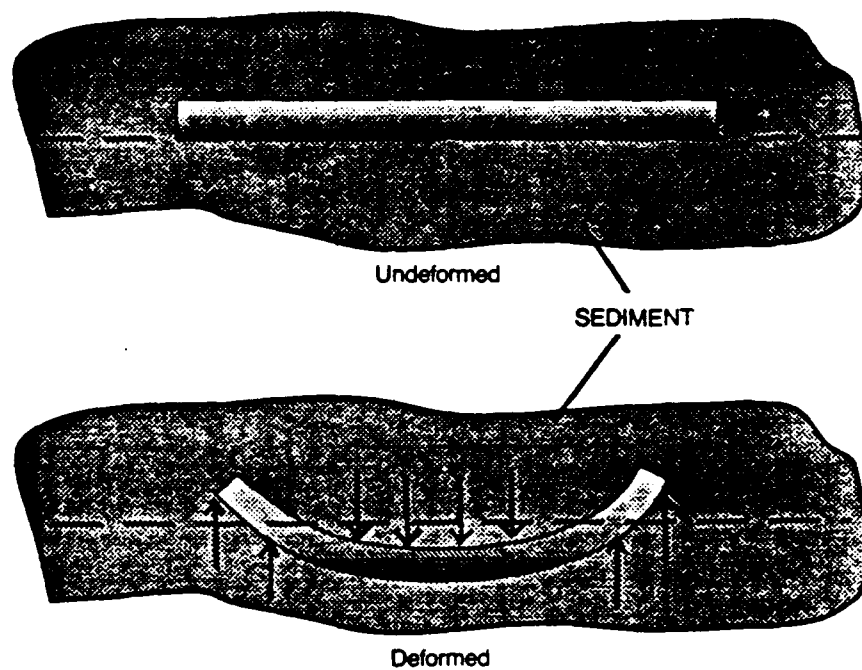
Figure 14. The duomorph behavior in sediment is parabolic, as shown by holographic techniques (Briar and others 1972).

Duomorph Laboratory Setup

The piezoceramic crystals comprising the duomorphs were excited with an alternating current at a frequency of 2 J0 h at a current level between 5 and 10 V (10 and 20 V peak to peak). The current generated by a Wavetek Model 178 programmable waveform synthesizer (Fig. 15). The application of alternating current caused one crystal to contract while the other expanded. The piezoceramic crystals in the duomorph converted the electric energy to mechanical energy. The resulting mechanical deflection was measured by the wire strain gauges mounted on each piezoceramic crystal. The strain gauges were 300 Ω resistors connected to a Wheatstone Bridge usually in a half-bridge configuration in a Model 1200 BLH Electronics, Inc., digital strain indicator. The bridge was carefully balanced in an unstrained mode before each testing. The dynamic output from the strain indicator was amplified using a Tektronix 502 differential amplifier and filtered when necessary using a Krohn-Hite Model 3100 filter. In general, the filter was necessary only to remove direct current (DC) offset. At frequencies lower than 100 Hz the filter was required to remove electronic "noise." The resulting output was photographed from a Tektronix AM 7623 oscilloscope. The shear modulus of the sediment was obtained by comparing the difference between the measured deflection of the duomorph in air and in the sediment. The difference in phase and amplitude is a measure of the material property.

Duomorph Data Reduction

The methods used to reduce data taken from the oscilloscope are outlined below:

1. Phase and amplitude of the input and output voltages are measured in air and in the sample with an oscilloscope. The waveforms displayed on the oscilloscope are usually photographed with a Polaroid camera and the photos used as a permanent record.

2. The wave form displayed on the oscilloscope represents the amount of dynamic strain detected by the strain gauges. The strain was used in the following equation to determine the modified moment ratio:
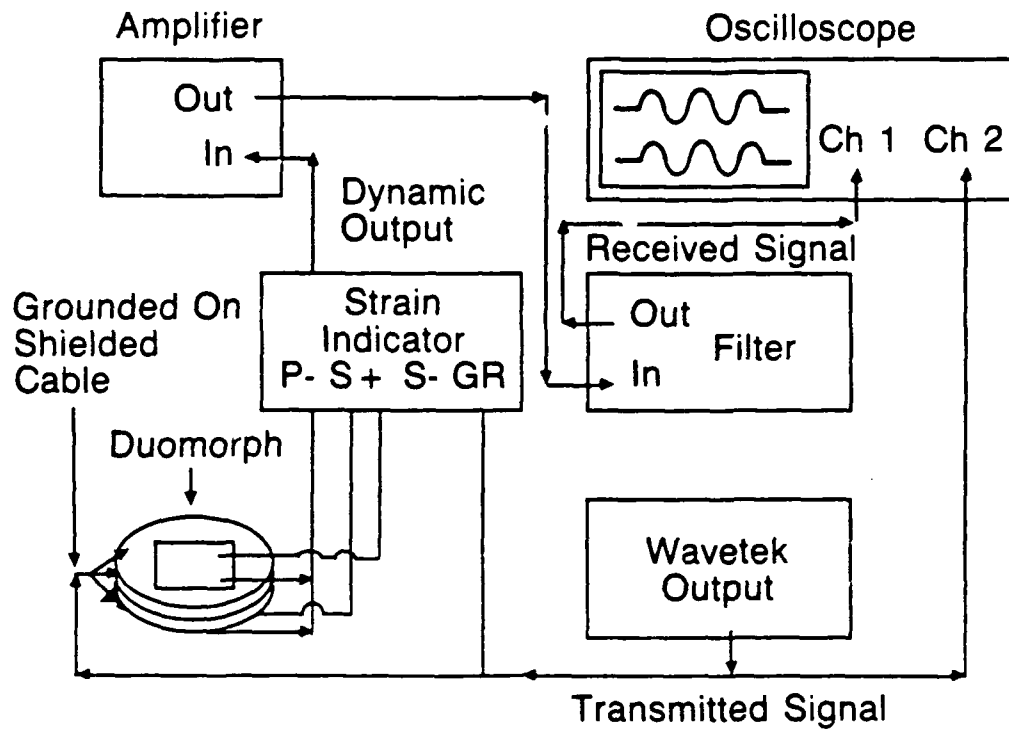
Figure 15. Schematic diagram illustrating the laboratory setup for measuring shear modulus using the duomorph sensors.

$$\left|\frac{Mc}{Mo}\right| = \frac{(es/ea) - k^*}{1 - k^*}$$ (12)

where es is the strain in sediment under a load, ea is the strain in air, and k^* is the electromechanical coupling coefficient, a measure of the piezoelectric effect. It is a constant dependent on disk design (for the duomorph with a 0.008-cm steel plate, $k^* = -0.664$) (Briar and others 1976).

$$\frac{1}{k^*} = 1 - \frac{3B\ hz\ (hz + t)\ (2 + Es\ t/Ez\ hz)}{h^2 \left[1 + (Es/Ez - 1)\ (t/h)^3 \right]}$$ (13)

where $B = 0.5\ (1 + hm/hz) = 0.86364$, hz = thickness of the piezoceramic crystal, t = height of the duomorph overall, Es = Young's modulus of steel plate, and Ez = Young's modulus of the piezoceramic crystal.

The modified moment ratio was used to determine the modulus, M, from a nomograph generated from analyses of the symmetrically constructed duomorph (Fig. 16, after Briar and others 1976). The difference in phase between air and sediment values was $-\theta$. The nomograph is entered from $-\theta$ and intersects M at some value, $\tan \phi$. The elastic modulus, E', was calculated using the following equation:

$$E' = \frac{MD}{a^3},$$ (14)

where a is the radius of the duomorph and D is the disk flexural rigidity.

Young's modulus, E^*, shear modulus, G, and shear wave velocity, Vs, are determined as follows (from Hamilton 1971):

$$E'' = E' + \tan \phi$$ (15)

$$E^* = \sqrt{E' + E''}$$ (16)

$$G = \frac{E^*}{2\ (1 + v)}$$ (17)
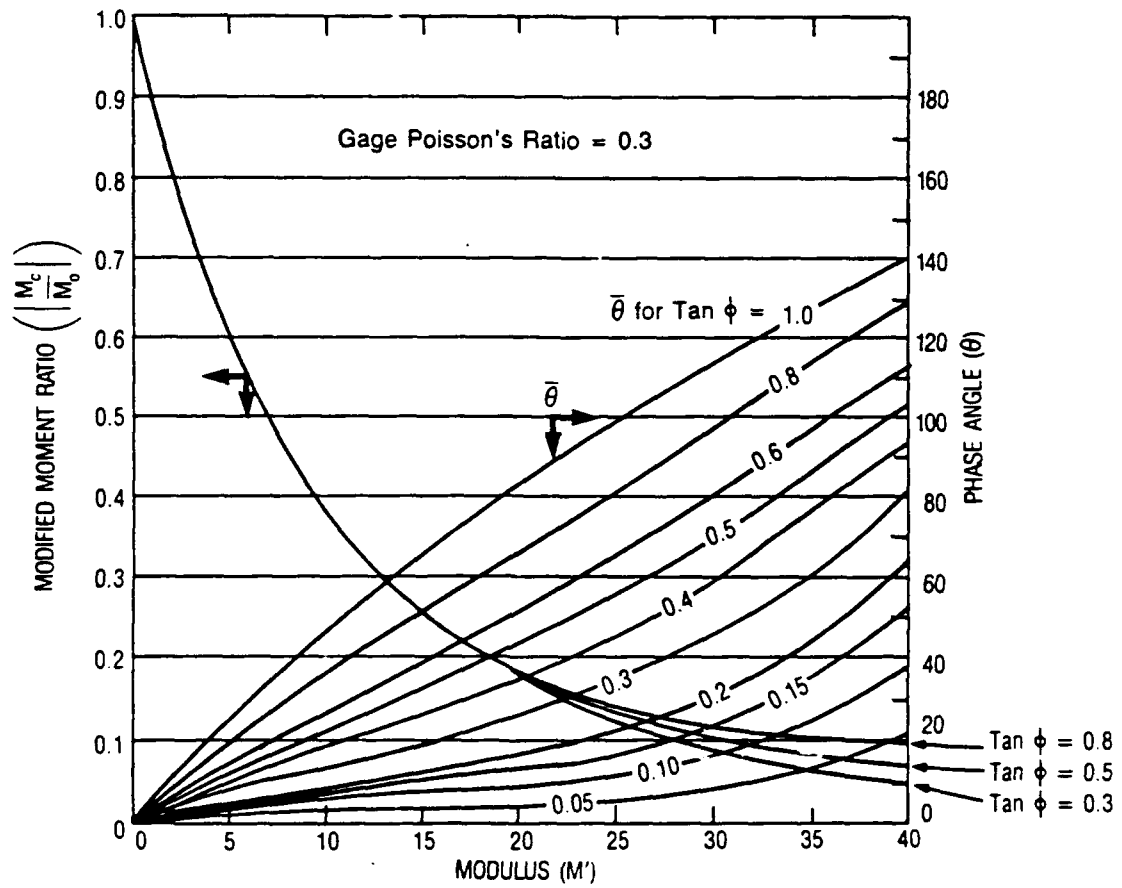
Figure 16. Experimentally derived nomograph used to calibrate M' (redrawn from Briar and others 1976).

where v is Poisson's ratio and is estimated to be ~0.49 for these samples, based on values calculated from similar periplatform ooze samples recovered from ODP Site 630 (Lavoie 1988).

$$Vs = \sqrt{\frac{G}{\rho}} \, , \qquad (18)$$

where ρ is the measured wet bulk density.

Simultaneously, a duplicate sample was tested in a second consolidometer fitted with compressional transducers in the base and cap. Compressional wave velocity is calculated from

$$Vp = \frac{x - x_0}{t_{sample} - t_0} \, , \qquad (19)$$

where x is the measured height of the sample as measured by linear velocity displacement transducers (LVDT) and recorded automatically on an Esterline Angus PD2064 data logger; x_0 is the distance between the transducers when placed together, taken as zero; t is the time taken from the oscilloscope between the transmitted and received peaks (usually second peaks) of the sample being measured; and t_0 is the time between the transmitted and received peaks when the measurement is made with the transducers placed together.

Measurements are made at 55 kHz or 60 kHz and 0.5 V. At least three and usually five to six measurements are made for each load during the consolidation testing. These velocity measurements are plotted and a curve fitted using Cricket Graph for the Macintosh. The regression equation thus obtained is used in an alternate calculation of G, which is used as a crude check of the duomorph results (Hamilton 1971):

$$G = (\rho \, Vp^2 - \beta) \, (3/4), \qquad (20)$$

where ρ is the wet bulk density measured using weight and volume techniques before and after testing. Intermediate values are interpolated. β is the bulk modulus, which obtains:

$$\beta = Av \left(\frac{1}{1 + e_0} \right) , \qquad (21)$$

where av, the coefficient of compressibility, is the slope from the consolidation curve at each loading (Fig. 9b).

$$av = \Delta e / \Delta p, \qquad (22)$$

where Δe is the change in void ratio between two load increments, and Δp is the change in pressure between the same two load increments:

$$Vs = \sqrt{\frac{G \text{ (calculated from measured Vp)}}{\rho}} . \qquad (23)$$

FABRIC

Fabric is defined here as (1) grain-to-grain relationships (shapes, orientations, nature of grain-to-grain contacts), (2) grain-to-matrix relationships (grain-supported vs. matrix-supported sediment), and (3) matrix component particle relationships (shapes, sizes, orientations, nature of particle-to-particle contacts). Grains are particles significantly larger than matrix size. Particles are said to be grains if there is room for matrix material to fit within pores formed by grains in contact. Texture differs from fabric in that texture is simply the measure of the particle diameters. The fabric is said to be grain supported when the grains are in contact with each other, and matrix supported when the grains are floating within the matrix particles. When the fabric is predominantly grain supported, the grains transmit stresses and may prevent consolidation of the matrix particles (Bennett and others 1989). Other important features include the number, shapes, and sizes of void spaces.

The fabric of a sediment ultimately determines the porometry of the sediment (Bennett and others 1980, Bennett and others 1989). The analysis of pore spaces contributes to an understanding of the relationship between porosity and permeability of a sediment. The porosity of a sediment is the ratio of the volume of the void spaces to the volume of the total sample. The total porosity of a sediment can be divided into interparticle porosity (or interconnected pore spaces) and intraparticle porosity (or pore spaces contained within individual grains and not necessarily

interconnected) (Fig. 17a,b). Permeability is a measure of the rate at which fluid can pass through the sediment and is largely controlled by the length of the effective drainage paths (Lambe 1951; Bryant and others 1975; Bennett and others 1989) and size of pore throats (Wardlaw and others 1988; Etris and others 1988).

METHODS

Laboratory determinations of porosity and void ratio were made using a helium-purged pycnometer. The consolidation analyses were made using Wykham Farrance consolidometers, adding loads incrementally from 1.53 kPa to 4600 kPa. For a complete discussion of the technique, see Lambe (1951). Three consolidometers were utilized: two were standard Wykham Farrance consolidometers, while the third was a NORDA-built consolidometer which incorporated compressional wave transducers in the cap and base of the cell. Consequently, the porous stone area was reduced in this cell and permeability was not measured (Fig. 18). Initial plans were to measure pore pressures during the consolidation process. However, dissipation of pore pressure occurred so quickly that it could not be accurately recorded by our data logger (or it was too small to register on the Validyne pressure transducers used). This port was subsequently blocked off. Samples tested in this cell are marked "vp" after the sample designation. Samples tested in the alternate cell are marked "duo," which stands for duomorph. The samples marked duo have been slit on the side with a razor and a duomorph inserted. These latter samples, therefore, have a large void space cut in them before consolidation, and more handling disturbance than the other samples. The assumption was that the void would "heal" itself after the addition of several loads.

Various techniques for studying the fabric of a sediment, principally marine clay sediments, were discussed by Bennett and others (1989), Bennett and others (1980), Bryant and Bennett (1988), and Ruzyla (1986), Bennett and others (1977), and Bennett (1976). Computer-assisted image analysis of pores was accomplished both by reflected and transmitted light microscopy (Etris and others 1988; Wardlaw and others 1988), Transmission Electron Microscopy (TEM; Bennett and others 1989) and SEM (Ruzyla 1986). For this study the SEM was used exclusively
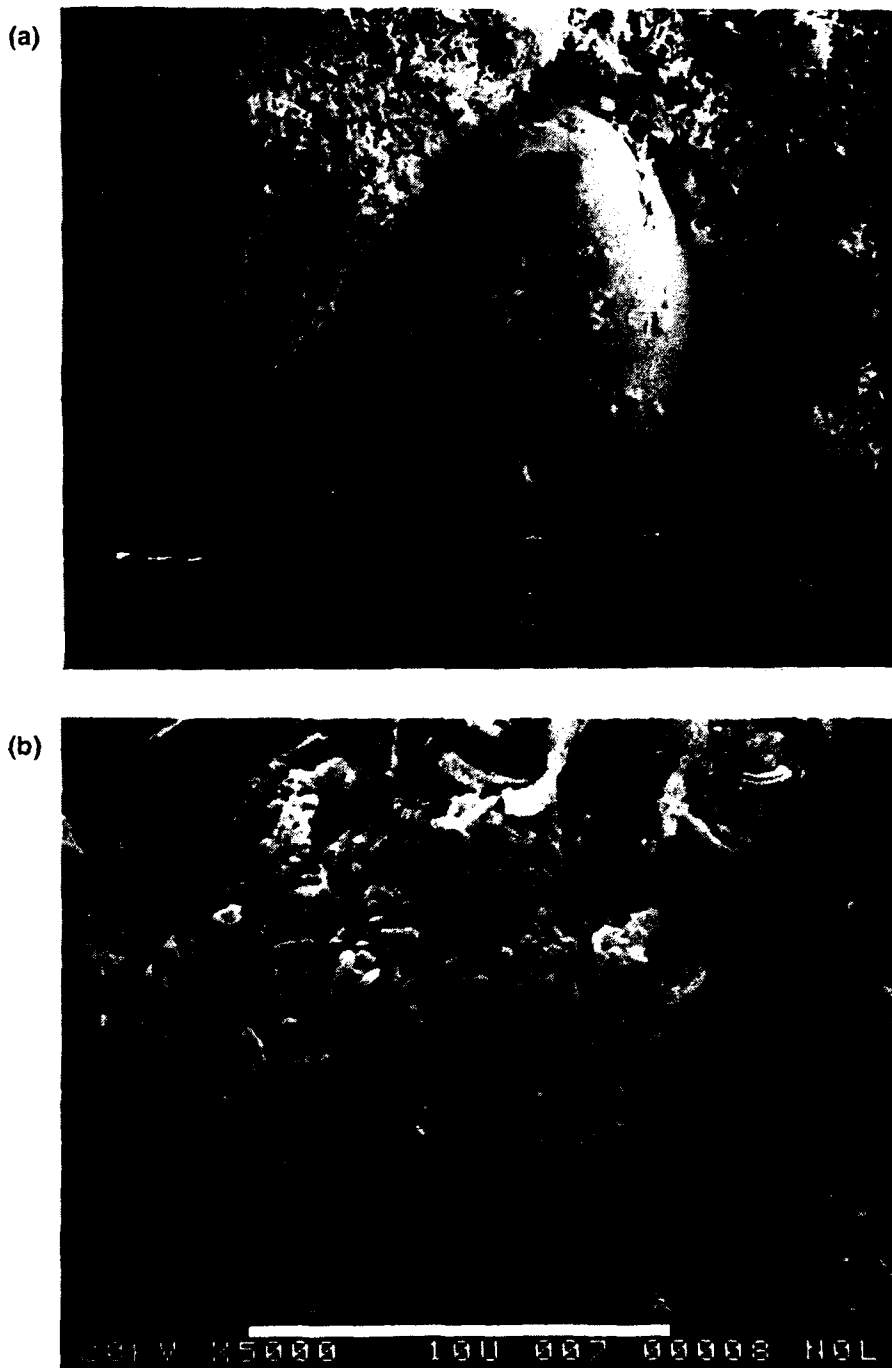
Figure 17. (a) Broken foraminifer grain illustrates typical intraparticle porosity. Sample is LBB 15H-1. Magnification is 1000X. (b) Calcareous dinoflagellate cyst in ES 7P-1 is a matrix particle also illustrating intraparticle porosity on a smaller scale. Magnification is 5000X.

Top Ring
(with O-ring)

Cap

Assembly Screw (2)

Upper Transducer
Assembly

Signal Leads

Cap Stone Screw (2)

Cap Stone

Assembly Guide Pin (2)

Outer Ring

Overflow Port

Sample Ring
(with O-ring)

Lower Transducer
Assembly

Pore Pressure
Stone Sleeve

Signal Leads

Base
(with 2 O-rings)

Adapter Plate

Pore Pressure
Port

Adapter Plate
Screw (2)

Pore Pressure
Stone

Stone Removal
Port Screw
(with O-ring)

Figure 18. NORDA consolidometer holder with compressional wave transducers embedded in the cap and base.

because the size of the grains and matrix particles was large enough to obtain good resolution. The porometry analysis of these carbonate samples was accomplished using the LeMont Image Analysis System.

Samples were prepared for the SEM by gently cutting a small (0.5 × 0.5 cm) square from the center of the sediment before and after consolidation. The interstitial fluid was replaced with 100% ethanol and then either critical point dried or air dried. No difference in sample quality was noted for the different drying procedures. After drying, carbonate samples were fractured to expose surfaces for observation and then coated with a gold-palladium film prior to observation with an AMRAY Model 1000A SEM.

Once a sample was in the SEM, the entire surface was scanned for a representative section and photographed. Quantitative pore-size analysis was done on the AMRAY utilizing a LeMont Scientific Model DA-10 Image Analyzer. The DA-10 is a computer-based system that operates by digitally scanning the electron beam across the sample at intervals small enough to detect the minimum feature of interest. When the SEM signal exceeds a preset threshold level, the system goes into an "on feature" mode in which it sweeps the beam across the feature in a grid pattern to determine the feature area, the perimeter, the geometric center, and the long and short axes. These morphometric data are stored on disk and are reported at the end of the analysis as a table of statistics on the analyzed population and as a size frequency histogram. For these analyses, the threshold was set so that only those pores that measured between 0.5 and 5 μm in the horizontal chord were analyzed. From a visual study of the micrographs, it was determined that pores with a long axis of greater than 5 μm were probably fracture artifacts and therefore were omitted from the analyses. Analyses were done at a magnification of 2000X on fields that were substantially free of these and other preparation artifacts.

Further characterization of the sediment was accomplished by washing a representative portion of the cube from which the SEM stubs were prepared. The coarse fraction was allowed to settle for 15 seconds before decanting the fine fraction. The washing procedure was repeated until the water

was completely clear after stirring the residue. The coarse fraction represents coarser than silt-sized (4ϕ) grains. The remaining fine fraction was saved and used to prepare smear slides for light microscopy. The coarse fraction was examined under reflected light using a Leitz Stereo Microscope. The fine fraction was examined with a Leitz Orthoplan Petrographic Microscope.

RESULTS

Consolidation

Consolidation results are presented in Table 5. Initial void ratios before consolidation range between 2.03 for ES 5P-1(2) (duo) and 1.0 for ES 7P-6. Final void ratios after consolidation to ~4500 kPa range between 0.94 for ES 10P-4 and 0.46 for ES 7P-6. The average difference between initial and final void ratios as a result of consolidation over all samples tested was 0.696, indicating a small volume change. In comparison, the initial void ratio (2.9) for Station 7, a sandy clay from the Mississippi Sound, was significantly higher than the average initial void ratio for the periplatform oozes (1.44). The final void ratio of 0.33 for Station 7 was much lower than the average final void ratio of 0.74 for the periplatform carbonates. Typical initial void ratios for deep-sea clays recovered from the upper 10 m ranged between 4.5 and 6 with a decrease in void ratio of 3 over ~4500 kPa (Bryant and Bennett, 1988). Other researchers reported even higher initial void ratios (4 to 10) from Gulf of Mexico and North Atlantic clays (Bryant and others 1981; Keller and Bennett 1970).

Figures 19 through 26 are the e-log-σ' curves for these samples presented sequentially by core. Examination of these curves shows that many of the virgin curves are monotonic. This is, in part, because there is only a small decrease in void ratio over the 4500 kPa of pressure applied during testing. Another factor that can produce flat curves is disturbance of the sample during coring and subsequent handling, some of which is unavoidable. Consequently, it was difficult in many cases to determine the maximum past pressure by the Casagrande method, which requires determining the point of maximum curvature. The results of trying to apply this method were ambiguous at best.

Table 5. Consolidation Results

Sample ID	Water Depth (m)	Test Type	w(0) (%)	w(f) (%)	k(0) cm/s	k(f) cm/s	Gs	e(0)	e(f)	n(0) Cons. (%)	n(f) Cons. (%)	e(0) Pyc.	e(f) Pyc.	n(0) Pyc. (%)	n(f) Pyc. (%)	rho(0) Pyc. Mg/m³	rho(f) Pyc. Mg/m³
ES 4P-1	1920	DUO	38	34	6.64×10^{-6}	1.75×10^{-6}	2.76	1.34	0.78	57.26	43.82	1.04	0.92	51	48	1.86	1.91
ES 4P-1	1920	VP	47	29			2.76	1.30	0.84	56.52	45.65	1.30	0.79	57	44	1.77	1.98
ES 4P-2	1920		72	52	3.76×10^{-6}	2.90×10^{-7}	2.76	1.89	1.01	65.40	50.24	1.98	1.43	67	59	1.59	1.73
ES 4P-3	1920		49	36	3.72×10^{-7}	2.59×10^{-7}	2.75	1.32	0.68	56.90	40.48	1.36	1.00	60	50	1.74	1.88
ES 4P-4	1920		53	38	2.64×10^{-6}	4.08×10^{-7}	2.75	1.47	0.76	59.51	43.18	1.46	1.03	59	51	1.71	1.86
ES 5P-1	1957	DUO	43	33	$9.95 \times 1C^{-6}$	7.32×10^{-7}	2.73	1.12	0.62	52.83	38.27	1.18	0.90	54	47	1.79	1.91
ES 5P-2	1957	VP	44	32			2.73	1.11	0.68	47.50	40.48	1.21	0.86	55	47	1.78	1.92
ES 5P-1(2)		DUO	81	42	5.09×10^{-4}	3.71×10^{-4}	2.72	2.03	0.92	67.00	47.92	2.22	1.13	69	53	1.53	1.81
ES 5P-1(2)		VP	65	34			2.72	1.56	0.89	50.94	47.09	1.75	0.92	64	48	1.62	1.89
ES 5P-2	1957		54	38	4.21×10^{-6}	6.94×10^{-7}	2.72	1.51	0.82	59.45	45.05	1.48	1.05	60	51	1.69	1.84
ES 5P-3	1957		45	33	1.13×10^{-5}	5.80×10^{-7}	2.76	1.52	0.70	60.32	41.18	1.24	0.92	55	47	1.79	1.92
ES 5P-4	1957		47	31	3.61×10^{-6}	3.30×10^{-7}	2.83	1.28	0.55	56.14	35.48	1.32	0.87	57	47	1.79	1.98
ES 5P-5	1957		59	36	6.64×10^{-6}	3.09×10^{-7}	2.71	1.65	0.64	62.26	39.02	1.06	0.97	62	49	1.66	1.87
ES 6P-1	1980	DUO	51	40	1.70×10^{-4}	4.44×10^{-7}	2.73	1.52	0.67	60.32	40.12	1.04	1.08	58	52	1.72	1.83
ES 6P-1	1980	VP	45	36			2.73	1.23	0.69	55.16	40.83	1.22	0.98	55	49	1.78	1.88
ES 6P-2	1980		47	35	4.40×10^{-5}	2.43×10^{-6}	2.80	1.70	0.84	62.96	45.65	1.33	0.99	57	50	1.77	1.94
ES 6P-3	1980		50	32	1.69×10^{-6}	9.78×10^{-7}	2.75	1.42	0.74	58.68	42.53	1.36	0.88	60	47	1.74	1.93
ES 6P-4	1980		51	38	2.50×10^{-6}	5.46×10^{-7}	2.77	1.45	0.72	59.18	41.86	1.40	1.05	58	51	1.74	1.76

LEGEND: CONS. refers to results from consolidation testing

Pyc. refers to derived from weight/volume techniques, a totally separate and unrelated measurement based on water content

w = water content
k = permeability
Gs = specific gravity
e = void ratio
n = porosity
rho = wet bulk density

Table 5. (cont.)

Sample ID	Water Depth (m)	Test Type	w(0) (%)	w(f) (%)	k(0) cm/s	k(f) cm/s	Gs	e(0)	e(f)	n(0) Cons. (%)	n(f) Cons. (%)	e(0) Pyc.	e(f) Pyc.	n(0) Pyc. (%)	n(f) Pyc. (%)	rho(0) Pyc. Mg/m³	rho(f) Pyc. Mg/m³
ES 7P-1	1815	DUO	52	43	5.131×10^{-4}	3.701×10^{-7}	2.72	1.57	0.57	61.09	36.31	1.41	1.15	59	53	1.71	1.08
ES 7P-1	1815		54	41	2.371×10^{-6}	6.901×10^{-7}	2.72	1.62	0.76	61.83	43.18	1.47	1.11	60	53	1.70	1.81
ES 7P-1	1815	VP	41	37			2.72	1.32	0.60	56.90	37.50	1.49	1.01	60	50	1.69	1.86
ES 7P-2	1815		48	33	7.661×10^{-5}	3.011×10^{-7}	2.77	1.46	0.95	59.35	48.72	1.32	0.91	57	48	1.76	1.93
ES 7P-4	1815		49	31	9.401×10^{-7}	2.291×10^{-7}	2.74	1.25	0.75	55.56	42.86	1.33	0.85	57	46	1.75	1.94
ES 7P-5	1815		56	37	2.181×10^{-6}	3.001×10^{-7}	2.75	1.61	0.77	61.69	43.50	1.54	1.03	61	51	1.69	1.86
ES 7P-6	1815		42	31	7.391×10^{-6}	1.151×10^{-8}	2.78	1.32	0.67	56.90	40.12	1.16	0.86	54	46	1.82	1.45
ES 7P-6	1815	DUO	40	32			2.78	0.46	0.67	59.35	40.12	1.14	0.91	53	48	1.86	1.96
ES 10P-2	1837	DUO	49	35	1.571×10^{-4}	5.441×10^{-7}	2.76	1.39	0.65	58.16	39.39	1.34	0.96	57	49	1.75	1.90
ES 10P-2		VP	49	32			2.76	1.17	0.65	53.92	39.39	1.34	0.87	57	47	1.75	1.94
ES 10P-3	1837		54	34	5.251×10^{-5}	3.721×10^{-6}	2.84	1.38	0.72	57.98	41.86	1.53	0.96	60	49	1.73	1.93
ES 10P-4	1837		53	33	1.411×10^{-5}	1.871×10^{-7}	2.80	1.56	0.94	60.94	48.45	1.48	0.92	60	48	1.73	1.94
LBB 5H-3			59	34	3.271×10^{-6}	6.411×10^{-7}	2.74	1.59	0.74	61.39	42.53	1.89	0.93	65	48	1.60	1.90
LBB 10P-1	1035	VP	39	29			2.77	1.18	0.71	54.13	41.52	1.07	0.79	52	44	1.86	1.99
LBB 10P-1	1035	DUO	44	33	4.831×10^{-4}	1.251×10^{-5}	2.77	1.36	0.62	57.63	38.27	1.22	0.91	55	48	1.78	1.92
LBB 14P-1			58	31	5.571×10^{-4}	2.801×10^{-5}	2.75	1.63	0.67	61.98	40.12	1.60	0.86	62	46	1.67	1.94
LBB15H-1			52	32	2.721×10^{-5}	7.501×10^{-7}	2.74	1.61	1.03	61.69	50.74	1.41	1.06	59	51	1.72	1.84
LBB 16P-1		DUO	44	34	2.771×10^{-3}	2.541×10^{-6}	2.77	1.33	0.79	57.08	44.13	1.22	0.93	55	48	1.80	1.92
LBB 16P-2			51	36	5.531×10^{-4}	3.111×10^{-4}	2.74	1.47	.055	59.51	35.48	1.73	0.97	58	49	1.73	1.88
LBB 16P-2		VP	40	34			2.74	1.16	0.63	53.70	38.65	1.10	0.92	52	48	1.83	1.91
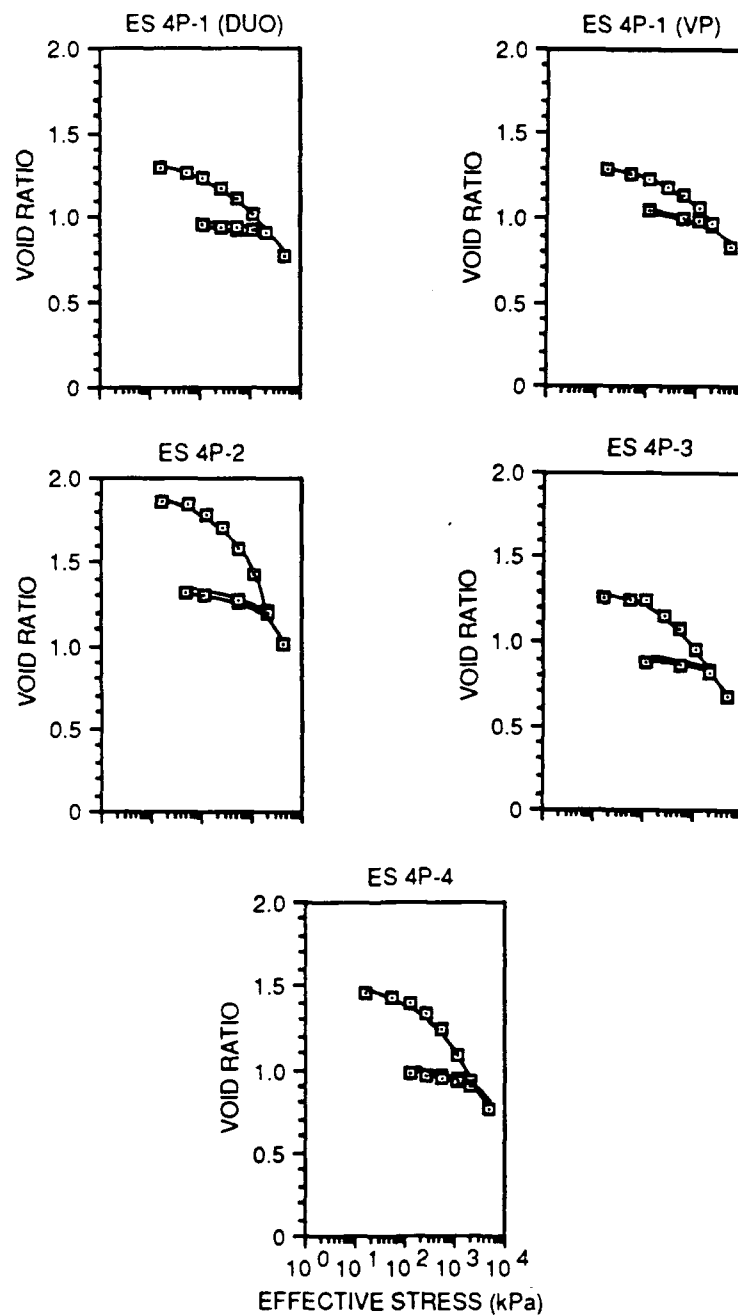
Figure 19. "e-log-σ'" curves for samples from ES 4P.
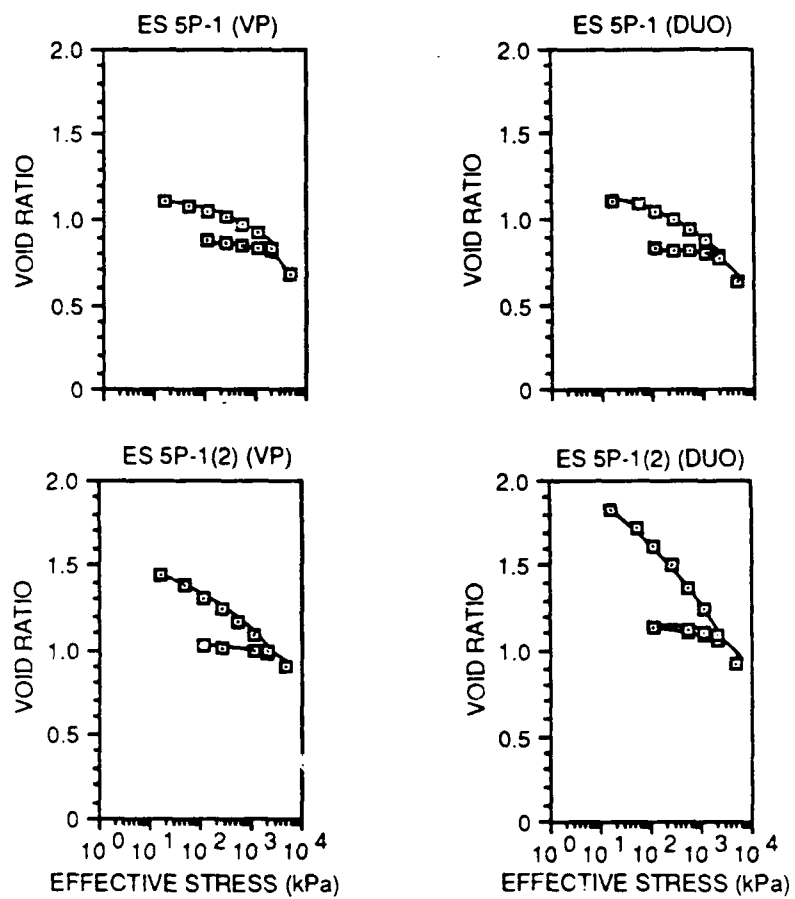
Figure 20. "e-log-σ' " curves for samples from ES 5P.
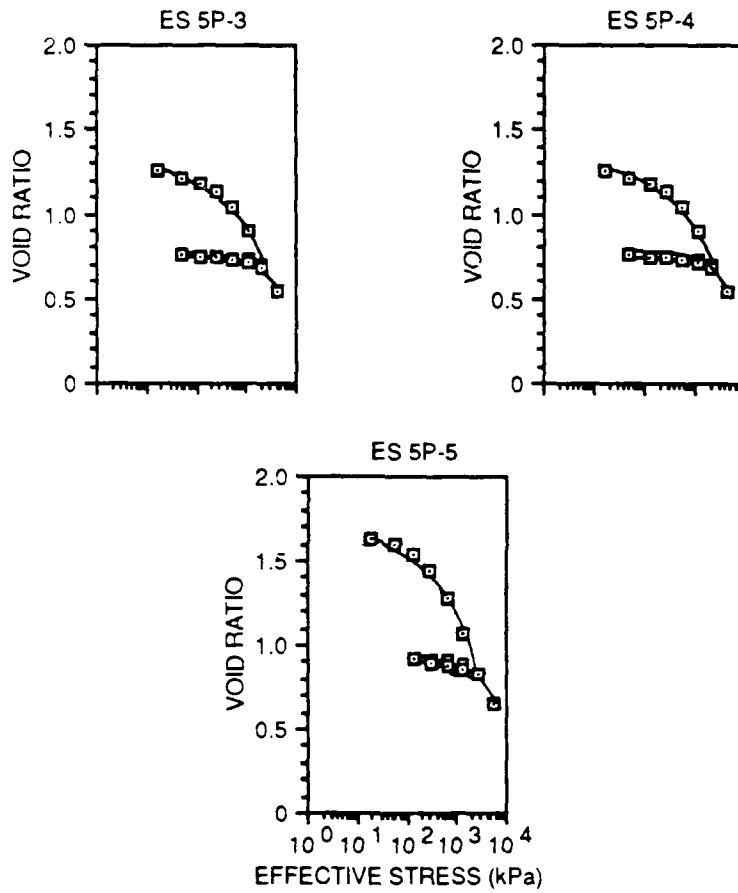
Figure 21. "e-log-o'" curves for samples from ES 5P (cont).
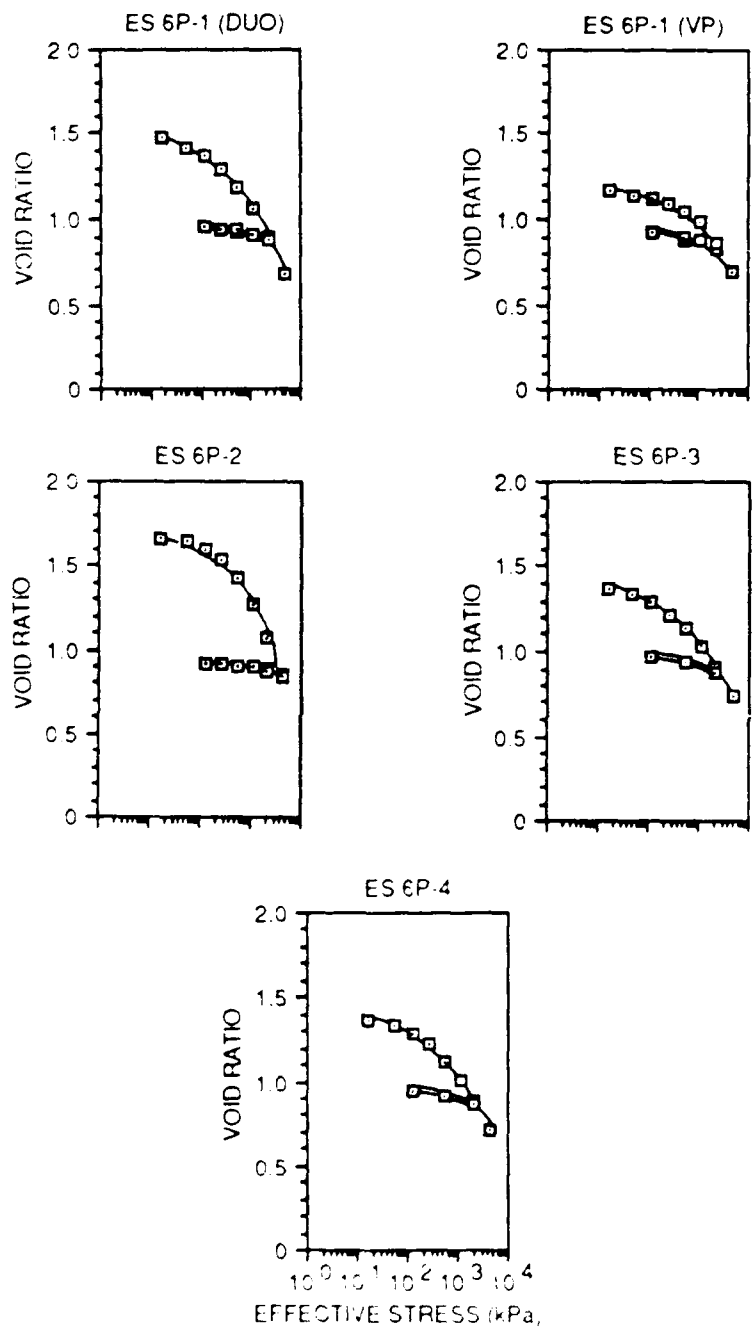
Figure 22. "e-log-σ'" curves for samples from ES 6P
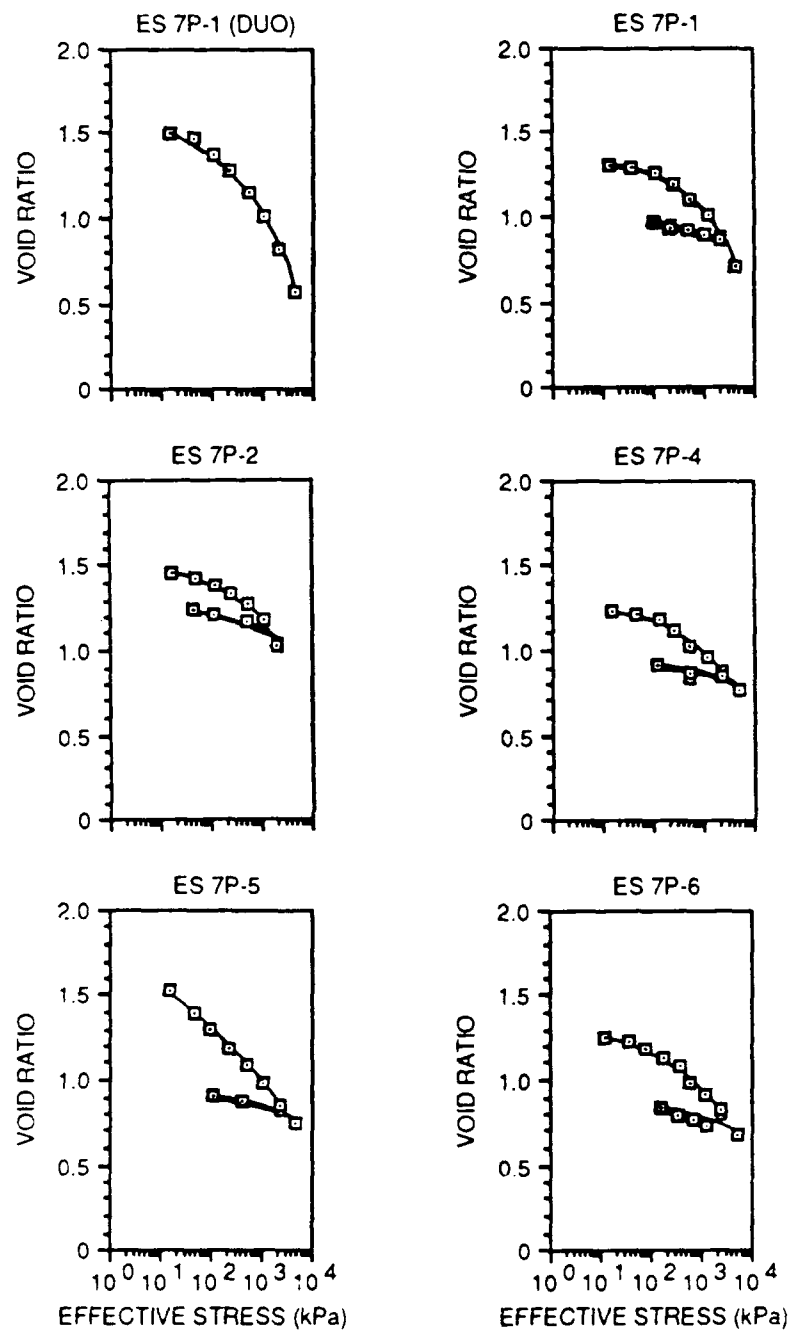
Figure 23. "e-log-σ'" curves for samples from ES 7P.
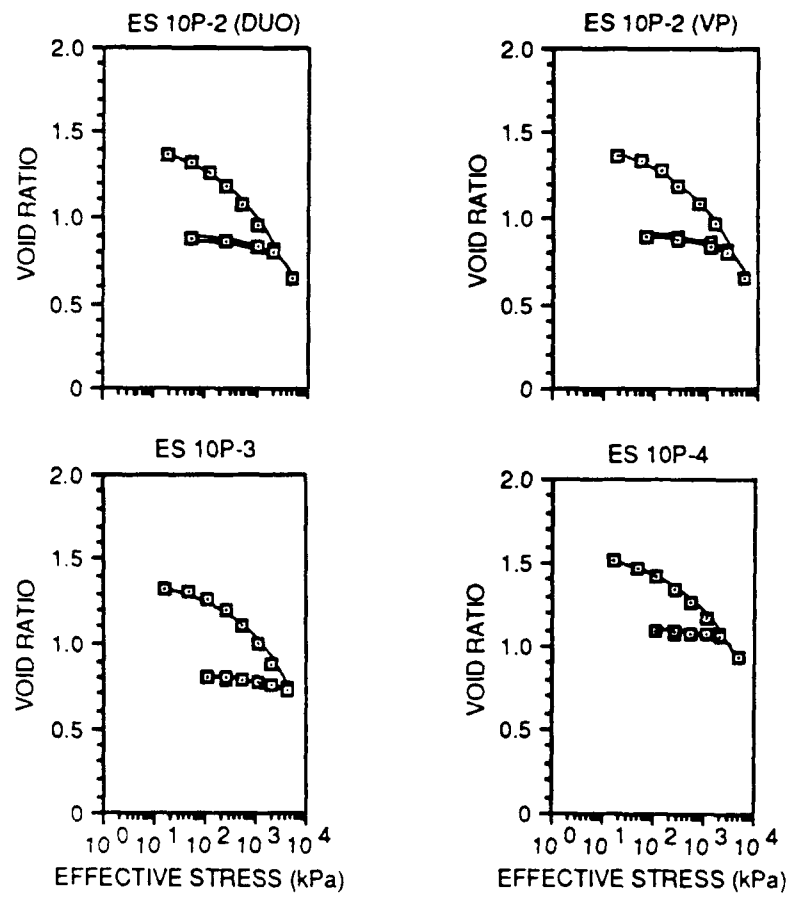
Figure 24. "e-log-σ'" curves for samples from ES 10P.
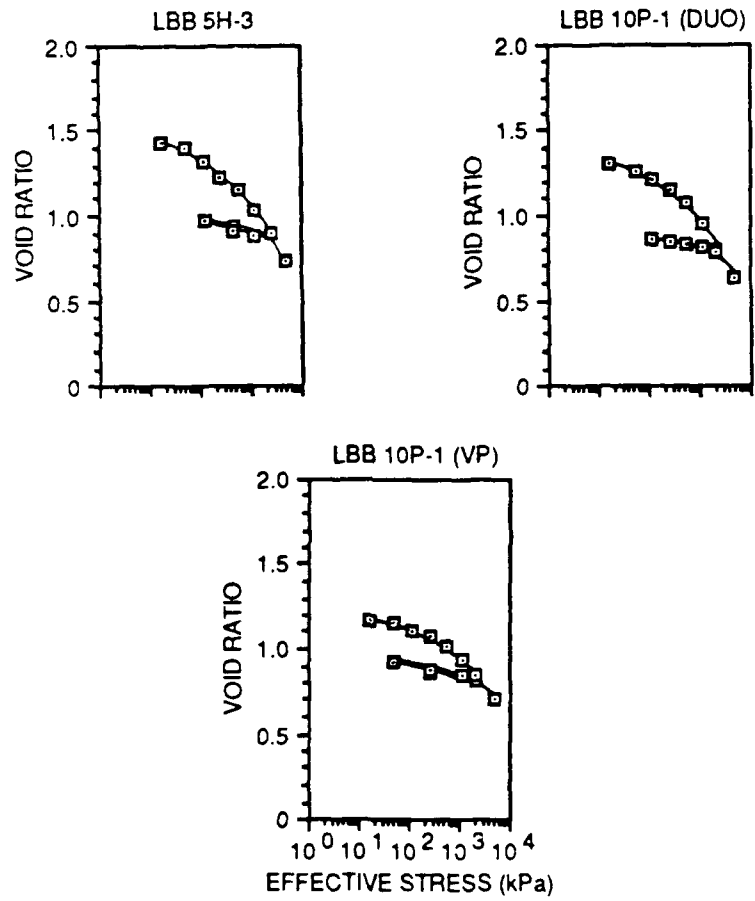
Figure 25. "e-log-σ'" curves for samples from LBB 5H and LBB 10P.
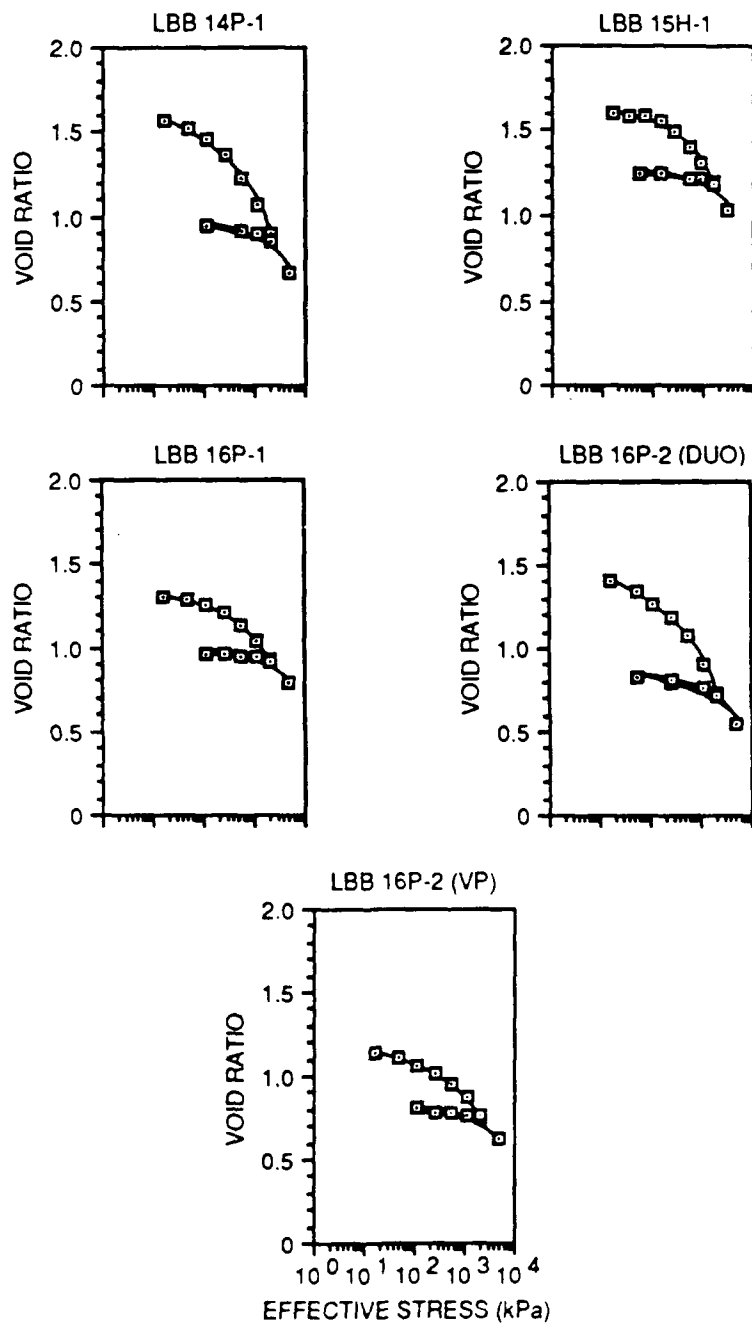
Figure 26. "e-log-σ'" curves for samples from LBB 14P, LBB 15H, and LBB 16P.

When the method was applied to these samples, the overconsolidation ratio (OCR) was very large for the surficial samples and decreased with depth in the core, for example, in core ES 4P.

ES 4P-1 (45-50 cm) OCR = 39.2

ES 4p-2 (130-135 cm) OCR = 10.3

ES 4P-3 (225-230 cm) OCR = 4.8

ES 4P-4 (355-360 cm) OCR = 2.3

Based on this technique, all of these samples must be considered overconsolidated within the upper few meters, with the overconsolidation state decreasing down the core.

The point in the e-log-σ' curves where the gradient changes significantly can be easily determined when the curves are plotted as e-σ' curves (Fig. 27). This is a typical time compression curve for these carbonates. The point where the gradient changes was plotted as a function of void ratio at that estimated depth (Fig. 28a) and as a function of porosity at that estimated depth (Fig. 28b) to show the range of estimated depths. These data are tabulated in Table 6.

The volume change as a result of consolidation testing was listed as percent volume change for each sample in Table 7. The volume lost was always greater for those samples tested with the duomorph inserted than for the duplicate samples tested without the duomorph. When the duomorph samples were ignored, the average volume lost was 27.86%. Figures 29 through 31 are graphs of volume change for the cores. The cores with the least volume change were ES 4P and ES 10P (Figs. 29 and 31); all samples in both cores were matrix supported. However, the differences in volume change between matrix supported and grain supported seemed to be very small (Table 7). In all cases, volume continued to decrease through ~4500 kPa. In these data, a change in slope indicated a change in the rate of consolidation that corresponds with the depth of gradient change determined from the e-σ' curves (Table 6).
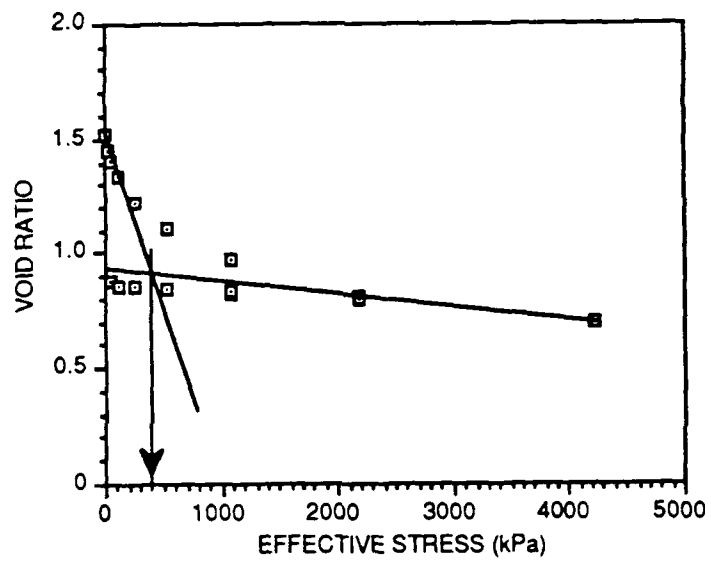
Figure 27. "e-σ'" curve. The effective stress where the gradient changes abruptly, can be determined easily by plotting the void ratio versus the linear effective stress. Here, the point where the gradient changes is 400 kPa, estimated to be ~56 m.
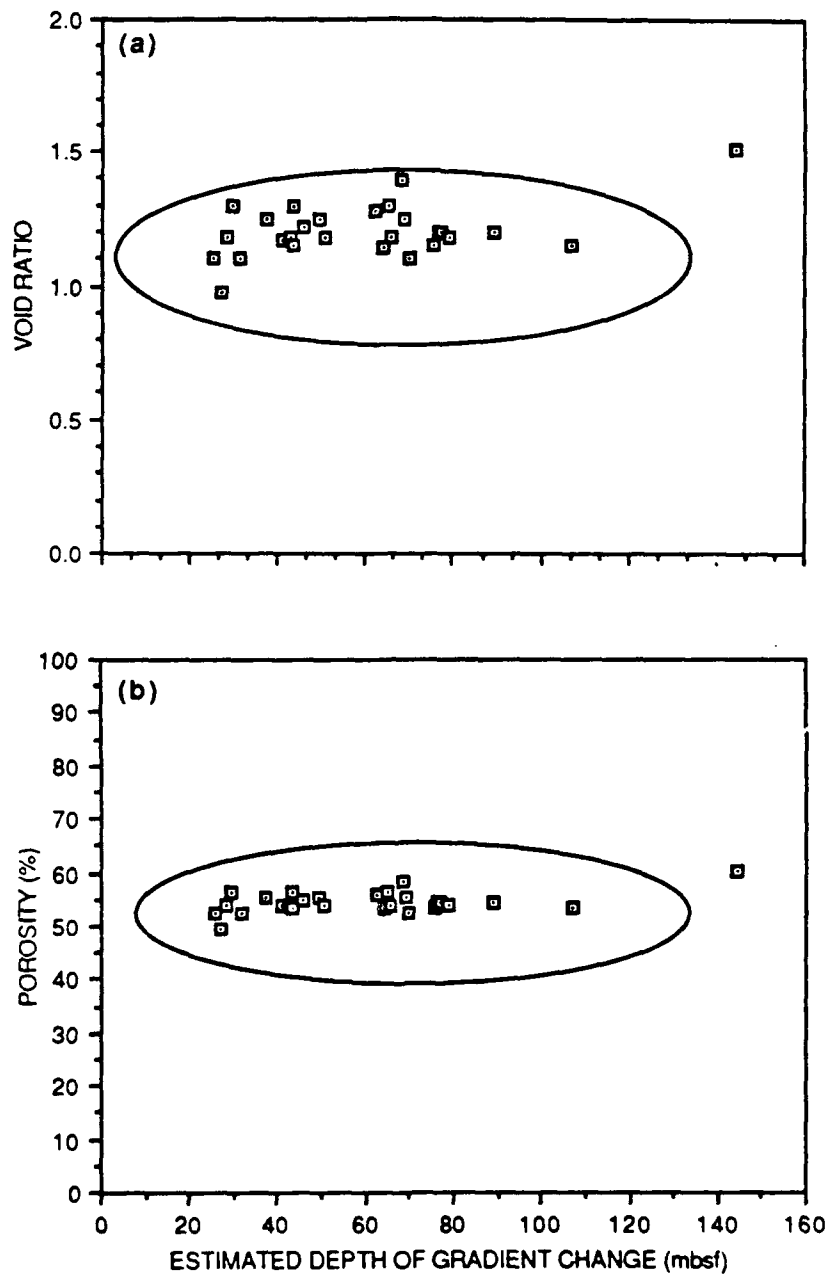
Figure 28. (a) Void ratio versus the estimated depth where the gradient changes, and (b) porosity versus estimated depth of gradient change. Void ratios and porosities fall within a narrow range while the estimated depth where the gradient changes ranges between ~26 and 144 m.

TABLE 6. Gradient Change

Sample ID	Est. Gradient Change (mbsf)	Pressure Change* (kPa)	Void Ratio	Porosity (%)
ES 4P-1	41.1	300	1.17	54
ES 4P-2	144.4	800	1.51	60
ES 4P-3	107.0	750	1.15	54
ES 4P-4	89.3	600	1.20	55
ES 5P-1	27.0	200	0.98	50
ES 5P-1(2)	77.1	450	1.20	55
ES 5P-2	69.0	450	1.25	56
ES 5P-3	70.0	525	1.10	52
ES 5P-4	76.7	575	1.20	55
ES 6P-1	30.0	220	1.30	57
ES 6P-2	68.4	500	1.40	58
ES 6P-3	64.2	450	1.14	53
ES 6P-4	42.8	300	1.18	54
ES 7P-1	75.6	500	1.15	54
ES 7P-1	65.2	425	1.30	57
ES 7P-2	62.4	450	1.28	56
ES 7P-4	31.7	225	1.10	52
ES 7P-5	46.0	200	1.22	55
ES 7P-6	25.7	200	1.10	52
ES 10P-2	49.2	350	1.25	56
ES 10P-3	43.4	300	1.15	54
ES 10P-4	43.4	300	1.30	57
LBB 5H-3	37.2	210	1.25	56
LBB 15H-1	102.7	700		
LBB14P-1	79.1	500	1.18	54
LBB 10P-1	28.4	210	1.18	54
LBB 16P-1	65.8	500	1.18	54
LBB 16P-2	50.7	400	1.18	54

* Point of inflection between primary and secondary consolidation.

Table 7. Percent Volume Change

Sample ID	(%) Volume Change Measured	Δe	(from consol)	Δe	(%) Volume Change (predicted by Schlanger and Douglas 1974)
ES 4P-1 (duo)	24	.6		13	24
ES 4P-1 (vp)	20	.5		11	20
ES 4P-2	28	.9		15	30
ES 4P-3	28	.6		16	28
ES 4P-4	29	.7		16	20
ES 5P-1 (duo)	24	.5		᠂᠄	24
ES 5P-1 (vp)	20	.4		12	20
ES 5P-1(2) (duo)	37	1.1		19	37
ES 5P-1(2) (vp)	26	.7		14	26
ES 5P-2	28	.7		15	27
ES 5P-3	32	.8		19	33
ES 5P-4	32	.7		21	32
ES 5P-5	38	1.0		23	38
ES 6P-1 (duo)	34	.9		20	34
ES 6P-1 (vp)	24	.5		14	24
ES 6P-2	32	.9		17	32
ES 6P-3	28	.7		16	28
ES 6P-4	31	.7		17	30
ES 7P-1 (duo)	39	1.0		25	39
ES 7P-1 (vp)	31	.6		19	31
ES 7P-1	33	.9		19	33
ES 7P-2	25	.5		11	21
ES 7P-4	22	.5		13	22
ES 7P-5*	32	.7		18	32
ES 7P-6*	28	.7		17	28
ES 7P-6 (duo)*		.5		18	27
ES 10P-2 (duo)	31	.7		19	31
ES 10P-2 (vp)	24	.5		15	24
ES 10P-3	28	.7		16	28
ES 10P-4	24	.6		12	24
LBB 5,1-3	33	.9		19	33
LBB 10P-1 (duo)	31	.7		19	32
LBB 10P-1 (vp)	22	.5		13	22
LBB14P-1*	37	1.0		22	37
LBB 15H-1	26	.6		11	22
LBB 16P-1*	23	.5		13	23
LBB 16P-1 (duo)*	37	.9		24	37
LBB 16P-1 (vp)*	25	.5		15	25

Legend: * indicates grain-supported or numerous grains
     ES = Exuma Sound
     LBB = Little Bahama
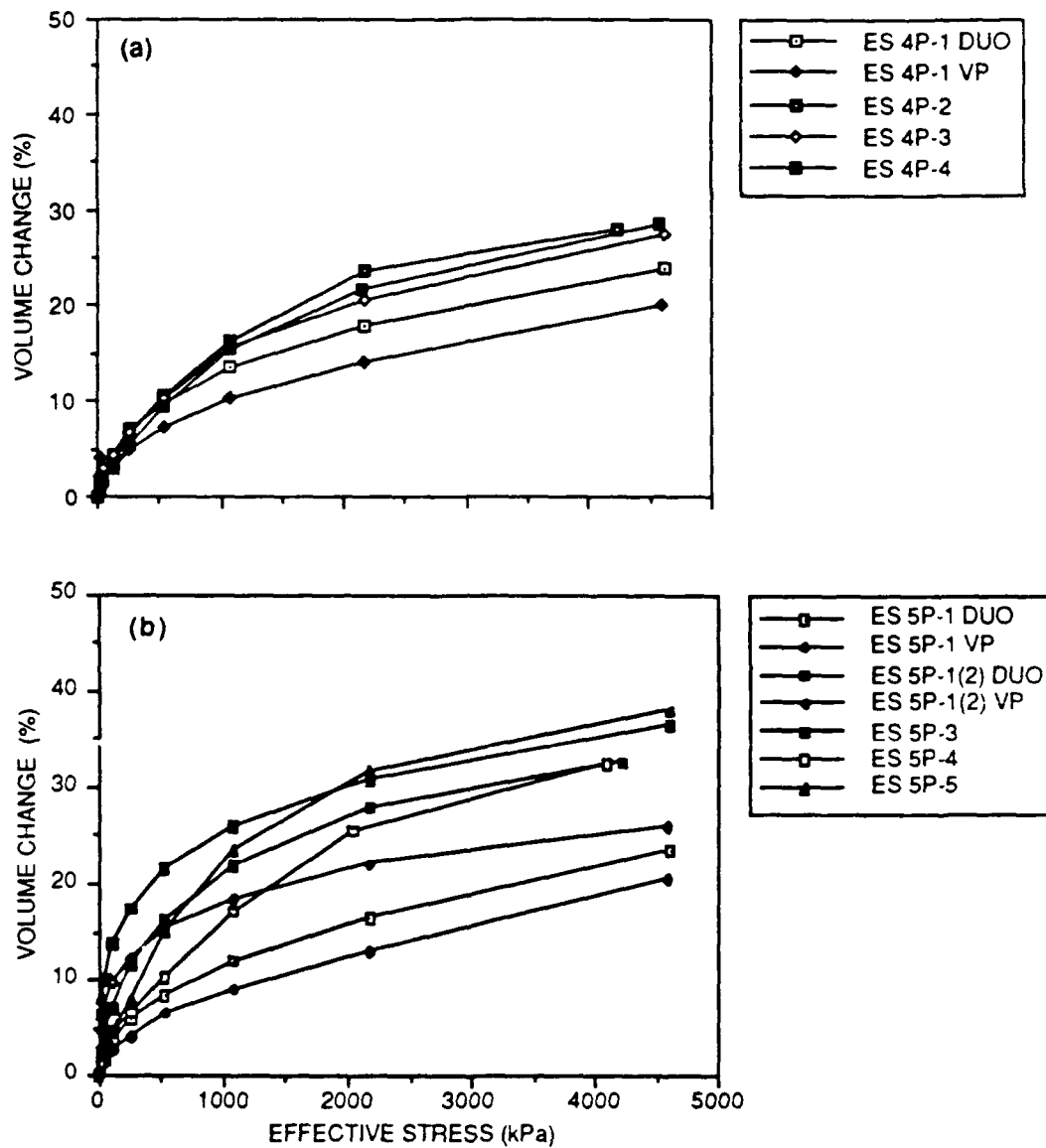
Figure 29. Plots of volume change versus effective stress for (a) ES 4P and (b) ES 5P.
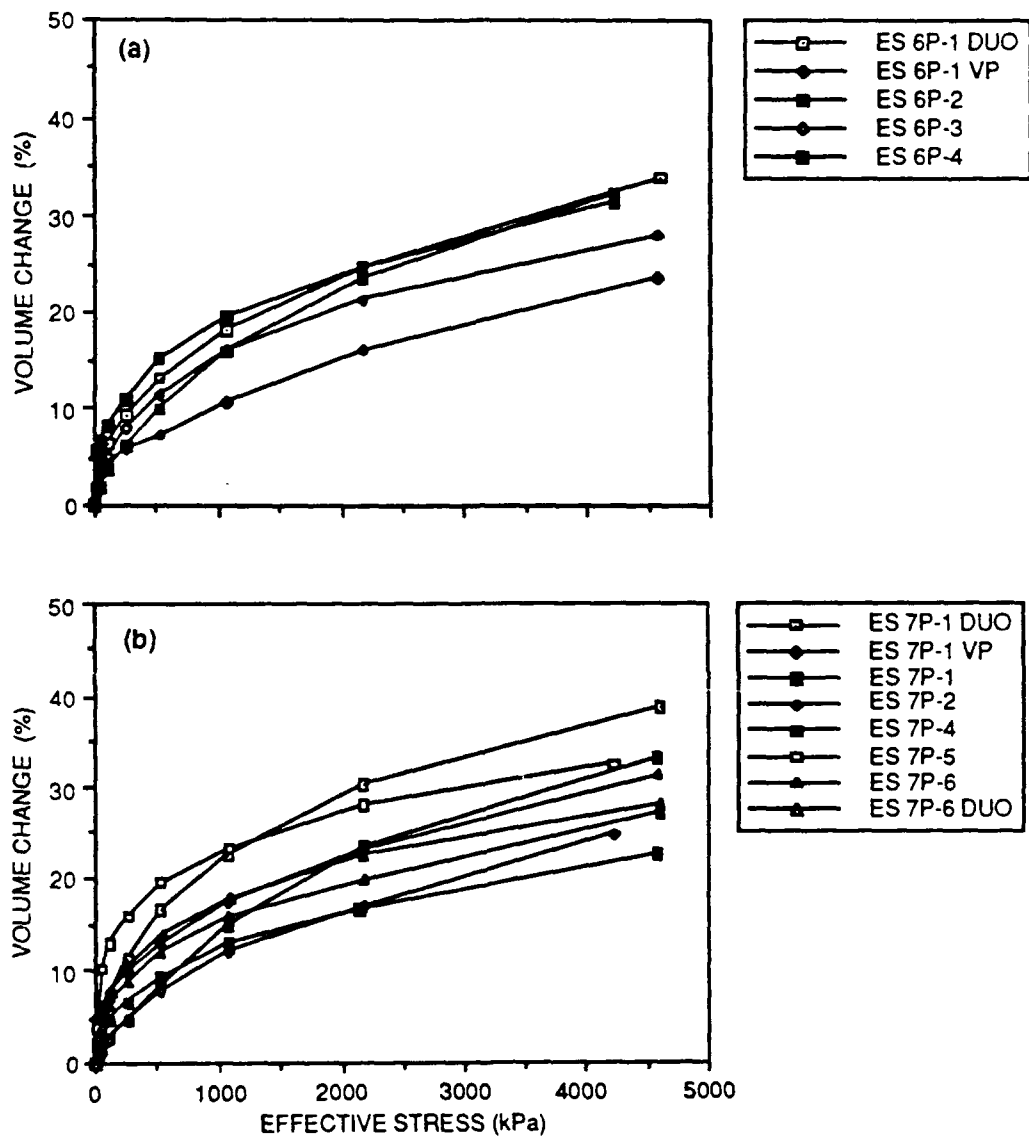
Figure 30. Piots of volume change versus effective stress for (a) ES 6P and (b) ES 7P.
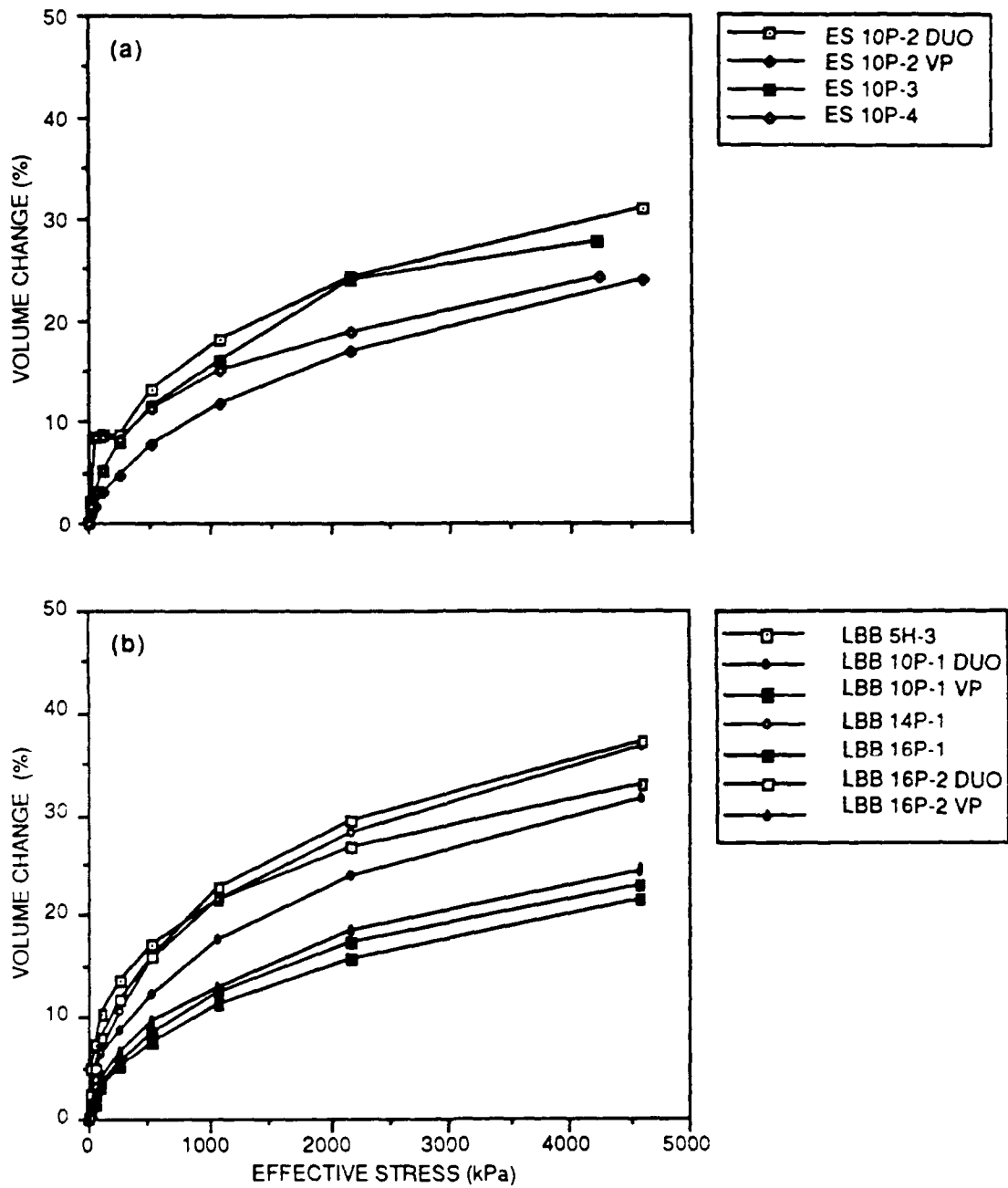
Figure 31. Plots of volume change versus effective stress for (a) ES 10P and (b) LBB cores.

Permeability, Porosity, and Density

Results of permeability measured in the laboratory are presented in Figures 32 through 39, along
with calculated permeability values. The data are presented sequentially by core. It is apparent in
many of the duomorph samples that the measured permeability, especially in the first few loads,
was significantly higher than the permeability calculated from consolidation data. This increase
may be the result of a very large void being created when the duomorph was inserted. In the matrix-
supported samples, such as ES 4P-1, this void may heal itself under a small load, while in some of
the grain-supported samples, such as ES 5P-1(2), it may not have closed even under 4500-kPa
effective stress. In several instances (e.g., LBB 16P-1), the sample seemed "soupy" when removed
from the consolidometer; the measured permeability was also very high for these samples.

In general, and if the duomorph samples are disregarded, permeability decreases an order of
magnitude over the course of testing. Permeability, for all the tested samples (except duomorph
samples) is plotted as a function of effective stress and depth in Figure 40a. The results can be
grouped as follows.

• duomorph samples with high initial permeability

• samples, generally matrix supported, with an initial permeability of about 1×10^{-5} and
1×10^{-6} cm/s

• samples, generally grain supported, with an initial permeability of 1×10^{-4} cm/s

To calculate reasonable regression equations, the matrix-supported samples were further
subdivided into two groups: those with an initial permeability of 1×10^{-5} cm/s and those with an
initial permeability of 1×10^{-6} cm/s. Regression equations that define these samples are listed.

• $k = 4.229 \times 10^{-4} (\sigma'^{-0.321})$ for grain-supported samples (Fig. 40b).

• $k = 2.69 \times 10^{-4} (\sigma'^{-0.664})$ for matrix-supported samples with an initial permeability of 1×10^{-5}
(Fig. 40c),

• $k = 2.045 \times 10^{-5} (\sigma'^{-0.432})$ for matrix-supported samples with an initial permeability of
1×10^{-6} (Fig. 40d),
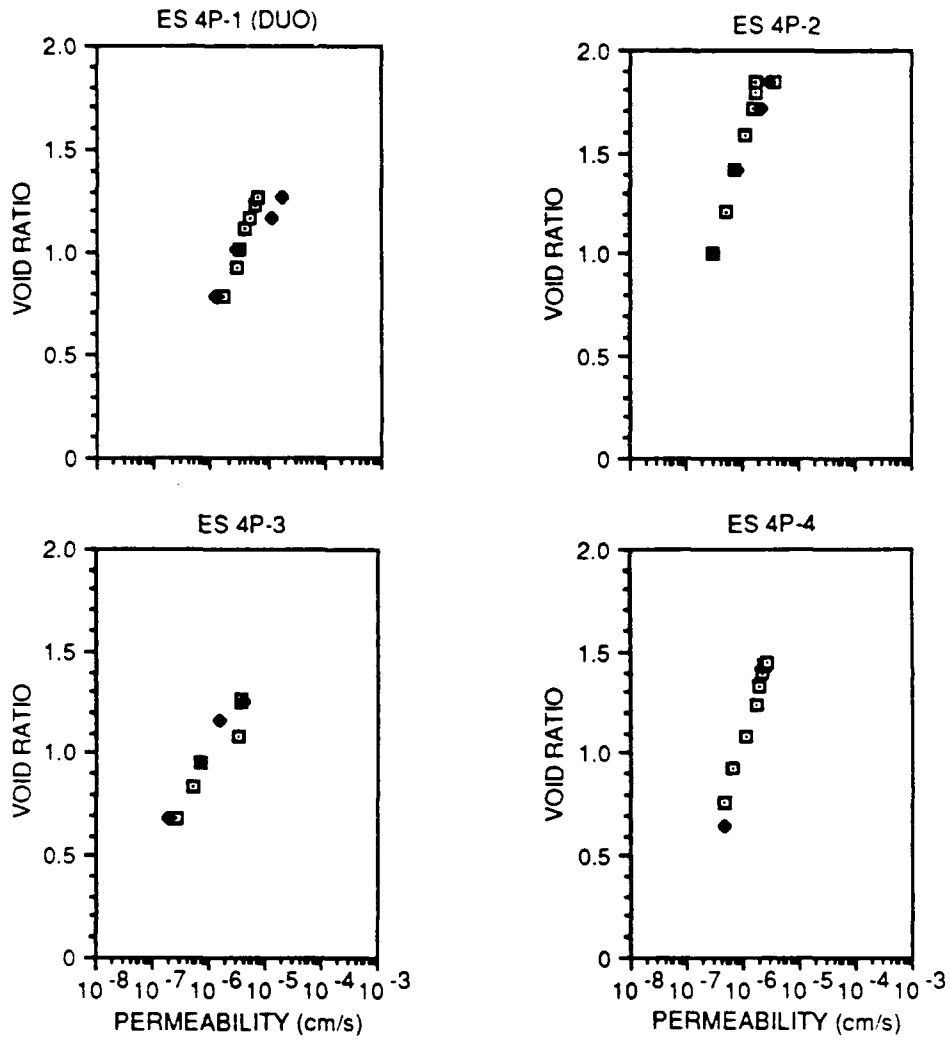
Figure 32. Core ES 4P: Permeability measured in the laboratory (open squares) and calculated (black diamonds) from Cv values which are derived from the graphs of change of height versus time since loading.
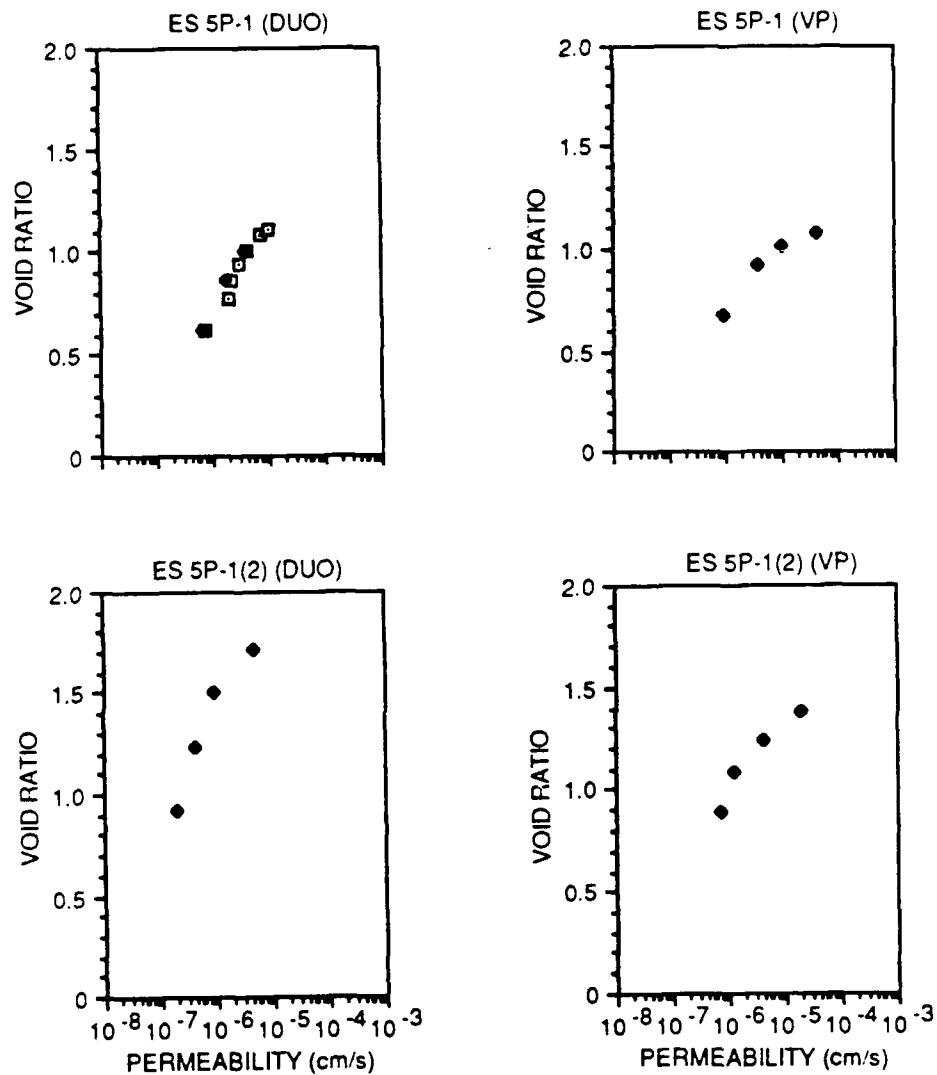
Figure 33. Core ES 5P: Permeability measured in the laboratory (open squares) and calculated (black diamonds) from Cv values which are derived from the graphs of change of height versus time since loading.
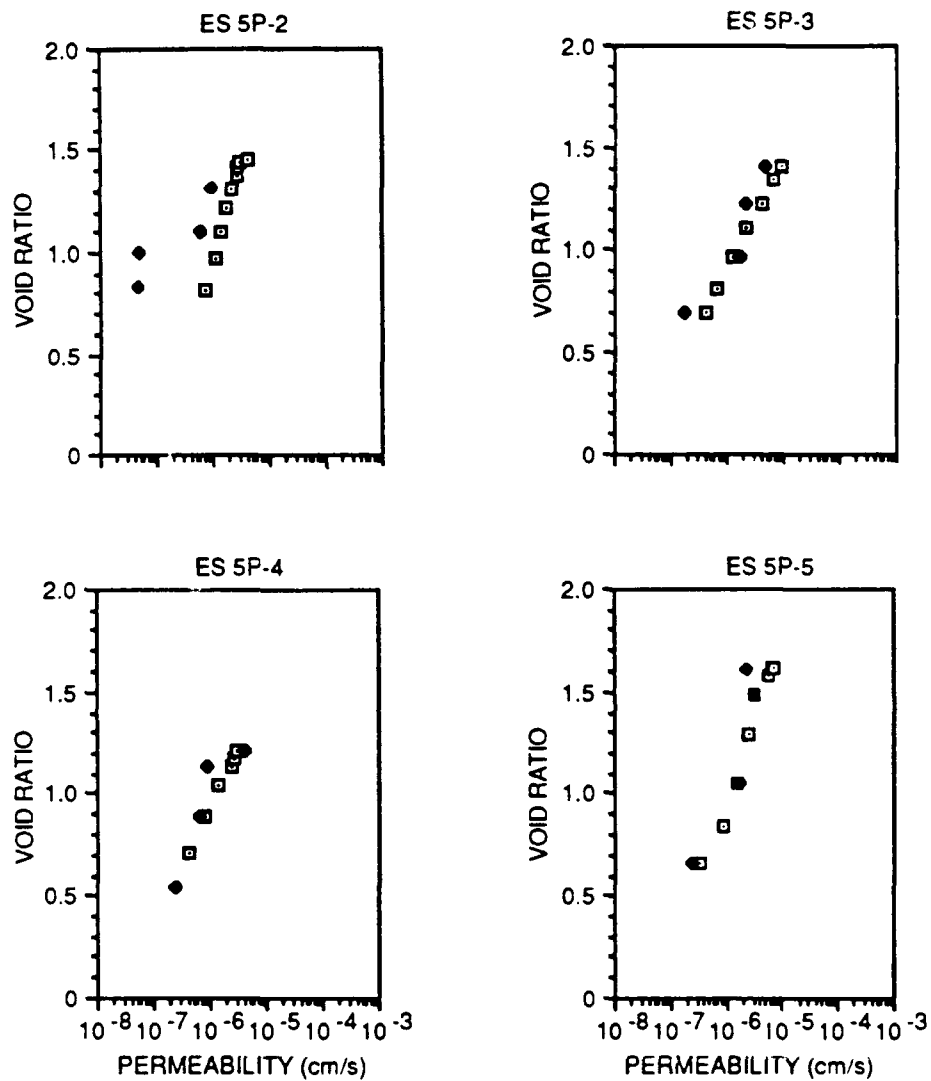
Figure 34. Core ES 5P (cont.): Permeability measured in the laboratory (open squares) and calculated (black diamonds) from Cv values which are derived from the graphs of change of height versus time since loading.
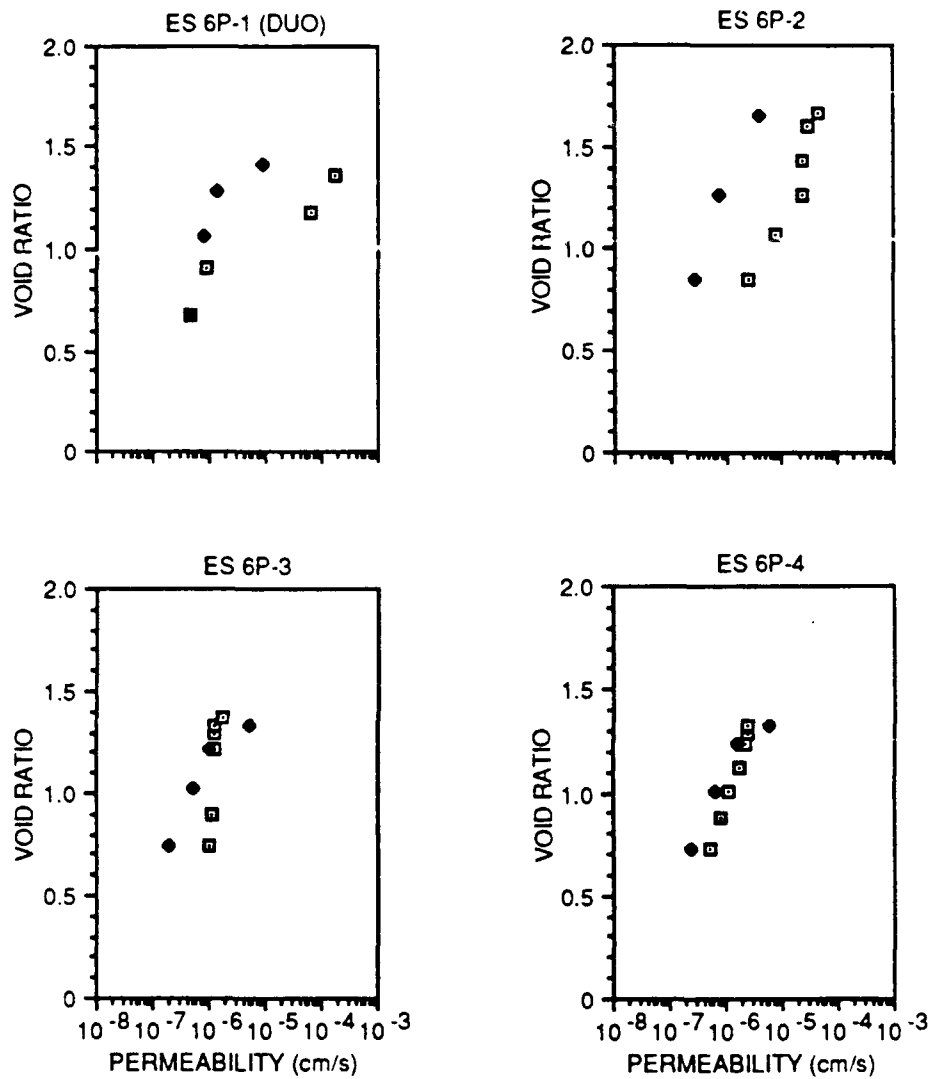
Figure 35. Core ES 6P: Permeability measured in the laboratory (open squares) and calculated (black diamonds) from Cv values which are derived from the graphs of change of height versus time since loading.
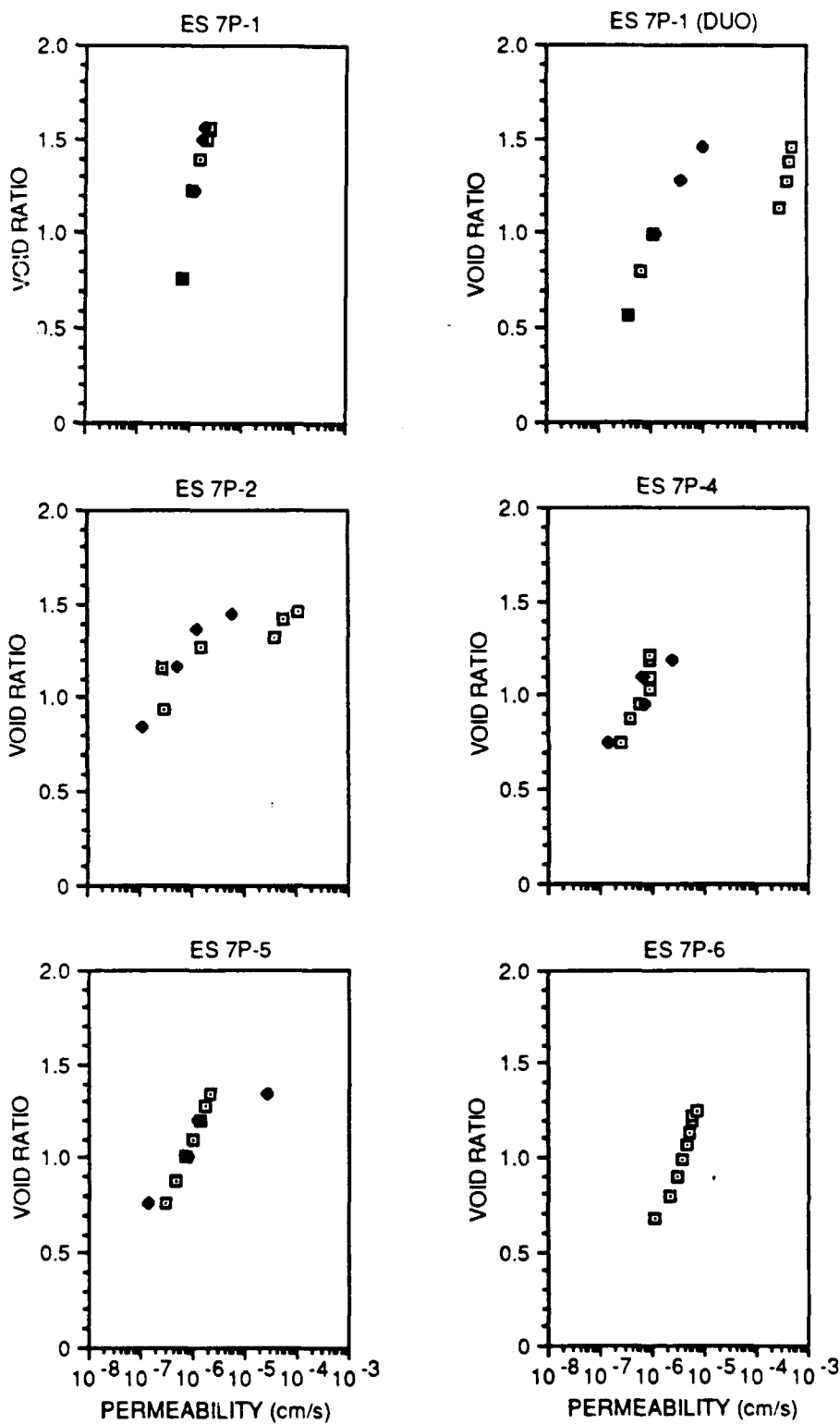
Figure 36. Core ES 7P: Permeability measured in the laboratory (open squares) and calculated (black diamonds) from Cv values which are derived from the graphs of change of height versus time since loading.
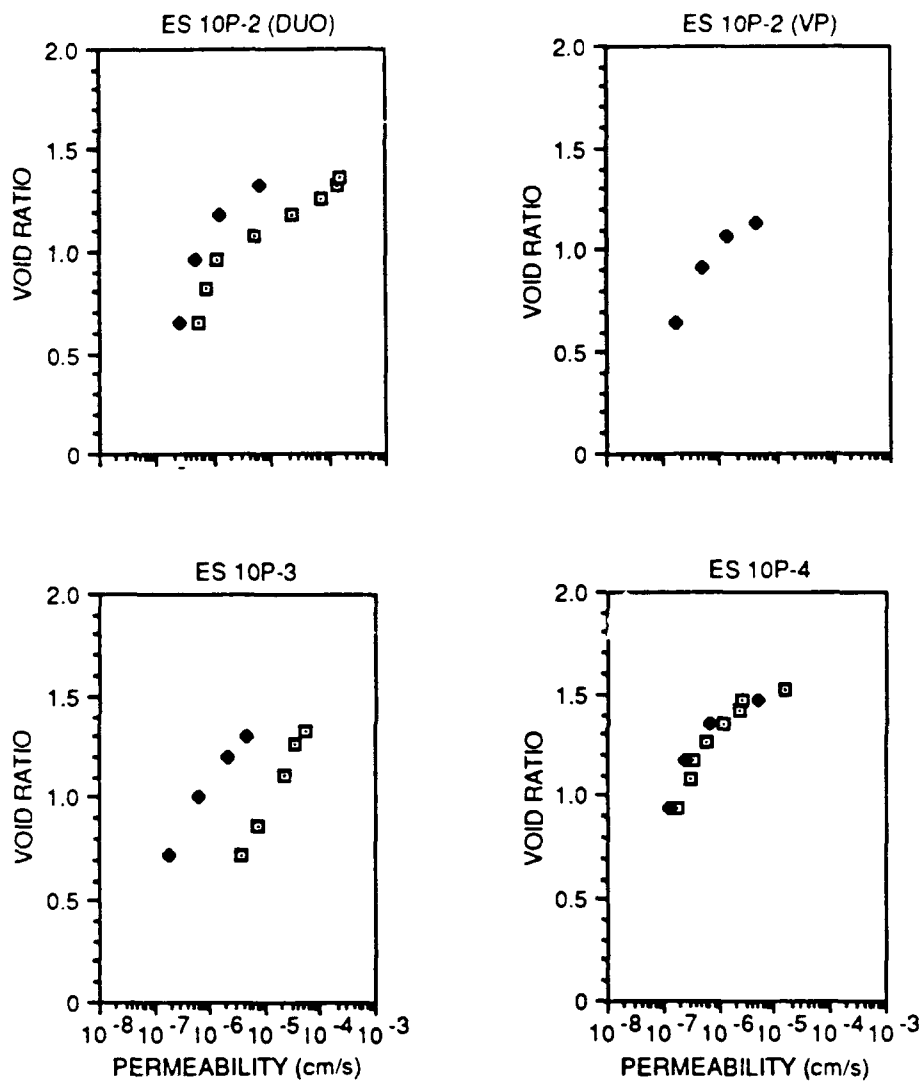
Figure 37. Core ES 10P: Permeability measured in the laboratory (open squares) and calculated (black diamonds) from Cv values which are derived from the graphs of change of height versus time since loading.
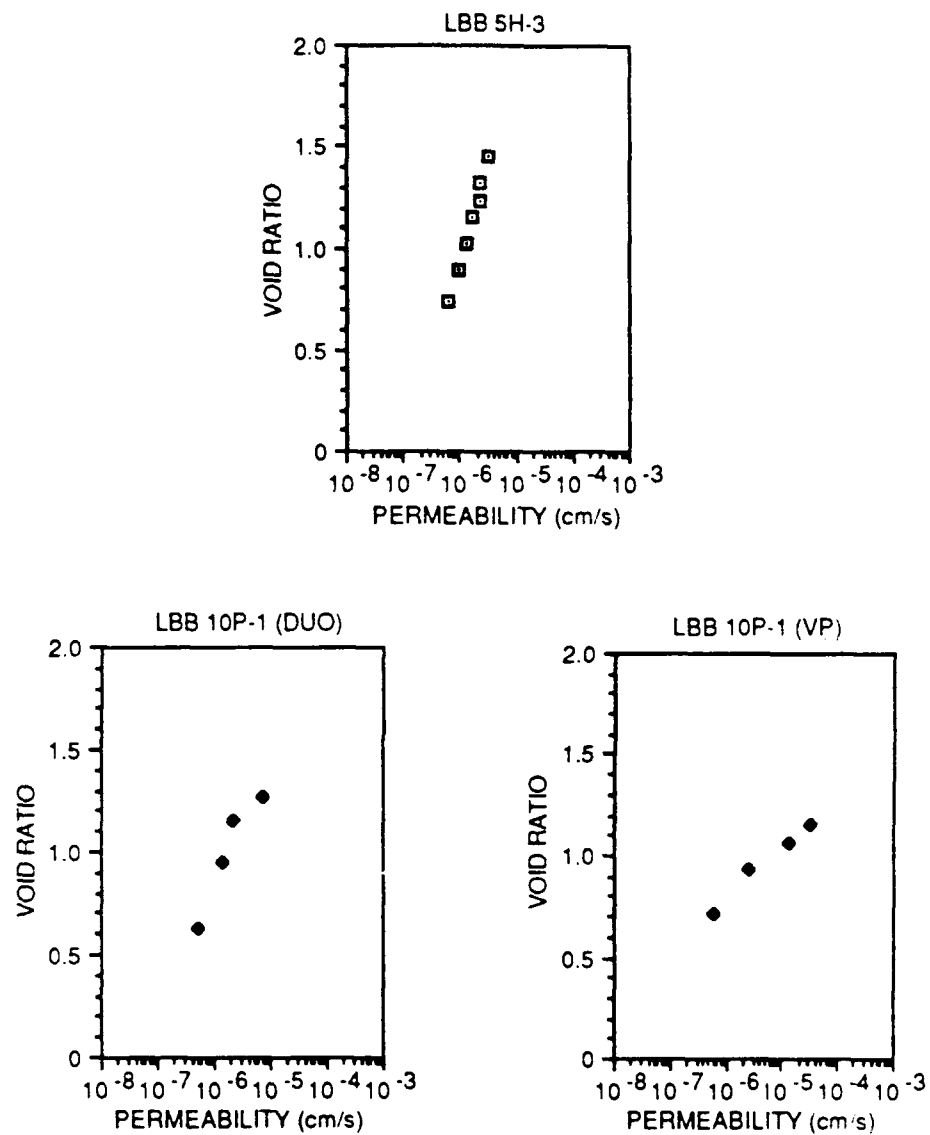
Figure 38. Core LBB 5H, LBB 10P, and LBB 10P: Permeability measured in the laboratory (open squares) and calculated (black diamonds) from Cv values which are derived from the graphs of change of height versus time since loading.
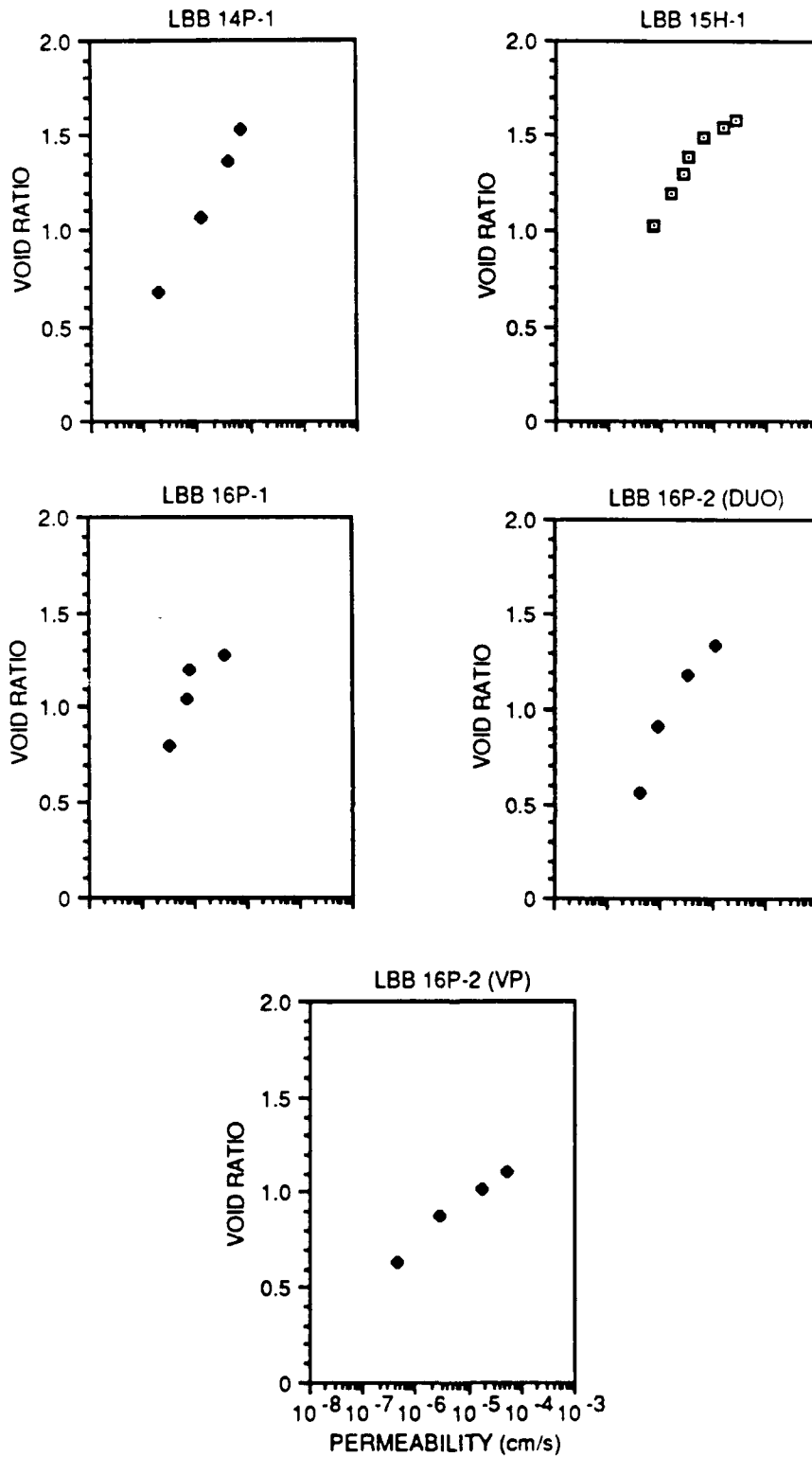
Figure 39. Core LBB 14P, LBB 15H, and LBB 16P: Permeability measured in the laboratory (open squares) and calculated (black diamonds) from Cv values which are derived from the graphs of change of height versus time since loading.
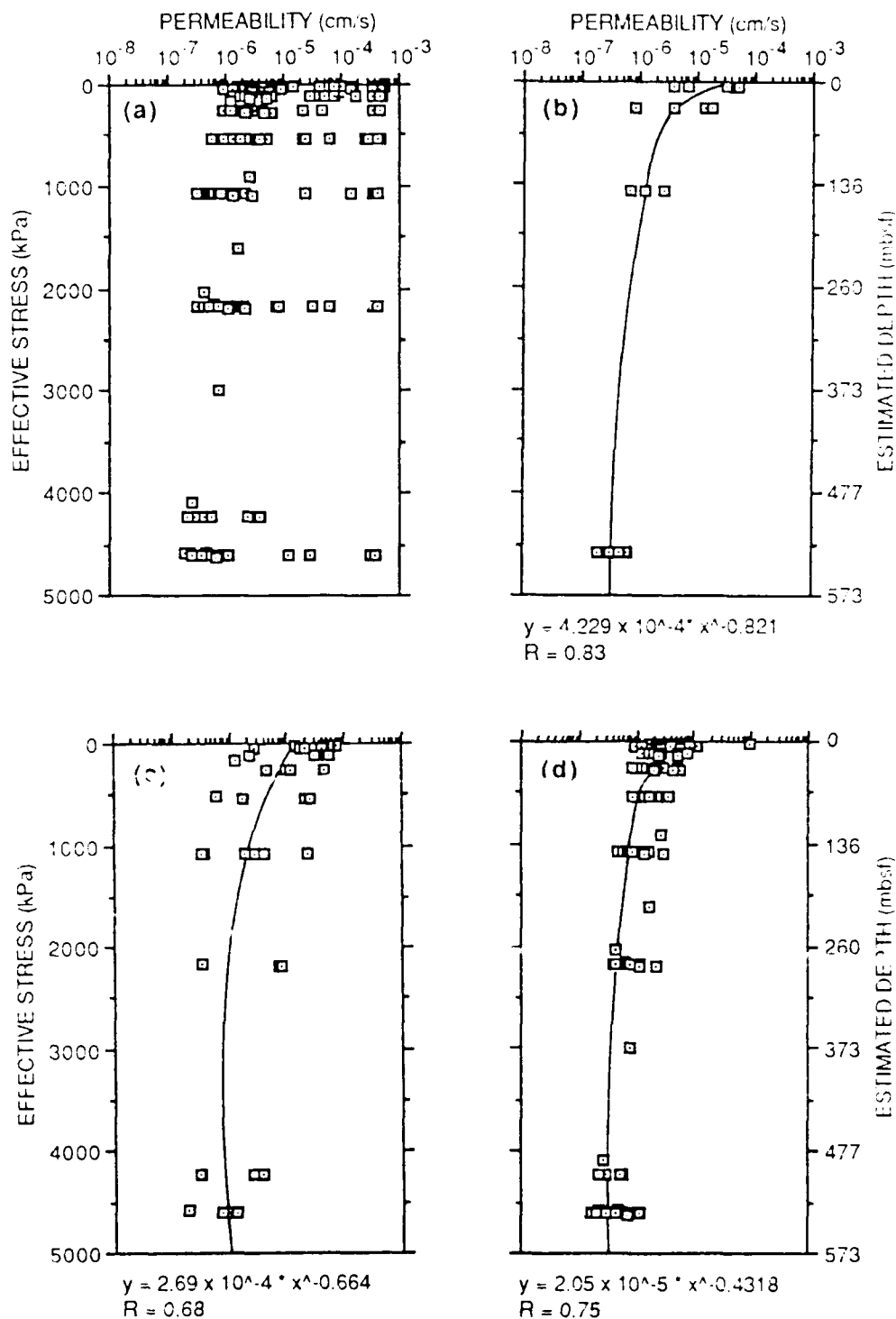
Figure 40. Measured permeability as a function of effective stress/depth for (a) all samples, (b) grain-supported samples, (c) matrix-supported samples with an initial permeability of 1×10^{-5} cm/s, and (d) matrix-supported samples with an initial permeability of 1×10^{-6} cm/s. Notation: caret ($\wedge$) signifies raised to a power.

where σ' is effective stress in kPa.

Total porosity was plotted for all samples as a function of effective stress and depth (Fig. 41). Because porosity varied over such a small range, the matrix-supported and grain-supported sample results were not separated. The regression that best describes these samples follows:

$$n = 0.58 - 1.028 \times 10^{-4}\,(\sigma') + 3.216 \times 10^{-4}\,(\sigma'^2) - 3.841 \times 10^{-12}\,(\sigma'^3). \tag{24}$$

The relationship between permeability and total porosity for all of the samples (Fig. 42a) follows:

$$k = 1.424 \times 10^{-4}\,(n^{6.739}). \tag{25}$$

The correlation with porosity was considerably worse for grain-supported samples than matrix-supported samples (Fig. 42b)

Wet bulk density as a function of effective stress and depth is presented in Figure 43. A linear regression equation was used because the only initial and final values were measured. Interpolated values would fall on a straight line, so they were not used. The following regression best describes all these samples:

$$\text{Wet bulk density} = 1.74 + 3.50 \times 10^{-5}\,(\sigma'). \tag{26}$$

Compressional Wave Velocity, Shear Modulus, and Shear Wave Velocity

Results of testing Exuma Sound and Little Bahama Bank samples are presented sequentially. Figures 44 through 50 are graphs of compressional wave velocity, shear modulus, and shear wave velocity for each sample. The individual compressional wave velocity data points were variable. Time delay was measured using a Vernier scale rather than reading from a digital time-delay readout, which resulted in some variability ($\pm.25$ milliseconds) in results. In addition, during the consolidation process, especially immediately after a load was added, it was observed that the height of the sample changed quite rapidly, but the time-delay recorded did not. There is a time lag that occurs before accurate velocity measurements can be made. Measurements made during the
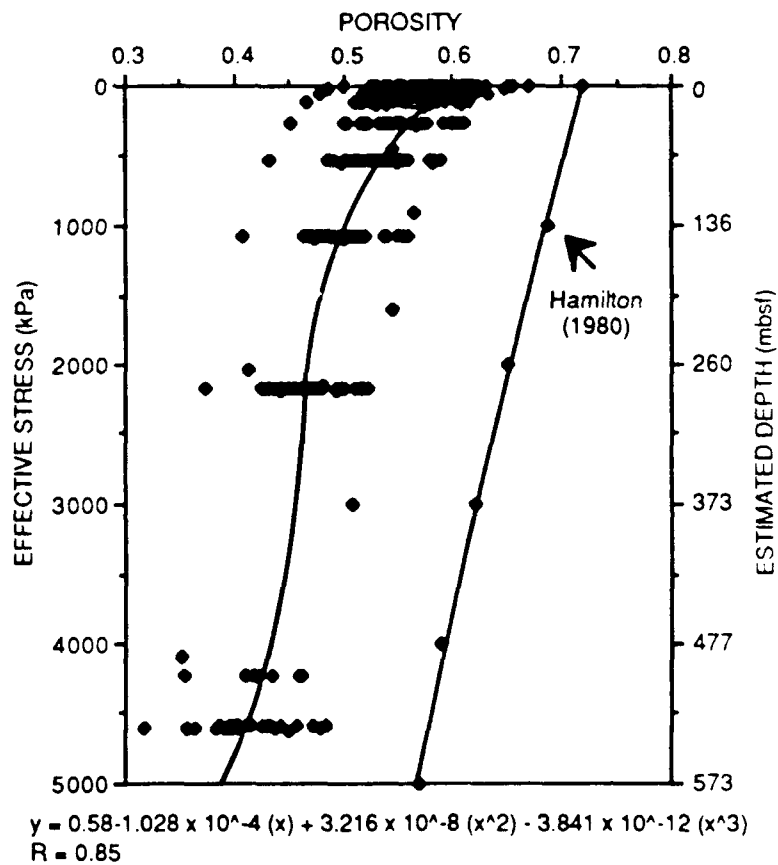
Figure 41. Measured porosity from all samples plotted as a function of effective stress/depth. Porosity predicted using Hamilton (1980) for deep water carbonate sediments is plotted for comparison.
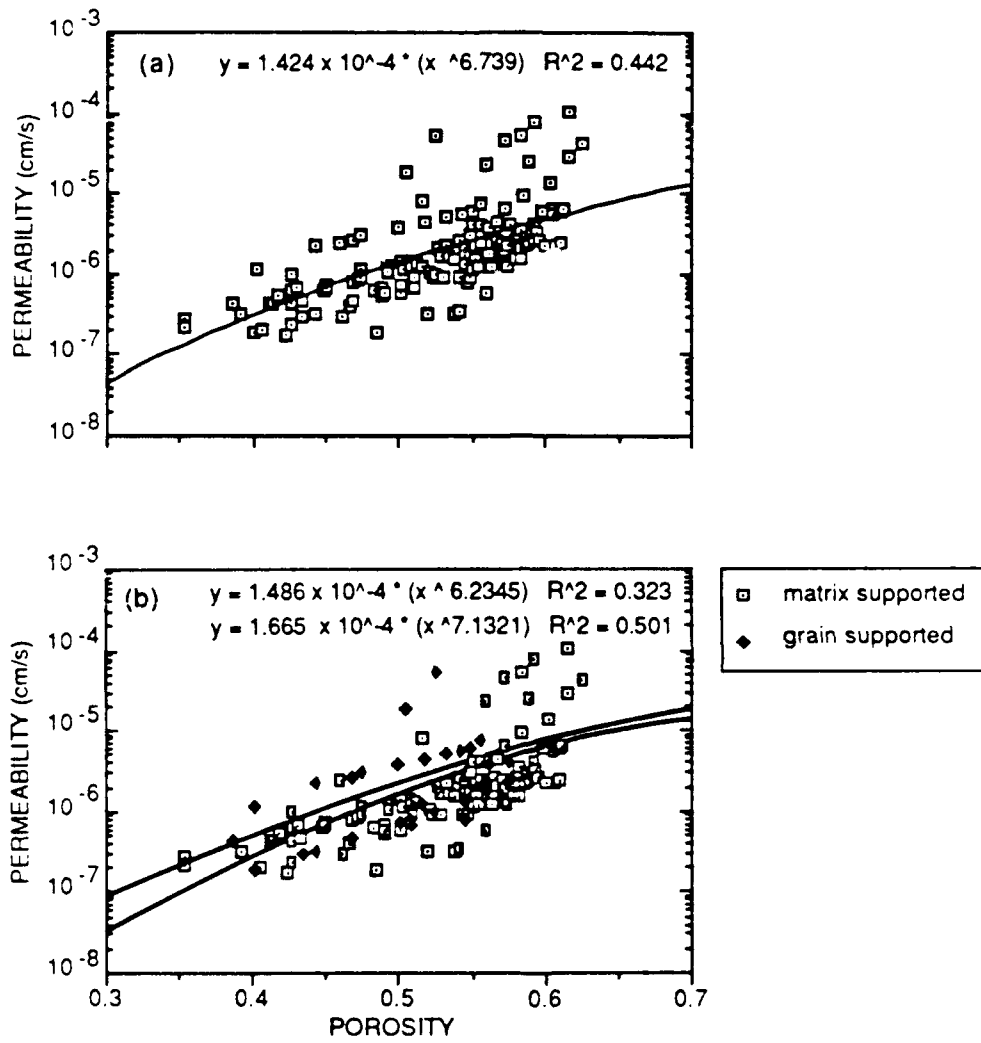
Figure 42. (a) Relationship between total porosity and permeability for all periplatform samples. (b) Porosity versus permeability is plotted separately for matrix-supported (R^2 = .32) and grain-supported (R^2 = .50) samples.
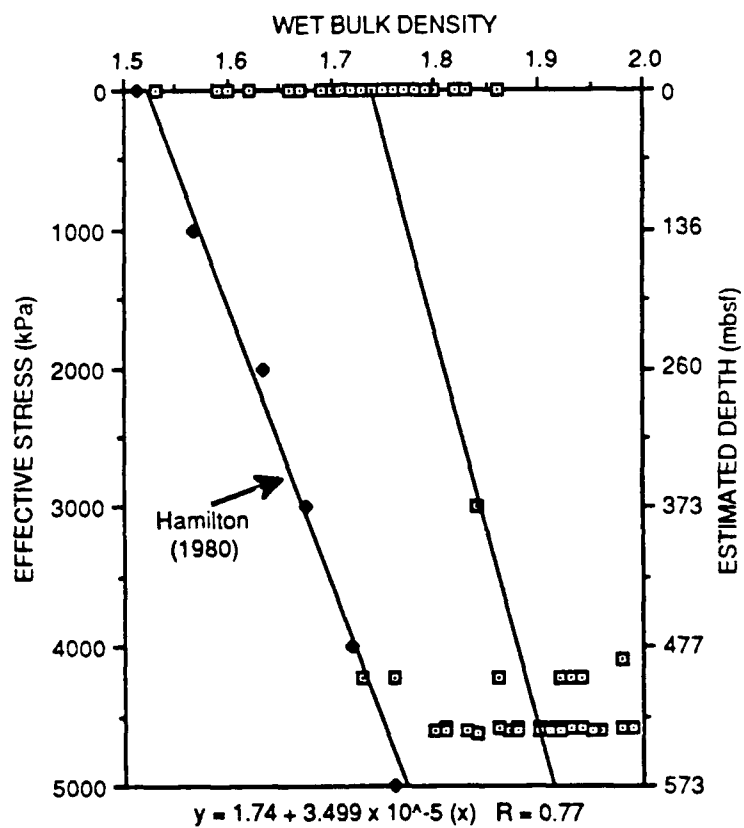
Figure 43. A comparison of density between Bahamian periplatform sediments and predicted values using regression equations derived for deep water carbonate sediments (Hamilton 1980).
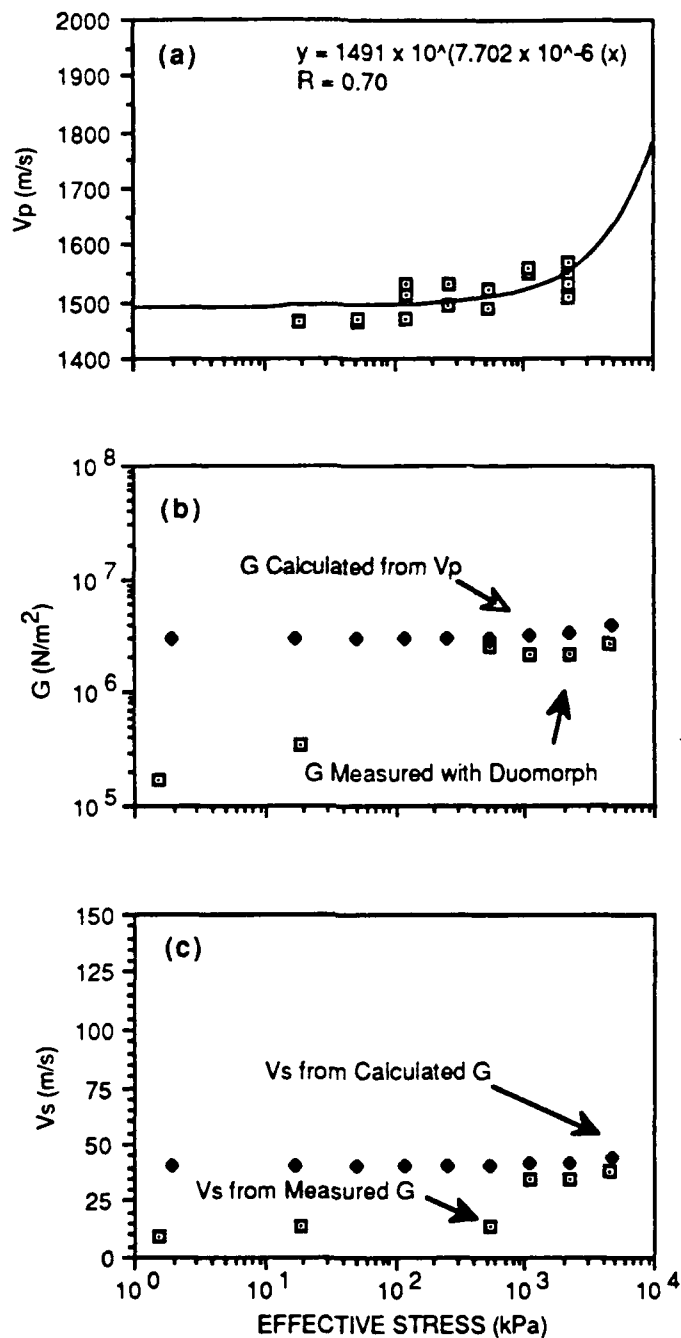
Figure 44. Laboratory measured acoustic properties of ES 4P-1. (a) Compressional wave velocity (Vp) values are taken from the virgin curve only. The resulting regression equation rather than actual values was used to calculate shear modulus (G). (b) Comparison of measured shear modulus using duomorphs and calculated shear modulus. (c) A comparison of shear wave velocity (Vs) derived using measured shear modulus and calculated shear modulus values.
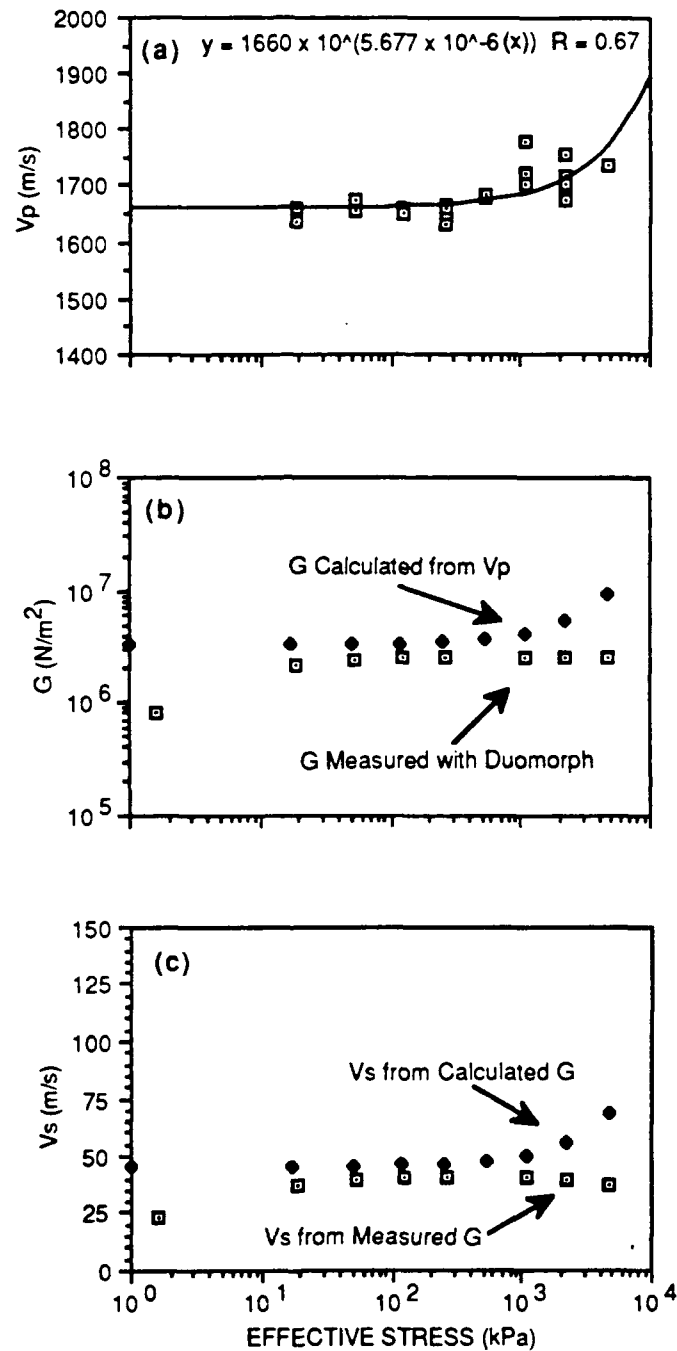
Figure 45. Laboratory measured acoustic properties of ES 5P-1(2). (a) Compressional wave velocity (Vp) values are taken from the virgin curve only. The resulting regression equation rather than actual values was used to calculate shear modulus (G). (b) Comparison of measured shear modulus using duomorphs and calculated shear modulus. (c) A comparison of shear wave velocity (Vs) derived using measured shear modulus and calculated shear modulus values.
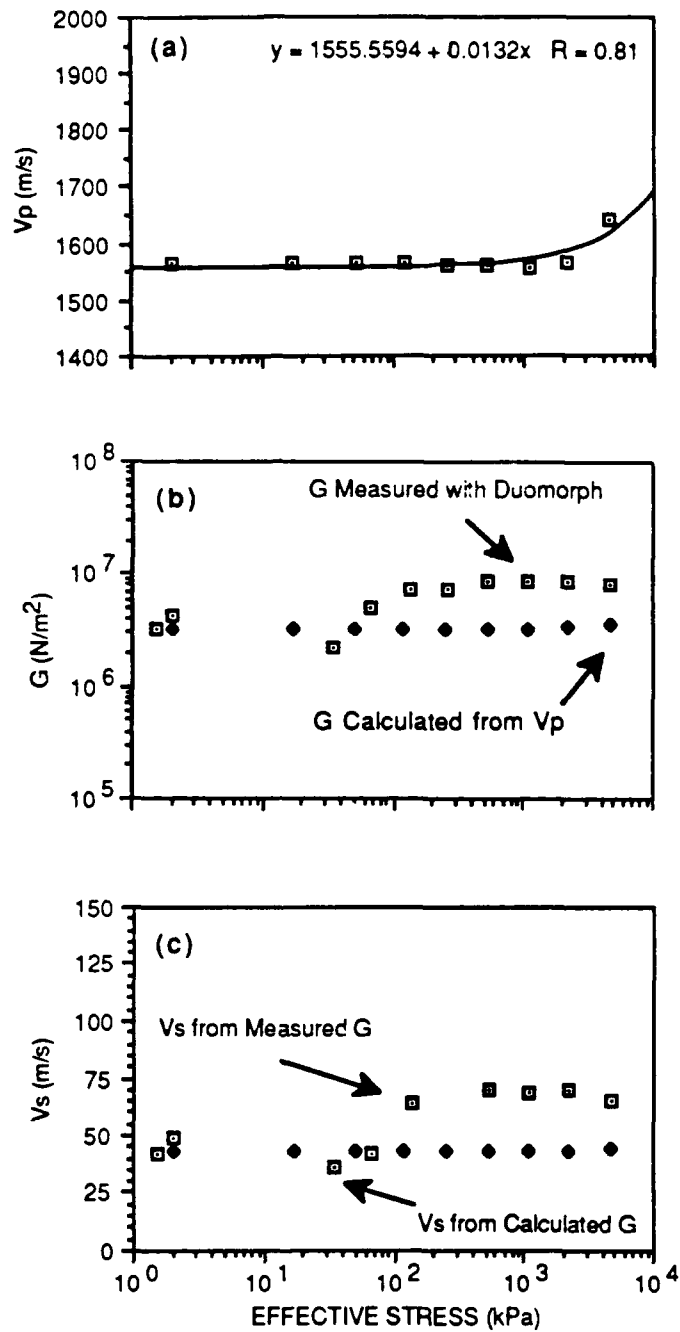
Figure 46. Laboratory measured acoustic properties of ES 6P-1. (a) Compressional wave velocity (Vp) values are taken from the virgin curve only. The resulting regression equation rather than actual values was used to calculate shear modulus (G). (b) Comparison of measured shear modulus using duomorphs and calculated shear modulus. (c) A comparison of shear wave velocity (Vs) derived using measured shear modulus and calculated shear modulus values.
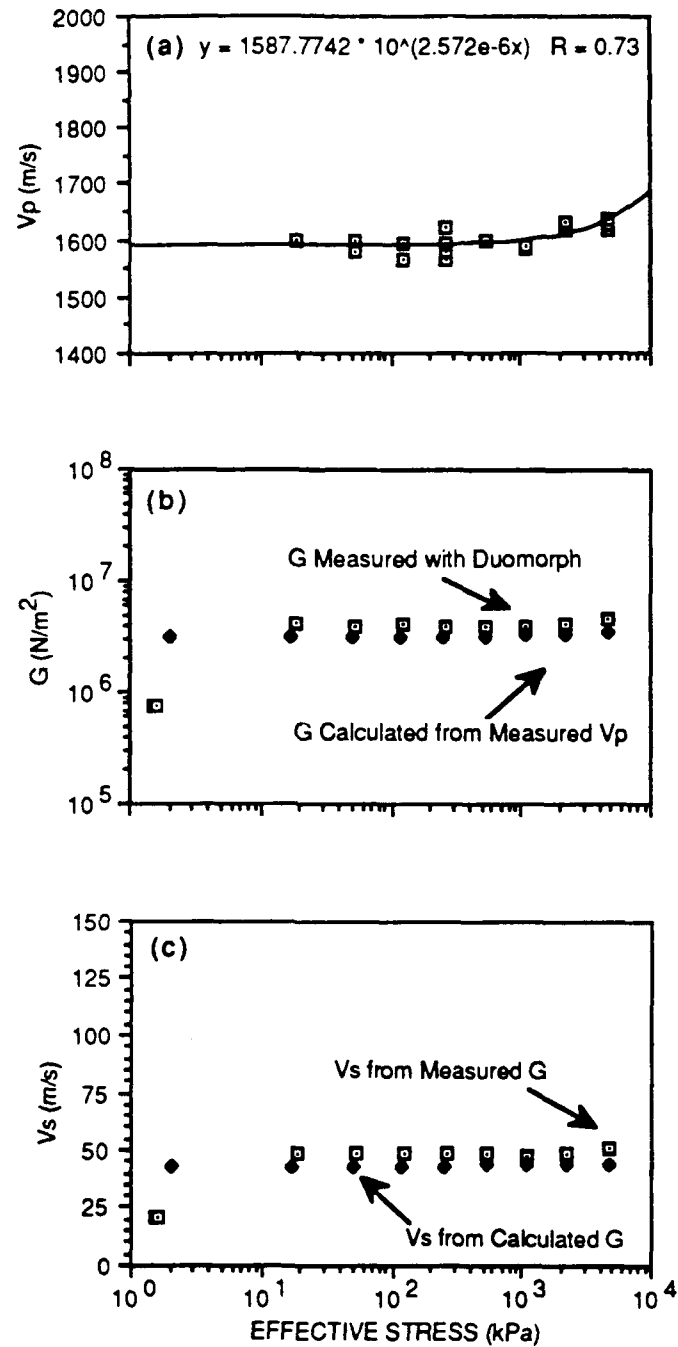
Figure 47. Laboratory measured acoustic properties of ES 7P-1. (a) Compressional wave velocity (Vp) values are taken from the virgin curve only. The resulting regression equation rather than actual values was used to calculate shear modulus (G). (b) Comparison of measured shear modulus using duomorphs and calculated shear modulus. (c) A comparison of shear wave velocity (Vs) derived using measured shear modulus and calculated shear modulus values.
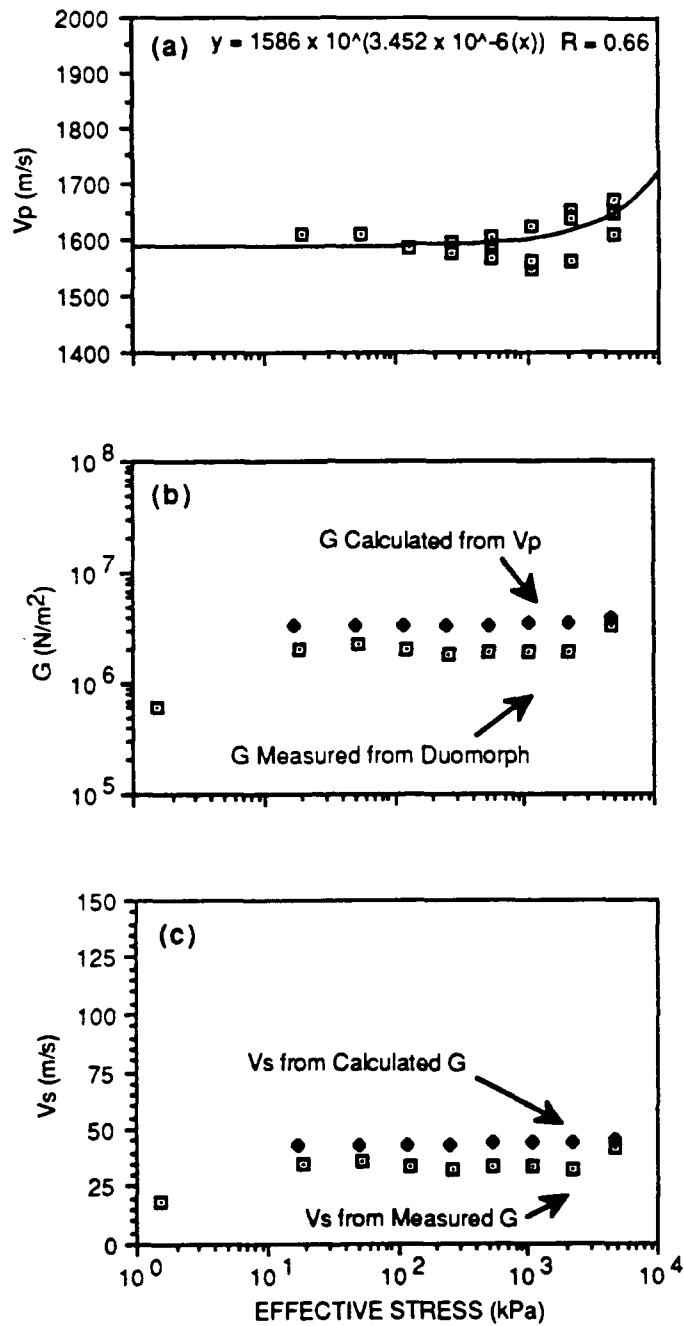
Figure 48. Laboratory measured acoustic properties of ES 10P-2. (a) Compressional wave velocity (Vp) values are taken from the virgin curve only. The resulting regression equation rather than actual values was used to calculate shear modulus (G). (b) Comparison of measured shear modulus using duomorphs and calculated shear modulus. (c) A comparison of shear wave velocity (Vs) derived using measured shear modulus and calculated shear modulus values.
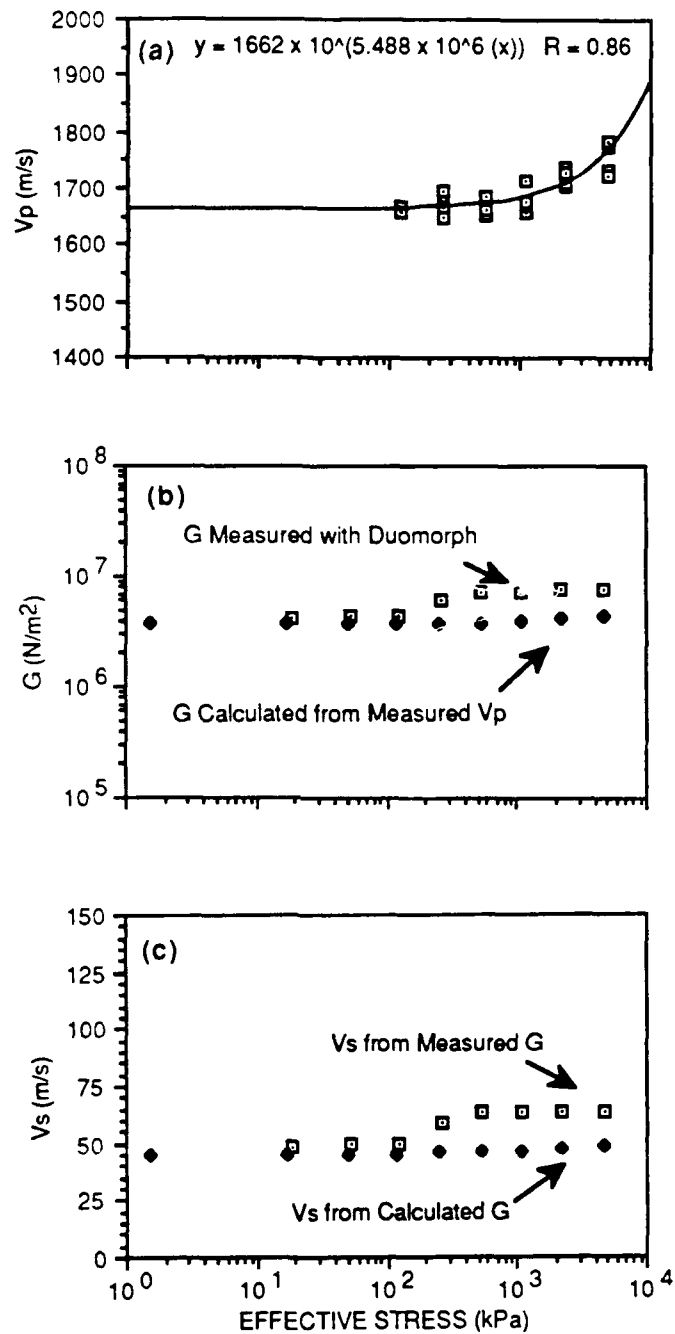
Figure 49. Laboratory measured acoustic properties of LBB 10P-1. (a) Compressional wave velocity (Vp) values are taken from the virgin curve only. The resulting regression equation rather than actual values was used to calculate shear modulus (G). (b) Comparison of measured shear modulus using duomorphs and calculated shear modulus. (c) A comparison of shear wave velocity (Vs) derived using measured shear modulus and calculated shear modulus values.
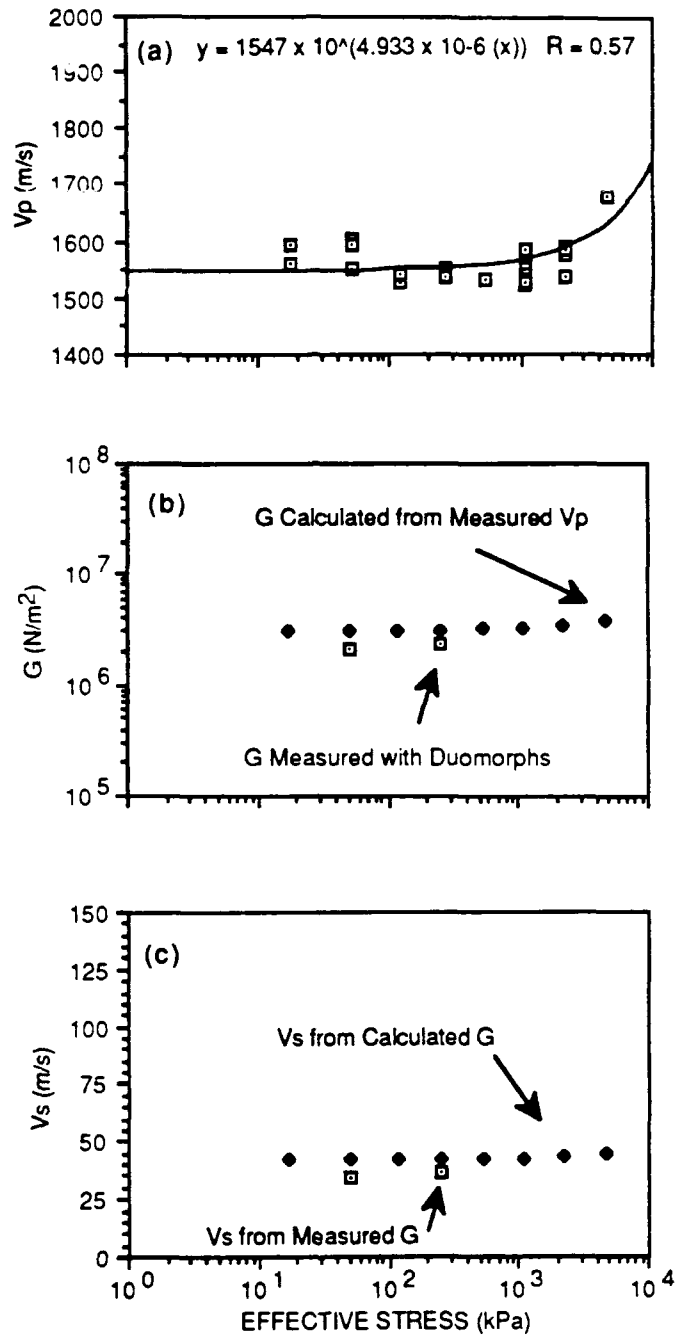
Figure 50. Laboratory measured acoustic properties of LBB 16P-2. (a) Compressional wave velocity (Vp) values are taken from the virgin curve only. The resulting regression equation rather than actual values was used to calculate shear modulus (G). (b) Comparison of measured shear modulus using duomorphs and calculated shear modulus. (c) A comparison of shear wave velocity (Vs) derived using measured shear modulus and calculated shear modulus values.

reload cycle were accordingly eliminated. The measurements presented are compressional wave velocity measurements made on the virgin curve. To smooth the numbers, a regression equation was used to calculate the shear modulus rather than the actual data points. The measured and calculated shear moduli are presented in the B portion of each illustration. In each case the measured shear modulus shows lower initial values, which possibly reflect seating problems in the consolidometer. Shear wave velocity derived from the calculated and measured shear modulus is presented in the C portion of each illustration. Wet bulk density values at each effective stress were interpolated between initial and final measured wet bulk density values. Because the wet bulk density used at each effective stress was the same for shear wave velocity calculated from the measured and calculated shear modulus, the shear modulus trends are mirrored in the shear wave velocity trends.

Table 8 is a concise summary of the shear modulus results, along with the related compressional wave velocity and shear velocity values. Values for measured shear modulus are given at 0 kPa (ambient laboratory pressures) and 120 kPa, which may be the upper limit of the duomorph resolvability. Calculated values for shear modulus are also given at 4500 kPa, since the compressional wave transducers from which the data were calculated are reliable at that effective stress. Shear wave velocity was calculated from measured shear modulus at 0 and 120 kPa and from the calculated shear modulus at 4500 kPa.

Compressional wave velocity varied between 1491 m/s for ES 4P-1 and 1663 m/s for ES 5P-1(2). The average velocity was 1585 m/s. Shear velocity as a function of effective stress showed little increase for many of the samples. Regression equations derived for each sample are listed by the appropriate graphs. The shear modulus of most of the samples ranged between 1.69×10^5 N/m^2 and 4.26×10^6 N/m^2 at ambient laboratory pressures, which resulted in shear velocities that ranged between ~10 m/s and 49 m/s. Shear modulus at 120 kPa ranged between 2.03×10^6 N/m^2 and 4.96×10^6 N/m^2, which resulted in shear wave velocities between 35 and 55 m/s. Calculated shear wave velocities at 4500 kPa ranged between 44 and 48 m/s, close to the values measured both at 120 kPa and 4500 kPa.

Table 8. Summary of Shear Modulus and Related Variables

Sample ID	V_p (0) (m/s)	V_p (4500 kPa) (m/s)	G_{meas} (0) (N/m²)	G_{meas} (~120 kPa) (N/m²)	G_{calc} (0) (N/m²)	G_{calc} (~120 kPa) (N/m²)	G_{calc} (4500 kPa) (N/m²)	$V_{s\,meas}$ (0) (m/s)	$V_{s\,meas}$ (~120 kPa) (m/s)	$V_{s\,meas}$ (4500 kPa) (m/s)
ES 4P-1	1491	1615	1.69×10^5	2.56×10^6	2.94×10^6	2.97×10^6	3.89×10^6	9.77	35	44
ES 5P-1(2)	1663	1743	8.20×10^5	2.51×10^6	3.32×10^6	3.41×10^6	3.80×10^6	27.67	45	46
ES 6P-1	1556	1615	4.17×10^6	4.96×10^6	3.23×10^6	3.24×10^6	3.67×10^6	48.40	54	44
ES 7P-1	1588	1631	7.66×10^5	4.12×10^6	3.21×10^6	3.22×10^6	3.62×10^6	21.33	49	45
ES 10P-2	1586	1644	5.98×10^5	2.03×10^6	3.33×10^6	3.35×10^6	4.05×10^6	18.48	36	46
LBB 10P-1	1661	1758	4.26×10^6	4.36×10^6	3.73×10^6	3.75×10^6	4.48×10^6	48.70	49	48
LBB 16P-2	1547	1628	2.09×10^6	-	3.11×10^6	3.12×10^6	3.75×10^6	34.76	-	45

A composite plot of compressional wave velocity as a function of effective stress/depth for all these samples is illustrated in Figure 51a. Plotted for comparison are projected values for a calcareous sediment computed using a regression equation developed for deep water calcareous sediments by Hamilton (1980). Figure 51b and 51c separately illustrate the compressional wave velocity data as a function of depth for matrix-supported samples and grain-supported samples respectively. The same Hamilton (1980) predicted curve is shown in Figures 51b and 51c again.

Shear modulus and shear wave velocity as a function of effective stress and estimated depth (Figs. 52a, b) for these samples can be described by the regression equations:

$$G = 9.46 \times 10^5 \ (\sigma'^{.2124})$$

(27)

$$Vs = 23.39 \ (\sigma'^{.0994}),$$

where σ' is in N/m^2 or kPa and the results are in N/m^2 and m/s respectively.

The shear wave velocity values shown in Figure 52b are calculated from the measured shear moduli. Also shown are shear wave velocity values calculated using an empirical regression equation developed by Hamilton (1980). Hamilton's values are dependent on measured compressional wave velocity. In this case, the compressional wave velocity measurements made on these samples were used with the Hamilton equations. When the Hamilton equation shear velocity is converted to shear modulus, using an average wet bulk density of 1.46 Mg/m^3 (recommended by Hamilton 1980), the resulting shear moduli are shown on Figure 52a.

Consolidation Related Fabric Changes

Changes associated with the consolidation process are summarized in Table 9. Samples are ranked in order of decreasing permeability. Both permeability and porosity values decrease as a result of consolidation. Laboratory measurements of initial permeability range between 10^{-3} and 10^{-5} cm/s for the grain-supported samples (LBB 16P-1 and LBB 10P-1) and LBB 15H-1, which had an aragonite needle matrix, and 10^{-6} cm/s for the remaining matrix-supported samples, where the
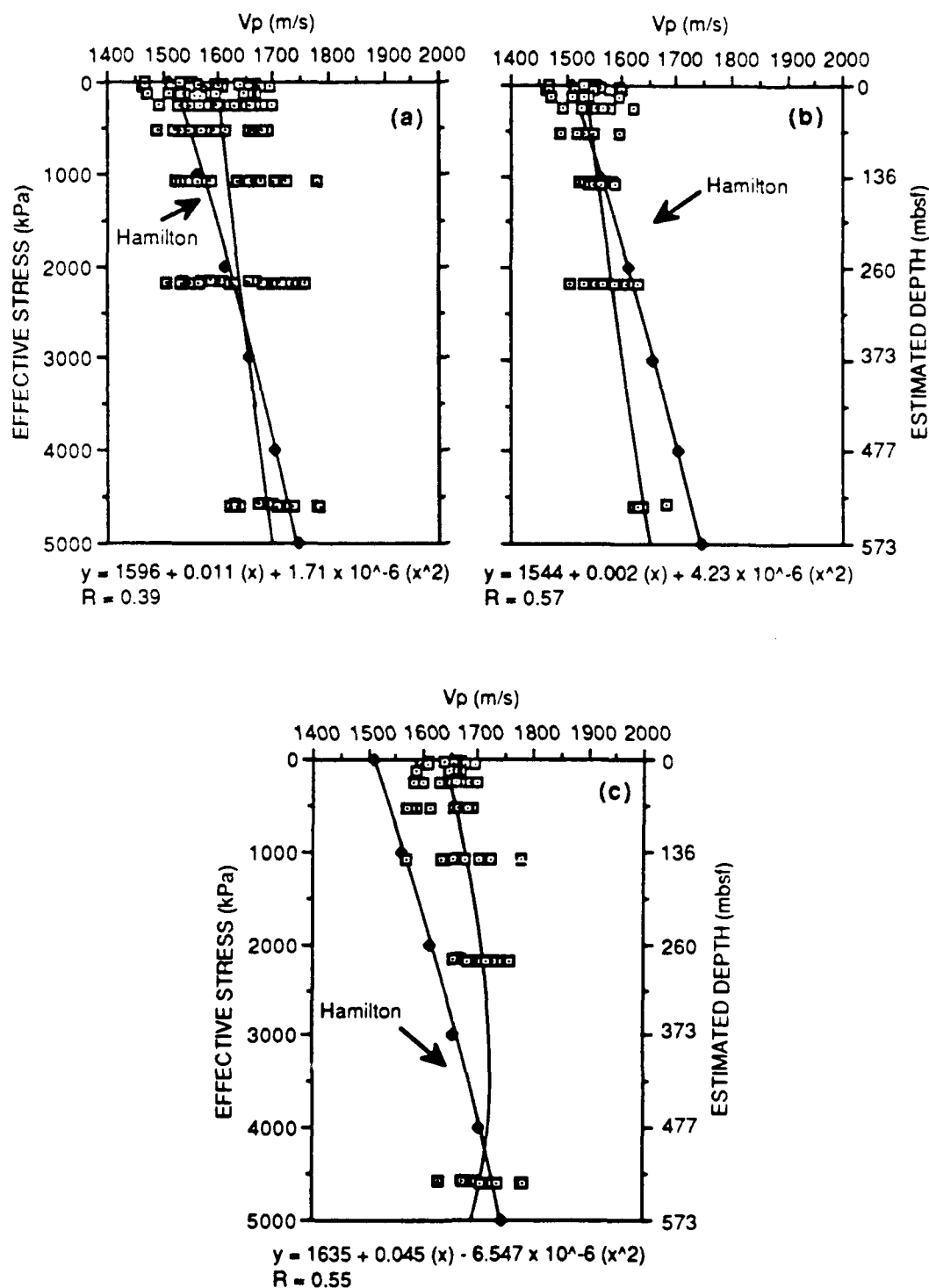
Figure 51. Compressional wave velocity as a function of effective stress and estimated depth. (a) All samples, (b) matrix-supported samples, and (c) grain-supported samples. The agreement between measured values from periplatform samples and Curve illustrating predicted compressional wave velocity versus depth, derived using Hamilton's regression equations based on deep water carbonates, is reasonably good.
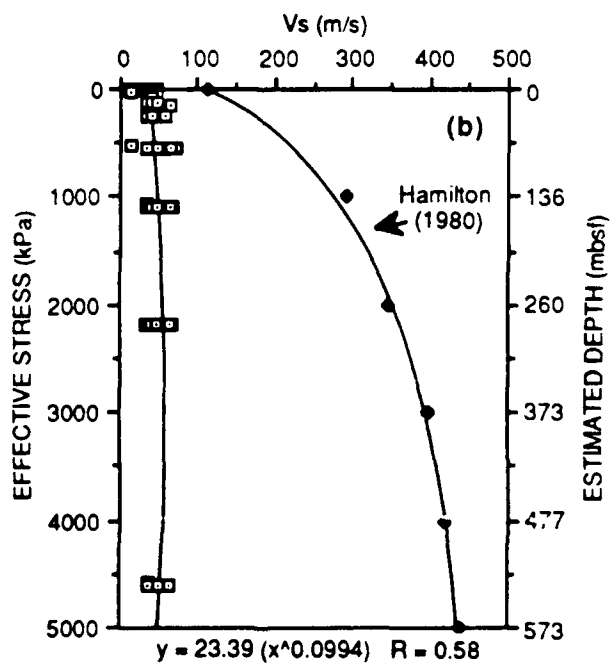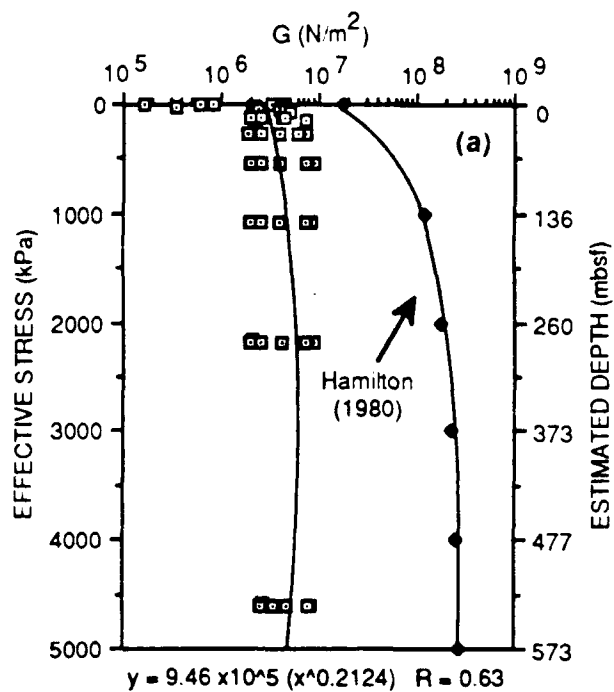
Figure 52. Comparison of (a) shear modulus and (b) shear wave velocity values measured on periplatform sediments and predicted using regression equations derived from deep water carbonates from Hamilton (1980).

Table 9. Consolidation Summary

Sample ID	ΔH	e (pre)	e (post)	n (pre) (%)	n (post) (%)	k (pre) (cm/s)	k (post) (cm/s)
LBB 16P-1 (90 cm)	21.91	1.33	0.79	55	48	2.77 1 $\times$ 10^{-3}	2.54 1 $\times$ 10^{-6}
LBB 10P-1 (532.5 cm)	31.34	1.36	0.63	55	48	3.10 1 $\times$ 10^{-5}	6.10 1 $\times$ 10^{-7*}
LBB 15H-1 (58 cm)	25.72	1.58	1.11	59	51	4.25 1 $\times$ 10^{-5}	4.14 1 $\times$ 10^{-5}
ES 10P-3 (250cm)	27.69	1.38	0.72	61	49	5.25 1 $\times$ 10^{-5}	2.80 1 $\times$ 10^{-6}
ES 6P-3 (292.5 cm)	33.82	1.42	0.60	60	47	1.69 1 $\times$ 10^{-6}	9.78 1 $\times$ 10^{-7}
ES 6P-4 (403 cm)	31.29	1.45	0.72	58	51	2.50 1 $\times$ 10^{-6}	5.46 1 $\times$ 10^{-7}
ES 7P-1 (87 cm)	32.97	1.62	0.76	60	53	2.37 1 $\times$ 10^{-6}	6.89 1 $\times$ 10^{-7}

Legend: ΔH — the change in height in percent reduction
          e — void ratio
          n — porosity
          k — permeability
          * k was calculated for this sample from consolidation data

matrix particles were predominantly coccoliths. In almost all cases, the final permeability was lower by an order of magnitude.

Details of the sample fabrics are outlined in Table 2. Except for LBB 16P-1, we could not visually recognize any changes in fabric after consolidation from SEM micrographs. Thin sections of LBB 15H-1 indicated that the fabric changed from matrix- to grain-supported as a result of consolidation (Fig. 53). The, plus a subjective feeling that the pores were smaller, led us to use image analysis in an attempt to quantify changes in pore dimensions.

Porometry results before and after consolidation are presented in Table 10 and in Figures 54, 55, and 56. The results were not statistically significant but the trends were consistent. We expected the pore sizes to decrease and the overall number of pores per unit area to increase as a result of consolidation. Samples with less than 50% aragonite behaved as expected: pore size decreased an average of 0.54 μm^2 and the number of pores increased an average of 38.6/unit area. Opposite results were observed for the aragonite-rich samples with needle matrices. The average pore size increased and the average number of pores per unit area decreased for LBB 15H-1 and ES 10P-3. No change in pore size was observed in the grain-supported LBB 16P-1.

DISCUSSION

Consolidation

The behavior of these samples supports the conclusion that carbonate sediments consolidate differently from marine clays. Initial void ratios and porosities for these samples were low when compared with terrigenous clays such as from Station 7, a sandy clay from the Mississippi Sound (Fig. 37). The initial void ratio (2.53) and porosity (72%) for Station 7 sample was considerably higher than the initial void ratios (between 1 and 2) and porosities (between 52 and 65%) measured from these carbonate samples. The final void ratio (0.33) and final porosity (24.81%) measured from Station 7 samples was lower than the final void ratios (0.6 – 1.01) and porosities (35 – 48%) measured from the Bahamian carbonates. The carbonate samples evidently experienced less
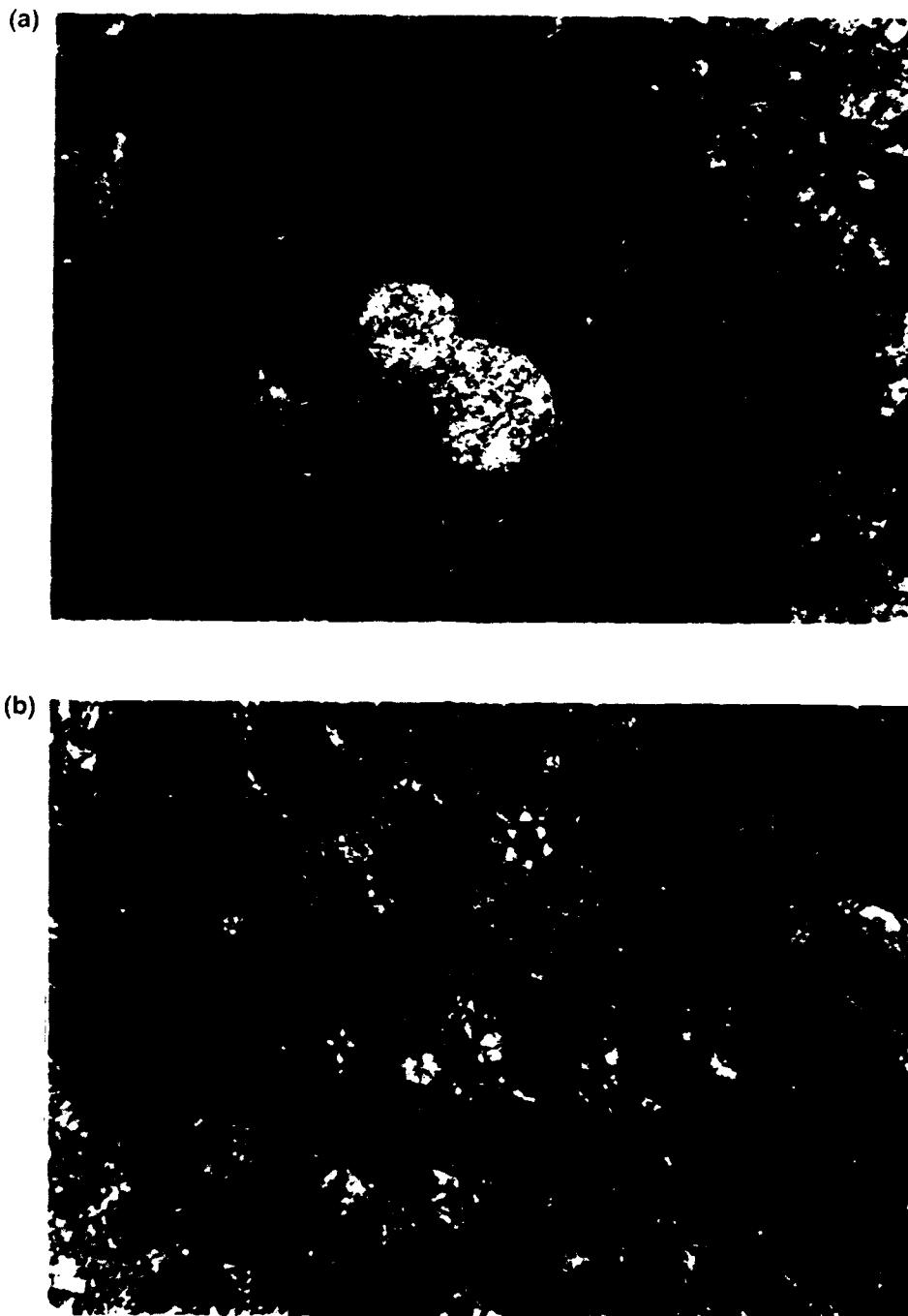
Figure 53. Thin sections from LBB 15H-1 (a) before consolidation and (b) after consolidation. The fabric was altered from (a) matrix-supported to (b) grain-supported as a result of consolidation.

Table 10. Porometry Summary

Sample ID	# Identified Pores	Averaged Pore Size (μm²)	Δ Pore Size (μm²)	W/L Ratio	Δ Unit Weight (Mg/m³)
LBB 15H-1 (Pre)	121	0.77	0.32	0.174	0.12
LBB 15H-1 (Post)	220	1.09		0.139	
ES 10P-3 (Pre)	354	0.82	2.42	0.212	0.20
ES 10P-3 (Post)	110	3.24		0.183	
LBB 16P-1 (Pre)	192	1.27	0	0.261	0.12
LBB 16P-1 (Post)	303	1.27		0.190	
ES 6P-3 (Pre)	162	0.97	−0.17	0.150	0.19
ES 6P-3 (Post)	176	0.80		0.177	
ES 6P-4 (Pre)	176	2.23	−0.97	0.166	0.12
ES 6P-4 (Post)	88	1.26		0.164	
ES 7P-1 (Pre)	284	1.22	−0.44	0.161	0.11
ES 7P-1 (Post)	345	0.78		0.198	
LBB 10P-1 (Pre)	152	1.57	−0.57	0.177	0.12
LBB 10P-1 (Post)	313	1.00		0.180	
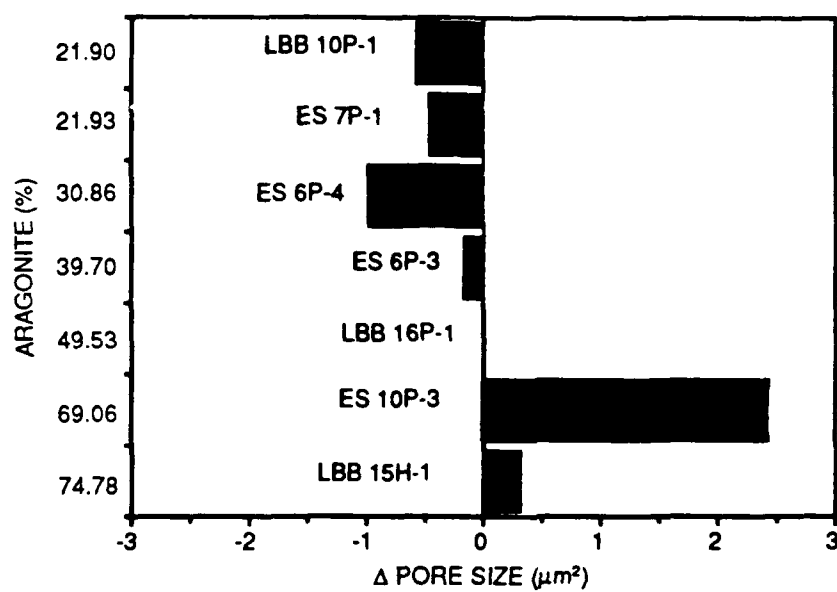
Figure 54. Change in average pore size as a function of aragonite content resulting from mechanical consolidation.
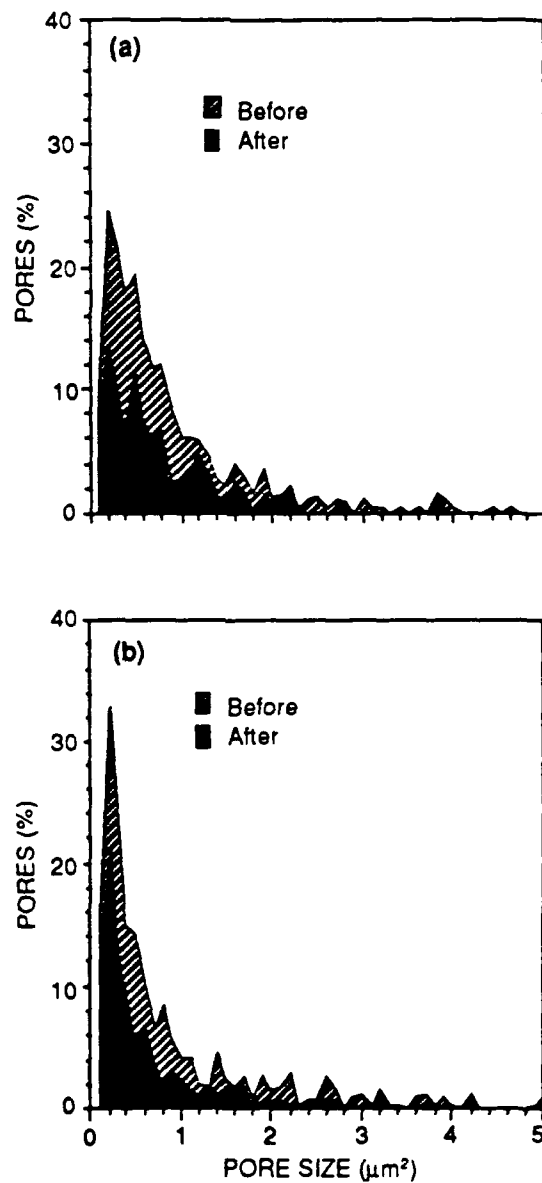
Figure 55. LBB 15H-1 (a) and ES 10P-3 (b), composed predominantly of aragonite and rich in needle matrices, experienced a reduction in numbers of very small pores (<1 μm^2) as a result of consolidation.
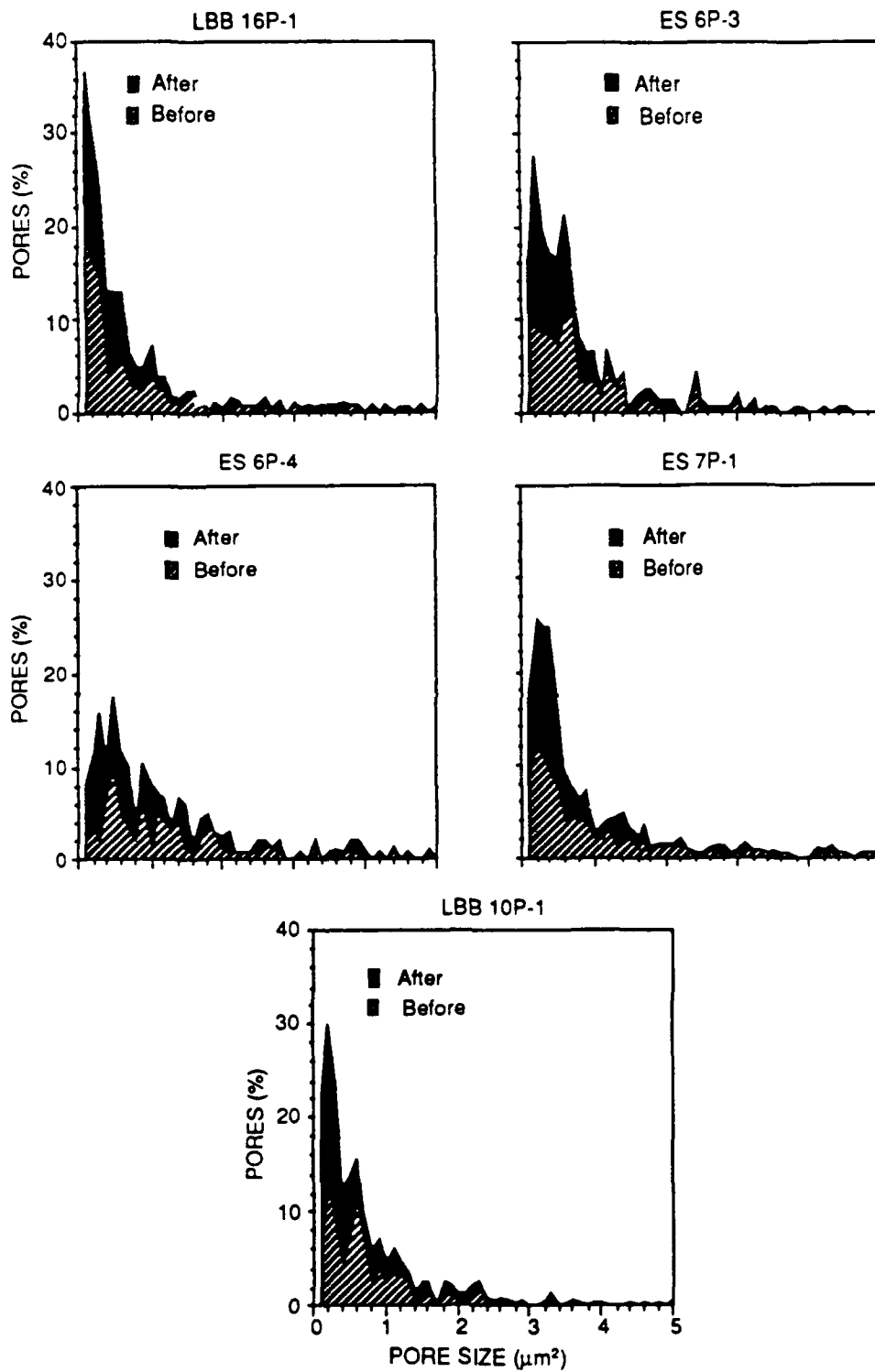
Figure 56. Samples with predominantly coccolith matrices experienced an increase in number of very small (<1 μm²) pores as a result of consolidation.

volume change and porosity reduction than the Station 7 sandy clay. Other researchers reported even greater reductions in void ratios and porosities in marine clays (Bryant and Bennett 1988; Bryant and others 1981; Keller and Bennett 1970). Thus, the results reported here suggest that the periplatform oozes undergo less volume change than marine clays and do not consolidate to as low a void ratio.

One reason for this fundamental difference between marine clays and marine carbonates may be found in the often-granular nature of the carbonates. Depending on the source, these grains may be hollow (e.g., foraminifer tests and pteropod shells), hollow but partially filled with clay-sized particles, or solid (e.g., fragments of algae or coral). Thus the behavior of carbonate sediments under consolidation can be expected to vary with the number of grains and the nature of the grains. These two factors may be related to the changes in void ratio and permeability observed here.

The volume change represented by the decrease in void ratio over all the periplatform samples is between 25% and 30%. Fruth and others (1966) reported ~30 – 35% compaction for samples of a carbonate mud facies at 44.9 bars (~4500 kPa) However, they reported only 15% consolidation for grapestone carbonate facies at that confining pressure. They suggested that the lack of consolidation observed in the grapestone facies results from grain support with no fracturing observed. These results illustrate the case in which the grains may be predominantly solid.

In the samples studied in this work, however, many of the grains were hollow, resulting in a different consolidation behavior. In these periplatform oozes, there was very little difference in amount of consolidation between grain-supported and matrix-supported samples; however, considerable grain crushing was observed, especially in grain-supported samples such as ES 6P-1(top) and LBB 16P-1 (Figs. 57a,b). These figures illustrate typical grain crushing observed in SEM micrographs after consolidation.

Others (Demars 1982; Valent and others 1982) noted considerable crushing of foraminifer grains, especially in grain-supported samples. The foraminifer grains contain significant amounts
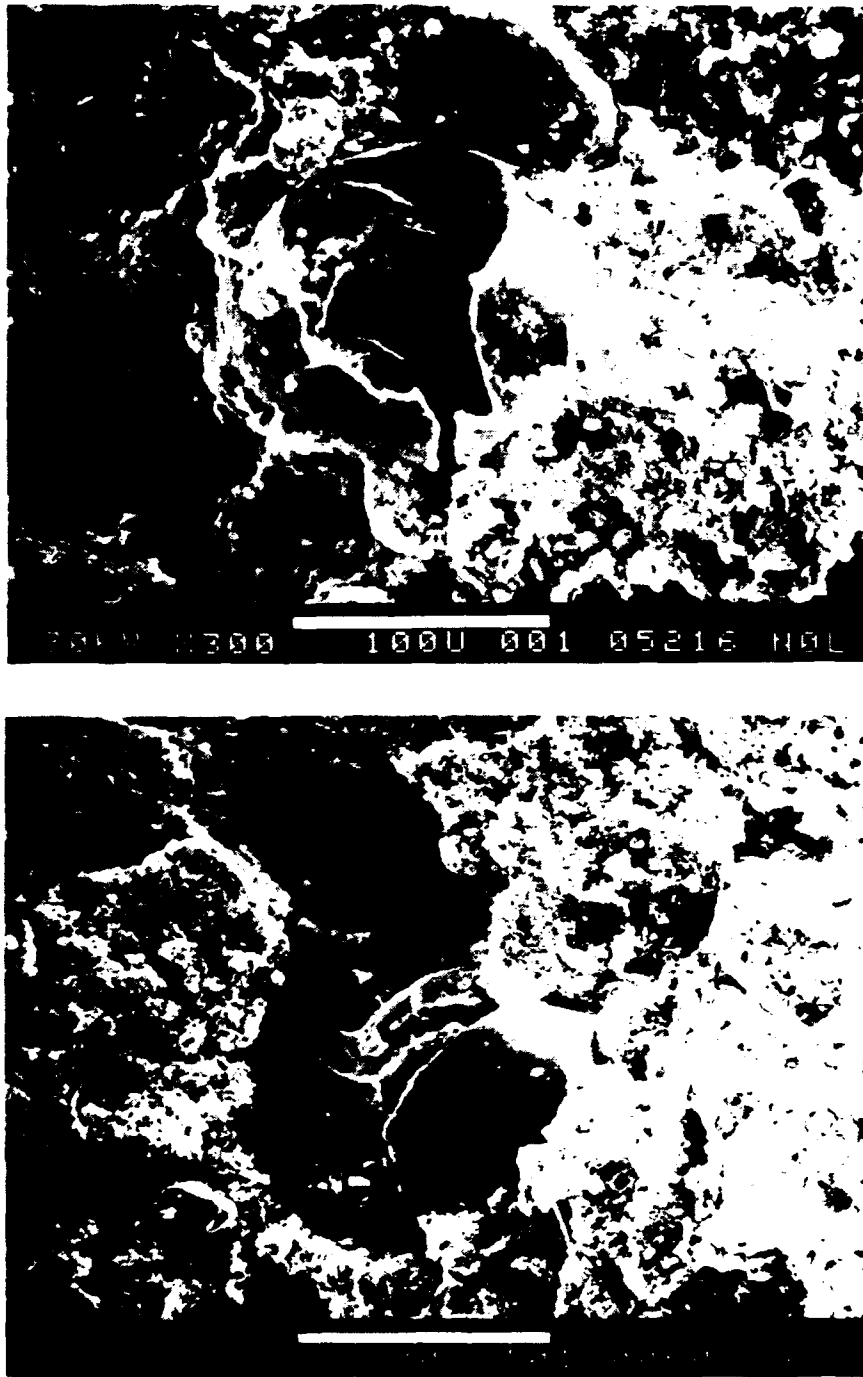
Figure 57. Typical crushing of grains during the consolidation process.

of intraparticle water, which is released as the grains are crushed. Therefore, a sediment which has undergone considerable grain crushing should exhibit a lower final porosity than one which has not. Final porosities at ~4500 kPa for the periplatform samples are all very similar, generally ranging between 35% and 45%, with no apparent differences between matrix- and grain-supported samples. Grain crushing of foraminifers (or equally hollow particles) may have occurred in the grain-supported samples in such an amount that the volume and porosity reduction equals that of matrix-supported samples.

When the volume change was calculated according to Schlanger and Douglas (1974), the agreement between the predicted and measured consolidation was extremely close (Table 7). Thus, the consolidation model proposed by Schlanger and Douglas for predicting volume change for deep-sea carbonates was also highly applicable to periplatform oozes of shallow- and mid-water depths when mechanical consolidation was the dominant volume change process.

The volume change noted for the duomorph samples was artificially high. An artificial void was created in the duomorph samples when the samples were split with a razor to allow insertion of the duomorph. The initial height, therefore, includes the height of the artificial void. Final volume change appeared to be greater than for samples without this artificially created void. Volume change for these samples should be disregarded.

The overconsolidation ratio with the maximum past preconsolidation pressure computed according to Casagrande did not appear to be useful for carbonate samples. Miller and Richards (1969) noted similar results. They stated that apparent overconsolidation of deep-water, fine-grained, clayey marine sediments tested in a laboratory consolidometer is common, but that the magnitude of the apparent overconsolidation of carbonates is likely to be greater than for clayey sediments.

Permeability and Porosity

Although the duomorph samples were disturbed, none were homogenized. Inserting the duomorph appears to result in a higher initial measured permeability than if the samples were left undisturbed.

The large void created by inserting the duomorph apparently allowed a quick flow of fluid through the sediment cell system until sufficient pressure either sealed or healed the void. The consequence of this disturbance is that whenever the duomorph is used, a duplicate consolidation test should be run, with permeability measured at the same time.

Initial measured permeability values reported were higher for grain-supported samples, generally 1×10^{-4} cm/s, than for the matrix-supported samples, generally between 1×10^{-5} and 1×10^{-6} cm/s. The grains in a grain-supported sediment allowed fast passage of pore fluids through the sediment by keeping the pore throats open, at least until grain crushing occurred. As the grains became crushed, the pore throats became filled, and slowed the passage of fluids. With increasing consolidation, therefore, the permeability decreased. The permeability as a function of effective stress/depth for grain-supported and matrix-supported samples is described by the regression equations listed previously.

As sediment consolidated and pore throats became constricted, the porosity decreased and the wet bulk density increased. The measured porosity as a function of effective stress/depth reported for these samples is described on Figure 41. Hamilton's (1976) predicted porosity values for a calcareous sediment derived from numerous heterogeneous DSDP sediments are plotted as a function of depth. His initial porosity of 72% was 10% higher than any porosity values reported here; consequently, his predicted values were also higher than measured values for these periplatform oozes. The measured wet bulk density for the periplatform oozes (Fig. 43) was higher than values reported by Hamilton (1976) for calcareous sediments. The DSDP sediments he used were deep sea carbonates; the higher porosity and lowerwet bulk density may be a consequence of different constituents in the sediments. The deep-sea carbonates were most likely predominantly foraminiferal oozes with a high proportion of hollow tests, which allow a higher porosity and lower wet bulk density. In contrast, the shallow- and mid-water depth carbonates, having a greater number of different types of constituents and fragments, many of which are solid, have a lower porosity and higher wet bulk density.

The relationship between permeability and porosity was derived by plotting the porosity and

permeability for each sample at each load. The resulting correlation coefficient of 0.44 (Fig. 42a) indicated that total porosity was not a particularly good predictor of permeability when all periplatform samples are considered together. In addition, the correlation coefficient of 0.32 for grain-supported samples was lower than the coefficient of 0.50 for matrix-supported samples (Fig. 42b). The grain-supported samples contained many foraminifers and other hollow grains that have a considerable amount of isolated pore space. Porosity may have been high, but not all the pore spaces allowed fluid flow; thus, a sample with high porosity may not necessarily have had a high permeability. Matrix-supported samples, which have fewer hollow grains, contained a greater number of connected pore spaces that allowed for fluid flow. Thus, the permeability was more closely related to porosity in these samples. In summary, the greater the number of hollow grains in a sample, the lower the correlation will be between porosity and permeability.

Compressional Wave Velocity, Shear Modulus, and Shear Wave Velocity

One of the goals of this study was to characterize the shear wave velocity of carbonate sediments accurately. As previously discussed, an early hypothesis was that shear wave velocity measurements made in the laboratory under ambient pressure may not be representative of *in situ* values and that the divergence between laboratory measurements and *in situ* values would continue to increase with increasing *in situ* subbottom depth. NORDA's bender-element shear velocity transducers are adequate only at ambient laboratory pressures. The duomorph technique developed by Briar and others (1972, 1976) seemed to offer an alternate and independent method for measuring the shear modulus and, therefore, the shear wave velocity if the techniques could be adapted for use in the consolidometer.

This study shows that the duomorph technique is a feasible alternative to the bender-element shear wave transducers. Actual data show the initial shear modulus and the shear wave velocity to be very low, to increase with effective stress to about 100 to 150 kPa, and then to level off. This pattern is consistent with all the samples tested. Two possibilities come to mind concerning the leveling off: either the duomorphs do not work above 150 kPa or the shear modulus and shear wave

velocity of the carbonate sediments simply do not increase significantly after 150 kPa of effective stress under mechanical consolidation are reached. Results from the testing the Station 7, Mississippi Sound, sandy clay suggest that the duomorph results are not valid at high pressures. since clays should continue to consolidate and display an increase in shear modulus and shear wave velocity with increasing effective stress. If this is the case, the duomorphs would have to be redesigned to withstand higher loads (an engineering problem), whereupon they would probably be too rigid to adequately work with soft sediments. However, the data reduction methods, which are based on theoretical parabolic motion of the duomorph, might be adjusted to account for the nonparabolic motion that is probably occurring under high loads. If this adjustment were made, the existing data could be reanalyzed.

As for the possible lack of consolidation in carbonate sediments, Matthews (1980) and Rezak (1974) noted that carbonate sediments do not consolidate as much as marine clays and that a marked increase in compressional wave velocity, for instance, occurs mainly at lithological boundaries as a result of cementation rather than consolidation. It is possible that we should not expect a continuous increase in related properties, such as shear modulus and shear wave velocity, in the absence of cementation.

In fact, shear modulus and shear wave velocity values calculated from measured compressional wave velocity at 120 kPa and higher were close to those measured by the duomorphs (Figs. 44 through 50). The measured compressional wave velocities reported here agree well with the predicted values of Hamilton (1980) (Fig. 51a). Thus, the currently used values for deep-sea carbonates are probably applicable to periplatform oozes recovered from shallow- and mid-water depths.

Shear modulus measured by the duomorphs was about 2×10^5 to 4×10^6 N/m^2 at 0 kPa and 3 to 5×10^6 N/m^2 at 120 kPa. These measurements translate to shear wave velocities between ~10 and 49 m/s at 0 kPa and from 35 to 54 m/s at 120 kPa. These values are very close to those reported by Schultheiss (1980), Schultheiss (1985), and Richardson and others (1988). Values reported by Schultheiss (1985) for nanofossil oozes at DSDP Leg 86, site 577, between 5 and

10 mbsf (~100 – 150 kPa), are from 35 to 39 m/s. Even at 93 mbsf, he reported a shear wave velocity of 39 m/s. This value translates to a shear modulus of 2.54×10^6 N/m^2 using his reported wet bulk density of 1.67 Mg/m^3. In a different type of sediment—beach sands of mixed grain size—Schultheiss (1980) reported only a slightly higher shear modulus of 6.6×10^6 N/m^2. For glass beads he reports 1.3×10^6 N/m^2 which compares to ~2 or 3×10^6 N/m^2 measured by the duomorphs in the glass bead test (Figure 61) reported here. Richardson and others (1988) report shear wave velocities of 20 m/s, in flocculent marine muds, to 80 m/s in hard packed sands. These values translate to 5.6×10^5 N/m^2 and $1.0^6 \times 10^7$ N/m^2 respectively.

Hamilton's regression equations (1980), however, indicate that shear modulus and shear wave velocity should be significantly higher at effective stress levels comparable to those in this study (Figs. 57a and 57b). Measurements made by Tugut and others (1987) support Hamilton's predictions. They report shear modulus values an order of magnitude higher in marine sands (Trevorrow and others 1988) and oolitic Bahamian carbonates than those reported by Schultheiss (1980, 1985) and here. It is not clear why there should be such a discrepancy among reports of shear modulus and shear wave velocity in carbonate sediments. Hamilton's regression equations for shear wave velocity are based partly on seismic data and partly on surficial compressional wave velocity measurements. Differences between seismically derived and laboratory -measured parameters are common. Tugut and others' values are measured on ooids that may be very similar to hard-packed, equally sized sands, which would result in higher values of shear modulus. Indeed, this seems to be the case in the Schultheiss (1980) experimental study in which he reports that sands with a narrow range of grain size have higher shear moduli (on the order of 1.9×10^7 N/m^2) than mixed sands (on the order of 10^6 N/m^2), which are similar to the grain distribution of the periplatform oozes.

Consolidation-related Fabric Changes

The objective of the fabric study was to document the effect of consolidation-related fabric changes on sediment properties. High permeability seemed to be a function of both grain support and aragonite needle content. LBB 15H-1 was almost entirely composed of randomly oriented

aragonite needles with only a few floating grains. This sample experienced only 25.7% height reduction, possibly because the aragonite needles, strong in the C direction, functioned as grain-supported particles that protected pore spaces. LBB 16P-1 was grain supported and experienced the least height reduction. Permeability was initially very high (Table 10). Permeability decreased by 3 orders of magnitude by the time 4604 kPa was achieved, probably as a result of observed grain crushing, which eliminated some of the previously protected fluid pathways.

The high permeability of aragonite and sand-rich samples was not necessarily predicted by porosity. The initial porosity was between 55% and 61% and the final porosity after consolidation between 47% and 53% for all samples. Laboratory measurements reflected total porosity, including intraparticle porosity. Often samples with a coccolith matrix and foraminifer grains had a high proportion of fluid contained within the grains, which contributed little to effective fluid flow since the pore spaces were not necessarily interconnected. As the porosity was reduced, the permeability may or may not have been reduced, depending on whether the reduction in porosity was in the interconnected pore spaces or in the intraparticle porosity. In contrast, the aragonite needle samples had little intraparticle porosity; most of the pore spaces acted as fluid conduits. The decrease in porosity after consolidation reflects only the constriction of interparticle void spaces as the grains became more tightly packed. It was expected that the permeability would decrease proportionally. However, permeability was actually a function of the size of the pore throats or the effective passageways. If the pore throat size remains unchanged, reduction in overall porosity or size of the void spaces will not affect the permeability. Thus the porosity may not be a good predictor of permeability unless the fabric and particle types are known.

Porometry

If a sediment is relatively homogeneous, it would be reasonable to expect the average pore size to decrease because the pore fluid is being driven out of the sediment and is allowing the particles (matrix and grains) to move closer to each other. Similarly, when a large amount of sample is compressed into a smaller area, the total number of particles and pores in the original sample stays the same but is compressed into a smaller volume. When the sample is observed through the

same window size, the number of particles and pores will be greater after consolidation for that window size than before consolidation. Thus, for the matrix-supported samples (Fig. 7a) and for LBB 10P-1 with a low aragonite content, the number of pores in the <5 μm size range increased after consolidation. In samples composed predominantly of aragonite needles, some pores may be enlarged at the expense of others. For example, a sediment composed of aragonite needles can be thought of as one large void interrupted by needles. If any of those needles were to be broken during consolidation, the pore spaces they separate would coalesce into one large pore with a volume greater than either of the two original pore spaces. Consolidation of LBB 15H-1 and ES 10P-3, both predominantly aragonite needles, resulted in larger average pore sizes after consolidation and a smaller number of pores in the scanned window, a logical result of the above scenario.

The pore areas of the carbonate samples scanned averaged between 5 and 8% of the total areas scanned. Laboratory measurements of porosity and void ratio on bulk samples indicates that only approximately 10% of the actual pore volume was identified by the image analysis. The remaining porosity is probably intraparticle porosity found within whole skeletal grains, such as pteropods (Fig. 17a), foraminifers, calcareous dinoflagellate cysts (Fig. 17b), and within small matrix elements, such as coccoliths. Large, shallow pore spaces (greater than 5 μm), seen as shades of gray on the photomicrographs because of sample relief, were also eliminated by the constraints established for the analysis. The remaining voids analyzed were most probably small pore spaces or pore throats. An increase in analyzed pore size may indicate an increase in pore throat size. In matrix-supported samples, therefore, the size of pore throats decreases, resulting in lower final permeabilities. In samples composed primarily of aragonite needles, it is difficult to distinguish between pores and pore throats.

Although limited in scope, the preliminary results obtained using a computerized image analysis system suggest that this approach, in conjunction with other techniques such as thin section analysis, may be useful in quantifying fabric descriptions.

CONCLUSIONS

1. Periplatform oozes consolidate differently than marine clays. They consolidate less overall and do not reach as low a void ratio as do marine clays under mechanical consolidation. The Schlanger and Douglas (1974) volume change model developed from deep-water carbonates appears to be equally applicable to shallow- and mid-water carbonate sediments when the dominant process is mechanical consolidation.

2. Compressional wave velocities of periplatform oozes measured here are similar to those predicted by Hamilton (1980). However, the shear modulus and shear wave velocity values are significantly lower than predicted by Hamilton, but are essentially the same as those measured by Schultheiss (1985) on nanofossil oozes.

3. The independent measurements of shear wave velocity using duomorphs duplicated the original bender element transducer measurements suggesting that the early measured values were valid and that duomorphs are a feasible alternative to shear wave bender-element transducers. Further theoretical work may have to be done to improve their performance at higher effective stress levels. In their present state, the duomorphs should be adaptable to an *in situ* configuration.

4. The relationship between permeability and porosity depends on the sediment fabric. Permeability, porosity, and porometry determinations reveal changes in fabric are difficult to determine in SEM micrographs.

5. In general, permeability decreases with consolidation. Samples composed of aragonite needles have the highest permeability, samples with coccolith matrices have the lowest. Grain-supported sediments tend to have higher permeabilities because the pore throats are protected by the grains and are less affected by consolidation than they are in matrix-supported sediments. Carbonate samples with grain-supported fabrics display slight changes in permeability until loads sufficient to cause grain crushing are reached. At that point, permeability suddenly decreases.

6. When samples of all fabric types are considered together, total porosity is not a good predictor of permeability. Intraparticle porosity may not be interconnected with interparticle porosity and may not contribute to permeability. Porosity in sediment with aragonite needle matrices is very different from porosity in sediments with matrices consisting of platey grains.

7. Changes in porometry due to consolidation are a function of fabric changes. Predominantly matrix-supported samples exhibited an increase in number of pores per unit area and a decrease in average pore size as a result of consolidation. Samples composed predominantly of aragonite needle matrices displayed opposite results.

CHAPTER III

GEOTECHNICAL AND GEOACOUSTIC PROPERTIES OF PERIPLATFORM SEDIMENTS: MODEL AND CONCLUSIONS

INTRODUCTION

The main thrust of this research is to develop a reliable geoacoustic model that can be used to estimate and predict geotechnical and geoacoustic parameters for periplatform sediments. The assumption is that sediments in the Bahamas can be used as a model for sediments in other carbonate regions. The parameters considered are those affected principally by mechanical consolidation; laboratory results are related to *in situ* conditions simply by translating effective stress to estimated subbottom depth. The model parameters (Table 11) are valid for the upper portions of the sedimentary column that have not been affected by widespread cementation. The main variables considered important in the characterization of sediments are type and fabric of the sediment; thickness of layers; density; porosity and permeability; and the acoustic properties compressional wave velocity, shear wave velocity, and shear modulus. Each variable will be discussed.

DISCUSSION

Sediment Type and Fabric

The physical and acoustic parameters in the model (Table 11) are considered to be valid for periplatform sediments that are recovered from banks and slopes to a water depth of ~2000 m. The physical and elastic properties of a sediment are primarily controlled by the properties of its constituents and their properties. Since the range of expected salinities is narrow, the properties of the pore fluid are nearly constant when temperature and pressure are fixed (Bachman 1985). Since periplatform sediments by definition are dominated by aragonite, high magnesian calcite and calcite, it is reasonable to expect that when porosity is about the same, periplatform sediment properties will be similar regardless of location. When modeling sediments, the initial decisions to

Table 11. Physical and Geoacoustic Properties of Periplatform Sediments

	Total	Grain-supported	Matrix-supported
Porosity			
(average)	56.5%		
as (f) of σ'	$n = 0.58 - 1.028 \times 10^{-4}(\sigma') + 3.216 \times 10^{-8}(\sigma'^2) - 3.841 \times 10^{-12}(\sigma'^3)$		
Permeability (cm/s)			
(average)	10^{-4}		10^{-5}, 10^{-6}
as (f) of σ'	$k = 4.229 \times 10^{-4}(\sigma'^{-.821})$;		$k = 2.69 \times 10^{-4}(\sigma'^{-.664})$, $k = 2.05 \times 10^{-5}(\sigma'^{-.4318})$
as (f) of n	$k = 1.486 \times 10^{-4}(n^{6.2345})$		$k = 1.665 \times 10^{-4}(n^{7.132})$
	$k = 1.424 \times 10^{-4}(n^{6.739})$		
Wet Bulk Density (Mg/m³)			
(average)	1.74	1.78	1.72
as (f) of σ'	$\rho = 1.74 + 3.499 \times 10^{-5}(\sigma')$		
Vp (m/s)			
(average)	1596	1635	1544
as (f) of σ'	$1596 + .011\,\sigma' + 1.71 \times 10^{-6}(\sigma'^2)$;	$1635 + .045(\sigma') - 6.547 \times 10^{-6}(\sigma'^2)$;	$1544 + .002\,\sigma' + 4.231 \times 10^{-6}(\sigma'^2)$;
Vs (m/s)			
(average)	23.39		
as (f) of σ'	$Vs = 23.39(\sigma'^{.0994})$		
as (f) of Vp	$Vs = -2.087 \times 10^5 + 258.98(Vp) - 8.031 \times 10^{-2}(Vp^2)$ {between 0-2000 kPa or Vp = 1580-1614}		
	$Vs = -1157.+ 1.3957(Vp) - 4.0164 \times 10^{-4}(Vp^2)$ {between 2001-5000 kPa or Vp = 1615-1695}		
G (N/m²)			
(average)	9.46×10^5 N/m²		
as (f) of σ'	$G = 9.46 \times 10^5(\sigma'^{.2124})$		

Legend:
Geotechnical properties (porosity, permeability, wet unit weight) (38 samples)
Geoacoustic properties (Shear modulus (G), compressional velocity (Vp), shear wave velocity (Vs)) (7 samples)

be made are (a) whether sediments are deep-water carbonates or periplatform sediments, and (b) whether they are grain or matrix-supported carbonate sediments. Carbonate sediments are those containing greater than 60% calcium carbonate (Wilson 1975). Below 2000 m and geographically distant from a carbonate bank, sediments are essentially all calcite. These are considered deep-water carbonate sediments and are more properly modeled using values and regression equations derived by Hamilton (1980). Sediments recovered from slopes that have a significant banktop component are mineralogically transitional between the deep-water carbonates and tropical shallow-water carbonates, which are dominated by aragonite and magnesian calcite (Dix and Mullins 1988). These periplatform sediments can be modeled using values and regression equations from Table 11. Sediments in the Bahamas are nearly devoid of a terrigenous component; they are derived from banktop production and planktonic organisms. As such, they are generally greater than 90% calcium carbonate. In this study, sediments were sampled from two end-member environments: northern Little Bahama Bank, considered to be an accretionary slope, and Exuma Sound, considered to be a by-pass slope (Austin, Schlager, Palmer and others 1986). It was assumed that deposition would be continuous over Little Bahama Bank, while most of the sediments in Exuma Sound would be deposited on the toe of the slope rather than on the slopes themselves. Because northern Little Bahama Bank has a such a gentle slope, samples were recovered from much shallower water depths than were samples from Exuma Sound. The slopes of Exuma Sound were steep enough so that the shallow depths were within the 3-mile restricted territorial limit where coring was not allowed. In general, samples from Little Bahama Bank were recovered in 450 to 1000 m of water, those from Exuma Sound in 1000 to 2000 m of water. Currents on Little Bahama Bank winnowed many of the fines, leaving coarse grained sediments. In contrast, the majority of samples recovered from 2000 m in Exuma Sound were matrix supported. The probability of finding grain-supported sediments was much higher on Little Bahama Bank than on Exuma Sound slopes. In general, coarse sediments will be found on the upper slopes and in shallow water. The coarse sediments will have a higher probability of being grain supported than fine-grained sediments that can be found in quiet environments and in deep water.

Layer Thickness

The thickness of the layers within the unconsolidated sediment and the location of significant reflectors (which can vary with frequency) can be determined from acoustic reflection profile records. Several factors determine the thickness of unconsolidated sediment. Turbidites, normally coarser grained with fewer metastable minerals, lithify much more slowly than the background periplatform ooze, which contains a large proportion of aragonite and high magnesian calcite (Eberli 1988, Mullins and others 1985, Dix and Mullins 1988). Dissolution of magnesian calcite and aragonite and the reprecipitation of calcite appears to be the major diagenetic process during shallow burial diagenesis (Mullins and others 1985), which frequently results in chalk-ooze couplets. Therefore, sediment that is matrix supported with a high proportion of aragonite and magnesian calcite can undergo calcitization and selective lithification between 30-50 mbsf (Mullins and others 1985a; Mullins and others 1985b). In Exuma Sound selective lithification occurred as shallow as 50 mbsf, while north of Little Bahama Bank, the beginnings of lithification were not found until depths ~150 to 200 mbsf (Austin, Schlager, Palmer and others, 1986).

Porosity Gradients

The total porosity differs very little between matrix- and grain-supported sediments. The average initial porosity for matrix-supported sediments is ~59% and for grain-supported sediments is ~56%. In the absence of measured porosity values, an estimate of ~57% to 60% for periplatform sediments can be used. To predict porosity as a function of depth, the following regression (Fig. 41) can be used:

$$n = 0.58 - 1.028 \times 10^{-4}(\sigma') + 3.216 \times 10^{-8}(\sigma'^2) - 3.841 \times 10^{-12}(\sigma'^3), \qquad (28)$$

where n is porosity and σ' is effective stress. Effective stress can be converted to depth in this and the following cases by using the formula

$$Depth = \sigma'/(\rho_t - \rho_{sw}), \qquad (29)$$

where σ' is the effective stress, γ_t is the unit weight of sediment, and γ_{sw} is the unit weight of seawater.

Permeability Gradients

Permeability varies widely between grain- and matrix-supported periplatform sediments, so an average permeability value cannot be used for all periplatform sediments. Permeability values varied between 10^{-3} and 10^{-6} cm/s. Grain-supported sediments have initial permeability values an order of magnitude higher than matrix-supported sediments, generally in the 10^{-4} cm/s range (Fig. 40). Matrix-supported sediments have initial permeabilities between 10^{-5} and 10^{-6} cm/s depending on the matrix material. Matrix-supported sediments with predominantly coccolith ooze as matrix material have initial permeability values in the 1×10^{-6} cm/s range while those matrix-supported sediments with a higher proportion of aragonite needles as matrix material have permeability values in the 10^{-5} cm/s range. To predict permeability as a function of effective stress the following regressions derived from these sediments may be used:

(a) $k = 4.229 \times 10^{-4} (\sigma'^{-0.821})$ for grain-supported sediments

(b) $k = 2.69 \times 10^{-4} (\sigma'^{-0.664})$ for matrix-supported sediments with an initial permeability of 1×10^{-5} cm/s

(c) $k = 2.05 \times 10^{-5} (\sigma'^{-0.432})$ for matrix-supported sediments with an initial permeability of 1×10^{-6} cm/s

As before, σ' is effective stress and can be converted to an estimated depth of burial.

Density Gradients

The wet bulk density of the various layers is important in the propagation of compressional and shear waves and is required by all of the acoustic prediction models. The critical questions are, how do laboratory measurements relate to *in situ* measurements and how much rebound has occurred as a result of coring and subsequent sample handling (Hamilton 1980)? A look at the consolidation curves (Figs. 19 to 26) shows a flat rebound curve, indicating very little expansion has occurred. Figure 43, wet bulk density plotted as a function of effective stress, was derived from laboratory

measurements before and after consolidation only. No values were interpolated. The average initial wet bulk density for all samples is 1.75 Mg/m³ with a standard deviation of 0.074 Mg/m³. The average initial wet bulk density for the grain-supported and matrix-supported sediments falls within the limits of error and can therefore be considered to be all the same. The regression derived from the initial and final wet bulk density is

$$\rho = 1.74 + 3.499 \times 10^{-5}(\sigma'), \tag{30}$$

where σ' is effective stress in kPa.

Compressional Wave Velocity

Accurate compressional wave velocity measurements are extremely important in acoustic prediction because at certain grazing angles, low-frequency sound energy can be returned to the water when positive velocity gradients are present (Hamilton 1980). Velocity gradients can also be used to compute layer thicknesses and to determine the depth of lithification in periplatform oozes. Table 11 outlines the differences in velocity between grain- (1635 m/s) and matrix-supported (1544 m/s) sediments. If the sediment fabric is unknown, an average of 1596 m/s can be used. To estimate compressional wave velocity as a function of depth, the regression equations derived from the laboratory-measured compressional wave velocity data agree reasonably well with Hamilton's predicted (1980) values (Fig. 51):

$Vp = 1596 + 0.011\sigma' + 1.71 \times 10^{-6}(\sigma'^2)$ for all samples

$Vp = 1635 + 0.045 (\sigma') - 6.547 \times 10^{-6}(\sigma'^2)$ for grain-supported samples

$Vp = 1544 + 0.002\sigma' + 4.231 \times 10^{-6}(\sigma'^2)$ for matrix-supported samples.

Again, σ' is effective stress and can be converted to estimated subbottom depth.

Shear Wave Velocity and Shear Modulus

The conversion of energy from compressional to shear waves occurs at boundaries with an impedance mismatch, and this converted energy is rapidly attenuated (Hamilton 1980). Therefore, a knowledge of shear wave values is a required parameter in most acoustic models. The shear

modulus, related to shear wave velocity and wet bulk density, is a more sensitive parameter than the bulk modulus for bottom predictions and is becoming widely used by modelers. There is considerable disparity in the reported values of shear wave velocity and shear modulus. Reported shear wave velocity values range from very low values of 20-45 m/s (Richardson and others 1988, Schultheiss 1985) to much higher values of ~100 m/s (Hamilton 1980). Similarly, Tugut and others (1987) reported shear modulus values of ~2 × 10^7 N/m^2, which can be converted to a shear velocity of ~100 m/s using a wet bulk density of 1.5 Mg/m^3. For the periplatform samples tested here, initial shear wave values averaged 23.39 km/s and, under 4500-kPa effective stress, final shear wave values averaged 45.36 m/s. At ambient laboratory pressures, the average measured shear modulus for these samples is 1.84 × 10^6 N/m*, at 120 kPa the averaged measured shear modulus is 3.42 × 10^6 N/m^2, and at 4500 kPa the average calculated (from measured compressional wave velocity) shear modulus is 3.89 × 10^6 N/m^2. Some of the disparity in reported values may result from different measurement techniques and/or from carbonate sediments that are indeed very dissimilar. In the absence of complete physical and fabric descriptions of the samples used, comparison of results may not be totally accurate. The increase with depth of shear wave velocity is much less than predicted for deep-water carbonate sediments (Fig. 52) but agrees well with values measured using bender-element techniques on coccolith oozes recovered from depths estimated as equivalent to 4500 kPa (Schultheiss 1985). Reasons for the small increase in shear wave velocity may be because the sediments undergo a small volume change and a small porosity decrease under mechanical consolidation. The shear wave velocity may increase in step-like fashion as a function of cementation rather than mechanical consolidation. Therefore, within the shallow burial regime for unconsolidated sediments, the following regression is suggested for estimating shear wave velocity as a function of effective stress or depth:

$$Vs = 23.39 \ (\sigma'^{\,0.0994}) \quad \text{average for all periplatform sediments.} \tag{31}$$

If the compressional wave velocity is known, the shear wave velocity can be estimated as follows (Fig. 58):
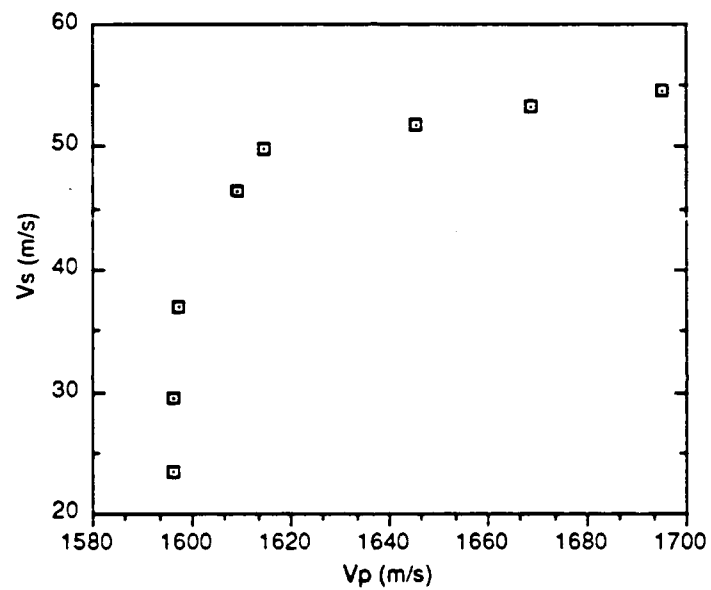
Figure 58. Shear wave velocity as a function of compressional wave velocity. $Vs = -2.087 \times 10^5 + 258.98\,(Vp) - 8.031 \times 10^{-2}\,(Vp^2)$ between 0 and 2000 kPa or $Vp = 1585\text{-}1614$ m/s. $Vs = -1157 + 1.396\,(Vp) - 4.016 \times 10^{-4}\,(Vp^2)$ between 2001 and 5000 kPa or Vp between 1615 and 1695 m/s.

$$V_S = -2.08^7 \times 10^5 + 258.98 \ (V_p) -8.031 \times 10^{-2}(V_p^2)$$

{between 0-2000 kPa or Vp = 1580-1614}

(32)

$$V_S = -1157 + 1.3957 \ (V_p) -4.0164 \times 10^{-4}(V_p^2)$$

{between 2001-5000 kPa or Vp = 1615-1695}

Shear modulus as a function of effective stress can be estimated:

$$G = 9.46 \times 10^5 (\sigma'^{\ 0.2124}),$$
(33)

where G is shear modulus, and σ' can be converted to depth as previously described.

CONCLUSIONS

1. Shallow-water Bahamian periplatform sediments can be used as a general model for sediments in other similar environments within the upper 50 to 150 mbsf where mechanical consolidation is the dominant diagenetic process.

2. The major differences in properties in periplatform sediments seem to be roughly controlled by fabric. Grain-supported sediments have higher permeabilities than matrix-supported sediments because the pore throats are protected by grains. The relationship between permeability and porosity is also controlled by the fabric; total porosity is not a good predictor of permeability. Matrix-supported sediments that have a higher proportion of metastable minerals and undergo diagenesis earlier and at shallower depths than grain-supported sediments. Therefore, the depth where consolidation is the dominant diagenetic process varies, depending on sediment composition and fabric.

3. Given the differences in fabric, physical and acoustic properties do vary as a function of effective stress and can be derived using regression equations listed in Table 11.

4. Duomorph technology offers a promising means of measuring shear modulus and shear wave velocity in the laboratory and eventually *in situ*, although further theoretical work may be required to improve interpretation of results at high effective stress levels.

LITERATURE CITED

Austin JA Jr, Schlager W, Palmer A, and others (1986) Proceedings Ocean Drilling Program, Initial Reports, 101. College Station, TX, 569 pp.

Austin JA Jr, Schlager W, Palmer A, and others (1988) Proceedings Ocean Drilling Program, Scientific Results, 101. College Station, TX, 501 pp.

Bachman RT (1985) Acoustic and physical property relationships in marine sediment. Journal of the Acoustical Society of America 78(2):616-621.

Bathurst RGC (1970) Problems of lithification in carbonate muds. Proceedings Geologists Association 81(3):429-440.

Bennett RH (1976) Clay fabric and geotechnical properties of selected submarine sediment cores from the Mississippi Delta. PhD dissertation, Texas A&M University, College Station, TX.

Bennett RH, Bryant WK, Keller GH (1977) Clay fabric and geotechnical properties of selected submarine sediment cores from the Mississippi Delta. NOAA Professional Paper 9, US Deptartment of Commerce, Rockville, MD, 86 pp.

Bennett RH, Bryant WR, Keller GH (1981) Clay fabric of selected submarine sediments: fundamental properties and models. Journal Sedimentary Petrology 51(1):217-232.

Bennett RH, Hooper JR, Bea R (1982) Geological and geotechnical research on seafloor stability of continental margins. Geo-Marine Letters 2:115-116.

Bennett RH, Fischer KM, Lavoie DL, Bryant WR, Rezak R (1989) Porometry and fabric of marine clay and carbonate sediments: determinants of permeability. Marine Geology 89:127-152.

Berger WH (1968) Planktonic foraminifera, selective solution and paleoclimatic interpretation. Deep Sea Research 15:31-43.

Berger WH, Adelseck CG, Mayer LA (1976) Distribution of carbonate in surface sediments of the Pacific Ocean. Journal Geophysical Research 81(15):2617-2627.

Briar H, Bills K, Schapery RA (1972) Development of an in-situ transmitter for solid rocket propellant surveillance. Air Force Rocket Propulsion Laboratory-TR-76-36, Edwards, CA, 93523, 172 pp.

Briar H, Bills K, Schapery RA (1976) Design and test of the operational in-situ gage for solid propellant surveillance. Air Force Rocket Propulsion Laboratory-TR-76-36. Edwards, CA, 93523, 131 pp.

Bryant WR, Hottman W, Trabant P (1975) Permeability of unconsolidated and consolidated marine sediments, Gulf of Mexico. Marine Geotechnology 1:1-14.

Bryant WR, Bennett RH, Katherman C (1981) Shear Strength, Consolidation, Porosity, and Permeability of Oceanic Sediments. In: Emiliani C (ed) The Sea 7: The Oceanic Lithosphere, John Wiley and Sons, New York, pp 1555-1616.

Bryant WR, Bennett RH (1988) Origin, physical, and mineralogical nature of red clays: The Pacific Ocean Basin as a model. Geo-Marine Letters 8:189-249.

Demars KR (1982) Unique engineering properties and compression behavior of deep-sea calcareous sediments, geotechnical properties, behavior, and performance of calcareous soils. In: Demars KR, Chaney RC (eds) Geotechnical Properties, Behavior, and Performance of Calcareous Soils, ASTM STP 777. American Society for Testing and Materials, pp 97-112.

Demars KR, Nacci VA, Kelly WE (1976) Carbonate content: An index property for ocean sediments. Offshore Technology Conference #2627, Dallas, TX, pp 97-106.

Dix GR, Mullins HT (1988a) A regional perspective of shallow-burial diagenesis of deep water periplatform carbonates from the northern Bahamas. In: Austin JA, Schlager W, and others, (eds) Proceedings Ocean Drilling Program, Scientific Results, 101, College Station, TX, pp 279-304.

Dix GR, Mullins HT (1988b) Rapid burial diagenesis of deep-water carbonates: Exuma Sound, Bahamas. Geology 16:680-683.

Droxler AW, Schlager W, Whallon CC (1983) Quaternary aragonite cycles and oxygen-isotope record in Bahamian carbonate ooze. Geology 11:235-239.

Dunn IS, Anderson LR, Kiefer FW (1980) Fundamentals of Geotechnical Analysis. John Wiley and Sons, New York, 414 pp.

Eberli GP (1988) Physical properties of carbonate turbidite sequences surrounding the Bahamas – implications for slope stability and fluid movements. In: Austin JA, Schlager W, and others, (eds) Proceedings Ocean Drilling Program, Scientific Results, 101, College Station, TX, pp 305-314.

Edmond JM (1974) On the dissolution of carbonate and silicate in the deep ocean. Deep-Sea Research 21:455-480.

Enos P, Sawatsky LH (1980) Pore networks in Holocene carbonate sediments. Journal Sedimentary Petrology 51:961-981.

Etris EL, Brumfield DS, Ehrlich R, Crabtree SJ (1988) Relations between pores, throats and permeability: a petrographic/physical analysis of some carbonate grainstones and packstones. Carbonates and Evaporites 3(1):17-32.

Fischer KM, Li H, Bennett RH, Dunlap, WA (submitted) Calculation of permeability coefficients of soils and marine sediments. Journal Sedimentary Petrology.

Folk R (1974) Petrology of Sedimentary Rocks. Hemphill Publishing Co., Austin, TX, 182 pp.

Fruth LS Jr, Omre GR, Donath FA (1966) Experimental compaction effects in carbonate sediments. Journal Sedimentary Petrology 36(3):747-754.

Hamilton EL (1971) Elastic properties of marine sediments. Journal Geophysical Research 76(2): 579-603.

Hamilton EL (1976) Variations of density and porosity with depth in deep-sea sediments. Journal Sedimentary Petrology 46(2):280-300.

Hamilton EL (1980) Geoacoustic modeling of the sea floor. Journal Acoustical Society America 68(5):1313-1340.

Hamilton EL, Bachman RT, Berger WH, Johnson TC, Mayer LA (1982) Acoustic and related properties of calcareous sediments. Journal Sedimentary Petrology 52(3):0733-0753.

Harwood GM, Towers PA (1988) Seismic sedimentologic interpretation of a carbonate slope, north margin of Little Bahama Bank. In: Austin JA, Schlager W, and others, (eds) Proceedings Ocean Drilling Program, Scientific Results, 101, College Station, TX, pp 263-278.

Johnson TC, Hamilton EL, Bachman RT, Berger WH (1978) Sound velocities in calcareous oozes and chalks from sonobuoy data: Ontong Java Plateau, Western Equatorial Pacific. Journal Geophysical Research 83(B1):283-289.

Keller GH, Bennett RH (1970) Variations in the Mass Physical Properties of Selected Submarine Sediments. In: Marine Geology, Elsevier Publishing Co., Amsterdam, The Netherlands, pp 215-223.

Kennett J (1982) Marine Geology. Prentice-Hall, Inc., Englewood Cliffs, NJ 07632, 812 pp.

Lambe TW (1951) Soil Testing for Engineers. John Wiley and Sons, New York, 165 pp.

Lambe TW, Whitman RV (1969) Soil Mechanics. John Wiley & Sons, Inc., New York, 553 pp.

Lambert DN, Lavoie DL, Nastav FL, Sawyer WB (1984) Revised environmental surveys of selected sites, Prepared during 1984 for the Theater Nuclear Warfare Project Office. Naval Surface Weapons Center, White Oak, NORDA Seafloor Geosciences Division Informal Technical Transmittal, 74 pp.

Lavoie DL (1984) Shallow water geoacoustic modeling: The Greenland, Iceland, United Kingdom Gap. NORDA Report No. 109, Stennis Space Center, MS.

Lavoie DL (1988) Geotechnical properties of sediments in a carbonate-slope environment: Ocean Drilling Program Site 630, Northern Little Bahama Bank. In: Austin JA, Schlager W, and others, (eds) Proceedings Ocean Drilling Program, Scientific Results, 101, College Station, TX, pp 315-326.

Lavoie DL, Matthews JE (1983) Sediments on the southeastern flank of the Bermuda Pedestal. NORDA Technical Note 198, Stennis Space Center, MS.

Matthews J E (1980) Heuristic physical property model for marine sediments. Journal Acoustical Society America 68(5):1361-1370.

Miller DG Jr, Richards AF (1969) Consolidation and Sedimentation—Compression Studies of a Calcareous Core, Exuma Sound, Bahamas, Sedimentology. Elsevier Publishing Company, Amsterdam, The Netherlands, pp 301-316.

Mitchell JK (1976) Fundamentals of Soil Behavior. John Wiley and Sons, New York, 422 pp.

Muller G, Gastner M (1971) The "karbonate-bombe," a simple device for determination of the carbonate content in sediments, soils and other materials. Neues Jahrbuch fuer Mineralogie Monatshefte 10:466-469.

Mullins HT, Land LS, Wise WW Jr., Seigel DI, Masters PM, Hinchey EJ, Price KR (1985a) Shallow subsurface diagenesis of Pleistocene periplatform ooze: Northern Bahamas. Sedimentology 32:480-494.

Mullins HT, Wise SW, Gardulski AF, Hinchey EJ, Masters PM, Siegel DI (1985b) Shallow subsurface diagenesis of Pleistocene periplatform ooze: Northern Bahamas. Sedimentology 32:473-479.

Rezak R (1974) Deep-sea Carbonates. In: Inderbitzen, A. L. (ed), Deep-Sea Sediments. Plenum Press, NY, pp 453-461.

Richards AF, Hamilton EL (1967) Investigation of deep-sea cores, III. Consolidation. In: Richards AF (ed) Marine Geotechnique, University of Illinois Press, pp 93-117.

Richardson MD, Muzi E, Troiano L (1988) Shear waves in sediments: A comparison of in situ and laboratory measurements. Abstract 38. The microstructure of fine-grained terrigenous marine sediments-from muds to shale. Naval Ocean Research and Development Activity, Stennis Space Center, MS.

Richart FA (1970) Vibrations of Soils and Foundations. Prentice-Hall, Inc., New Jersey, 414 pp.

Ricken W (1987) The carbonate compaction law: a new tool. Sedimentology 34:571-584.

Ruzyla K (1986) Characterization of pore space by quantitative image analysis. Society Petroleum Engineers Formation Evaluation, pp 389-398.

Schlager W, James NP (1978) Low-magnesian calcite limestones forming at the deep-sea floor, Tongue of the Ocean, Bahamas. Sedimentology 25:675-702.

Schlager W, Ginsburg RN (1981) Bahama carbonate platforms—the deep and the past. Marine Geology 44:1-24.

Schlanger SO, Douglas RG (1974) The pelagic ooze-chalk-limestone transition and its implications for marine stratigraphy. In: Pelagic Sediments: on Land and Under the Sea. Hsu KJ, and Jenkyns HC (eds), International Association of Sedimentologists Special Publication No. 1, Blackwell Scientific Publications, Oxford, England, pp 117-148.

Schultheiss PJ (1980) Simultaneous measurement of P & S wave velocities during conventional laboratory soil testing procedures. Marine Geotechnology 4(4):343-367, Wormley, Godalming, Surrey, U.K.

Schultheiss PJ (1983) The Influence of Packing Structure and Effective Stress on Vs, Vp, and the Calculated Dynamic and Static Moduli in Sediments. In: (Page NG, ed) Acoustics and the Sea-Bed. Bath University Press, Bath UK, pp 19-27.

Schultheiss PJ (1985) Physical and geotechnical properties of sediments from the Northwest Pacific: Deep Sea Drilling Project Leg 86. In: Heath GR, Bruckle LH, and others (eds), Initial Reports, Deep Sea Drilling Project, 86, US Government Printing Office, Washington, pp 701-722.

Shinn EA, Halley RB, Hudson JH, Lidz BH (1977) Limestone compaction: an enigma. Geology 5:21-24.

Shinn EA, Robbin DM (1983) Mechanical and chemical compaction of fine-grained shallow-water limestones. Journal Sedimentary Petrology 53:595-618.

Silva AJ (1974) Marine Geomechanics: Overview and Projections. In: Inderbitzen, A. L. (ed), Deep Sea Sediments, Plenum Press, New York, pp 45-76.

Skempton AW (1970) The consolidation of clays by gravitational compaction. Quarterly Journal Geologic Society, London, 125:373-411.

Swart PK, Guzidowski M (1988) Interstitial-water chemistry and diagenesis of periplatform sediments from the Bahamas, ODP Leg 101. In: Austin JA, Schlager W, and others, (eds) Proceedings Ocean Drilling Program, Scientific Results, 101, College Station, TX, pp 263-380.

Taylor DW (1948) Fundamentals of Soil Mechanics. John Wiley and Sons, New York, 700 pp.

Terzaghi K (1925) Principles of soil mechanics settlement and consolidation of clay. Engineering News-Record, pp 874-878.

Terzaghi RD (1940) Compaction of lime mud as a cause of secondary structure. Journal Sedimentary Petrology 10:(2)78-90.

Timoshenko S, Woinowsky-Krieger S (1959) Theory of Plates and Shells. McGraw-Hill Book Company, Inc., New York, pp 51-78.

Trevorrow M, Yamamoto T, Tugut A, Abbott C, Badiey M, Goodman D, Ando K (1988) High resolution bottom shear modulus profiler experiments on the New Jersey Shelf, Summer, 1987. Rosenstiel School of Marine and Atmospheric Science TR-88-002, Miami, FL, 233 pp.

Turgut A, Yamamoto T, Abbott C, Badiey M, Trevorrow M, Goodman D (1987) Higher resolution bottom shear modulus profiler: a shallow water real-time OBS array. Rosenstiel School of Marine and Atmospheric Science TR-87-007, Miami, FL, 48 pp.

Valent PJ, Altschaeffl AG, Lee HJ (1982) Geotechnical properties of two calcareous oozes. In: Demars KR, Chaney RC (eds) Geotechnical Properties, Behavior, and Performance of Calcareous Soils, ASTM STP 777. American Society for Testing and Materials, pp 79-95.

Wardlaw NC, Mckellar M, Li Y (1988) Pore and throat size distributions determined by mercury porosimetry and by direct observation. Carbonates and Evaporites 3:1-15.

Wilson, JL (1975) Carbonate Facies in Geologic History. Springer-Verlag, New York, 471 pp.

APPENDIX A: DUOMORPH THEORY AND TESTING

DUOMORPH THEORY

The purpose of this section is to show the derivation of sediment modulus from measured strains using the duomorph sensor. The duomorph is considered to be an embedded gauge. Classical linear plate theory can be used to represent the gauge. An exhaustive discussion of plate theory can be found in Timoshenko and Woinowsky-Krieger (1959) and will not be repeated here. The medium is assumed to be viscoelastic and infinite in extent. A complete discussion of the relationship between medium and duomorph response to stress can be found in Briar and others (1972, 1976). Only the highlights will be presented here.

The basic relationship between the sediment modulus and duomorph response is outlined in the equation below (Briar and others 1976). This equation describes the relations between the sediment modulus Es, the deflection of the gauge w(r,z), and the distribution of forces across the sensor, P(r).

$$\frac{2\pi}{3} Es\,\omega\,(r,\,0) = \frac{1}{r} \int_0^r P\,(r')\,Ke\,(M)\,r'\,dr' + \int_0^c P\,(r')\,Ke\,(N)\,dr', \qquad (A1)$$

where

$M = (r'/r)2$,

$N = 1/M$,

$$Ke\,(\lambda) = \int \frac{d\theta}{\sqrt{1 - \lambda\sin^2\theta}} \quad \text{(complete elliptical integral)},$$

where

c = radius of the vibrating disk,

w(r,z) = displacement at coordinates r and z in the disk,

r = radial distance from center of disk,

z = distance from the neutral axis of the disk,

p(r) = distribution of forces causing a displacement w(r,0) of the disk,

Es = modulus of sediment which is a function of time (or frequency) and temperature.

This is a completely general equation and applies to both static and dynamic operations with the gauge. To solve the equation, all that is required is the distribution of P(r) or equivalently, w (r,0).

Figure 40 illustrates the gauge design and its behavior on bending. The outside rim of the gauge moves above the undeformed plane, while the center moves in opposition below the plane. Thus, the stress distribution p(r) is a simple parabola (Briar and others 1976). This stress distribution function, p(r) was obtained experimentally by Briar and others (1972) using holographic techniques. A holder was constructed to hold the duomorph while voltage was applied to the crystal. The interference holograms (laser created) showed only slight departures from the parabolic shape of the disk under excitation.

The form of the relation presented below is the most direct and convenient for analyzing duomorph data.

$$E^* = 12.23 \frac{D}{a^3}\left[\frac{Vs/Vrs}{Va/Vra}-1\right], \qquad (A2)$$

where

D is the rigidity of the duomorph sandwich,

a is the radius of the sandwich,

Va is the voltage input to the duomorph in air,

Vra is the voltage output of the duomorph when in air,

Vs is the voltage input to the duomorph in sediment,

Vrs is the voltage output of the sensor on the duomorph, when tested in sediment.

The complex modulus can be written in its usual form of

$$E^* = E' + E'',$$ (A3)

where E' is the real component of E^* and E" is the imaginary component of E^*.

The constant 12.23 was derived from the analysis and includes the stress distribution measurements for P(r) given above (Eq A1) (Briar and others 1976).

The rigidity D is given by the equation:

$$D = \frac{ts^3 (Es - Ez) + Ez\, t^3}{12\, (1 - v^2}, $$ (A4)

where

Es is the tensile modulus of the steel plate,

Ez is the tensile modulus of the piezoceramic crystals,

ts is the thickness of the steel plate,

t is the thickness of the entire sandwich,

v is Poisson's ratio for the sandwich.

A value of D = 2.587 N/m was obtained for our working duomorphs when the following material properties were inserted into Equation A4.

Es = 1.9×10^{11} N/m^2 (from manufacturer)

Ez = 6×10^{10} N/m^2 (Piezo Electric Products, Inc., Metuchen, NJ)

ts = 2.032×10^{-4} m (0.008 inches)

t = 7.62×10^{-4} n (0.03 inches)

v = .33 (estimated)

For dynamic testing, additional considerations are required:

$$Vp = Vp_0\, e^{i\omega t}$$ (A5)

$$Vrp = Vrp_0 \ e^{i(\omega t + \phi)}$$

$$Va = Va_0 \ e^{i\omega t}$$

$$Vra = Vra_0 \ e^{i(\omega t - \psi)},$$

where

Vp$_0$ and Va$_0$ are the amplitudes of the input voltages in sediment and in air, respectively;

Vrp$_0$ and Vra$_0$ are the amplitudes of the output voltages in propellant and in air, respectively;

t is time;

ω is frequency;

ϕ and ψ are the phase shifts in sediment and in air.

Taking the ratios of the voltages for tests in sediment and in air give

$$\frac{Vp}{Vrp} = \frac{Vp_0}{Vrp_0} e^{-i\phi} \tag{A6}$$

and

$$\frac{Va}{Vra} = \frac{Va_0}{Vra_0} e^{-i\phi} \tag{A7}$$

Combining equations A1, A4, A5, and A6 gives,

$$E^* = 12.23 \frac{D}{a^3} \left[\left(\frac{Vp_0}{Vrp_0} \right) \left(\frac{Vra_0}{Va_0} \right) e^{-i(\phi - \psi)} - 1 \right] \tag{A8}$$

TESTING

A multitude of variables are described below that can affect the performance of the duomorph. Considerable testing, also described below, was performed to assure that carbonate sample results are valid.

1. **Aging.** The piezoceramic crystal's electrical characteristics may change by as much as 10% in the first month. After the first year, the annual change becomes quite small (Briar and others 1976). The first five duomorphs constructed for this project were made from piezoceramic crystals that were about 5 years old. The remaining duomorphs were constructed from piezoceramic crystal that had been aged approximately 6 months.

2. **Effects of Potting Compound.** The greatest problem with potting the duomorphs was to create a relatively impermeable coating that was thin enough so that the effects of the compound on duomorph activity is negligible. The concern was that the potting compound used to coat the duomorphs would restrict the flexing of the duomorphs or, if too thick, act as a shock absorber and not allow the transmission of vibration to the material itself. When the potting compound was very thin, it would allow the passage of salt water around the strain gauges at the point where the wires flex. Thus, a compromise had to be found so that the coating was thick enough to withstand flexing and keep the duomorphs water-free, yet thin enough to allow unrestricted duomorph motion so that stress could be transmitted to the sediment. The results of testing uncoated and coated duomorphs indicated that the measured amplitudes are slightly and consistently higher with the duomorphs coated. In addition, there appears to be a phase shift between the coated and uncoated duomorphs. However, since the results are based on a ratio of air to sediment values, the effects of this amplitude increase and phase shift does not affect the final results. Shear modulus determined using dry cornstarch (Argo) with both coated and uncoated duomorphs is the same throughout the range of loading.

3. **Frequency Effects.** Frequency tests were run several times. Dry cornstarch was loaded into the consolidometer and duomorph measurements were made. The waiting period was approximately 0.5 hour between addition of loads. The results are repeatable. As the frequency was increased, the resulting shear modulus was lowered (Fig. 59). A saturated carbonate sample (ES 10P-3) was tested at 258 kPa. The resulting values for shear modulus (G), Young's modulus (E^*), the real part of Young's modulus (E'), and the imaginary part of Young's modulus (E'') is illustrated in Figure 60.
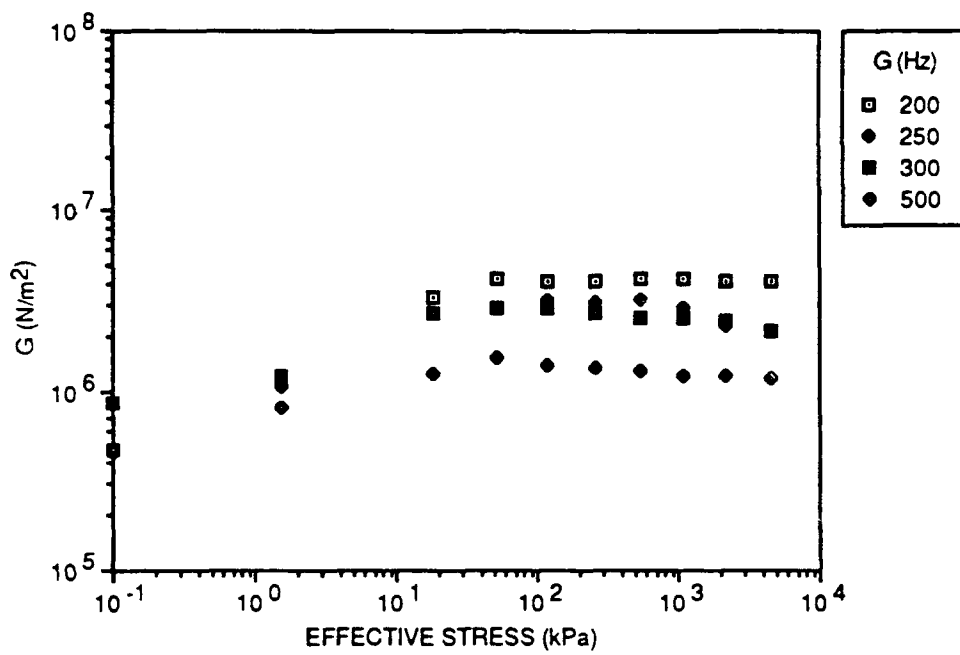
Figure 59. Shear modulus as a function of frequency. As the frequency is increased, measured shear modulus goes down.
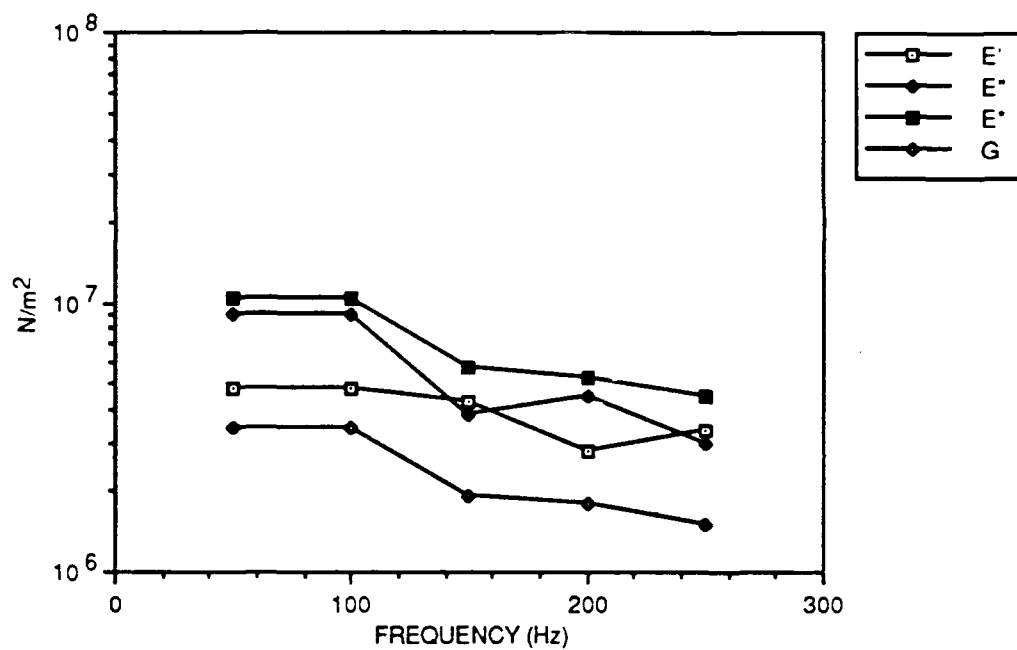
Figure 60. Results of testing ES 10P-3 under 258 kPa at various frequencies. Young's modulus (E*), the real (E') and imaginary (E") parts of Young's modulus, and shear modulus (G) decrease with increasing frequencies above 100 Hz.

4. Resonance Frequency. Resonance frequency was found be about 2 kHz for most of the duomorphs in air. It was expected that the resonance frequency would decrease considerably under loading, and it was known that the duomorphs had to be operated at a lower frequency than resonance (Briar and others 1976). The operating frequency of 250 Hz was chosen because (1) it is less than 25% of resonance frequency, (2) there is little decrease in G at frequencies higher than 250 Hz, and (3) the signal was strong and reliable at that frequency. In addition, at higher frequencies (1 kHz), the bond between the strain gauges and piezoceramic crystals was stressed and separated after only a few days. At 250 Hz the bonding seems to hold as long as the duomorph remains water-impermeable.

5. Glass Bead Tests. Initial tests were performed using glass microbeads. The rationale was that the size of manufactured glass beads would be uniform and the tests could be performed dry; therefore, the total load would be the effective stress on the sample. Initially, an uncoated duomorph was used. However, the glass beads abraded the strain indicators and caused the duomorph to fail. Results using a coated duomorph were equally discouraging (Fig. 61). The lack of increase in shear modulus as the effective stress was increased is possibly the result of the following.

1. Cavitation: Since the glass beads have no inherent cohesion, the flexing of the duomorph edges forms a cavity, so the duomorph is effectively vibrating in air after the first few vibrations.

2. Bridging: The glass beads are packed tightly enough so that no further consolidation is possible. With the glass beads forming a grain-supported medium, crushing would have to occur before an increase in shear modulus could be recorded by the duomorph.

6. Cornstarch Tests. Argo cornstarch is soft, fine-grained medium that was chosen to replace glass beads as a testing medium. It is nonabrasive, and fairly reproducible results could be obtained. It was used to test the duomorphs in an uncoated state, and to test the effects of frequency and amplitude variations on duomorph output. Figure 62a illustrates the results. Shear modulus was repeatable over several tests using identical frequencies and voltage. A pattern of increasing the voltage as the load was increased (analogous to increasing the spring resistance in a vane shear test)
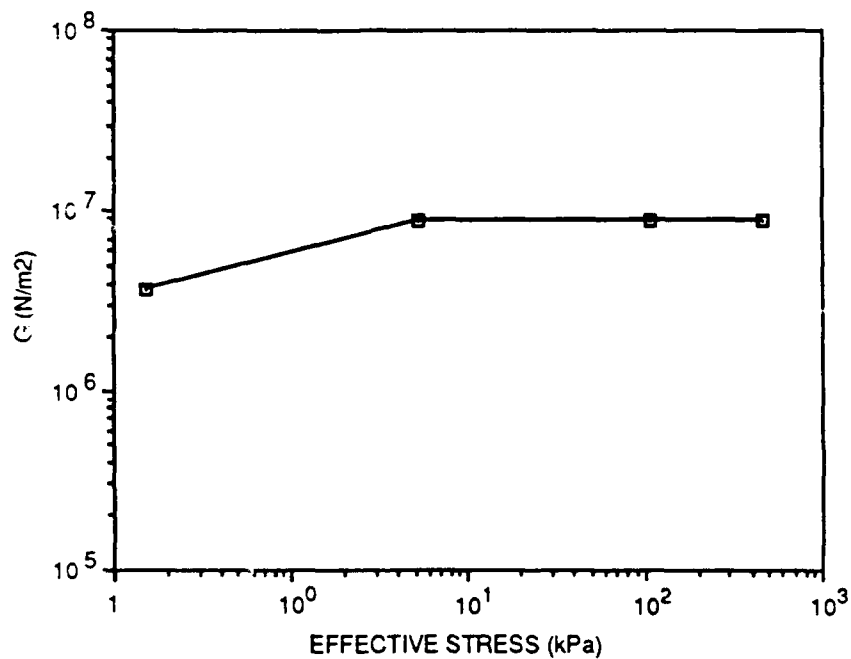
Figure 61. Results of duomorph testing using glass beads. The lack of increase in shear modulus as the effective stress was increased is possibly the result of (1) cavitation—since the glass beads have no inherent cohesion, the flexing of the duomorph edges forms a cavity so the duomorph is effectively vibrating in air after the first few vibrations; (2) bridging—the glass beads are packed tightly enough so that no further consolidation is possible. With the glass beads forming a grain-supported medium, crushing would have to occur before an increase in shear modulus could be recorded by the duomorph.
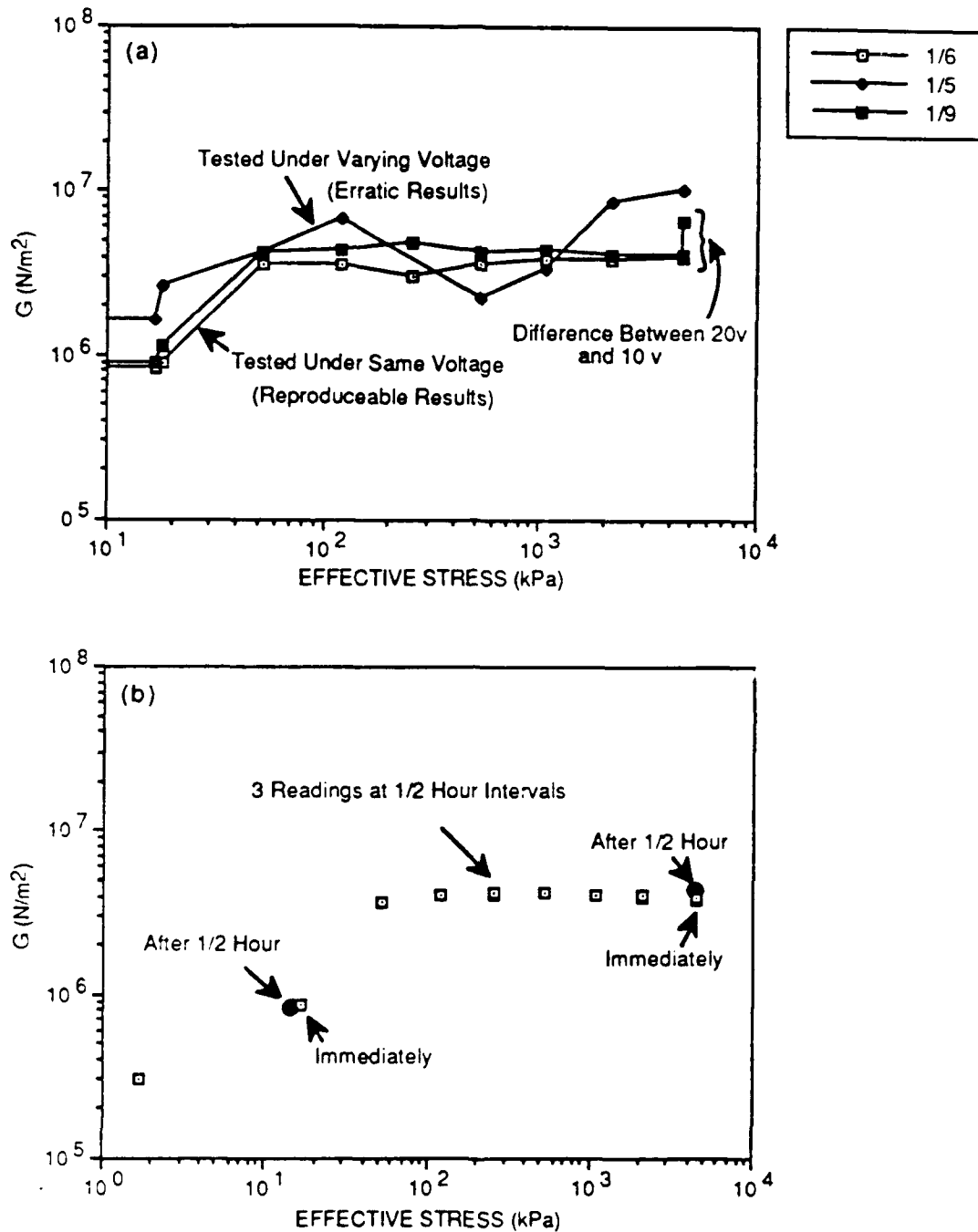
Figure 62. Results of duomorph testing using cornstarch. (a) Shear modulus was repeatable over several tests using identical frequencies and voltage. A pattern of increasing the voltage as the load was increased, analogous to increasing the spring resistance in a vane shear test, was tried but it was difficult to reproduce the same results twice. When the voltage was varied, results were erratic. (b) Readings taken at various intervals after loading were not significantly different.

was tried, but it was difficult to reproduce the same results twice. When the voltage was varied, results were erratic. Results varying the amplitude between 2 and 30 V indicated that the resulting values are higher for a higher voltage. The difference between 10 and 20 V at 4200 kPa is the difference between 4.10×10^6 and 6.48×10^6 N/m^2. This is the largest difference that was obtained. Results are specific to a given frequency and voltage. It was decided to use 10 V (20 V p-p) throughout the testing because the signal was clean and good at that setting.

Time is not a factor in testing dry cornstarch. Readings taken at 0, 30, 60, and 90 minutes were virtually identical with readings taken 8 hours after loading (Fig. 62b).

7. Lime Mud. In an attempt to use a material closer to that in which we are interested, a lime mud from the type located in Florida Back Bay was dried, ground, and tested in the same fashion as the cornstarch. Results (Fig. 63) gave a fairly typical curve found in all the duomorph testing. That is, the shear modulus increases to about 100-150 kPa and then plateaus or increases only slightly. This was found with all the carbonate samples, wet or dry.

8. Mississippi Sound Sandy-clay. To test the shape of the results curve, a sandy-clay was tested from the Mississippi Sound. Results (Fig. 64 a,b) indicate that the shear modulus increased to about 158 kPa and then leveled instead of continuing to increase as expected with increasing effective stress. It is assumed from this that the duomorphs do not give accurate results when loaded past about 150 kPa effective stress. The problem may be that the underlying assumptions and data reduction methods are based on parabolically distributed interface pressure, and under a load of 150 kPa and greater, the neutral axis may shift, resulting in a nonparabolic shape. It may be possible in the future to derive new data reduction techniques and reanalyze the data for the higher loads.
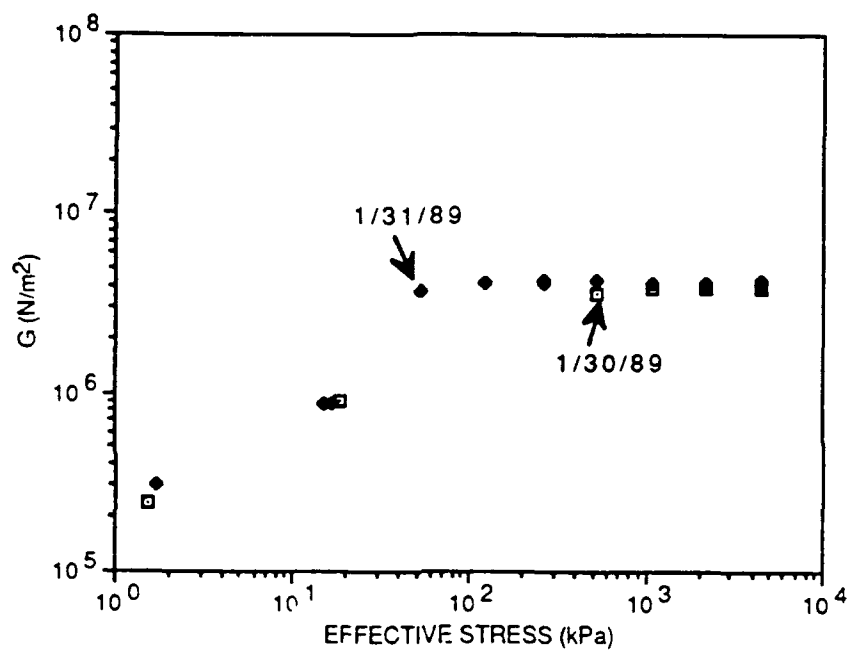
Figure 63. Results of duomorph testing using dried Florida Back Bay lime mud illustrate the typical curve found in all the duomorph testing.
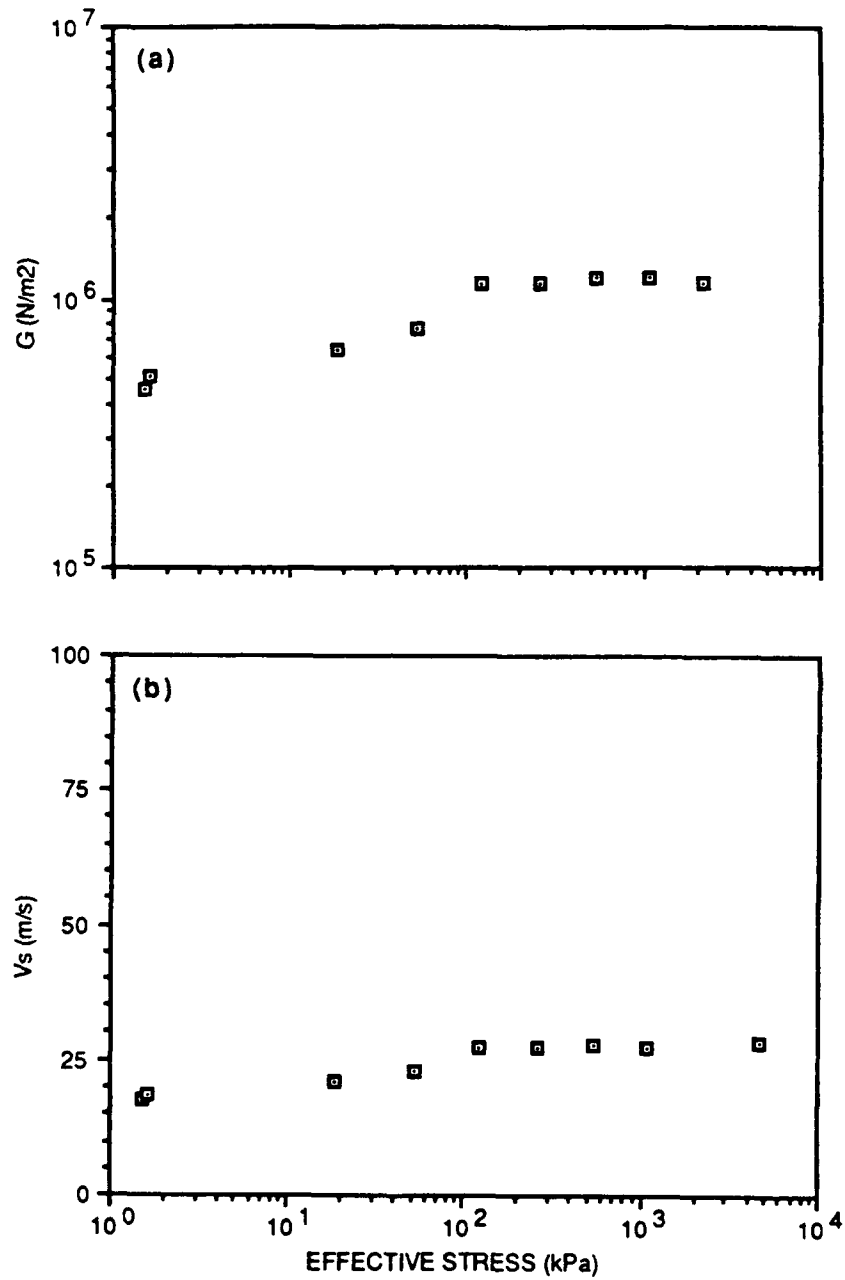
Figure 64. (a) Shear modulus and (b) shear wave velocity results using a sandy clay recovered from the Mississippi Sound. Since shear modulus and shear wave velocity (calculated from shear modulus) increase only to 158 kPa, it is assumed that the duomorphs do not give accurate results when loaded past about 150 kPa effective stress.

APPENDIX B: REPRESENTATIVE SCANNING ELECTRON MICROGRAPHS OF PERIPLATFORM SEDIMENTS
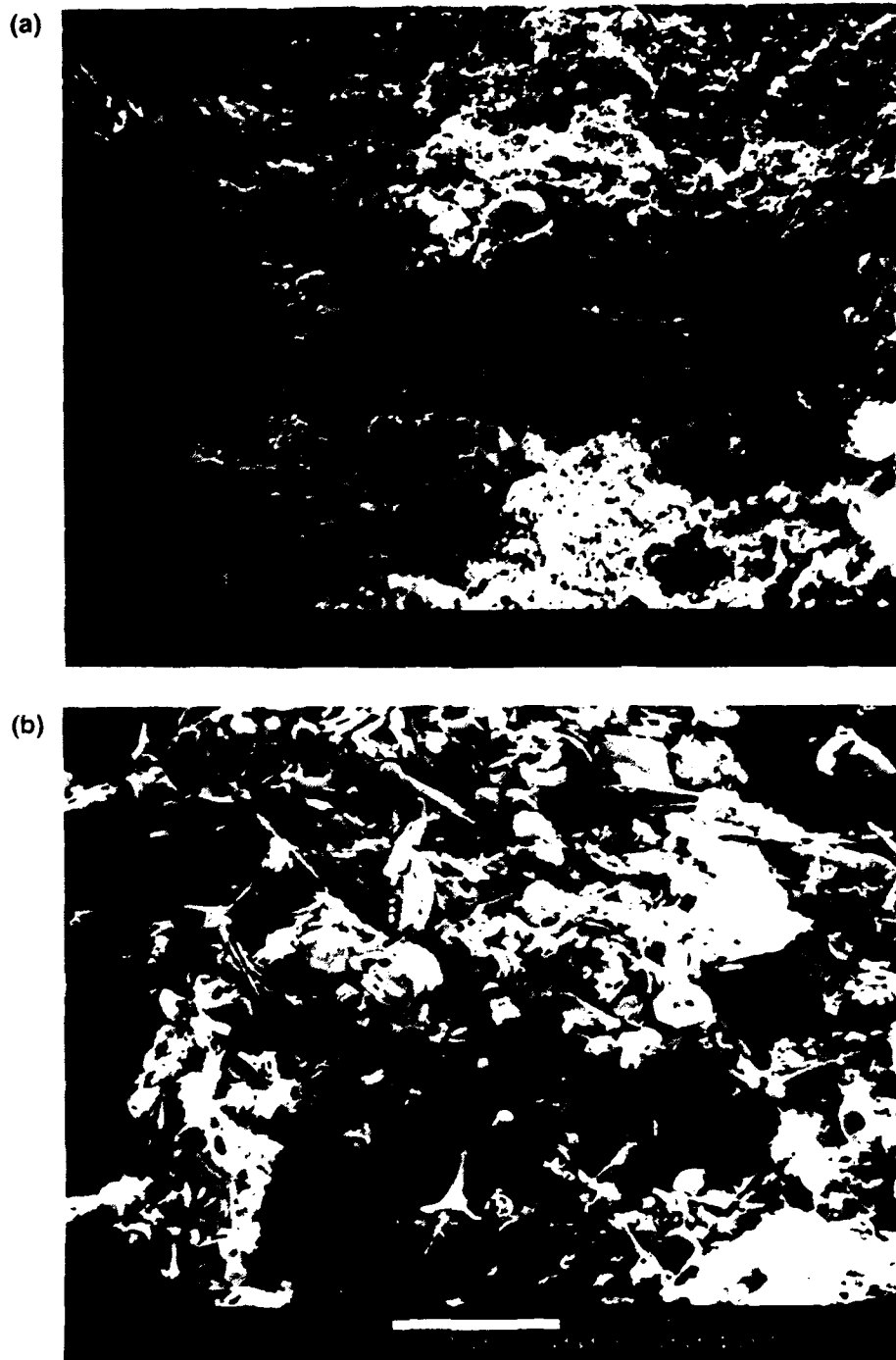
Figure 65. ES 4P-1 is a matrix-supported sediment. Photomicrographs are taken before consolidation testing. (a) Illustration of matrix-grain relationship showing only floating grains, mostly foraminifers. Magnification is 200X. (b) Matrix is composed predominantly of coccolith shields, fragments of shell, and spicules. Magnification is 2000X.

(a)

(b)
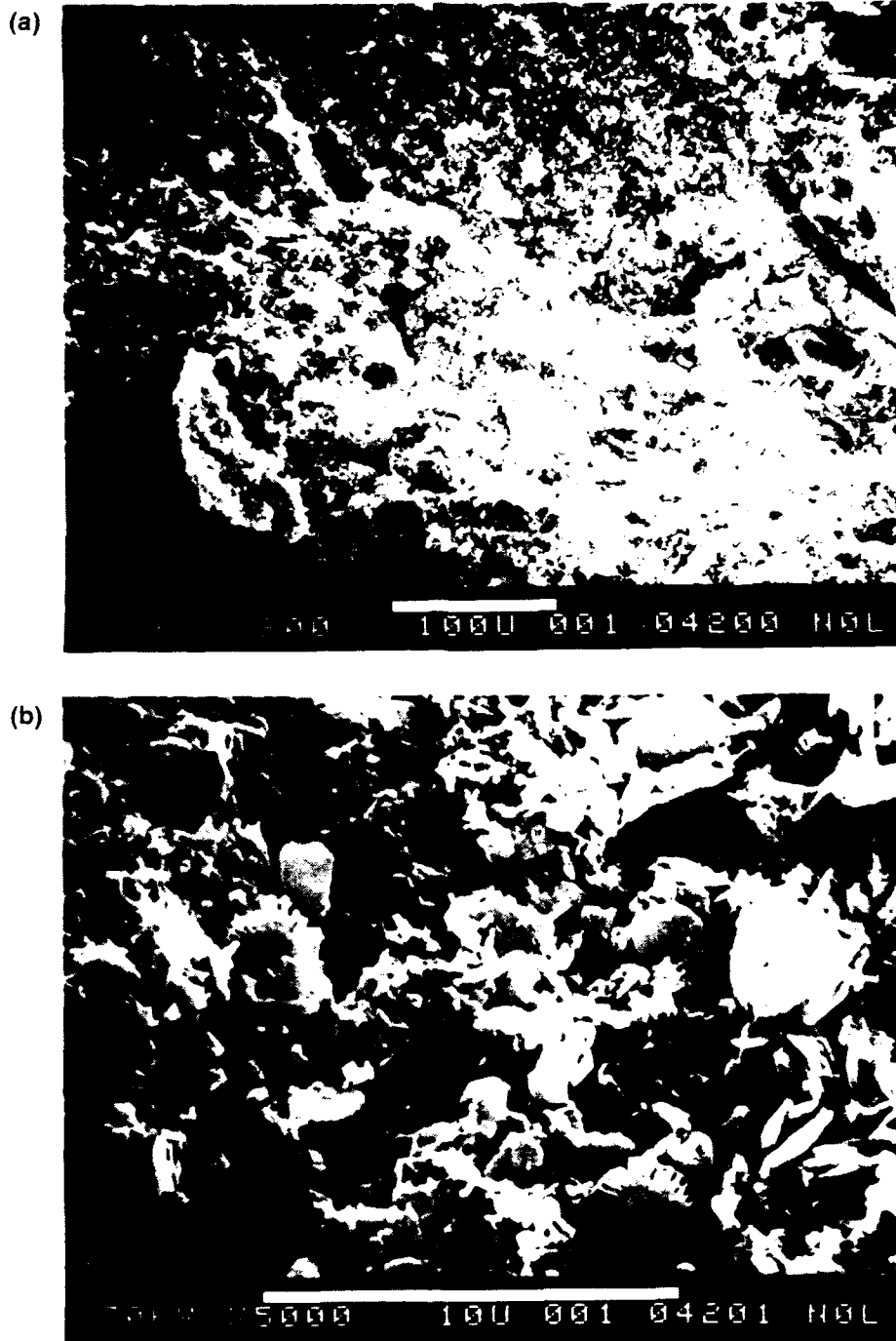
Figure 66. ES 4P-2 is a matrix-supported sediment. (a) Numerous embedded grains are predominantly foraminifers and shell fragments. Magnification is 200X. (b) Matrix particles are coccolith shields and shell fragments identified as calcite by Kevex microprobe. Magnification is 5000X.
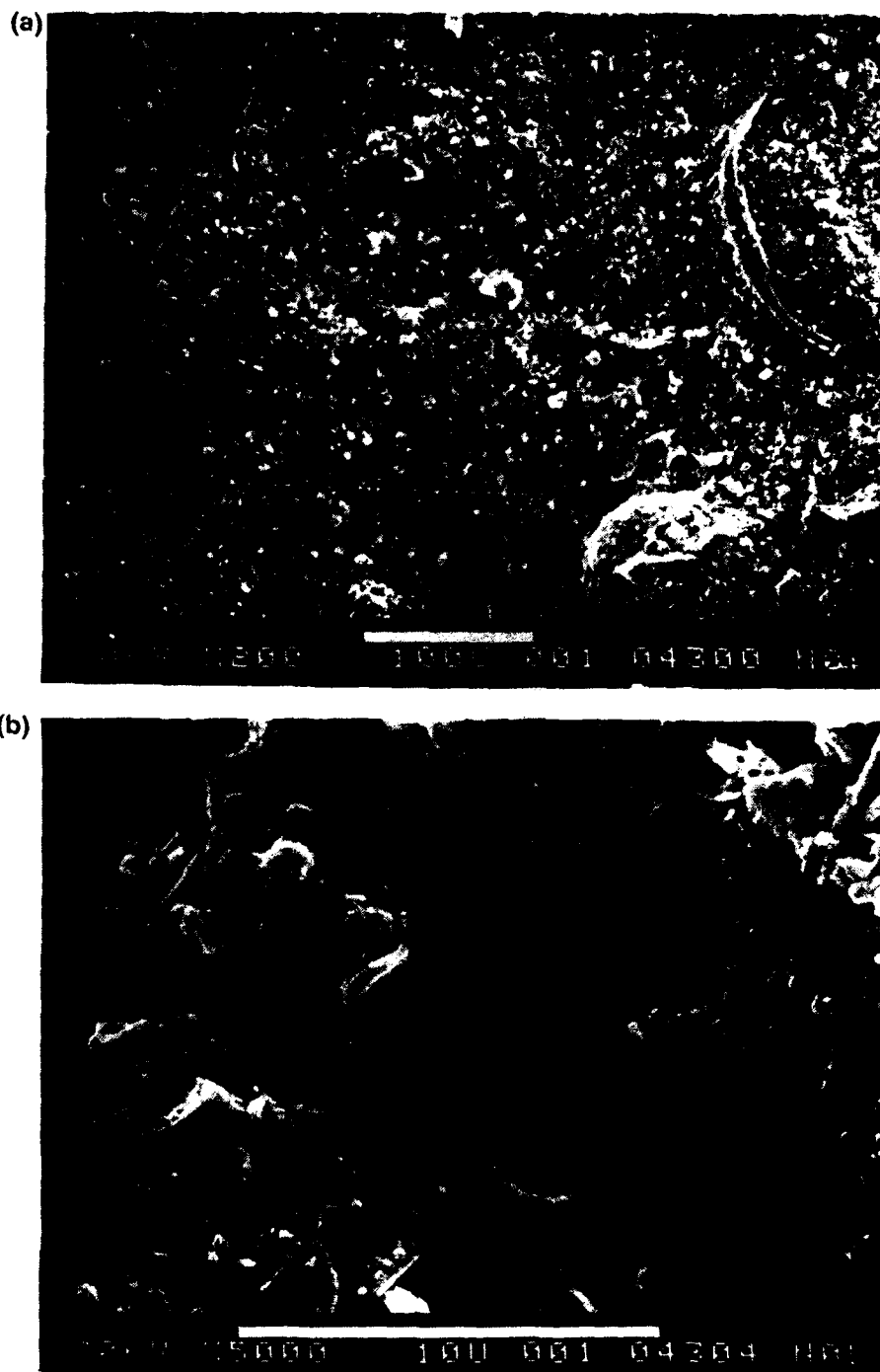
Figure 67. Photomicrograph ES 4P-3 illustrating the matrix-to-grain relationship. (a) Only floating grains are evident. Magnification is 200X. (b) Matrix has a high proportion of calcite shell fragments and coccoliths. Magnification is 5000X.
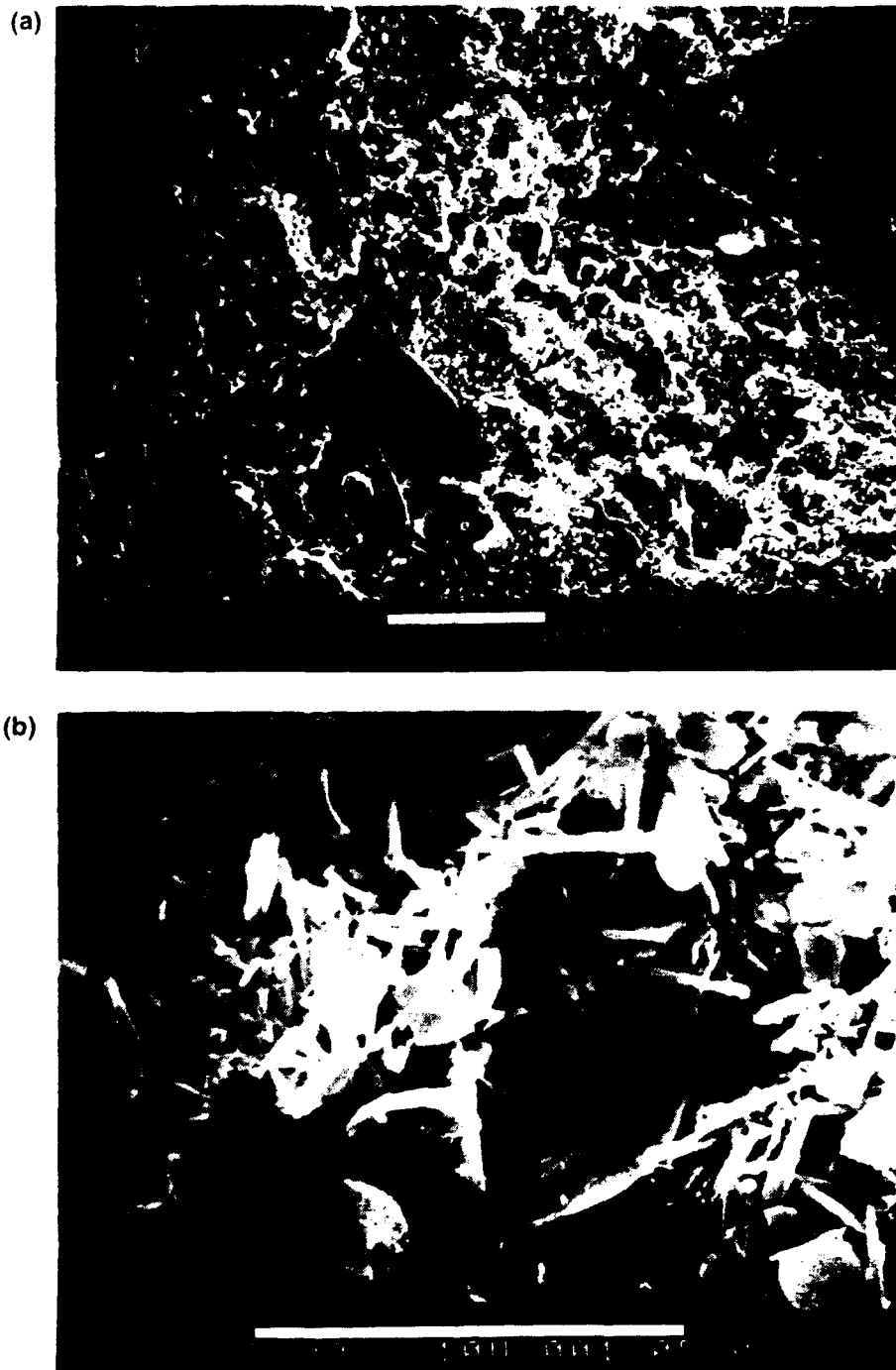
Figure 68. ES 5P-1(2) is probably matrix supported but has numerous small grains. (a) Grains are predominantly pteropod fragments. Photomicrograph was taken before consolidation. Magnification is 190X. (b) Matrix particles are coccoliths, rhabdoliths, shell fragments, and aragonite needles. Magnification is 5100X.
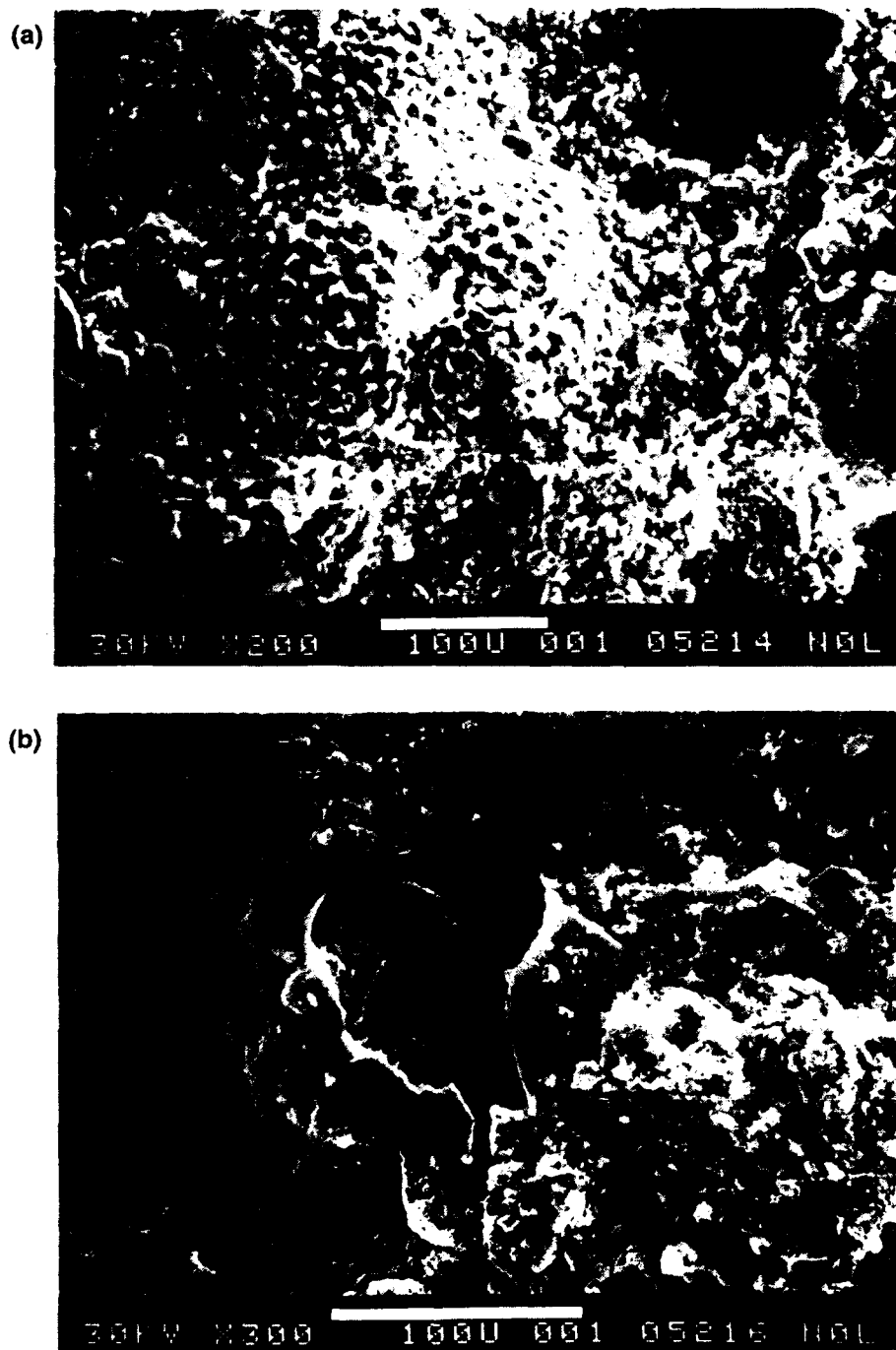
Figure 69. Photomicrograph of ES 5P-1(2) taken after consolidation. (a) After consolidation, grains such as the foraminifer are deeply embedded in the matrix and remain unbroken. Sediment is grain supported as a result of consolidation. Magnification is 200X. (b) Grains more fragile than foraminifers are often crushed as a result of consolidation under 4000 kPa of pressure. Magnification is 300X.
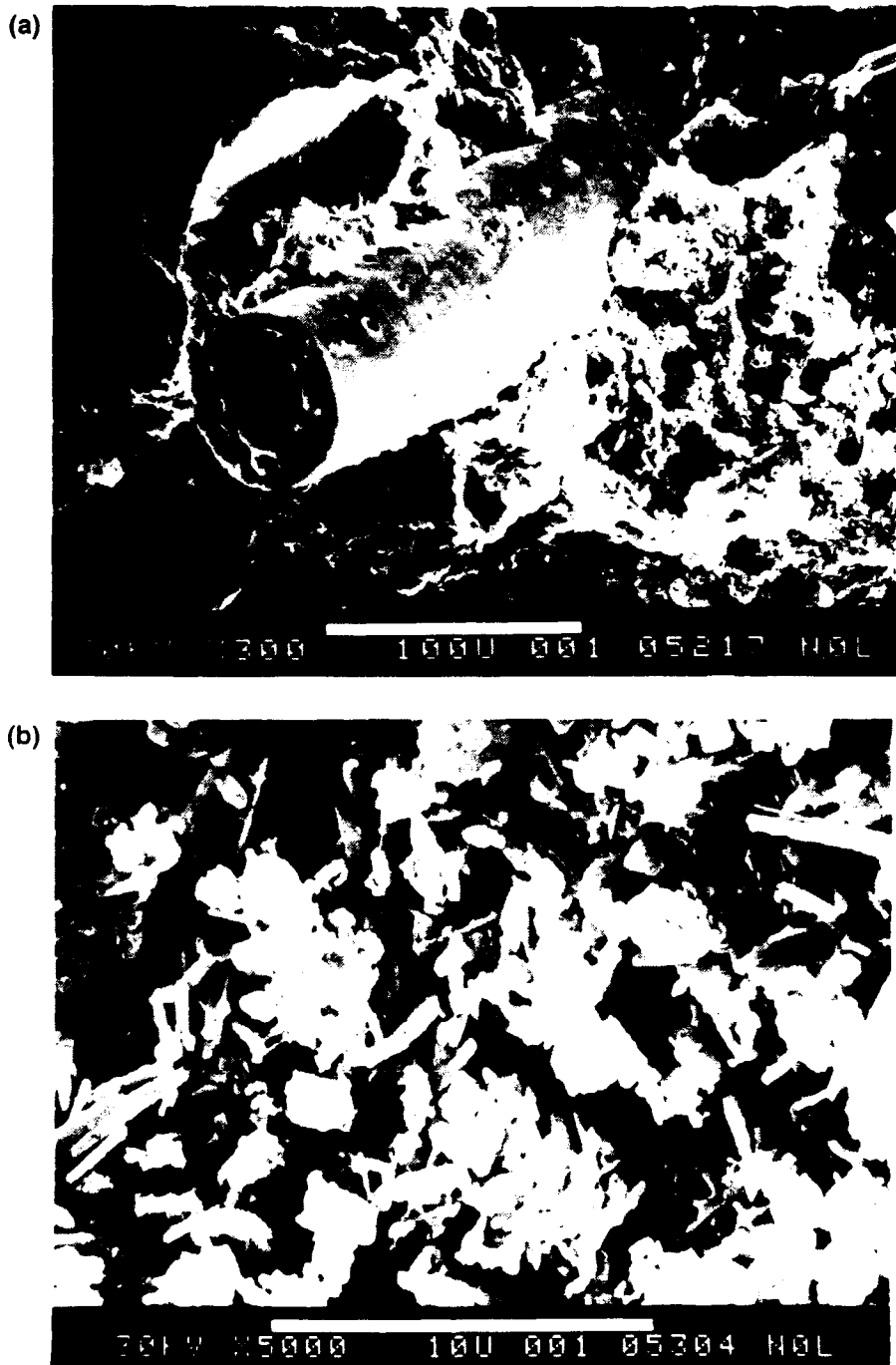
Figure 70. (a) ES 5P-1,2) after consolidation. Typical pteropod fragment (identified in many samples) illustrated here. Magnification is 300X. (b) ES 5P-3 is matrix supported. Overgrowths on coccolith shields and rounded nature of particles indicated diagenetic alteration. Magnification is 5000X.
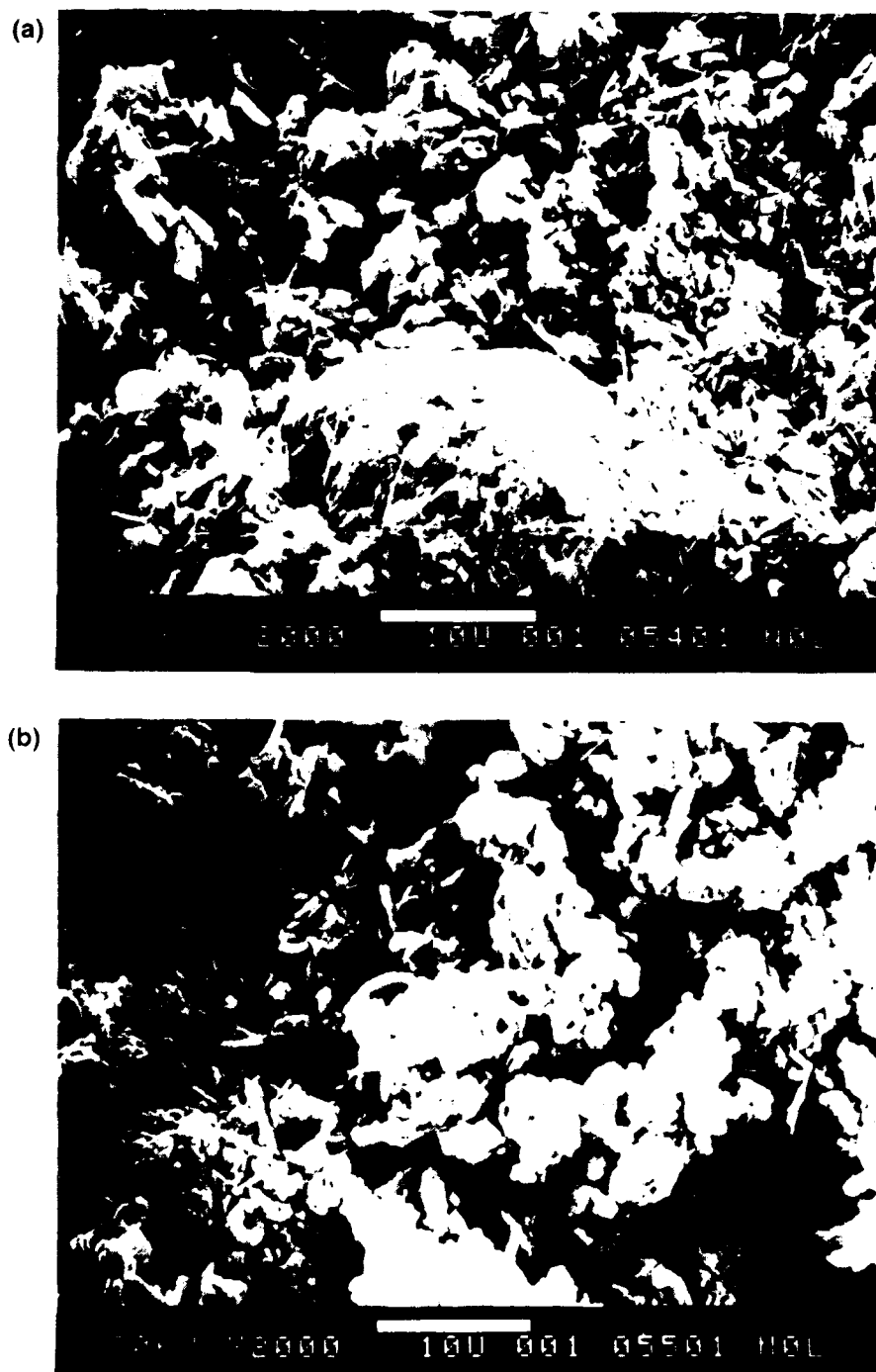
Figure 71. (a) ES 5P-4 is matrix supported. Only a few large grains are evident. Matrix is composed primarily of worn coccolith shields and particles, indicating diagenetic alteration has occurred before sampling. Magnification is 2000X. (b) ES 5P-5 is matrix supported. Coccolith shields are almost entirely overgrown, indicating considerable diagenetic alteration by 4.8 mbsf. Magnification is 2000X.
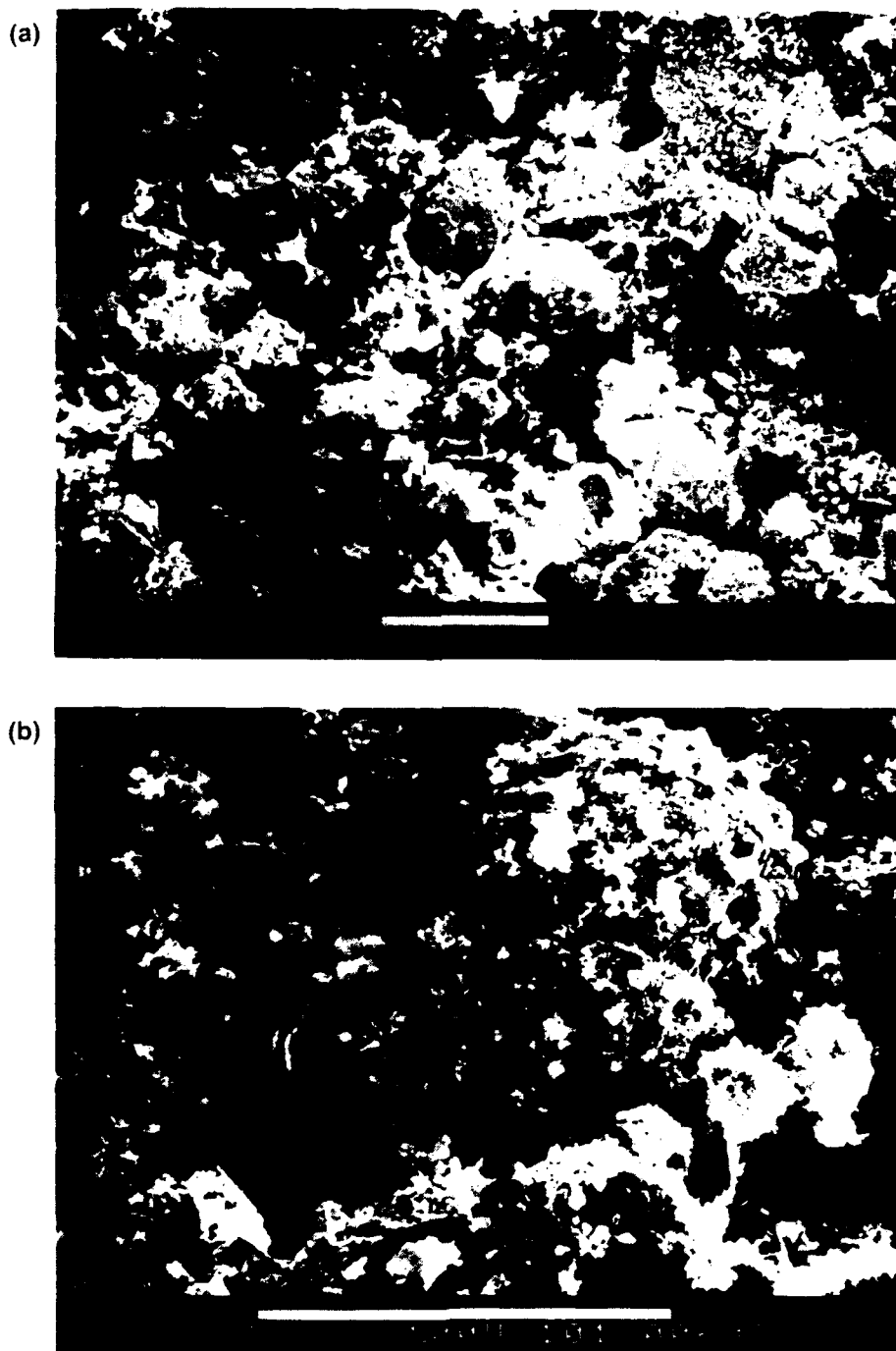
Figure 72. The top portion of ES 6P-1 is grain supported. (a) Many grains are difficult to identify but include pteropods and foraminifers. Matrix material is difficult to focus on because of the prevalence of large grains. Photomicrograph was taken before consolidation. Magnification is 200X. (b) Typical grains in ES 6P-1. Note the grain-to-grain contact between all grains. Image analysis could not be done because the analysis of pores would have been of the pores in the grains and not in the sample. Magnification is 500X.
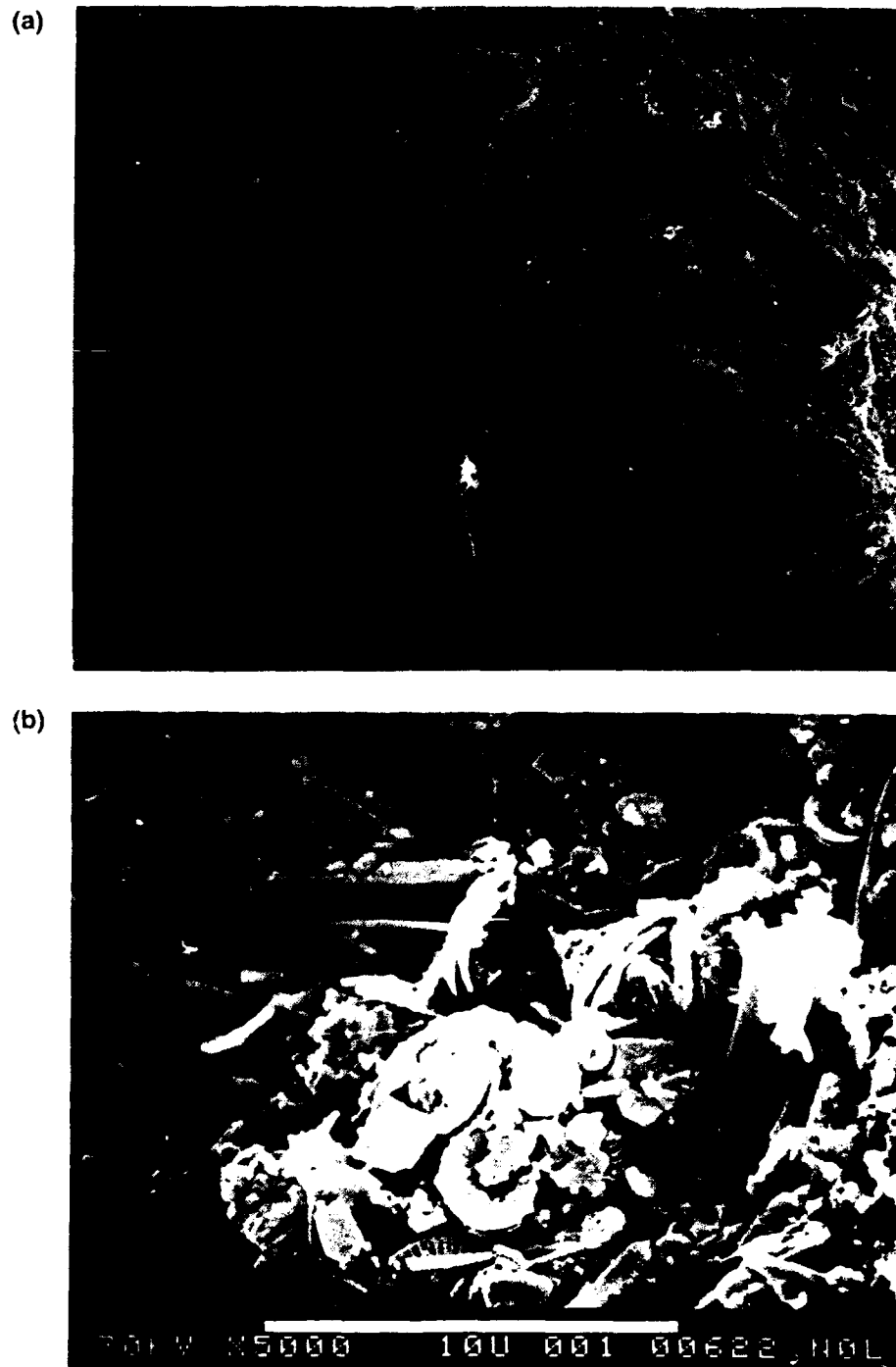
Figure 73. (a) The bottom portion of ES 6P-1 had numerous grains but was not grain supported. Grains are predominartly pteropods. Image analysis was done on this portion of ES 6P-1. Magnification is 21X. (b) Matrix of bottom portion of ES 6P-1 consists of broken fragments and coccolith shields. Magnification is 5000X.
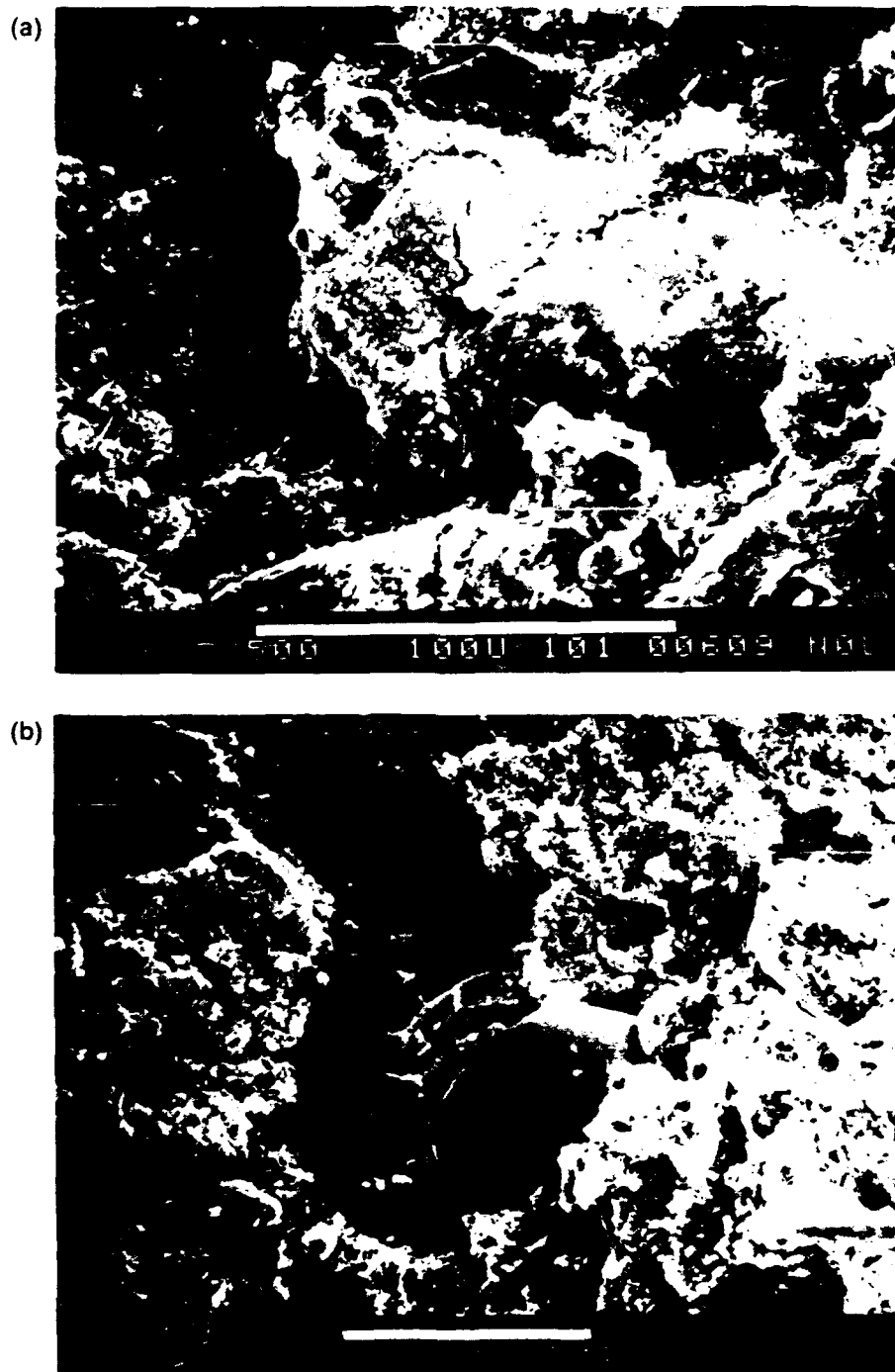
Figure 74. ES 6P-1 taken after consolidation. Grains have become densely packed into the matrix material. Sample appears to be grain supported as a result of consolidation. Magnification is 500X. (b) Grain crushing is common after consolidation to ~ 4000 kPa. Magnification is 300X.
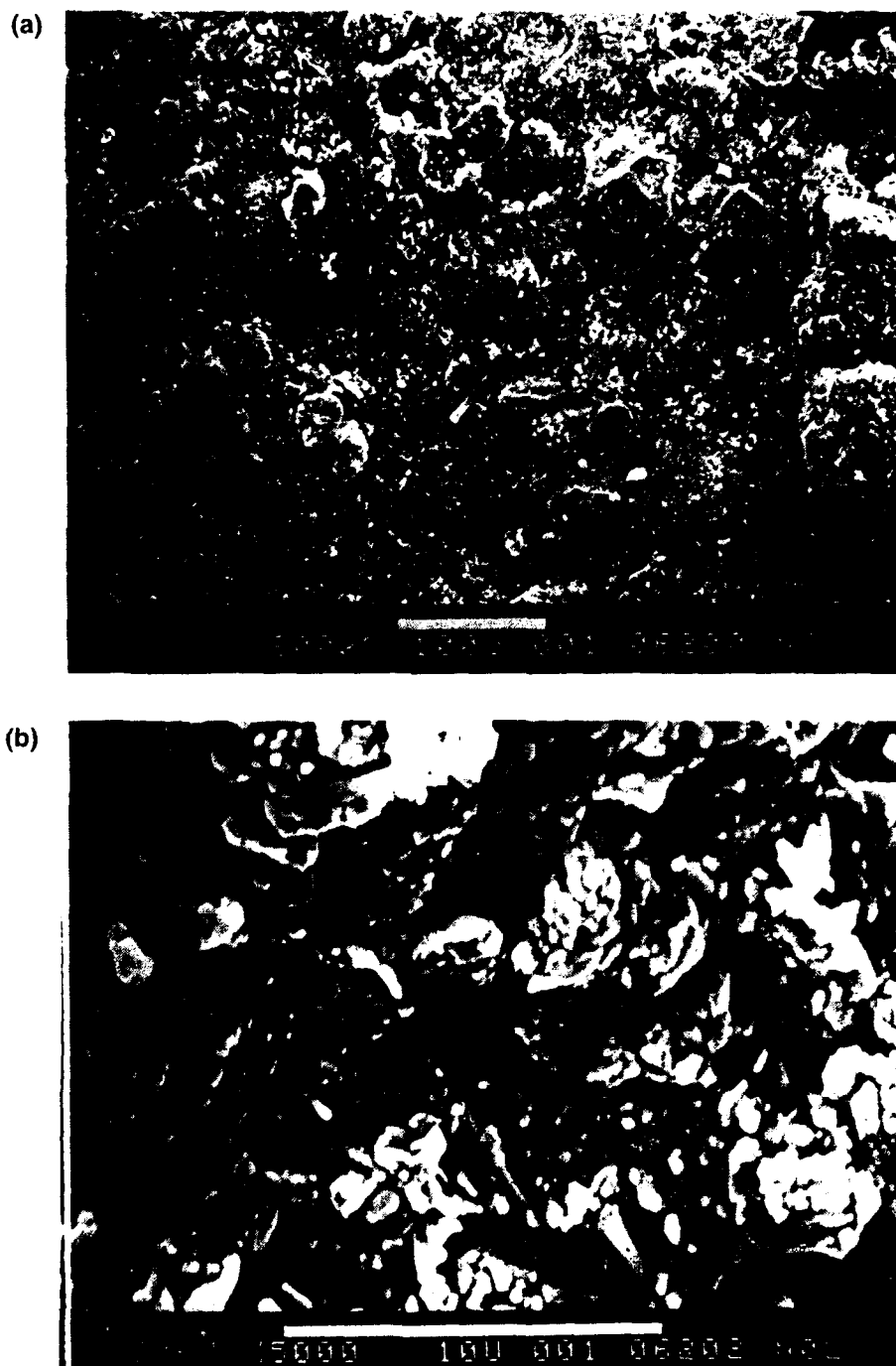
Figure 75. ES 6P-2 is matrix supported. (a) Grains are unidentifiable agglomerates. Magnification is 200X. (b) Matrix consists of very altered coccoliths and unidentifiable particles, typical of chalk. Magnification is 5000X.
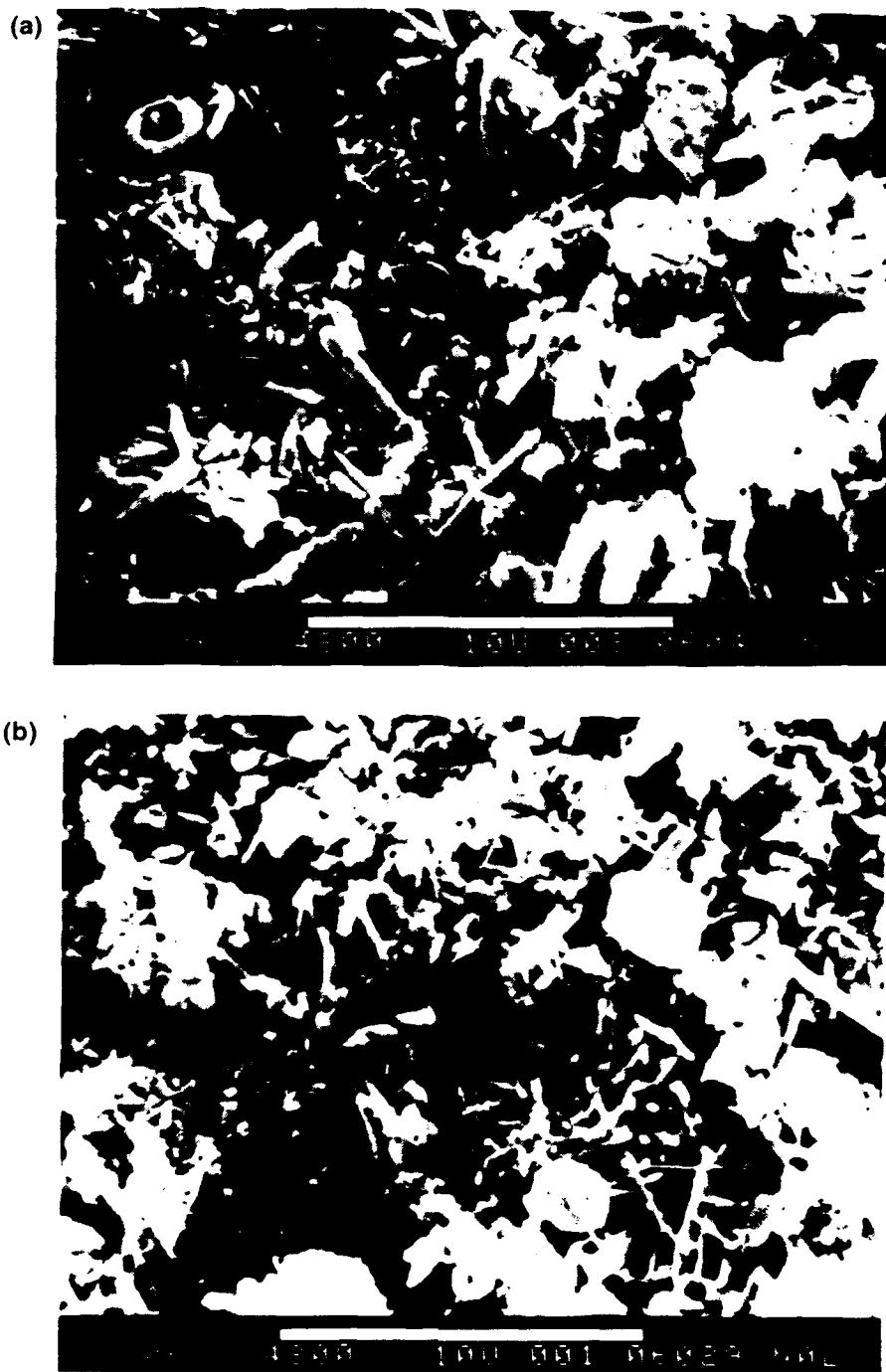
Figure 76. (a) ES 6P-3 before consolidation. Matrix consists primarily of coccoliths and fragments from larger shell fragments. Large particle is a calcareous dinoflagellate cyst. Magnification is 4800X. (b) Differences in fabric before and after consolidation were difficult to detect by visual examination of SEM micrographs. Magnification is 4800X.
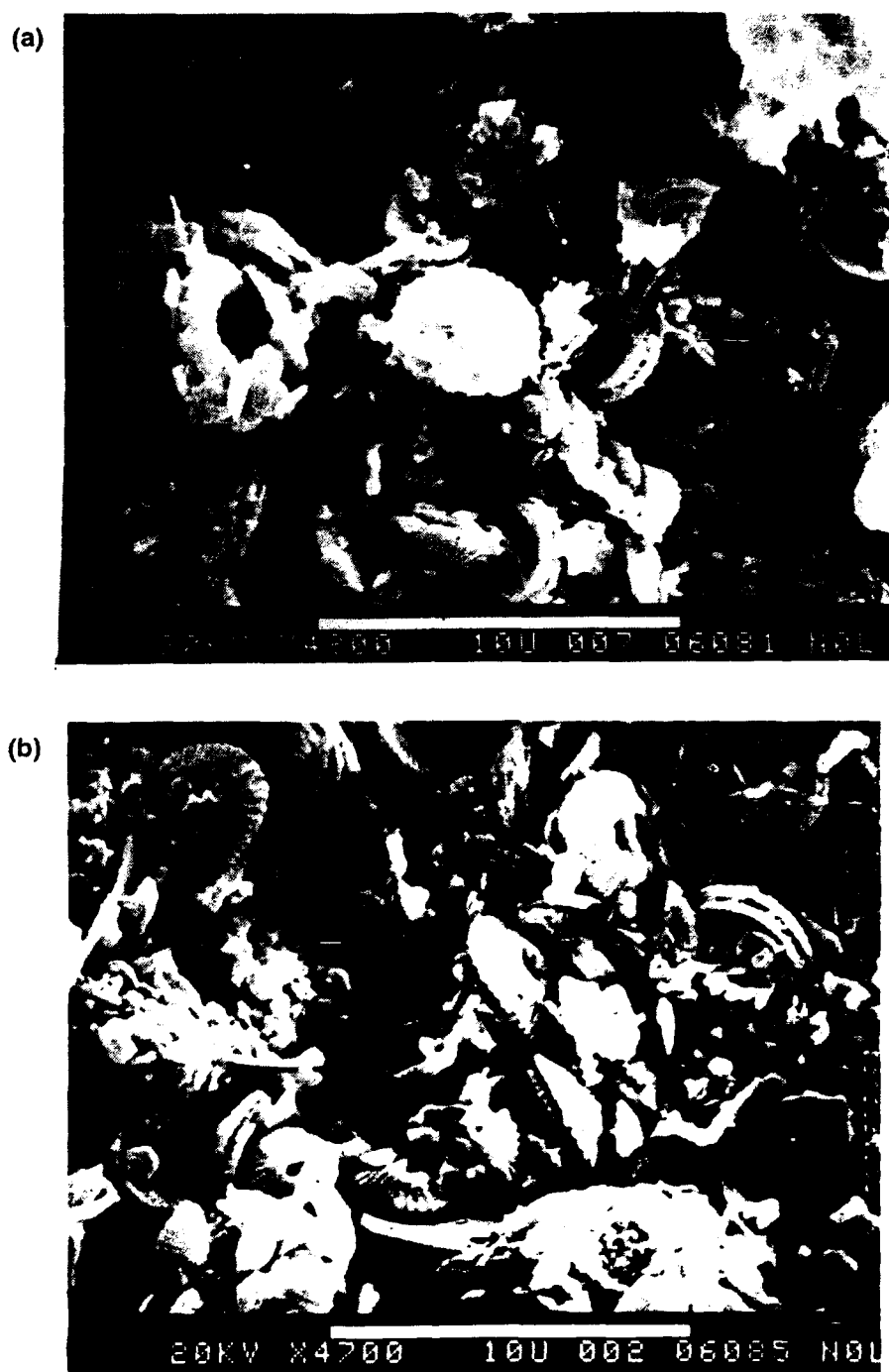
Figure 77. (a) ES 6P-4 before consolidation. Matrix consists predominantly of coccoliths. Rhabdoliths and shell fragments are also present. Grains were not evident in this sample. Magnification is 4800X. (b) ES 6P-4 after consolidation. No differences in fabric were detectable visually before and after consolidation. Magnification is 4700X.
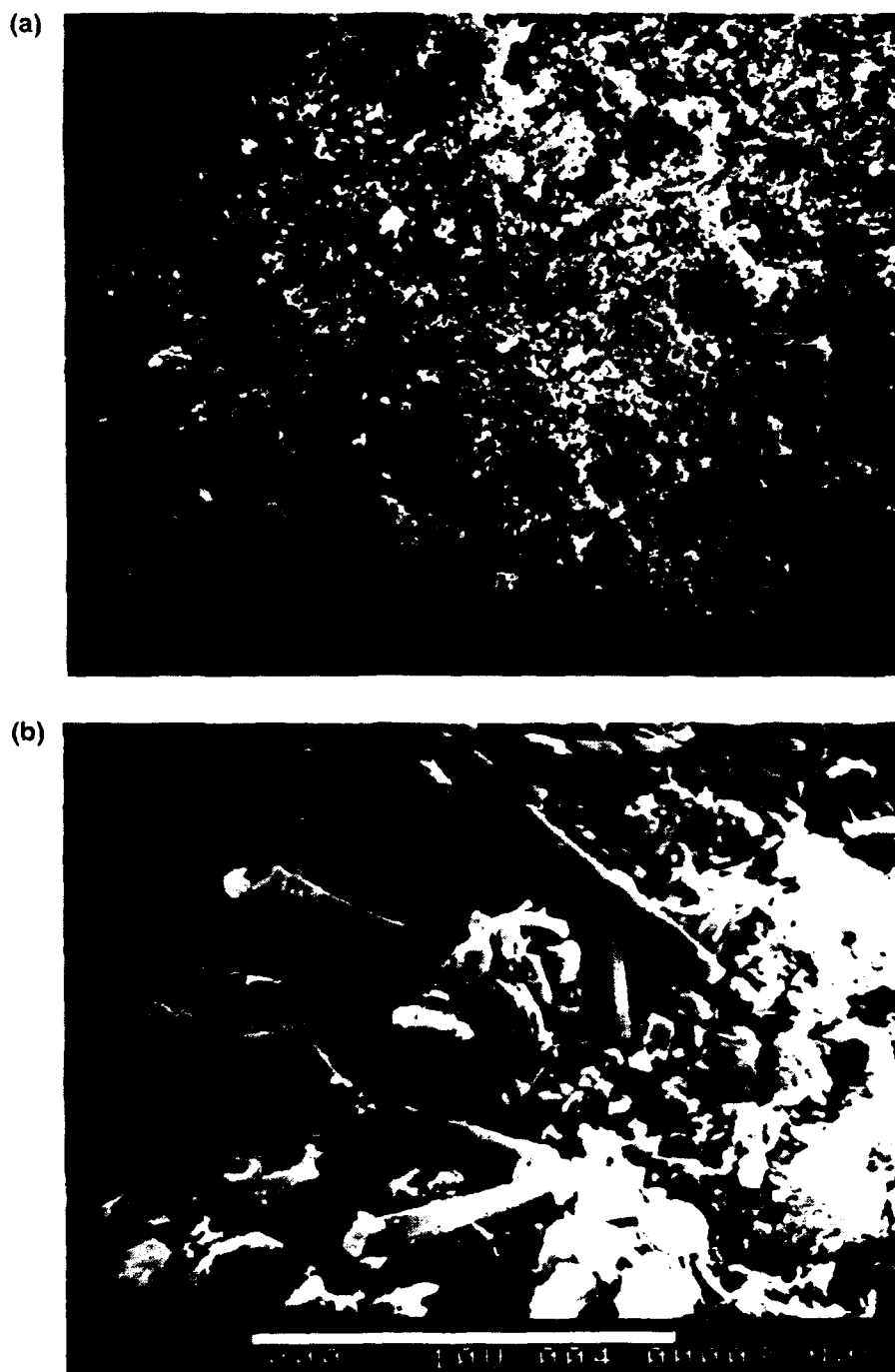
Figure 78. ES 7P-1 is matrix supported. (a) Few grains are present. Magnification is 200X. (b) Matrix contains numerous shell fragments, long spicules and coccolith shields. Some alteration is present. Magnification is 5000X.

(a)

(b)
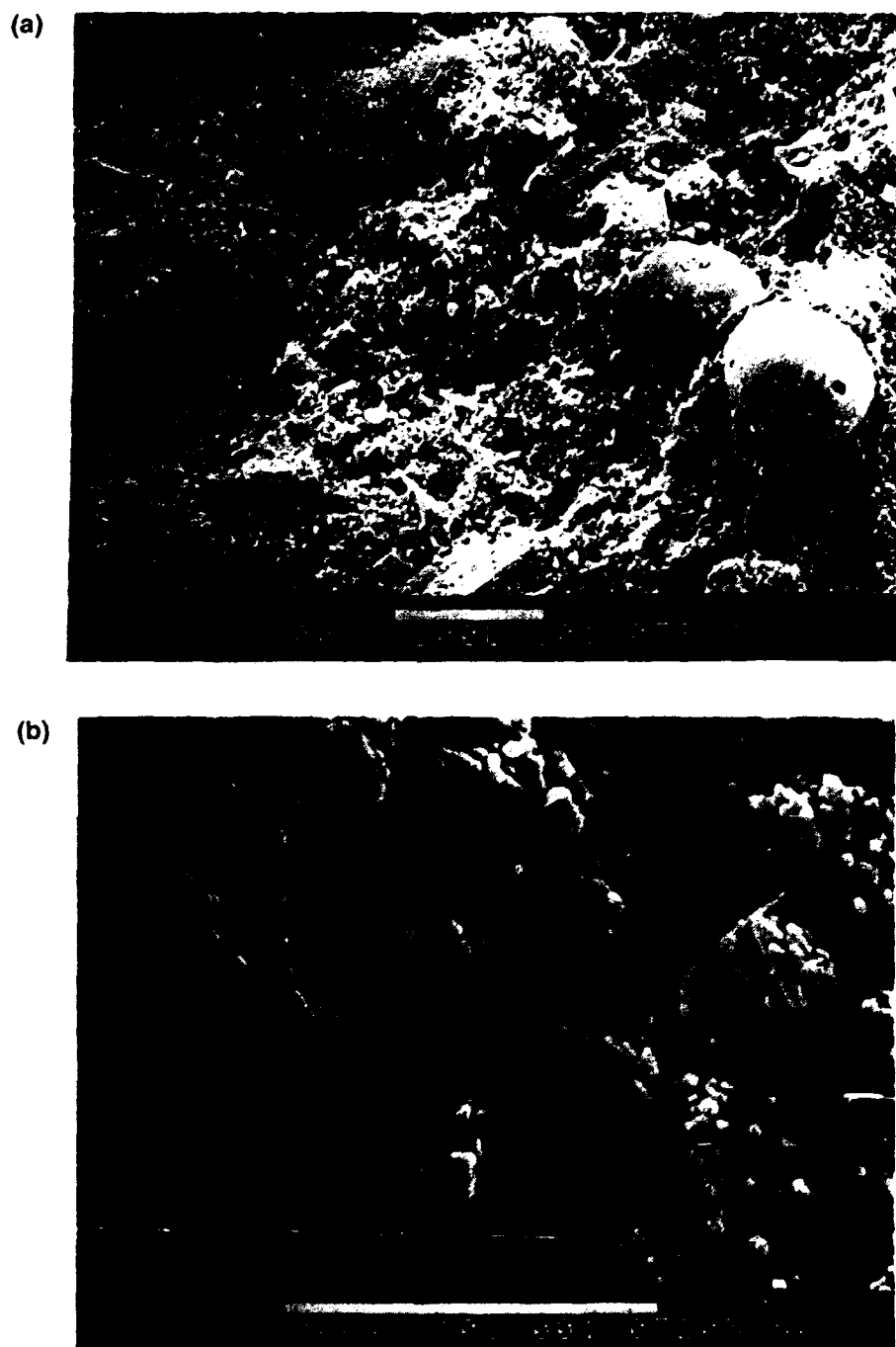
Figure 79. (a) ES 7P-2 is matrix supported with floating grains. predominantly foraminifers. Magnification is 200X. (b) Matrix particles are significantly altered by diagenetic processes. Note overgrowths on coccolith shields typical of chalk. Magnification is 5000X.
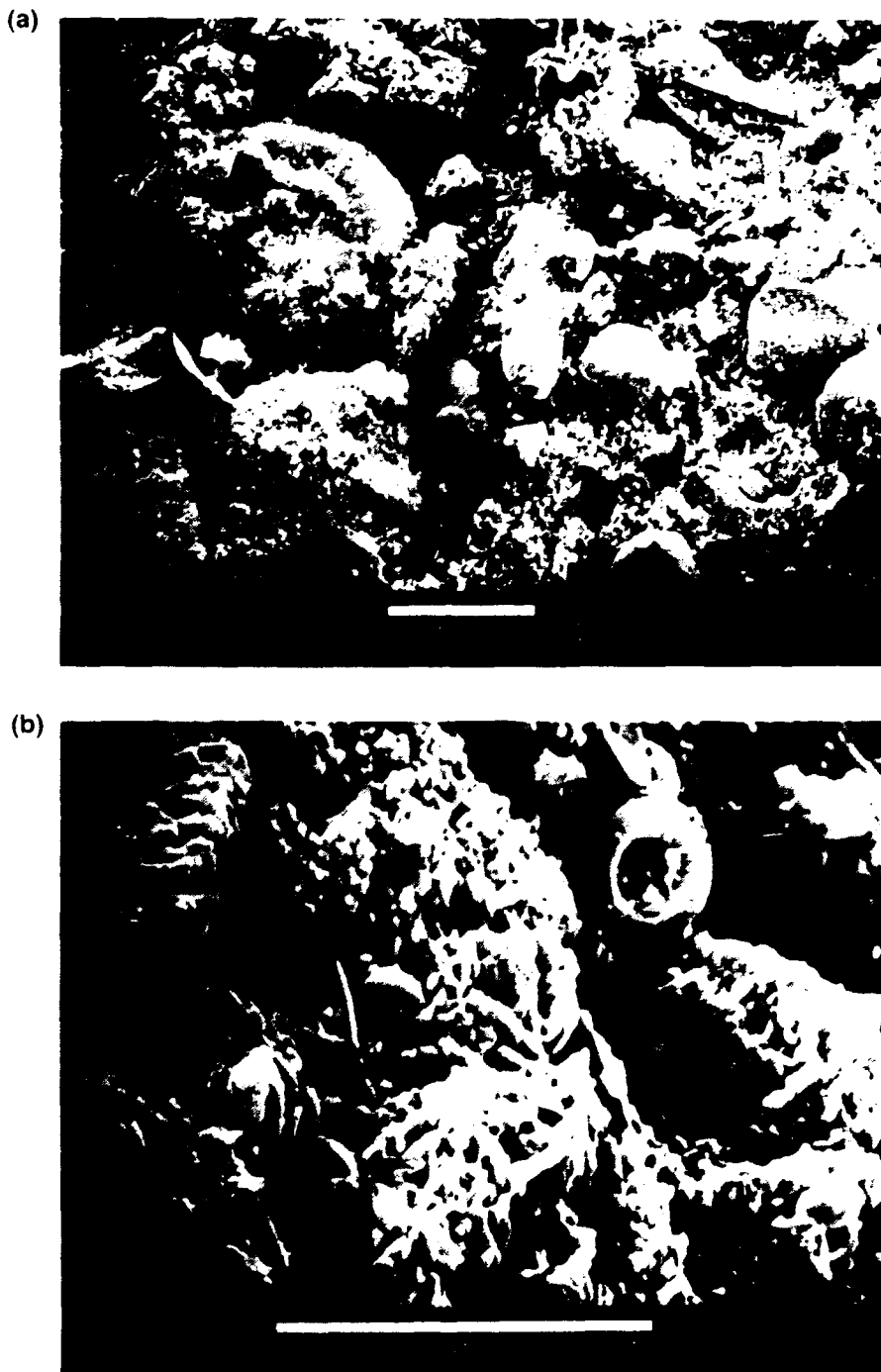
Figure 80. ES 7P-5 is grain supported. (a) Grains are rounded and often unidentifiable. Note contacts between grains. Magnification is 200X. (b) Matrix consists of coccoliths and aragonite needles that are probably part of shell fragments. Note the rounded nature of the particles, indicating the diagenetic alteration that has occurred. Magnification is 5000X.
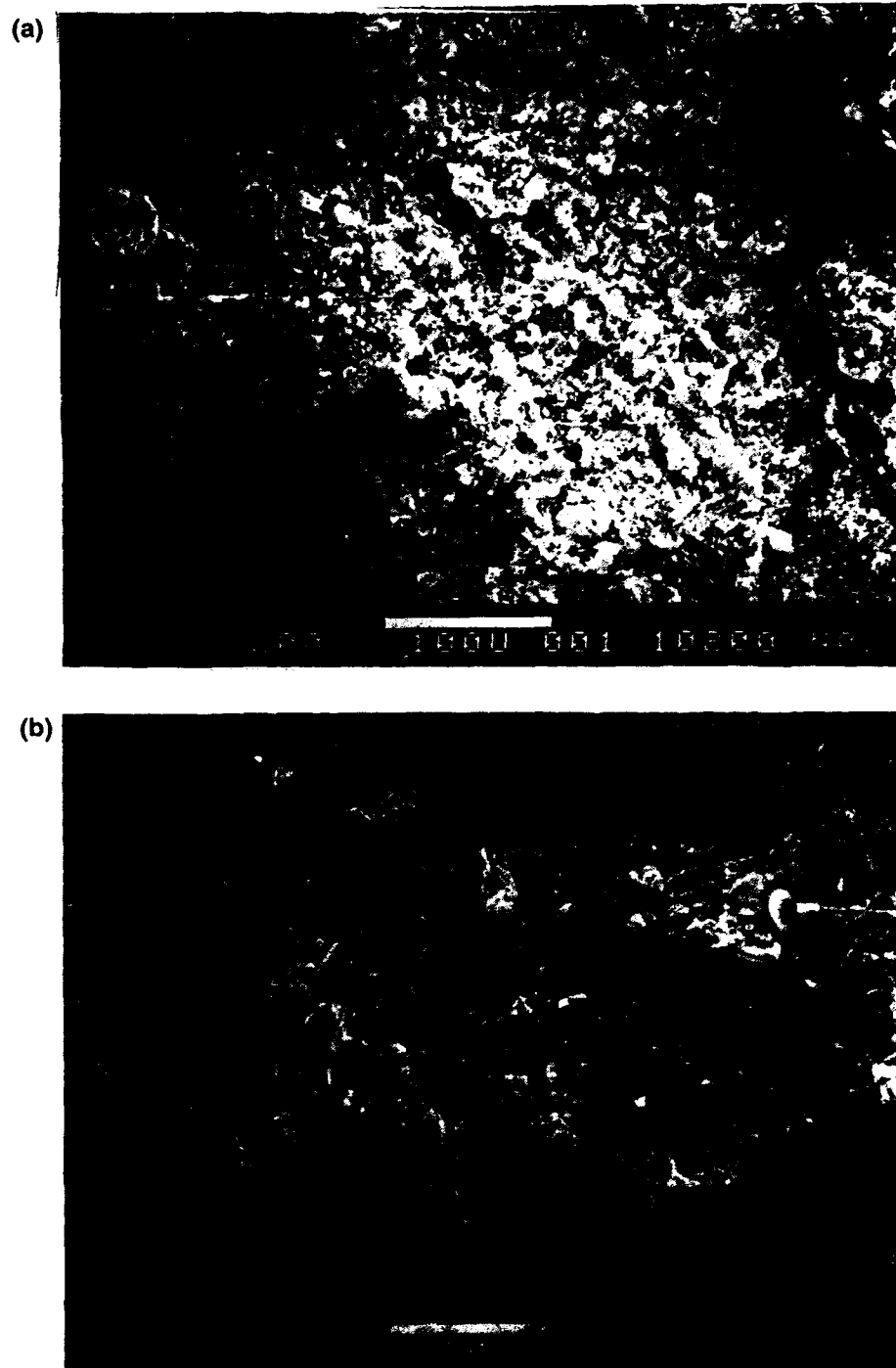
Figure 81. (a) ES 10P-2 is matrix supported. Few grains could be found during SEM analysis. Magnification is 200X. (b) Matrix consists of coccolith shields and unidentifiable particles Magnification is 2000X.
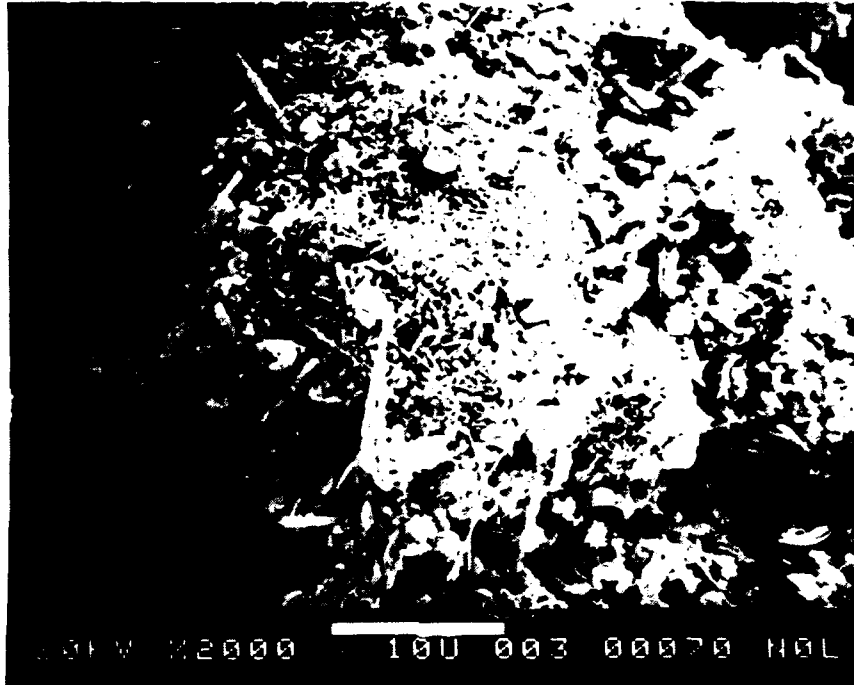
Figure 82. ES 10P-3. Aragonite needles are part of a large shell fragment and do not form the matrix material until they become disaggregated. Magnification is 2000X.
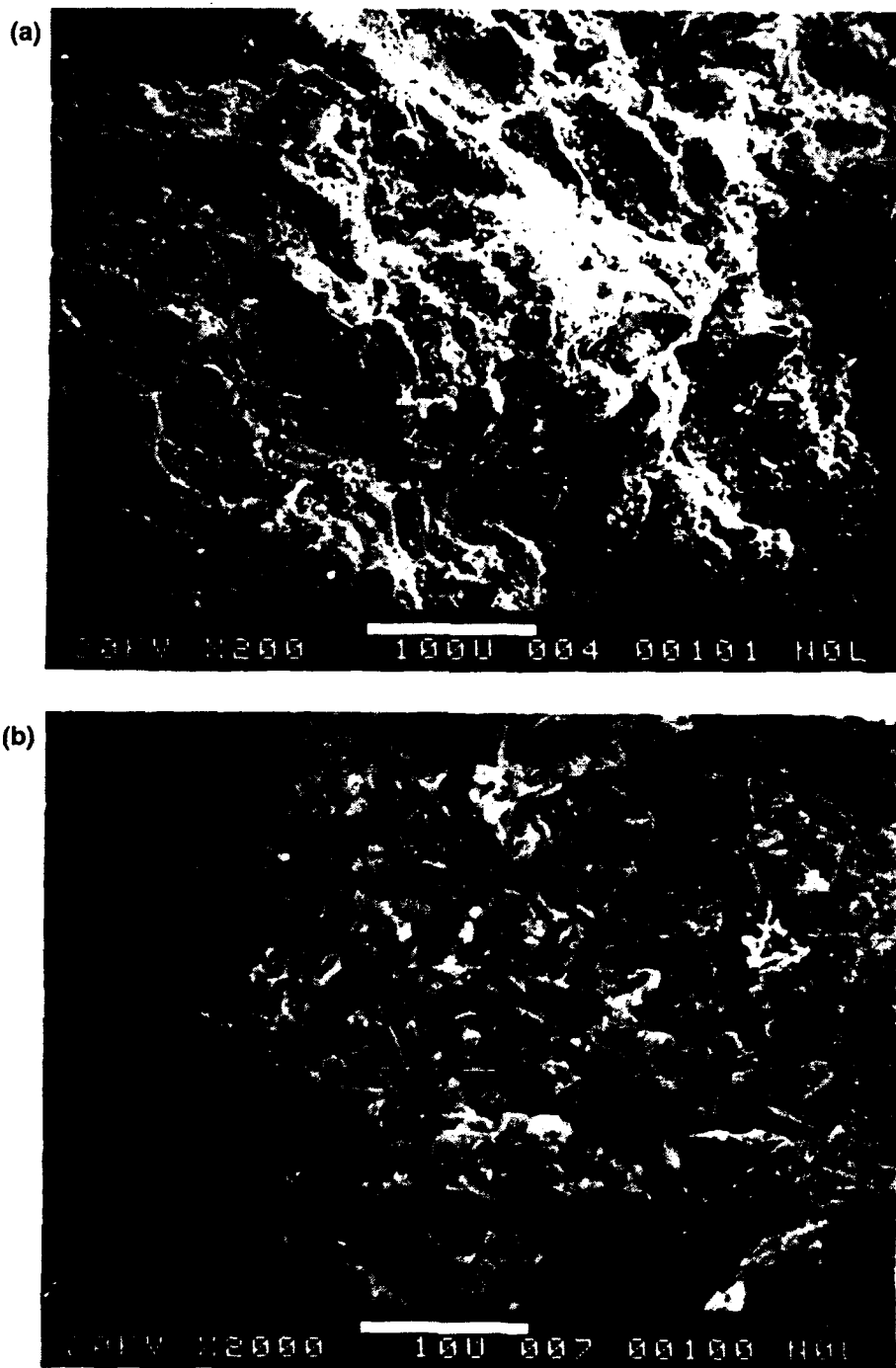
Figure 83. (a) LBB 10P-1 is grain supported; grains are mostly foraminifers and pteropods. Magnification is 200X. (b) Matrix is a coccolith ooze. Magnification is 2000X.

(a)

(b)
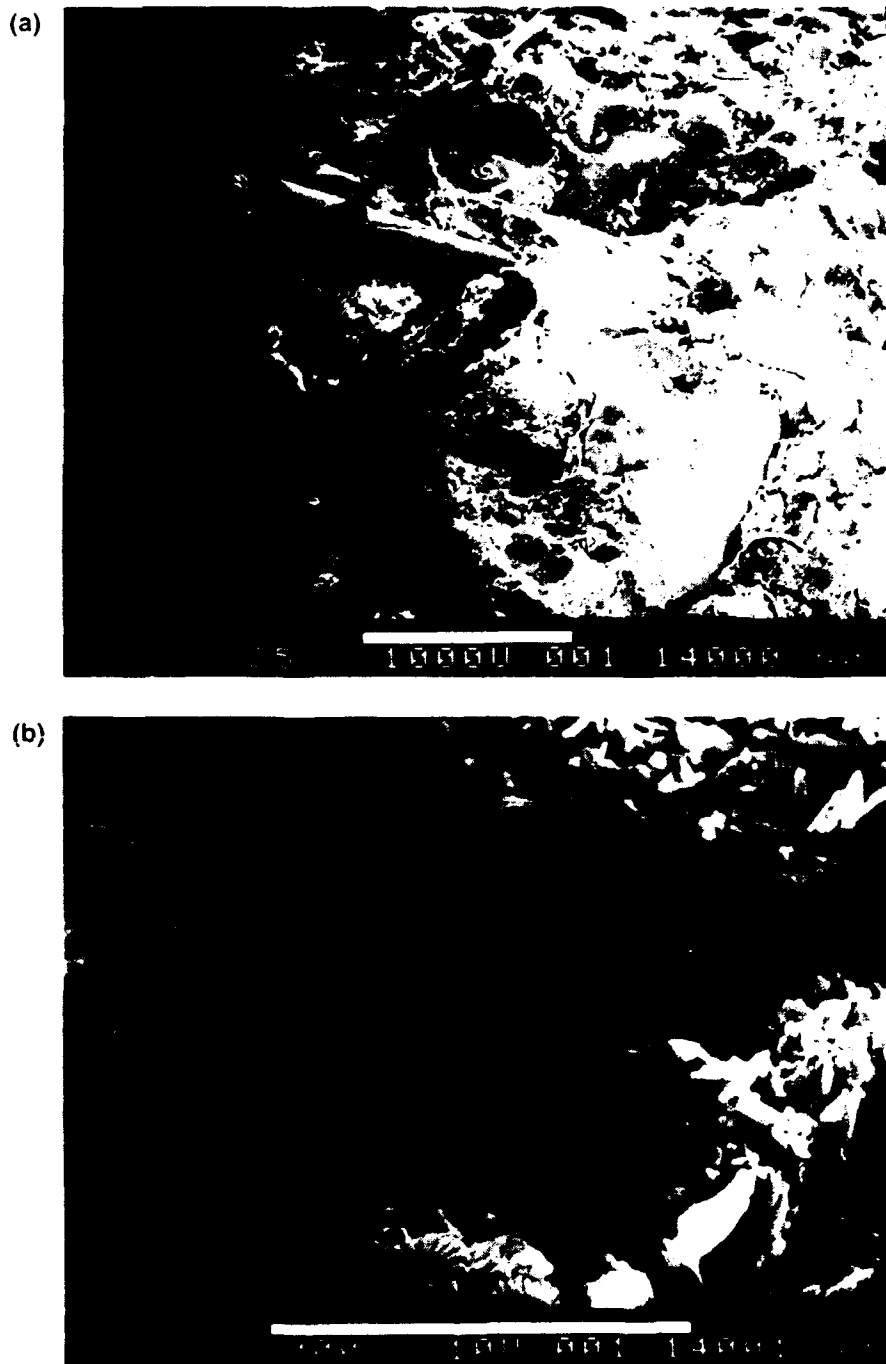
Figure 84. LBB 14P-1 is a pteropod ooze. (a) Grains are probably in contact, making this a grain-supported sediment. Magnification is 25X. (b) Matrix consists of aragonite needles and coccolith shields. Magnification is 5000X.
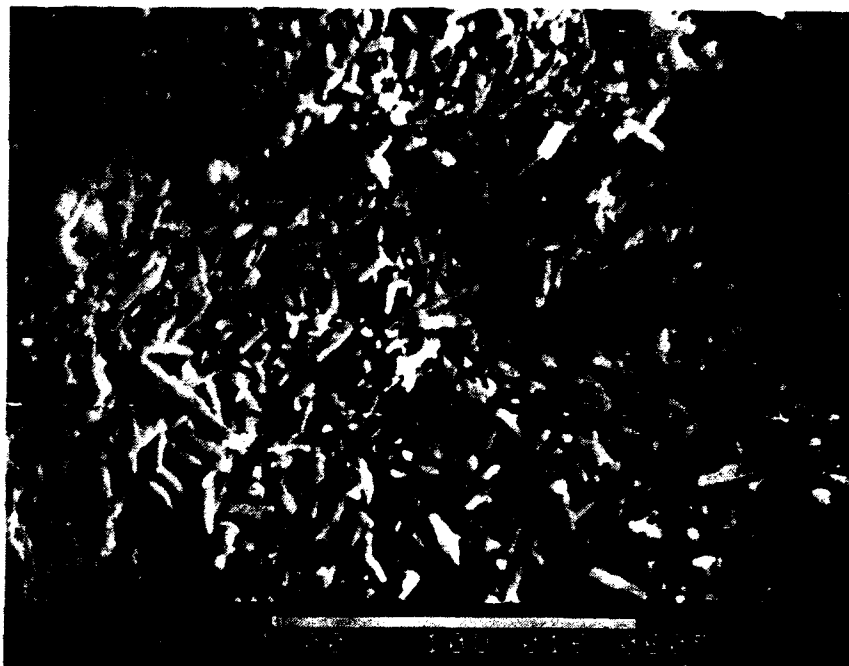
Figure 85. LBB 15H-1 is matrix supported. Matrix is entirely composed of aragonite needles that were probably disaggregated from large shell fragments composed of aragonite needles such as the one near the bottom of the photomicrograph. Magnification is 4800X.

(a)

(b)
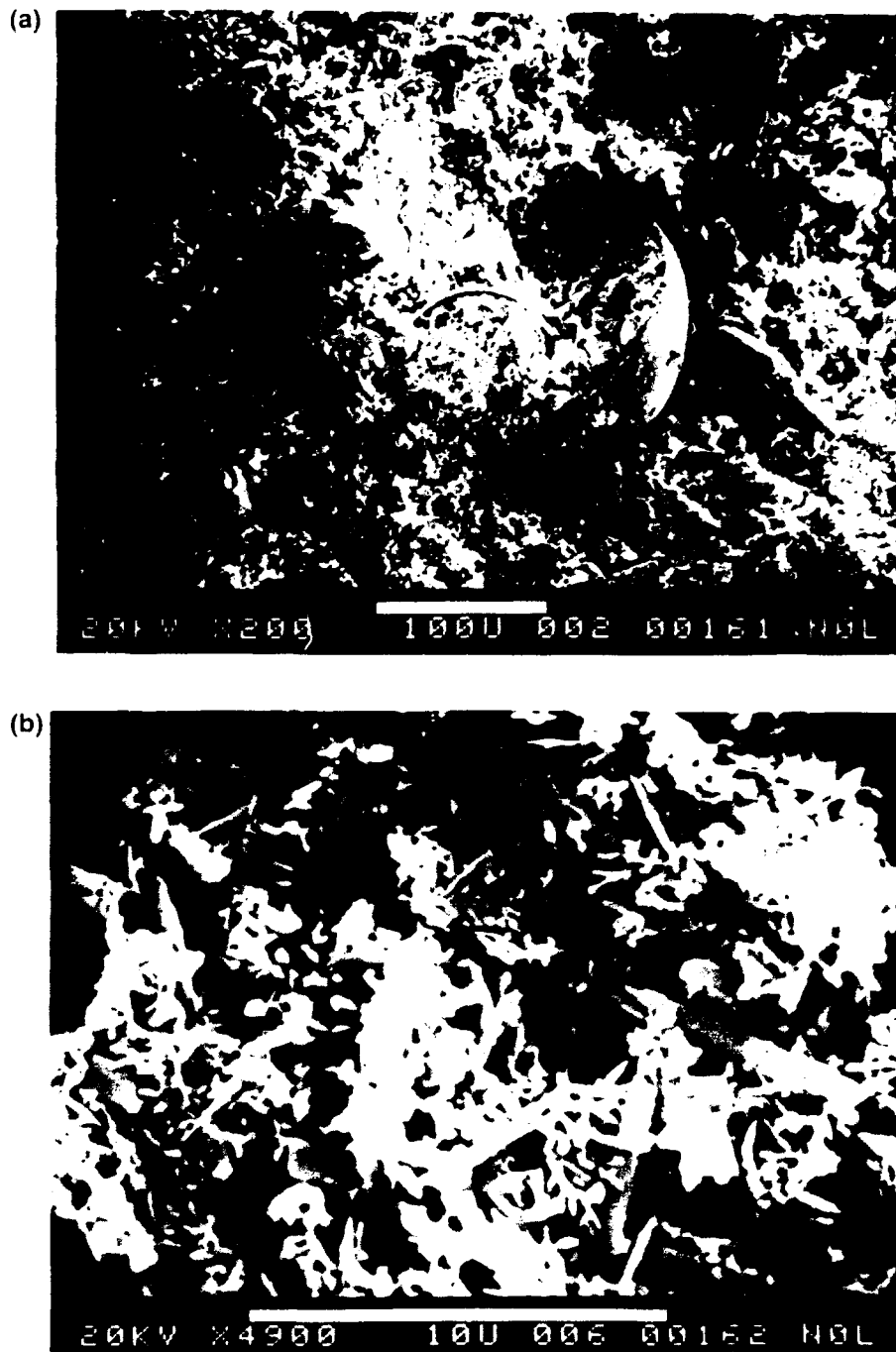
Figure 86. LBB 16P-1 is grain supported. (a) Many large grains appear to be in contact. Most of the grains are various size foraminifers. Magnification is 200X. (b) Matrix is composed of both aragonite needles and coccolith shields in approximately equal proportions. Magnification is 4900X.
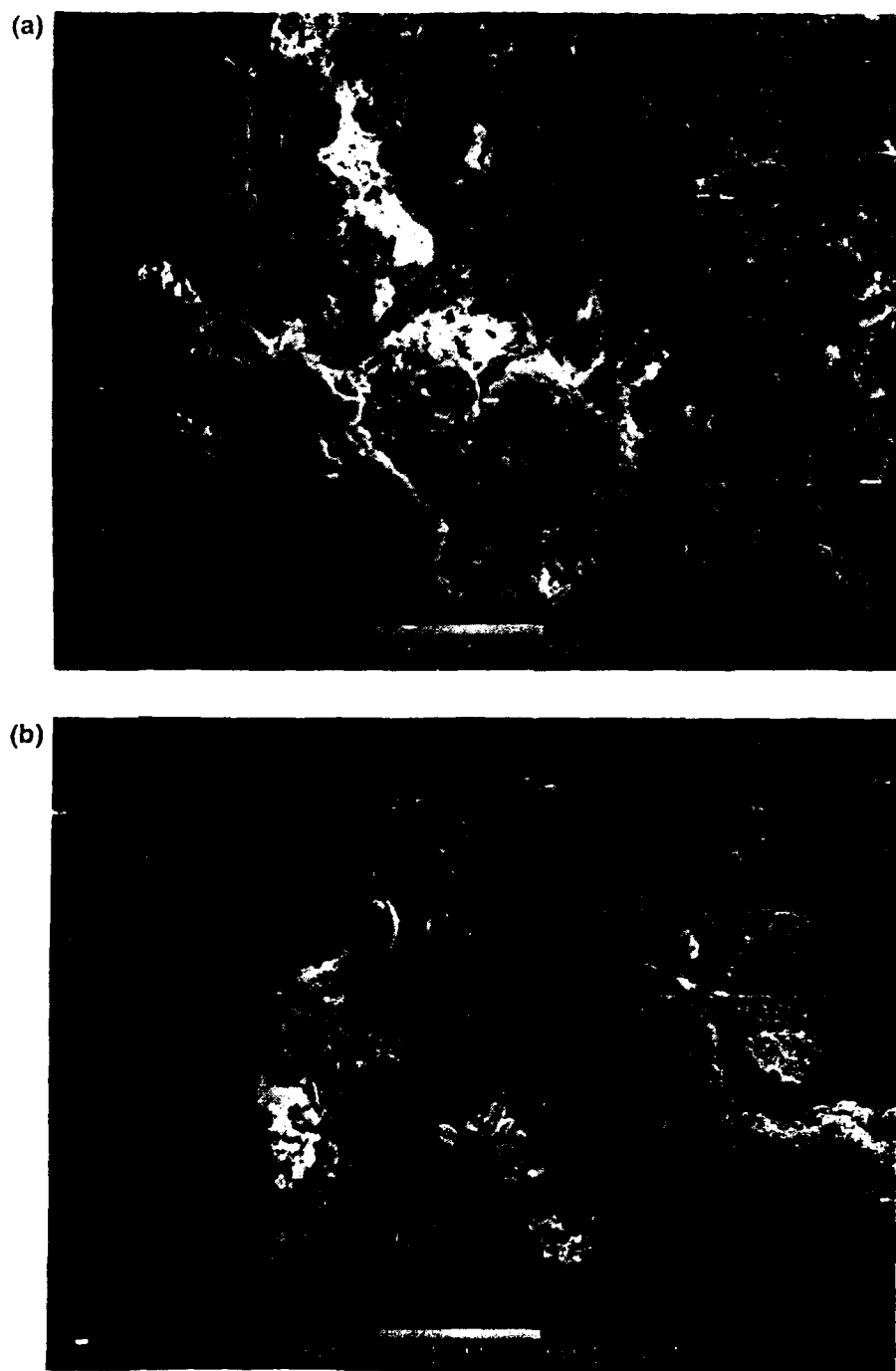
Figure 87. LBB 16P-2 is grain supported. (a) Foraminifers comprise the bulk of the grains. Magnification is 200X. (b) Matrix is composed of coccoliths and unidentifiable particles. Magnification is 2000X.

VITA

Dawn L. Lavoie
Research Marine Geologist, Code 361
Naval Ocean Research and Development Activity
Stennis Space Center, MS 39529
(601) 688-4659

EDUCATION

University of New Orleans New Orleans, LA.	1982	M.S. Geology. Thesis title: "Sediments on the Southeastern Flank of the Bermuda Pedestal"
University of Rhode Island Kingston, R.I.	1973	M.A. Counseling and Student Personnel
University of New Hampshire, Durham, N.H.	1970	B.A. Sociology, minor in Psychology

TECHNICAL SPECIALITIES

Marine Geotechnique. Engineering properties of sediments including consolidation and triaxial shear testing.

Geoacoustic modeling, including development of regional geological/geophysical/ geotechnical syntheses, field sampling and data analysis.

EXPERIENCE

1982-1989 NORDA, Marine Geologist, Geophysics Branch (1982-1984), Marine Geotechnical Branch (1984-1989), National Space Technology Laboratory (NSTL), MS 39529

1979-1982 Computer Sciences Corporation, Assoc. Chemist, NSTL, MS 39529

1976-1977 Division of Vocational Rehabilitation, Rehab. Counselor, Providence, R.I.

1973-1976 Mount Saint Joseph College, Dean of Students, Wakefield, R.I.

HONORS

Phi Beta Kappa   (academic honor)
Sigma Xi   (research honor)
Alpha Kappa Delta   (sociology honor)
Sigma Gamma Epsilon   (psychology honor)

Outstanding Performance Award, NORDA, 1984
Superior Achievement Award, NORDA, 1985
Outstanding Performance Quality Step Increase, 1988

HOME   98177 Golf Club Drive, Bay St. Louis, MS 39520. (601) 255-7742.

Distribution List

Applied Physics Laboratory
Johns Hopkins University
John Hopkins Road
Laurel MD 20707

Applied Physics Laboratory
University of Washington
1013 NE 40th St.
Seattle WA 98105

Applied Research Laboratory
Pennsylvania State University
P.O. Box 30
State College PA 16801

Applied Research Laboratory
University of Texas at Austin
P.O. Box 8029
Austin TX 78713-8029

Assistant Secretary of the Navy
Research, Engineering & Systems
Washington DC 20350-2000

Chief of Naval Operations
Washington DC 20350-2000
Attn: OP-71
        OP-987

Chief of Naval Operations
Oceanographer of the Navy
Washington DC 20392-1800
Attn: OP-096
        OP-96B

David W. Taylor Naval Research Center
Bethesda MD 20084-5000
Attn: Commander

Defense Mapping Agency
Systems Center
12100 Sunset Hill Rd #200
Reston VA 22090-3207
Attn: Director
        Code SGWN

Director of Navy Laboratories
Crystal Plaza #5, Rm. 1062
Washington DC 20360

Fleet Antisub Warfare Tng Ctr-Atl
Naval Station
Norfolk VA 23511-6495

Fleet Numerical Oceanography Center
Monterey CA 93943-5005
Attn: Commanding Officer

National Ocean Data Center
1825 Connecticut Ave., NW
Universal Bldg. South, Rm. 406
Washington DC 20235
Attn: G. Withee, Director

Naval Air Development Center
Warminster PA 18974-5000
Attn: Commander

Naval Air Systems Command HQ
Washington DC 20361-0001
Attn: Commander

Naval Civil Engineering Laboratory
Port Hueneme CA 93043
Attn: Commanding Officer

Naval Coastal Systems Center
Panama City FL 32407-5000
Attn: Commanding Officer

Naval Facilities Engineering
Command HQ
200 Stovall St.
Alexandria VA 22332-2300
Attn: Commander

Naval Oceanographic Office
Stennis Space Center MS 39529
Attn: Commanding Officer

Naval Oceanography Command
Stennis Space Center MS 39529
Attn: Commander

Naval Oceanographic & Atmospheric
Research Laboratory
Stennis Space Center MS 39529-5004
Attn: Code 100
        Code 110
        Code 105
        Code 115
        Code 125L (10)
        Code 125P
        Code 200
        Code 300
        Code 400

Naval Oceanographic & Atmospheric
Research Laboratory
Liaison Office
Crystal Plaza #5, Rm. 802
Arlington VA 22202-5000
Attn: B. Farquhar

Naval Ocean Systems Center
San Diego CA 92152-5000
Attn: Commander

Naval Postgraduate School
Monterey CA 93943
Attn: Superintendent

Naval Research Laboratory
Washington DC 20375
Attn: Commanding Officer

Naval Sea Systems Command HQ
Washington DC 20362-5101
Attn: Commander

Naval Surface Warfare Center
White Oak
10901 New Hampshire Ave.
Silver Spring MD 20904-5000
Attn: Commander
        Library

Naval Surface Weapons Center
Dahlgren VA 22338-5000
Attn: Commander

Naval Underwater Systems Center
Newport RI 02841-5047
Attn: Commander

Naval Underwater Systems Center Det
New London Laboratory
New London CT 06320
Attn: Officer in Charge

Office of Naval Research
800 N. Quincy St.
Arlington VA 22217-5000
Attn: Code 10D/10P, Dr. E. Silva
        Code 112, Dr. E. Hartwig
        Code 12
        Code 10

Office of Naval Research
ONR Branch Office
Box 39
FPO New York 09510-0700
Attn: Commanding Officer

Office of Naval Technology
800 N. Quincy St.
Arlington VA 22217-5000
Attn: Code 20, Dr. P. Selwyn
        Code 228, Dr. M. Briscoe
        Code 234, Dr C. Votaw

Scripps Institution of Oceanography
University of California
P.O. Box 6049
San Diego CA 92106

Space and Naval Warfare
Systems Command
Washington DC 20363-5100
Attn: Commander

Woods Hole Oceanographic Institution
P.O. Box 32
Woods Hole MA 02543
Attn: Director

Oceanography Department
Texas A&M University
College Station TX 77843
Attn: Dr. William Bryant
        Dr. Richard Rezak
        Dr. Aubrey Anderson

Dept. of Civil Engineering.
Soils Dev.
Texas A&M University
College Station TX 77843
Attn: Dr. Wayne Dunlap

Dr. Homa Lee
Mailstop 999
U.S. Geological Survey
345 Middlefield Rd.
Menlo Park CA 94025

Dr. Marcel Lavoie
43 Madbury Rd.
Durham NH

Mr. Chester Leone
RFD #3
Laconia NH

REPORT DOCUMENTATION PAGE

Form Approved
OMB No. 0704-0188

1. Agency Use Only *(Leave blank)*.	2. Report Date.	3. Report Type and Dates Covered.
	July 1990	Final

4. Title and Subtitle.

Geotechnical and Geoacoustic Properties of Periplatform Sediments

5. Funding Numbers.

Program Element No. 61153N

Project No. 03207

Task No. 330

Accession No. DN255014

6. Author(s).

Dawn L. Lavoie

7. Performing Organization Name(s) and Address(es).

Ocean Science Directorate
Naval Oceanographic and Atmospheric Research Laboratory
Stennis Space Center, Mississippi 39529-5004

8. Performing Organization Report Number.

NOARL Report 9

9. Sponsoring/Monitoring Agency Name(s) and Address(es).

Naval Oceanographic and Atmospheric Research Laboratory
Stennis Space Center, Mississippi 39529-5004

10. Sponsoring/Monitoring Agency Report Number.

11. Supplementary Notes.

13. Abstract *(Maximum 200 words)*.

Periplatform sediments from the slopes north of Little Bahama Bank and Exuma Sound were studied extensively for use as a model for sediments in other similar environments within the upper 50 to 150 m below the sea floor where mechanical consolidation is the dominant diagenetic process. The depth at which consolidation is the dominant diagenetic process varies, depending on sediment fabric and grain size. Matrix-supported sediments have a higher proportion of metastable minerals and undergo diagenesis earlier and at shallower depths than grain-supported sediments.

Periplatform sediments consolidate differently than marine clays. Overall, they consolidate less and do not reach as low a void ratio as do marine clays under mechanical consolidation. A volume change model developed from deep-water carbonates appears to be equally applicable to shallow-water and midwater carbonates when consolidation is the dominant process. The major differences in periplatform sediment properties affected by consolidation seem to be roughly controlled by fabric grain size and particle type. Grain-supported sediments have higher permeabilities than matrix-supported sediments because the pore throats are protected by grains. The relationship between permeability and porosity is also controlled by the fabric; total porosity is not a good predictor of permeability. In addition, porometry changes during consolidation revealed changes in pore size and numbers that were a function of matrix composition and grain support.

Physical and acoustic properties vary as a function of effective stress and have been derived for both grain- and matrix-supported periplatform sediments. Compressional wave velocities of periplatform sediments are similar to those predicted using regression equations derived for deep-water carbonates. However, shear modulus and shear wave velocity, measured using duomorphs in the laboratory during consolidation, are significantly lower than predicted using deep-water regression equations. Duomorph technology was used successfully to measure shear modulus and shear wave velocity in the laboratory, although further theoretical work may have to be done to improve their performance at high effective stress levels.

14. Subject Terms.

sedimentology, permeability, geoacoustics, penetration, penetrometers, geotechnical properties

15. Number of Pages.
193

16. Price Code.

17. Security Classification of Report.	18. Security Classification of This Page.	19. Security Classification of Abstract.	20. Limitation of Abstract.
Unclassified	Unclassified	Unclassified	None